Bioactive glass nanoparticles for therapeutic applications

Sarah Louise Greasley

Department of Materials

Imperial College London

This dissertation is submitted for the fulfilment of the degree of

Doctor of Philosophy (PhD)

September 2015

Declaration of Originality

Unless otherwise referenced or acknowledged, all work presented in this thesis is my own and was carried out in the laboratories of Imperial College London during the period of October 2012 to September 2015.

Sarah Greasley, September 2015

Copyright

The copyright of this thesis rests with the author and is made available under a Creative Commons Attribution Non-Commercial No Derivatives licence. Researchers are free to copy, distribute or transmit the thesis on the condition that they attribute it, that they do not use it for commercial purposes and that they do not alter, transform or build upon it. For any reuse or redistribution, researchers must make clear to others the licence terms of this work.

Acknowledgements

I would firstly like to thank my supervisors Professor Julian R. Jones and Dr Alexandra E. Porter for their patient guidance, expertise and continual support throughout my PhD. It has been a fantastic experience being part of the JRJ research group and I thank everyone who has made the last three years so much fun. In particularly I would like to thank Dr Shu Chen for running all of the cell experiments presented in this thesis and for kindly helping me in an area with which I was not familiar. I would also like to thank Dr Yuliya Vueva for her collaboration and for using my nanoparticles in her nano-composite scaffolds which are discussed as part of this thesis. Additionally, the progress made with mesoporous particles would not have been possible without the work done by my MSc student Konstantinos Pietris as part of his research project.

I'd also like to thank many of the staff members within the Materials Department. Ben Chan, for continual support with fixing the ICP, and Mahmoud Ardakani and Ecaterina Ware for their advice, teaching and guidance on the TEM, as well as their help to prepare FIB samples. Thanks also to Richard Sweeney for help and discussions on XRD.

Thanks also goes to Dr Rona Chandrawati from the Stevens group for discussions on nanoparticle functionalisation and help with optical and fluorescent imaging of particles coupled with FITC.

The Imperial-UCL-Warwick-Kent sol-gel collaboration has also been vital for many of the conclusions drawn from this work. Thanks must go to Professor John Hanna and Sam Page at the University of Warwick for running and analysing my solid state Nuclear Magnetic Resonance samples. Thanks also to Slobodan Sirovica and Dr Richard A. Martin from the University of Aston for running SAXS measurements for me on my samples at the European Synchrotron Radiation Facility.

Finally, this research has been funded by the Engineering and Physical Sciences Research Council (EPSRC). I am very thankful for this financial support which has enabled me to complete this PhD.

Abstract

There is great therapeutic potential for bioactive glass nanoparticles, as they can be internalised within cells and achieve sustained intracellular delivery of active ions. Bioactive glass nanoparticles are also used in nano-composites. The Stöber process is commonly used for synthesising spherical silica particles. This thesis reports a comprehensive study of how the process variables can be systematically altered to obtain monodispersed particles of specific sizes in the range 20 – 500 nm. Modification of the Stöber process so that the particles can contain cations such as calcium, which can impart bioactivity, while maintaining monodispersity, is therefore highly desirable.

Here, both zinc and calcium incorporation is achieved, with a homogenous distribution and without affecting the size, dispersity or morphology of the particles. However, careful characterisation shows that much of the cations were not incorporated and a washing step was essential, which suggests that previous reports are likely to have overestimated the amount of calcium incorporated. A maximum of 8.9 ± 1.1 mol % CaO and 22.7 ± 0.8 mol % ZnO was incorporated into the particles. Monodispersed mesoporous silica particles were also synthesised in this thesis, containing up to 18.5 ± 2.7 mol % Ca and 21.5 ± 1.3 mol % Zn. The differences in incorporation between the two cations were attributed to the different roles that they play within the silicate network. Whilst calcium acts purely as a network modifier, zinc can also act as a network former. These differences are seen to affect % cation incorporation, surface area, network connectivity and subsequent degradation. Nanoparticles of 80 - 100 nm were readily internalised by cells, where they were located both within vesicles and also as individual particles within the cytoplasm (having escaped from the endosomal pathway). SiO_2-ZnO mesoporous particles were also seen to subsequently degrade rapidly inside cells, demonstrating preferential toxicity to cancer cells due to pH sensitive intracellular release of toxic Zn^{2+} ions.

SiO_2-CaO particles were successfully functionalised and show great potential for incorporation into nano-composites for bone regeneration.

Contents

Declaration of Originality 2

Copyright 2

Acknowledgements 3

Abstract 4

List of Figures 9

List of tables 14

List of abbreviations 15

1 Introduction 19

1.1 Thesis Roadmap 20

2 Literature review 22

2.1 Bioactive Glass 22

2.1.1 The structure of bioactive glass 22

2.1.2 Mechanisms of bioactivity and the role of cations 23

2.2 Nanoparticle uptake and biological effects 26

2.2.1 Effect of particle size on cell uptake 27

2.3 Nanoparticles for cancer treatment 29

2.3.1 Nanoparticles for drug delivery 29

2.3.2 Inorganic nanoparticles and ionic therapy 30

2.4 Sol-gel synthesis of bioactive glass nanoparticles 32

2.4.1 Processing methods of bioactive glass 32

2.4.2 The Stöber Process: Basic hydrolysis and condensation of silicon alkoxides 34

2.4.3 Mechanism of particle growth 35

2.4.4 Control of particle properties 37

2.4.5 Incorporation of cations 42

2.4.6 Mesoporous particles 45

2.5 Bioactive glass nano-composite scaffolds for bone regeneration 47

2.5.1 Nanoparticle Functionalisation 51
2.5.2 Nano-composite synthesis 52
2.6 Research objectives 56
3 Instrumentation 58
3.1 Transmission electron microscopy (TEM) 58
3.1.1 Energy dispersive X-ray spectroscopy (EDS) 59
3.1.2 Scanning transmission electron microscopy (STEM) 59
3.2 X-ray fluorescence (XRF) 59
3.3 Dynamic light scattering (DLS) 60
3.4 Fourier transform infrared (FTIR) 60
3.5 Inductively coupled plasma - optical emission spectroscopy (ICP-OES) 60
3.6 X-ray diffraction (XRD) 61
3.6.1 Small-angle X-ray scattering (SAXS) 61
3.7 Solid state Nuclear Magnetic Resonance (NMR) 62
3.8 Focused Ion Beam - Scanning Electron Microscopy (FIB-SEM) 62
3.9 Zeta Potential 63
3.10 Nitrogen Adsorption 63
4 Synthesis of silica nanoparticles and control of particle size 65
4.1 Introduction 65
4.2 Materials and methods 65
4.2.1 Particle Synthesis 65
4.2.2 Particle characterisation 66
4.3 Results & Discussion 67
4.4 Conclusions 72
5 Cation incorporation in to silica nanoparticles 73
5.1 Introduction 73
5.2 Materials and methods 73
5.2.1 Particle Synthesis 73

5.2.2 Acid digestion composition analysis 75
5.2.3 Particle sectioning using FIB 75
5.2.4 Particle characterisation 75
5.3 Results & Discussion 77
5.3.1 Adjustments to method 77
5.3.2 Mechanism of cation incorporation 78
5.3.3 Composition analysis 83
5.3.4 Structural differences between particles 86
5.4 Conclusions 96
6 Synthesis of mesoporous silica nanoparticles and incorporation of cations 97
6.1 Introduction 97
6.2 Materials and methods 97
6.2.1 Particle Synthesis 97
6.2.2 Particle characterisation 99
6.3 Results & Discussion 100
6.3.1 Synthesis of mesoporous silica nanoparticles 100
6.3.2 Cation incorporation into mesoporous particles 102
6.4 Conclusions 113
7 Particle degradation and fate within cells 114
7.1 Introduction 114
7.2 Materials and methods 115
7.2.1 Cell studies 115
7.2.2 Ion dissolution studies 117
7.3 Results and discussion 119
7.3.1 Cell uptake of SiO_2-ZnO particles 119
7.3.2 Particle toxicity 126
7.3.3 Particle degradation 130
7.4 Conclusions 139

8 Functionalisation of particles and incorporation into nano-composites 140
8.1 Introduction 140
8.2 Materials and methods 140
8.2.1 Functionalisation 141
8.2.2 Fluorescein Coupling 141
8.2.3 Particle characterisation 141
8.2.4 NP-Alginate nano-composite synthesis 141
8.2.5 Nano-composite characterisation 142
8.3 Results & Discussion 143
8.3.1 Functionalisation 143
8.3.2 Nano-composite Synthesis 146
8.4 Conclusions 149
9 Overall conclusions and future work 150
9.1 Future Work 152
References 154
Appendix 1 – STEM-EDS of cell cytoplasm 166
Appendix 2 – STEM-EDS on dissolution products 167

List of Figures

Figure 2.1 - 2D structure of bioactive glass.....23
Figure 2.2 - Examples of cell uptake mechanisms of nanoparticles by endocytosis. 28
Figure 2.3 - Overview of how the sol-gel process can be adapted to produce different materials. Modified from [85]. 33
Figure 2.4 - Base-catalysed hydrolysis. 34
Figure 2.5 - Schematic representation of the concentration of precipitating species before and after nucleation. Modified from [85]. 36
Figure 2.6 - Schematic illustrating the nucleation and aggregation mechanism of particle growth. 37
Figure 2.7 - Final particle sizes obtained by reacting 0.28M of TEOS with various concentrations of water and ammonia in ethanol, modified from [86]. The red lines shown correspond to the concentrations required to form particles of 200nm. 39
Figure 2.8 - Bioactive glass nanoparticles produced using a variety of different methods, demonstrating the difficulties in producing monodispersed particles a) Xia *et al.* [110], b) Luz *et al.* [111], c) Labbaf *et al.* [82], d) de Oliveira *et al.* [114]. 43
Figure 2.9 - Schematic illustrating the evolution of calcium distribution during sol-gel processing. Modified from [84]. 44
Figure 2.10 - Schematic phase diagram showing mesophases of cetyl trimethylammonium bromide (CTAB) in water with increasing concentration. Modified from [126]. 45
Figure 2.11 - Mesoporous bioactive glass nanoparticles produced using a sol-gel method. Modified from [63]. 47
Figure 2.12 - Photograph of a human femur with an X-ray microtomography image of a region of the cancellous bone. Modified from [16]. 48
Figure 2.13 - Schematic of a class II silica/polymer II hybrid material [132]. 50
Figure 2.14 - Schematic of carbodiimide (EDC/NHS) carboxyl-to-amine crosslinking reaction. Modified from [152,156]. 56
Figure 3.1 - Schematic of a TEM operating in imaging mode. Modified from [157]. 59
Figure 3.2- Schematic of XRD setup. Modified from [158]. 61
Figure 3.3 – Updated IUPAC classification of physisorption isotherms. Modified from [161]. 64
Figure 4.1 - Schematic showing the synthesis of silica nanoparticles. 66
Figure 4.2- A) Mean particle size of silica particles (DLS) as a function of water and ammonium hydroxide concentration for 0.28M TEOS. Error bars show the standard deviation from the mean (n=3). B) DLS results showing particle size distribution with increasing ammonium hydroxide concentration for 0.28M TEOS and 6M H_2O. 67

Figure 4.3 - TEM images of silica particles produced using 0.28M TEOS, 6M H_2O and varying concentrations of ammonium hydroxide: A) 0.056M NH_4OH B) 0.11M NH_4OH C) 0.17M NH_4OH D) 0.28M NH_4OH E) 0.40M NH_4OH F) 0.57M NH_4OH G) 0.85M NH_4OH H) 1.13M NH_4OH. 68
Figure 4.4 - TEM images of silica particles produced using 0.28M TEOS, 0.28M NH_4OH and varying concentrations of water: A) 3M H_2O B) 6M H_2O C) 9M H_2O D) 12M H_2O E) 15M H_2O. 69
Figure 4.5- A comparison of DLS (number mean) and TEM results for silica particles showing variation of mean particle size with: A) ammonium hydroxide concentration for 0.28M TEOS and 6M H_2O and B) water concentration for 0.28M TEOS and 0.28M NH_4OH. Error bars for TEM results show the standard deviation of particle size in each sample (n=100). 69
Figure 4.6 - Standard deviation as a % of particle size calculated from TEM results (n=100). 71
Figure 4.7 - Mean particle size of silica particles (DLS) as a function of ammonium hydroxide concentration for 6M H_2O and increasing TEOS concentrations. Error bars show the standard deviation of mean size (n=3). Inset shows heterodispersed particles at high TEOS and NH_4OH concentrations. 71
Figure 5.1 - Schematic showing the method of incorporation of calcium in to silica nanoparticles. 74
Figure 5.2 - Particles of different sizes after the addition of calcium nitrate and calcination (before the introduction of the step in which the supernatant was removed and particles were re-dispersed in distilled water). Particles are made with 0.28M TEOS, 6M H_2O and increasing ammonium hydroxide concentrations: A) 0.17M NH_4OH, B) 0.28M NH_4OH, C) 0.40M NH_4OH, D) 0.51M NH_4OH .78
Figure 5.3 - SAXS data for: (A) silica particles, after drying at 60°C; (B) silica particles, heated to 680˚C; (C) SiO_2-CaO particles synthesised with 0.28M TEOS, 0.17M NH_4OH, 6 M H_2O and a Ca:Si ratio of 1.3:1, after drying at 60°C and (D) SiO_2-CaO particles heated to 680˚C. (courtesy of Slobodan Sirovica, University of Aston). 79
Figure 5.4 - TEM images of silica particles (0.28M TEOS, 0.17M NH_4OH, 6 M H_2O) A) before the addition of calcium B) after the addition of calcium (Ca:Si ratio of 1.3:1) and heating to 680˚C and C) after subsequent washing in ethanol. 80
Figure 5.5 - XRD patterns of Si particles doped with Zn A) After drying, B) After heating at 680˚C and C) after washing in 1M NaOH. 81
Figure 5.6 - Distribution of elements through FIB cross sections of 500 nm particles of composition 94.6 mol% SiO_2, 5.4 mol% CaO, using AZtec imaging software on TEM. 82
Figure 5.7 - Distribution of elements through FIB cross sections of 500 nm particles of composition 98.6 mol% SiO_2, 1.4 mol% ZnO, using AZtec imaging software on TEM. 83
Figure 5.8 - Incorporation of calcium in 100 nm particles (0.28 M TEOS, 6 M H_2O, 0.17 M NH_4OH) as a function of Ca added relative to Si 84

Figure 5.9 - ICP results showing incorporation of Ca into 100 nm particles (0.28 M TEOS, 6 M H_2O, 0.17 M NH_4OH) and Zn into 80 nm particles (0.28 M TEOS, 6 M H_2O, 0.14 M NH_4OH) as a function of the element added relative to 100 mol% Si. 85
Figure 5.10 - TEM images of silica NPs containing cations Zn and Ca added in an 8:1 ratio relative to Si: A) Zn, B) Ca. 86
Figure 5.11- XRD patterns of A) 100 nm Stöber particles and B) 100 nm silica particles doped with 9% Ca (after calcination and washing). 87
Figure 5.12- XRD patterns of silica particles doped with an increasing percentage of Zn (after calcination and washing). 87
Figure 5.13 - A) HR-TEM of 23Zn particles showing small crystalline areas corresponding to zinc silicate oxide (willemite Zn_2SiO_4) within the nanoparticles B) Diffraction pattern of a crystalline area within nanoparticle (courtesy of Dr Shu Chen, Imperial College London). 88
Figure 5.14– HR-TEM of 9Ca particles showing amorphous morphology (courtesy of Dr Shu Chen, Imperial College London). 90
Figure 5.15 - FTIR spectra of silica NPs containing different concentrations of Zn and Ca cations after calcination and washing (unless stated). 91
Figure 5.16- 29Si MAS NMR spectra for (A) 100Si particles (unheated) (B) 9Ca particles (unheated) (C) 100Si particles (heated) and (D) 9Ca particles (heated) (courtesy of Sam Page, University of Warwick). 92
Figure 5.17 - 1H MAS NMR spectra for (A) 100Si particles (heated) and (B) 9Ca particles (heated) (Courtesy of Sam Page, University of Warwick). 94
Figure 5.18 - 29Si MAS NMR spectra (left) and 1H MAS NMR spectra (right) for Zn containing particles (11Zn, 16Zn and 23Zn) (courtesy of Sam Page, University of Warwick). 95
Figure 6.1 - TEM images of mesoporous particles synthesised using methods from literature. A) Lin *et al.* 2005 [68], B-D) Shimura & Ogawa, 2007 [120], E,F) Shi *et al.* 2010 [121], G,H) Nooney *et al.* 2002 [122], I) Chang *et al.* 2013 [70], J) Cui *et al*. 2013 [180] 101
Figure 6.2 - TEM images of mesoporous silica nanoparticles synthesised using method by Chang et al. [70] at A) Low magnification and B) High magnification. 102
Figure 6.3 - TEM images with EDS spectra (below) for mesoporous silica nanoparticles with incorporated cations A) 22Zn and B) 19Ca. 103
Figure 6.4- ICP results showing incorporation of Ca and Zn into mesoporous silica nanoparticles (as a function of the element added relative to 100 mol% Si). 103
Figure 6.5 - Nitrogen sorption isotherms for mesoporous silica nanoparticles containing different concentrations of Ca and Zn cations 106

Figure 6.6 - Pore size distribution of mesoporous silica nanoparticles containing different concentrations of Ca and Zn cations , obtained by DFT analysis of nitrogen sorption data. 107
Figure 6.7- XRD patterns of mesoporous silica nanoparticles containing different concentrations of Ca and Zn cations after calcination and washing. 109
Figure 6.8 - FTIR spectra of mesoporous silica nanoparticles containing different concentrations of Ca and Zn cations, after calcination and washing. 110
Figure 6.9 - ^{29}Si MAS NMR spectra (left) and ^{1}H MAS NMR spectra (right) for mesoporous silica nanoparticles containing different concentrations of Ca and Zn cations (courtesy of Sam Page, University of Warwick). 111
Figure 6.10 - Effect of Zn and Ca cation incorporation on network connectivity of mesoporous silica nanoparticles. 111
Figure 7.1 - Experimental setup for ionic dissolution study of bioactive glass nanoparticles in solution. 119
Figure 7.2 - TEM images showing particle uptake of dense 11Zn NPs into MCF-7 cells after 24h incubation at a concentration of 50 μg.ml^{-1} (courtesy of Dr Shu Chen, Imperial College London) showing active uptake of clusters of particles by macropinocytosis and interactions of both individual and clusters of particles with the cell membrane. 120
Figure 7.3 - TEM image of MCF-7 cell showing internalised particles after 24 h exposure to dense 80 nm 11Zn NPs at a concentration of 50 μg.ml^{-1} (courtesy of Dr Shu Chen). Particles can be seen both within vesicles and in the cytoplasm. 120
Figure 7.4 - TEM image of MCF-7 cell after 24 h exposure to dense 80 nm 11Zn NPs at a concentration of 50 μg.ml^{-1} showing particles appearing to diffuse directly through the cell membrane (courtesy of Dr Shu Chen). 123
Figure 7.5- TEM images of 100Si and 11Zn nanoparticles found in a lysosome of a MCF-7 cell after 24 h exposure. The lysosome in a control cell is also shown. (Courtesy of Dr Shu Chen). Unlike the pure silica particles, the zinc containing particles appear to affect the morphology of the lysosome. 124
Figure 7.6 - TEM images of dense 80 nm 11Zn particles internalised by an MCF-7 cell after 24 h exposure at a concentration of 50 μg.ml^{-1}. STEM-EDS results show that zinc is still present inside the particles (area 1), although is not present outside the particles (area 2). (Courtesy of Dr Shu Chen). 125
Figure 7.7- TEM images after 24 h exposure of A,B) Mesoporous 100Si particles inside an MCF-10a cell (low and high mag) and C,D) Mesoporous 14Zn particles inside an MCF-7 cell (low and high mag). An area of STEM-EDS showing the absence of zinc is also shown (courtesy of Dr Shu Chen). 126

Figure 7.8 - Cell viability assay (WST-1) results for MCF-7 and MDA-MB-231 cell lines exposed for 24, 48 and 72 h with Zn^{2+} ions (from $Zn(NO_3)_2$), 11Zn NPs and 100Si NPs of 80 nm at concentrations 25 - 250 $\mu g.ml^{-1}$ (n=3) (courtesy of Dr Shu Chen). 128
Figure 7.9 - Cell viability assay (WST-1) results for MCF-7, MDA-MB-231 and MCF-10A cell lines exposed for 24 h to A) 14Zn MSNs and B) 100Si MSNs of 80nm at concentrations 25 - 250 $\mu g.ml^{-1}$ (courtesy of Dr Shu Chen). 129
Figure 7.10 - Ion release profiles for particles over 24 h in ALF. 131
Figure 7.11 - Ion release profiles for particles over 24 h in MEM. 132
Figure 7.12- Ion release profiles for particles over 24 h in MEM + FBS. 133
Figure 7.13 - Dark field TEM images of MCF-7 cell showing internalised dense 80 nm 11Zn NPs particles after 24 h exposure at a concentration of 50 $\mu g.ml^{-1}$ (courtesy of Dr Shu Chen). 138
Figure 8.1 - TEM images showing morphology of SiO_2-ZnO bioactive glass nanoparticles (0.28M TEOS, $6MH_2O$, 0.14M NH_4OH) A) Before functionalisation, B) After functionalisation with APTES. 143
Figure 8.2 - Zeta potential measurements of bioactive glass nanoparticles before and after functionalisation with APTES. 144
Figure 8.3 - FTIR results for 100nm SiO_2-CaO nanoparticles before and after functionalisation with APTES. 145
Figure 8.4 - Optical microscope images of functionalised NPs + FITC, Non-functionalised NPs + FITC and functionalised NPs (no FITC). Corresponding fluorescent microscope images are shown below. 146
Figure 8.5- Photos of 3D printed NP-Alginate scaffold A) Before freeze drying and B) After freeze drying (courtesy of Dr Yuliya Vueva). 147
Figure 8.6 - A) SEM image (courtesy of Dr Yuliya Vueva) and B) TEM image (courtesy of Dr Shu Chen), of a freeze dried NP-Alginate nano-composite scaffold. 147
Figure 8.7 - 3D printed scaffolds after 24 hour immersion in dH_2O for A) NP-Alginate nano-composite scaffold and B) silica-alginate hybrid scaffold (without NPs) (courtesy of Dr Yuliya Vueva). 148
Figure 8.8 - Mechanical testing results for silica-alginate scaffolds showing the compressive strength under A) Dry conditions, and B) Wet conditions (courtesy of Dr Yuliya Vueva) 148

List of tables

Table 2.1 Summary of BGNP/polymer composites 53
Table 5.1- Summary of particles produced containing different quantities of cations. 85
Table 5.2- Peak list for Willemite, Zn_2SiO_4 89
Table 5.3 - Q distributions obtained from single pulse 29Si MAS NMR spectra for dense particles (courtesy of Sam Page, University of Warwick). 95
Table 6.1 - Methods used for the synthesis of mesoporous silica nanoparticles. 98
Table 6.2 - Summary of mesoporous nanoparticles produced containing different quantities of cations. 104
Table 6.3 - Q distributions obtained from single pulse 29Si MAS NMR spectra for mesoporous silica nanoparticles containing different concentrations of Ca and Zn cations (courtesy of Sam Page, University of Warwick). 110
Table 7.1 - Reagents used for making artificial lysosomal fluid (ALF) [188-191]. 118
Table 7.2 - Zeta potential measurements for particles in distilled water and cell culture media. 121
Table 7.3 - TEM images of particles before and after 24 h dissolution in ALF, MEM and MEM + FBS. 134

List of abbreviations

70S30C	30 mol% CaO, 70 mol% SiO_2
ADSC	Adipose-derived stem cell
ALF	Artificial lysosomal fluid
APTES	3-aminopropyltriethoxysilane
APTS	3-aminopropyltrimethoxysilane
BET	Brunauer–Emmett–Teller
BGNP	Bioactive glass nanoparticle
BJH	Barrett–Joyner–Halenda
CMC	Critical micelle concentration
CME	Calcium methoxyethoxide
CNT	Carbon nanotube
CPTS	Chloropropyltriethoxysilane
CTAB	Cetyl trimethylammonium bromide
DCC	Dicyclohexyl carbodiimide
DMEM	Dulbecco's modified Eagle's medium
DFT	Density functional theory
DLS	Dynamic light scattering
EDC	1-(3-Dimethylaminopropyl)-3-ethylcarbodiimide hydrochloride
EDS	Energy-dispersive X-ray spectroscopy
EISA	Evaporation-induced self-assembly
EPR	Enhanced permeability and retention
ER	Estrogen receptor

FBS	Fetal bovine serum
FDA	Food and drug administration
FIB	Focused Ion Beam
FITC	Fluorescein isothiocyanate
FTIR	Fourier transform infrared
GPTS	3-glycidyloxypropyltrimethoxysilane
HAADF	High angle annular dark field
HCA	Hydroxycarbonate apatite
HER2	Human epidermal growth factor receptor 2
hMSC	Human mesenchymal stem cell
HR-TEM	High resolution transmission electron microscopy
ICP-OES	Inductively coupled plasma-optical emission spectroscopy
IR	Infrared
IUAPC	International Union of Pure and Applied Chemistry
MAS	Magic angle spinning
McPTS	3-mercaptopropyltriethoxysilane
MEM	Minimum essential medium
MPS	Mononuclear phagocyte system
MPTS	Methacryloxypropyltriethoxysilane
MSC	Mesenchymal stem cell
MSN	Mesoporous silica nanoparticle
NBO	Non bridging oxygen
NC	Network connectivity

NHS	N-hydroxysuccinimide
NIR	Near-infrared
NLDFT	Nonlocal density functional theory
NMR	Nuclear magnetic resonance
NNLS	Non-negative least squares
NP	Nanoparticle
PBS	Phosphate buffer saline
PCL	Polycaprolactone
PDI	Polydispersity index
PEG	Polyethylene glycol
PGA	Polyglutamic acid
PGLA	Poly(lactide-co-glycolide)
PLLA	Poly(L-lactide)
QD	Quantum dot
PR	Progesterone receptor
RI	Refractive index
RLMCA	Reaction-limited monomer-cluster aggregation
ROS	Reactive oxygen species
SAXS	Small-angle X-ray scattering
SBF	Simulated body fluid
SDD	Silicon Drift Detector
SEM	Scanning Electron Microscopy
STEM	Scanning transmission electron microscopy

TEM	Transmission electron microscopy
TEOS	Tetraethyl orthosilicate
THF	Tetrahydrofuran
TNBC	Triple-negative breast cancer
VTS	Vinyltriethoxysilane
XRD	X-ray diffraction
XRF	X-ray fluorescence

1 Introduction

The use of nanotechnology in medicine is a rapidly growing field and there are a large variety of nano and sub-micron particles currently being developed for medical applications. Nanomedicine can be defined as “the use of nanoscale or nanostructured materials in medicine that according to their structure have unique medical effects” [1]. Due to their size and large surface area to volume ratio, the properties of nanoparticles differ to those of the bulk materials. A nanoparticle is typically described as "a particle having one or more dimensions of the order of 100nm or less"; although sub-micron particles still exhibit many of the same characteristics and the terms are often used interchangeably. Additionally, mesoporous nanoparticles can be defined an nanoparticles which have a modal pore size ranging from between 2 and 50 nm [2]. There is a huge potential for the use of nano and sub-micron particles in a wide variety of medical applications including drug delivery, therapy, *in vivo* imaging, *in vitro* diagnostics, ‘theranostics’ [3,4], biomaterials and active implants [1]. This thesis focuses on the synthesis of inorganic nanoparticles for therapeutic applications. Specifically it will look at bioactive glass nanoparticles (consisting of a silicate network modified by Zn or Ca ions) for cancer treatment and incorporation into nano-composite scaffolds for bone regeneration respectively.

It is estimated that over 2.2 million grafting procedures are performed annually worldwide, with bone being the second most commonly transplanted tissue after blood [5]. A synthetic alternative is therefore highly desirable. The first bioactive glass was discovered by Larry Hench in 1969 and found to form a strong bond with bone, as well as encouraging bone regrowth [6]. Since its discovery, bioactive glass has been synthesised in several forms (including nanoparticles) using a variety of different processing methods and incorporating multiple different cations within a silicate network. However, the main drawback of bioactive glass scaffolds for use in load bearing applications are their mechanical properties. There is consequently much research currently being conducted on the synthesis of bioactive glass hybrids and nano-composite materials with an organic phase to increase toughness. SiO_2 – CaO bioactive glass systems have been shown to be highly bioactive [7-9], with body fluid providing an adequate source of phosphate ions for hydroxycarbonate apatite (HCA) formation. This work will therefore focus on the synthesis of bioactive glass nanoparticles with a target composition of 70S30C (30 mol% CaO, 70 mol% SiO_2) for subsequent incorporation into nano-composite scaffolds for bone regeneration applications. Whilst silica nanoparticles of a variety of sizes have been routinely synthesised in literature, the addition of calcium has been seen to significantly complicate the synthesis process and the incorporation of high levels of calcium has not been achieved.

Although most literature on bioactive glasses currently focuses on bone regeneration applications, the ability of bioactive glass to degrade and deliver ions *in vivo*, makes it extremely desirable for multiple therapeutic applications including cancer treatment. Cancer is currently one of the leading causes of death worldwide. It results in 29% of all deaths in the UK, with 161,823 deaths in the UK due to cancer in 2012 [10]. Current non-surgical cancer treatments involve radiation and chemotherapy which cause toxicity to the patient and also kill healthy cells. There is consequently an increasing desire to be able to develop therapies that specifically target cancer cells, with a rapidly growing interest in nanotechnology. Nanoparticle based therapeutics (primarily liposomes) have been used for decades as drug delivery vehicles for anticancer drugs, with ten therapies currently approved for clinical use and many more in clinical trials [11]. However, new research (*in vitro* and *in vivo*) into inorganic ZnO nanoparticles has shown that they are able to cause toxicity to cancer cells without the need for a complex drug delivery system [12]. The release of Zn^{2+} ions from ZnO particles as a result of rapid dissolution in the acidic cancer microenvironment has been shown to induce damage to the plasma membrane and mitochondria leading to preferential apoptosis of cancer cells [13]. Here, the aim is to incorporate zinc into silica nanoparticles to provide a more controlled and sustained release of toxic Zn^{2+} ions to cancer cells by a pH sensitive release mechanism. Although zinc containing bioactive glass systems have been synthesised in literature [14,15], zinc has not previously been incorporated into bioactive glass nanoparticles.

1.1 Thesis Roadmap

A review of current literature related to this thesis is conducted in Chapter 2, focussing on bioactive glass, the synthesis of nanoparticles and their effects within the body. Throughout this project a variety of techniques will be used to characterise the particles produced. All instrumentation used and the theory behind it will be described in Chapter 3.

The first aim of this thesis will be to perform a comprehensive study of how the process variables can be altered to obtain monodispersed silica nanoparticles of specific sizes in the range 20 – 500 nm (Chapter 4). Subsequently, in Chapter 5 the incorporation of Zn and Ca cations will be investigated for cancer treatment and bone regeneration applications respectively (whilst aiming to maintain the size, morphology and dispersity of the silica particles). Investigation into mesoporous silica nanoparticles and the addition of both Zn and Ca will be conducted in Chapter 6, with the hypothesis being that these particles should degrade faster than their dense counterparts. In Chapter 7 dissolution studies will be carried out on all particles produced, in an attempt to understand the degradation mechanisms of the particles in various solutions *in vitro*. Cell studies will also be performed on the Zn containing particles in order to investigate particle uptake and

preferential toxicity in cancer cells. Finally, Chapter 8 will look at the functionalisation and incorporation of calcium containing bioactive glass nanoparticles into a nano-composite scaffold, before the final conclusions and future work are presented in Chapter 9.

2 Literature review

2.1 Bioactive Glass

Bioactive glasses are essentially silicate glasses modified by the addition of other elements. The term "bioactive" refers to a material that stimulates a beneficial biological response from human cells [16]. Bioactive glasses have been used as a material to incorporate multiple cations including Ca, Na, P, K, Sr, and Zn, which is possible due to their amorphous structure. The very first bioactive glass, invented by Larry Hench at the University of Florida in 1969, was 45S5 Bioglass® (with composition 46.1 mol% SiO_2, 24.4 mol% Na_2O, 26.9 mol% CaO and 2.6 mol% P_2O_5) [6]. It was the first artificial material that was found to chemically bond to bone and the field of bioactive ceramics was created. However, since then many different elements have also been incorporated into the silica network, which are desirable for a variety of biological reasons. An example of this is strontium which can be released from Sr-doped bioactive glasses at the required quantities to inhibit osteoclast activity in osteoporosis sufferers [17].

Current bioactive glass products which have been FDA approved for clinical use include NovaBone and Novamin®, which are microparticles of the 45S5 composition, both of which have been shown to degrade, releasing soluble silica, calcium and phosphate ions in to the body, resulting in osteoinduction. This demonstration of bioactive glass as a material for the delivery of ions for ionic therapy has various potential applications. Here, we will focus on the incorporation of Ca ions for bone regeneration and Zn ions into silica nanoparticles for cancer treatment.

2.1.1 The structure of bioactive glass

The structure of bioactive glass is dependent on the quantities of different elements incorporated into the silicate network and the different roles that they play in modifying that network. Silicate glasses are formed from a network of silica tetrahedra connected by oxygen bonds such that each silicon atom is connected to 4 oxygen atoms. This gives the network a connectivity of Q^4 where 4 is the number of -Si-O-Si- bridging oxygen bonds. In these glasses Si is known as the 'network former'. Calcium and sodium can be added to the network where they act as 'network modifiers', disrupting the silicon network by the formation of non-bridging oxygen bonds such as $-Si-O^- {}^+Na$ (shown in Figure 2.1). This reduces the Q number of the network.

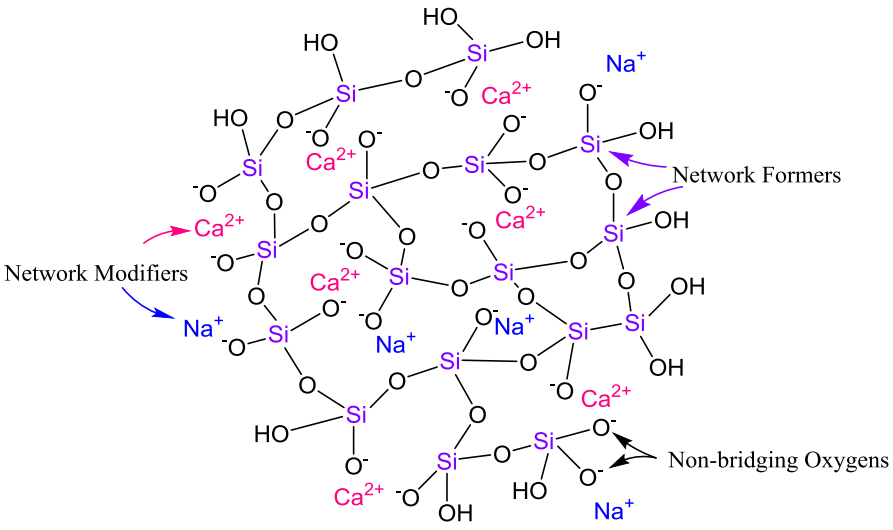


Figure 2.1 - 2D structure of bioactive glass.

A cation can act as either a network modifier (e.g. Ca, Na), a network former (e.g. Si), or an intermediate (e.g. Mg, Zn) [18] depending on its size to charge ratio [19]. An intermediate, such as Zn^{2+}, is an element which can act as both a network modifier and a network former, creating either non-bridging oxygen's or resulting in the presence of Si-O-Zn bonds within the network. Unlike silica which is exclusively found in tetrahedral coordination, zinc can sometime be present as 5 or 6-coordinate species [20]. Calcium (which acts as a network modifier) has also been reported to have a Ca-O coordination of 5 or 6 [21,22]. When both Zn and Ca are present in a glass, Zn acts as network former with the negatively charged (2-) ZnO_4 tetrahedra attracting Ca^{2+} ions and removing them from their network modifying role. If there are not enough Ca^{2+} ions (or alternative alkaline ions) present to balance the charge created by the Zn network, the Zn ions will instead act as a network modifier [23,24]. Phosphorous, on the other hand generally remains isolated from the silicate network as orthophosphate (PO_4) units, charge balanced by calcium and sodium cations [25].

By understanding the structural role of ions within the bioactive glass network it is possible to predict their release and the potential for therapeutic applications.

2.1.2 Mechanisms of bioactivity and the role of cations

A bioactive material can be defined as 'a material that stimulates a beneficial response in the body' [16]. The level of bioactivity of a material is dependent on its surface chemistry and relates to the extent of the response that it generates within the body. In the case of bone regeneration applications a bioactive material should be both osteoinductive and osteoconductive. Osteoinduction is the process by which host mesenchymal stem cells are stimulated to differentiate

into bone-forming osteoblasts [26] and osteoconduction refers to bone growth on the surface of the material in contact with host bone. Bonding to host bone is desirable as it forms a stable bond at the bone-material interface in contrast to a bio inert material which triggers fibrous encapsulation. Bioactivity is often predicted *in vitro* by whether a biologically active HCA layer forms on the surface of the glass when placed in Simulated Body Fluid (SBF). HCA is a naturally occurring mineral (often referred to as 'bone mineral'), containing both calcium and phosphorous ions, and makes up about 50% of natural bone by weight.

The mechanism of bioactivity in bioactive glasses is a multi-step process [27]. Initially cations in the glass network exchange with H^+ ions from solution to form Si-OH (silanol) bonds. This is followed by condensation and re-polymerisation of some Si-OH bonds, resulting in a silica rich surface layer (Si-OH + Si-OH → Si-O-Si). Calcium and phosphate ions then begin to migrate to the surface forming an amorphous calcium phosphate film, which incorporates OH^- and CO_3^{2-} anions from solution to become a crystalline HCA layer. Adsorption of biological molecules onto the HCA and the action of macrophages allows osteogenic cells to attach to the surface [27].

The original 45S5 composition was melt-derived, where components are melted in a crucible and quenched to make a glass. Sodium carbonate is used as a flux to lower the melting point, which introduces sodium as a network modifier. An alternative method of glass making is a bottom up process named sol-gel (section 2.4). As melting is not part of the process, sodium is not a necessary component. It was originally believed that a glass required both phosphorous and calcium components in order to form a successful bond to bone via the formation of an HCA layer, however more recently it has been proved that phosphorous is not an essential constituent, with body fluid providing an adequate source of phosphate ions for HCA formation [28]. While binary glasses of up to 90 mol% silica have demonstrated bioactive capabilities [28], most research into binary glasses currently focuses on the 70S30C composition which has shown promising results and is thought to be a suitable composition for bone tissue regeneration [7-9]. Glass scaffolds of composition 70 mol% SiO_2, 30 mol% CaO have been demonstrated to be bioactive, supporting the growth, infiltration, proliferation and differentiation of osteoblasts [9]. However, a systematic study has not been carried out to compare the effects of different sol-gel compositions *in vivo.*

It is clear that the early stages of bioactivity are linked closely to dissolution, which is dependent on the connectivity of the network. Thus, glasses with a lower Q number will also be more bioactive and the bioactivity of a glass can be increased by adding increasing amounts of network modifiers such as calcium. It has also been shown that ionic dissolution products from the glasses, in the form of

silicon and calcium ions, up-regulate genes found in osteoblasts, directly stimulating osteogenesis at the genetic level [29].

More recently there has been research done on the incorporation of additional ions such as zinc into bioactive glasses [18-20,23,24,30-37]. Zn is naturally found in the body and is important for a wide variety of healthy bodily functions from enzyme activation to gene expression and childhood growth [38]. As well as antibacterial properties [19,23,39], small quantities of Zn have also been shown to promote the initial stages of wound healing [30,38,40], improve osteoblast adhesion to scaffolds [18,33] and promote cell proliferation, osteogenic differentiation [15,18,23] and bone formation [30,37,39]. In addition to the benefits from zinc ion release, Zn incorporation into SiO_2-CaO bioactive glasses has been shown to delay dissolution and enhance the growth of the surface calcium phosphate layer to provide an improved bonding interface for bone [41]. However, in high quantities it is known to be toxic [42] and has also been seen to promote osteoarthritis [40]. Therefore, it is important to understand the mechanism of zinc incorporation and subsequent dissolution in order to get controlled release at the desired level. As zinc acts as both a network former and network modifier it can have different effects on the mechanism of bioactivity. Network modifiers will reduce the connectivity of the silica network resulting in faster degradation. Additionally, when it acts a network former, the Si-O-Zn bonds weaken the silica structure resulting in a lower glass transition temperature (T_G) [35] and faster degradation of the resultant bioactive glass. Si-O-Zn bonds have been seen to remain intact at neutral pH although degrade rapidly under acidic conditions (pH 4.5) [19]. However, in comparison to Ca^{2+} ions, Zn^{2+} ions have a smaller radii and therefore when acting as a network modifier, the resultant structure is comparatively more compact and dissolution rate of the glass is shown to decrease [18]. The substitution of Zn for Ca into bioactive glass systems produces denser glasses with a higher chemical stability [32].

Until now most literature has looked at the incorporation of zinc into multi component glass, substituting it for a variety of elements. The overall effect of Zn on the bioactivity of the glass and its role within the network has been seen to be highly dependent on its concentration and the composition of the glass [35], although it is generally agreed that it tends to result in slower dissolution [42] and reduced release rates of other ions [20]. However, the exact role of zinc and the effect of its incorporation alone on the silica network are still unclear. There are also differences between melt-derived [18,19,30] and sol-gel glasses [31-34] and as yet, no research has been done on its incorporation into silica nanoparticles.

The mechanisms of bioactivity and degradation are likely to be accelerated in nanoparticles, compared to larger samples of the same composition, due to a larger surface area to volume ratio. Nanoparticles could also be used to release ions intracellularly for targeted ionic therapies.

2.2 Nanoparticle uptake and biological effects

Both the physical and chemical properties of nanoparticles differ substantially to those of the bulk materials. As nanoparticles can be manipulated at the same microscopic scale as common biological subjects such as cells (10 - 100 µm), viruses (20 - 450 nm) and proteins (5 - 50 nm), they have attracted tremendous attention for various biomedical applications. The field of nanomedicine attempts to exploit these characteristics of nanoparticles for the development new diagnostics and therapies for treatment of human diseases.

Nanomaterials can move throughout the body, depositing in target organs and penetrating cells where they may trigger undesirable cellular responses or even cell death [43]. Hence, it is thought that nanoscale materials affect biological behaviour at the cellular, subcellular and right down to the protein level [44]. Understanding the *in vitro* interaction of nanoparticles with biological cells, i.e. cell uptake mechanism, intracellular distribution and physicochemical change caused by nanoparticles, is a critical initial step toward their successful application. First of all, nanoparticles must be evaluated *in vitro* at the cellular level before they can be tested *in vivo* at the tissue, organ, and body levels. Secondly, as nanoparticle bio-reactivity is strongly linked with nanoparticle-cell interactions, sufficient knowledge of this interaction must be gained first in order to optimise the properties of nanoparticles for various therapeutic applications.

The unique physico-chemical properties of nanoparticles pose many challenges to current methods for assessment of toxicity which were designed for chemical toxicology. Dhawan and Sharma reviewed the toxicological effects of some of the most widely used nanoparticles. For metal oxide nanoparticles these range from membrane damage and induction of inflammatory responses, to DNA damage and apoptosis [45]. The interaction of nanoparticles with biological cells is dependent on the size, shape, charge and surface properties of the nanoparticles and is also specific to different cell types [46]. For example, positively charged nanoparticles have been shown to have greater internalisation efficiency [47]. Surface chemistry has also been shown to affect the formation and composition of the protein corona on silica nanoparticles in physiological environments, which in turn affects particle agglomeration, uptake and ultimately cytotoxicity [48]. Huang *et al.* found that particles with larger aspect ratios had a greater rate of cell uptake and a larger impact on different aspects of cellular function including cell proliferation, apoptosis and cytoskeleton formation [49]. Cancer cells in particularly have also been found to be more greatly affected by nanoparticles due to

their faster metabolism rates resulting in more rapid effects [50]. Therefore nanoparticles should not be viewed as passive carriers for therapeutic applications but can also be designed to play an active role in determining biological effects.

One of the major challenges faced by nanoparticle therapies is clearance by the mononuclear phagocyte system (MPS). When particles enter the bloodstream, opsonisation is likely to occur, forming a protein corona on the particle surface and making them more recognisable to macrophages. This can be reduced by alteration of charge on the particle surfaces or by PEGylation, with studies suggesting that uptake by macrophages occurs fastest for either highly positively or negatively charged particles [11]. Nanoparticle size also has a large effect on particle uptake and circulation time. Particles larger than 200 nm are preferentially cleared by spleen, while particles of <5.5 nm are removes my renal filtration [51]. Therefore both size and surface properties are crucial in nanoparticle design for therapeutic applications to ensure that particles do not cause any undesired effects and reach their destination before either releasing their cargo or being cleared from the body.

2.2.1 Effect of particle size on cell uptake

Particle size has a large effect on the behaviour of the nanoparticles *in vivo*. The size of nanoparticles affects macrophage uptake of particles, route of uptake into cells [52], tissue distribution, particle agglomeration [53] and elimination [54].

Particles of less than 30 nm can diffuse directly through the cell membrane via carrier proteins by a process known as facilitated diffusion. However, larger particles are taken up by the endocytic pathway in which the particle fuses with the cell membrane and becomes enclosed in a vesicle. The vesicle then fuses with lysosomes, which results in a major drop in pH (lysosomal fluid has a pH of ~4.5) as well as the release of enzymes, and the particle is digested. There are two types of endocytosis; phagocytosis and pinocytosis. Phagocytosis (illustrated in Figure 2.2) only occurs in specialised cells known as macrophages and involves the digestion of large particles (>250 nm) via large vesicles called phagosomes. Macrophages can engulf particles of up to 10 µm in diameter [52,55] using this method. Pinocytosis on the other hand, can occur in all cells. It is primarily the uptake of fluid, although macro-pinocytosis (also shown in Figure 2.2) can potentially allow for the uptake of particles up to 5 µm in diameter [55]. Other forms of pinocytosis, which operate on smaller length scales, are protein mediated (e.g. clathrin-mediated and caveolin-mediated).

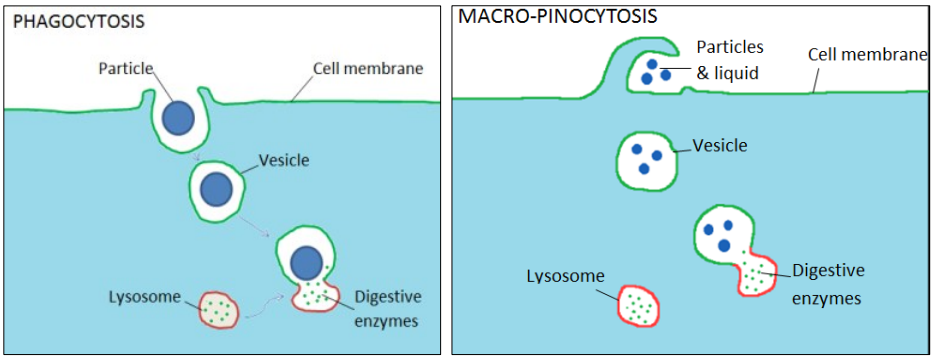


Figure 2.2 - Examples of cell uptake mechanisms of nanoparticles by endocytosis.

Due to the variety of uptake mechanisms over different length scales it is likely that particle size will have a large effect on uptake into cells. Cho *et al.* found that increasing the size of silica nanoparticles from 50 to 200 nm increased the number of particles trapped by macrophages [54]. However, in non-phagocytic cells increasing size from 50 – 500 nm results in reduced uptake due to cholesterol depletion resulting in increased efficiency of uptake inhibition [56]. As well as affecting mechanisms of uptake, a variation in particle size was shown to affect their fate within cells. For example, particles of 500 nm clustered around the periphery of cells instead of being delivered to lysosomes [56]. Lu *et al.* found that maximum uptake of mesoporous silica nanoparticles by human cervical cancer cells (HeLa cells) occurred at 50 nm [57]. However, particles of size 50 nm or less were excreted from the body more rapidly [54] and agglomerated faster [53].

Particle toxicity has also been shown to be linked directly to particle size as well as concentration of particles internalised [58]. Park *et al.* investigated the effect of size on the cytotoxicity of silica nanoparticles ranging from 10 to 400 nm on embryonic stem cells [59]. They found that particles of 80 or 400 nm in size had no adverse effects, whereas particles of 10 and 30 nm inhibited differentiation of stem cells above a critical concentration [59]. In agreement with these findings, Tsigkou *et al.* [60] found that bioactive glass particles of ~215 nm were internalised by bone marrow derived stem cells (MSCs) and fat derived stem cells (ADSCs) without causing toxicity or differentiation, even when the particles degraded inside the cells.

In current literature there are many contradicting opinions about the effects of nanoparticle size on particle uptake and effect on cells. However, in practice most nanomedicines tend to be in the size range of 5 – 250 nm as particles within this size range are assumed to be internalised by cells and generally have similar properties based on anatomical responses [52].

2.3 Nanoparticles for cancer treatment

One of the main applications for nanoparticles in medicine is for cancer treatment. It has been seen that particle uptake is dependent on both particle properties and cell-type. Tumours in particular have an increased capillary permeability with which gives rise to the "enhanced permeability and retention (EPR) effect" and can result in increased nanoparticle uptake into tumour tissue without the need for active targeting [61]. Experiments suggest that particles in the 50 - 100 nm size range can penetrate throughout large tumours when dosed into the circulatory system [62].

Oncology has been influenced for several years by nanoparticle therapies which have been FDA approved and are already in clinical use to treat several different types of cancer [11]. Nanoparticles have a huge potential for use in a variety of therapeutic applications and their size and charge can be modulated to allow for intracellular uptake without causing harm to the surrounding tissues. It is also possible to load mesoporous particles with therapeutic molecules (drugs and particularly genes) [63] to allow for localised and even intracellular delivery. As discussed, nanoparticles have been seen to accumulate preferentially in cancerous tissue due to the EPR effect. Additionally they can be functionalised with molecular ligands to allow for active targeting or receptors on the tumour surface [64].

2.3.1 Nanoparticles for drug delivery

Liposomes were the initial method of drug-delivery using nanoparticles approved for clinical use. They have been successfully used to encapsulate and deliver doxorubicin, (a powerful and toxic chemotherapeutic drug) for the treatment of metastatic breast cancer and recurrent ovarian cancer with comparable efficacy and reduced cardiotoxicity compared to doxorubicin [65]. Polymer particles are also extensively used to deliver drug loads, with their greatest advantage being the ability to tailor properties such as degradation and hydrophobicity, as well as allowing for further surface functionalisation. Encapsulation of drugs in polymeric nanoparticles can allow for controlled release in response to the local environment by diffusion through the polymer matrix as a result of swelling, or either surface or bulk erosion mechanisms [11]. However concerns in polymer systems arise due to the fact that there is often much structural heterogeneity, reflected by a high polydispersity index (PDI) [66].

An ideal drug carrier system would be readily internalised by cells, inherently non-cytotoxic, and either degrade or be excreted from the body after delivery of its cargo to the required location. The intrinsic biocompatibility and dissolution characteristics of silica within aqueous systems make mesoporous silica nanoparticles an ideal candidate for drug delivery *in vivo* [67]. Chung *et al.* [46] observed that mesoporous silica nanoparticles (MSNs) were internalised by human mesenchymal

stem cells (hMSCs) without the need for specific transfection agents and without affecting cell viability, growth or differentiation. It has also been shown that 110 nm MSNs were internalised by fibroblast cells, where they accumulated in the cytoplasm without causing any cytotoxic effects [68]. This localisation in the cytoplasm is desirable for drug release within cells.

One of the major challenges affecting all drug delivery systems, including mesoporous silica nanoparticles, is the prevention of premature release of anticancer drugs before arrival at the target destination. Various method have been utilised in literature to create particles which only release their drug load when subjected to a certain stimulus. These may include stimuli specific to the local tumour environment such as a reduced pH and elevated secretion of particular enzymes, or external stimuli such as heat or light. Enzyme specific release has been demonstrated by MSNs functionalised with polysaccharide derivatives and loaded with doxorubicin, where lysosomal enzymes degrade the capping polysaccharides resulting in drug release [69]. Many drug delivery systems for cancer treatment also exploit the drop in pH from about pH 7.4 in healthy tissue to pH 6.5 - 6.8 in the extracellular environment of solid tumours [11]. Chang *et al.* developed MSNs with a reductively sheddable pH responsive polymer shell, loaded with doxorubicin in the form of hydrochloride salt (DOX) [70]. Additionally, Huang *et al.* investigated a number of different mesoporous silica nanoparticle structures for carrying a drug cargo and demonstrated that the release can be controlled by capping the pores of the nanoparticles with a polyelectrolyte coating [67]. Muhammad *et al.* also used MSNs as a carrier for doxorubicin and sealed the nanopores using acid-decomposable, luminescent ZnO quantum dots (QDs) in order to inhibit premature drug release [71].

A system which uses external stimuli for drug release comprises of core-shell nanoparticles consisting of a magnetic iron oxide core in a mesoporous silica shell [72]. The mesoporous silica is loaded with the anticancer drug camptothecin, while the entrances of the mesopores are blocked with 2-nitro-5-mercaptobenzyl alcohol functionalised CdS nanoparticles through a photocleavable carbonate linkage. This linkage can then be broken down under UV light resulting in camptothecin release. The magnetic properties of the nanoparticle carrier and subsequent responsiveness to light irradiation make targeted treatment of cancer using this system possible [72].

2.3.2 Inorganic nanoparticles and ionic therapy

Inorganic nanoparticles tend to have excellent physicochemical properties and their synthesis methods can often allow for precise control over their size and shape in comparison to polymer-based nanoparticles. However the inability of many inorganic particles to degrade has raised concerns about long term effects and limited their application in this area [11]. The most widely used inorganic nanoparticles are MSNs for the advantages described previously, although their

therapeutic applications are currently limited to drug delivery. Carbon based nanostructures on the other hand (eg carbon nanotubes, CNTs) and gold nanoparticles both possess inherent photothermal properties which can allow for direct cancer treatment without the need for anticancer drugs and therefore bypass the issues associated with premature release. Au nanocages [73] and CNTs [74] can be used for the photothermal destruction of tumours due to excessive local heating as a result of applying continuous near-infrared (NIR) light.

Due to their size and their ability to be taken up by cells, nanoparticles can also be used for the intracellular delivery of ions. In particular, the effect of ZnO nanoparticles in mammalian cells has been extensively studied in recent years. In 2012, a review on their toxicity was conducted by Vandebriel *et al.* [75]. ZnO nanostructures exhibit much more toxicity than other metal oxides with the most likely cause of toxicity being due to the induction of oxidative stress due to high levels of reactive oxygen species (ROS) [76]. There have also been recent studies on the use of ZnO nanomaterials in cancer therapy. Muller *et al.* reported pH dependent toxicity of ZnO nanowires in macrophages with rapid dissolution at lysosomal pH and release of Zn^{2+} ions resulting in cell death [77]. Sasidharan *et al.* also reported preferential toxicity of ZnO nanocrystals (regardless of their size or surface chemistry) towards cancer cells due to rapid dissolution in the acidic cancer microenvironment. Another theory behind preferential cytotoxicity of ZnO nanoparticles towards cancer cells is due to the fact that rapidly dividing cells are inherently more susceptible to increased levels of Zn^{2+} ions due to their fast rate of metabolism [50]. It has also been observed that malignant cells show depleted zinc levels, suggesting that restoration of elevated zinc levels (tolerated by healthy cells) will result in tumour suppression and cytotoxicity in cancer cells [78]. The toxicity of ZnO nanoparticles is now widely attributed to preferential dissolution in an acidic environment resulting in increased levels of Zn^{2+} ions leading to disruption of cellular zinc homeostasis, mitochondrial damage and subsequently apoptosis [12].

Zinc containing bioactive glasses have also been found to cause cytotoxicity due to release of Zn^{2+} ions and induced oxidative stress [42]. They also exhibit the same pH dependent release as ZnO. Chen *et al.* [19] have developed 'smart' acid-degradable zinc-releasing silicate glasses for antibacterial applications which remain stable under normal physiological conditions (pH 7.35-7.45) but release zinc rapidly when it is needed as the pH decreases during an infection. The same theory could be applied to zinc containing silicate nanoparticles which would allow for the delivery of zinc intracellularly only once the particles have been taken up by cells and been engulfed by lysosomes or in the acidic tumour environment. Our hypothesis is that the incorporation of zinc into bioactive

glass nanoparticles consisting primarily of a silicate network will allow for a localised and sustained release of Zn ions to cancer cells, without the need for additional modifications or drug loading.

2.4 Sol-gel synthesis of bioactive glass nanoparticles

2.4.1 Processing methods of bioactive glass

Bioactive glasses can be processed by one of two routes; sol-gel or melt-derived. Traditionally bioactive glasses were made by a melt-derived method in which the components are heated at temperatures in excess of 1100˚C followed either by casting, or quenching and grinding to form powders [79]. The development of the sol-gel processing method, allowed the production of glasses with the same composition to be achieved at lower temperatures. The sol-gel method also offers numerous other benefits due to differences in physical and chemical properties. Sol-gel–derived powders have been shown to be more homogeneous and exhibit a higher level of porosity and intrinsically higher surface areas than melt derived glasses [80], leading to enhanced levels of bioactivity due to an increased number of sites for apatite nucleation [81]. They can also remain bioactive at higher silica contents due to the fact that H^+ ions act as a network modifier, resulting in a broad distribution of network connectivity and increased dissolution. The presence of H^+ ions also results in a high concentration of silanol bonds, Si-OH, which act as nucleation sites for apatite [82].

Sol-gel processing methods have been widely used to produce silica networks by hydrolysis and condensation reactions. It is a chemistry-based process involving the gelation of a colloid-like suspension [83]. A silicate precursor is required, which typically takes the form of a silicon alkoxide, such as tetraethyl orthosilicate (TEOS). Silicon alkoxides hydrolyse under both acidic and basic conditions, after which polycondenation occurs and Si-O-Si bonds start to form, creating a sol of dispersed nanoparticles. In the acid-catalysed system, particles aggregate as condensation continues to form a three-dimensional gel network [84,85]. However, under basic conditions, repulsive forces between the silica nanoparticles make it possible to synthesise monodispersed spherical nanoparticles [86]. Monodispersed, spherical silica nanoparticles are routinely produced in this way using the Stöber process, described in detail in section 2.4.2. Figure 2.3 shows how differences in processing methods can have a large effect on the end product of the reaction, allowing a variety of different materials to be manufactured using the sol-gel technique [85]. Under acidic catalysis, before the gelation process is complete, the sol can be applied as a coating, mixed with polymer to from a hybrid or pulled in to fibres. Alternatively, after the gelation step is complete, the 3D network can aged (to increase the thickness of the inter-particle necks and reduce the risk of failure) followed by drying (to remove all liquid from the interconnected pore network) and stabilisation. The

stabilisation step involves thermal treatment above 600˚C to remove the surface silanol (Si-OH) bonds from the pore network and produce a chemically stable ultraporous structure. Heating to above 600˚C is also sufficient to burn off any by-products such as nitrates, if additional compounds are added to the sol. The resulting xerogel, which will be of a reduced volume, can subsequently either be ground to form powders or heated at an elevated temperature of 900-1150˚C to eliminate pores and form a dense ceramic. To avoid shrinkage, the gel can alternatively be dried under supercritical conditions, resulting in the production of an aerogel.

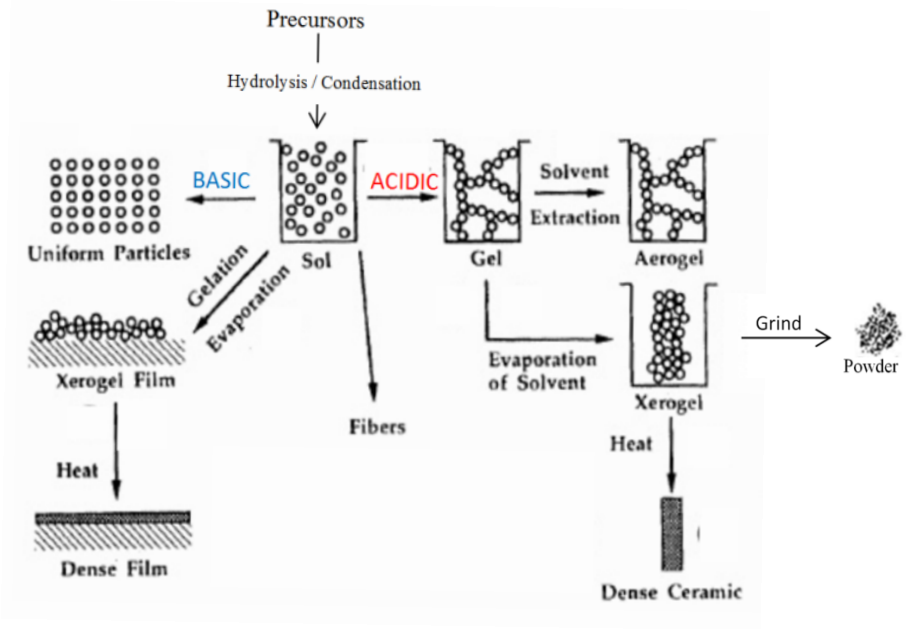


Figure 2.3 - Overview of how the sol-gel process can be adapted to produce different materials. Modified from [85].

However, the relatively limited commercial success of bioactive glasses has been due to processing limitations. Both melt-derived and sol-gel bioactive glass scaffolds can now be successfully produced by a variety of methods, including foaming [87], and more recently melt-derived scaffolds have also been created by 3D printing (or 'robocasting') [88]. Although difficulties still remain in trying to synthesise porous coating, fibres and in particular nanoparticles. Whilst bioactive glass particulates in the micron range have been widely used for many years, these tend to be highly irregular in shape with a large size distribution. Research is now focussing on the ability to produce monodispersed, spherical particles in the nanometre range for use in composite materials. Control of particle size and dispersity is important for homogeneity and in controlling whether particles are internalised by cells. Melt derived bioactive glass nanoparticles can be produced by a flame synthesis method [89], or by grinding bulk material. However, despite being in the nanometre range, the particles are both highly irregular and show a large degree of agglomeration. Another method which could be used to

produce bioactive glass nanoparticles and which allows for a far more precise control of particle size is a microemulsion technique. In microemulsions, colloidal dispersions of water are stabilised by a surfactant film in oil [90]. By altering the surfactant, particles can be created of a variety of sizes all with minimum agglomeration. However, this thesis will focus on sol-gel processing methods which have been extensively studied due to the benefits described above. Sol-gel techniques are commonly used to produce a variety of bioactive glass compositions and morphologies at low temperatures. They allow for manipulation of the material at a molecular level making them an ideal route for the bottom up synthesis of materials on the nano-scale.

Sol-gel processing has been used routinely for the synthesis of silica nanoparticles, although the addition of calcium to form nanoparticles of bioactive glass is far from trivial [16]. Before investigation can be carried out into the incorporation of calcium, it is first necessary to gain a full understanding of the sol-gel process and the formation of silica nanoparticles.

2.4.2 The Stöber Process: Basic hydrolysis and condensation of silicon alkoxides

Both hydrolysis and condensation reactions occur simultaneously during the mixing stage of the sol-gel process. They can be either acid or base-catalysed, although here we will primarily consider the base catalysed system which results in the formation of nanoparticles. Hydrolysis occurs by nucleophilic attack on the silicon atom by the oxygen contained in water [85]. Under basic conditions the water dissociates to from nucleophilic hydroxyl anions which then react with the silicon atoms, displacing the –OR groups to form Si-OH bonds as shown in Figure 2.4.

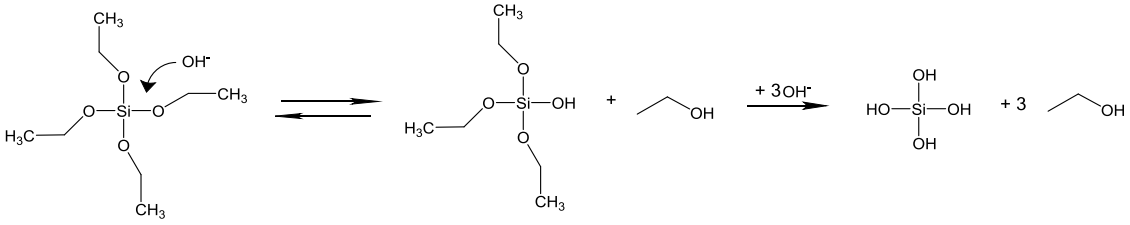


Figure 2.4 - Base-catalysed hydrolysis.

Condensation occurs simultaneously and can take one of two forms (shown by equations 1 and 2) resulting in the formation of a silica network, cross-linked through bridging oxygen bonds. As these reactions continue, the silica network becomes larger and larger through the process of polymerisation.

Alcohol condensation: $-\mathrm{Si}-\mathrm{OR} \quad + \quad \mathrm{HO}-\mathrm{Si}- \quad \leftrightarrow \quad -\mathrm{Si}-\mathrm{O}-\mathrm{Si}- \quad + \quad \mathrm{ROH}$ [1]

Water condensation: $-\mathrm{Si}-\mathrm{OH} \quad + \quad \mathrm{HO}-\mathrm{Si}- \quad \leftrightarrow \quad -\mathrm{Si}-\mathrm{O}-\mathrm{Si}- \quad + \quad \mathrm{H_2O}$ [2]

Silica network formation is greatly influenced by the relative rates of hydrolysis and condensation reactions and the pH of the surrounding environment. In a basic environment the presence of excess OH^- ions catalyses the reactions promoting particle growth. This can allow for control of particle size as described in section 2.4.4. The OH^- ions also make the production of monodispersed particles possible by adsorbing to particle surfaces and preventing agglomeration due to mutual repulsion [91].

Equations 3 and 4 show the overall reactions for the production of silica spheres by the hydrolysis of TEOS in a basic solution [85].

HYDROLYSIS: $$Si(OC_2H_5)_4 + 4H_2O \rightarrow Si(OH)_4 + 4C_2H_5OH \quad [3]$$

CONDENSATION: $$Si(OH)_4 \rightarrow SiO_2 + 2H_2O \quad [4]$$

Stöber *et al.* were the pioneers of this system, producing silica nanoparticles under basic conditions. They developed a controlled method of producing spherical silica particles of uniform size, in the range of 0.05 – 2 μm, by the hydrolysis of alkyl-silicates and subsequent condensation in alcoholic solutions, using ammonium hydroxide as a catalyst [86]. The Stöber process is simple; TEOS is added to a solution of water, alcohol and ammonium hydroxide under agitation. One of the advantages of the method is the ability to control particle size, distribution and morphology by systematic variation of reaction parameters [92]. Although many papers have adapted the Stöber process with various concentrations in their own investigations [93-102], the synthesis methods have become increasingly complex with no clear benefits. Bogush *et al.* developed a modified version of the Stöber process using a seeded growth technique which enabled them to prepare more uniform particles with higher mass fractions of silica [93]. However, it required multiple stages making preparation far more time consuming. Park *et al* prepared silica nanoparticles by a semi-batch process using a micro feed pump with a constant flow rate, feeding a TEOS and ethanol solution into a reactor containing a second solution of water, ethanol and ammonia [99]. Rao *et al.* also used an adaption of the original Stöber process, adding ammonium hydroxide dropwise, 20 minutes after the addition of TEOS. They also used a significantly lower concentration of TEOS [100]. However, no justification was given for these changes and no advantages were evident.

2.4.3 Mechanism of particle growth

It is well known that the sol chemistry affects the rates of hydrolysis and condensation, which in turn affects nucleation, aggregation and growth of particles [85,97]. It was initially believed that the mechanism of particle growth in the basic TEOS system followed LaMer and Dinegar's theory of monomer addition [103], illustrated in Figure 2.5. As the concentration of alkoxide is increased to the supersaturation point, nucleation becomes extremely rapid. However, as the reaction continues,

formation of particles reduces the concentration of alkoxide to below the point C_o beyond which further nucleation is unlikely. At this point the particles grow by diffusion until the concentration is reduced to the equilibrium solubility, C_s. If this monomer addition model was correct, then theoretically a single particle size could be achieved by producing a single burst of nucleation to consume excess solute, before allowing particle growth to occur by the addition of hydrolysed monomers. The most likely mechanism for the growth of particles in this way is by reaction-limited monomer-cluster aggregation (RLMCA) [85] which states that the probability of monomer attachment is governed by local structure. There are many collisions between monomer (a silicate tetrahedron in this case) and cluster before a bond is formed, with all potential growth sites being sampled by the monomer. In basic conditions, all cluster sites are reactive and occupied with equal probability, therefore giving rise to spherical particles [85].

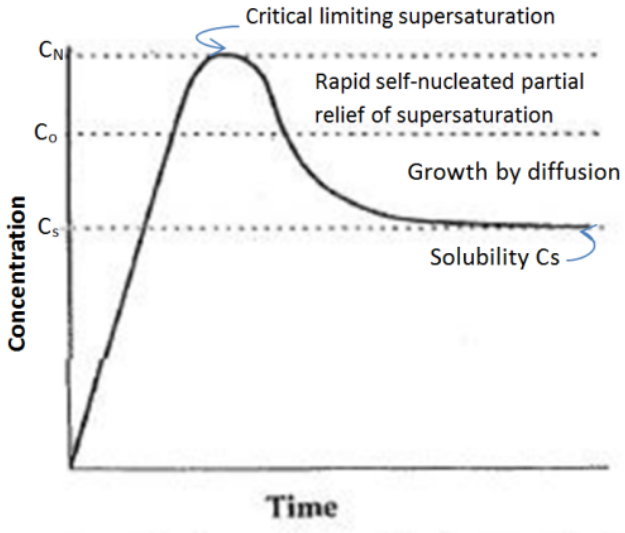


Figure 2.5 - Schematic representation of the concentration of precipitating species before and after nucleation. Modified from [85].

However, temporal studies of silica particles produced by the Stöber process have shown that alkoxide concentration exceeds the critical supersaturation value for a substantial fraction of the process and nucleation therefore proceeds for most of the reaction period [102]. If LaMer's monomer addition mechanism was true then this would result in particles of a large range of sizes, which is known not to occur. Alternatively, it is proposed that particle growth follows a nucleation and aggregation mechanism [104,105] (illustrated by Figure 2.6), in which initial negatively charged particles (<10 nm) are unstable due to their size, resulting in aggregation and a collective reduction in surface area. Competition between nucleation and aggregation is dependent on reactant concentrations and has a large effect on final particle properties such as size [105]. Uniformity in particle size can be

achieved with this mechanism as a result of size dependent aggregation rates [102,105] determined by colloid interaction potentials [104]. The aggregation rate is fastest between small-large particles and slowest between large-large particles [105]. Initial particles restructure through a process known as Ostwald ripening in which aggregates dissolve and then reprecipitate, consuming smaller particles to form larger more stable ones. However, Ostwald ripening cannot account for the rapid growth of particles in the 45 - 250 nm range. It is predicted that RLMCA occurs on two length scales with the smaller particles now acting as monomers [85]. This theory is supported by Feeney *et al.* [106] and also backed up by work carried out by Lee *et al.* [105] and Harris *et al.* [98].

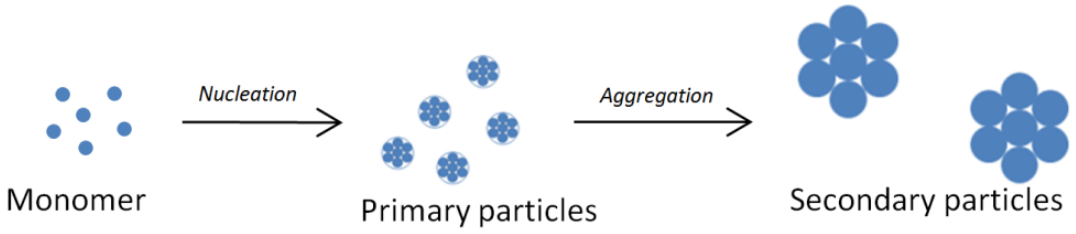


Figure 2.6 - Schematic illustrating the nucleation and aggregation mechanism of particle growth.

It is now generally believed that both mechanisms are partially responsible for the growth of silica nanoparticles, with controlled aggregation occurring in the initial stages of the reaction until the colloids become stable. Once the soluble silica concentration has dropped below the critical nucleation concentration, it is hypothesised that monomer addition subsequently occurs on the surface of the aggregated particles in accordance with LaMer and Dinegar's theory of monomer addition [103], leading to smoothing of the colloid surface [93,97,101]. This proposal has had some support as the likely mechanism for particle growth. However, there are still doubts about its ability to adequately describe the early stages of particle growth and the size and structure of the initial nanostructures [97].

2.4.4 Control of particle properties

Since 1968 it can be seen that the Stöber process has been used repeatedly to successfully create monodispersed silica nanoparticles. One of the advantages of the sol-gel method is the ability to control particle size, distribution and morphology by systematic variation of reaction parameters [92]. However, the process's extreme sensitivity to the effects of temperature, pH and reactant concentrations has affected reproducibility and consistent trends have not always been observed [94,99]. Whilst there have been many attempts to demonstrate how each of these variables affects the final particle properties, most papers use different concentrations and processing methods, making comparison extremely challenging. For example, whereas Bogush *et al*. carried out all experiments at

25˚C [93], all of the experiments conducted by Park *et al.* were carried out between 55 and 65˚C [99] , making the results incomparable. There is still much disagreement in the field and the original paper published by Stöber *et al.* [86] and that of Bogush *et al.* [93] remain the most comprehensive studies.

2.4.4.1 Effect of reactant concentrations

Solution chemistry affects the rates of hydrolysis and condensation, which in turn affects the nucleation, aggregation and growth of particles [97]. Competition between nucleation and aggregation is dependent on reactant concentrations and has a large effect on final particle properties such as size [105]. Lee *et al.* found that when the ammonia concentration was high (0.3M) or the water concentration was optimal for a maximum in size (9 M), aggregation was fast compared to nucleation and the main aggregation event was between the fresh nuclei and the large aggregates. In contrast, when the ammonia concentration was low (0.1 M) or the water concentration not optimal then nucleation was fast compared to aggregation and a significant amount of intermediate size particles remained for as long as the nucleation rate was high [105]. This trend was also confirmed by Van Blaaderen *et al* .[101].

It is clear that particle properties; the size of the particles, their standard deviation, the speed of particle formation and particle shape are all interlinked and dependent not only on the concentration of individual reactants, but on the relationships between them and the exact synthesis method used. However, as yet, a clear study has not been performed to determine these relationships. This will be rectified in this thesis.

Effect of reactant concentrations on final particle size

Stöber initially stated that the concentration of TEOS has no effect on particle size and produced the graph shown in Figure 2.7, displaying the final particle sizes obtained by reacting 0.28M of TEOS with various concentrations of water and ammonia in ethanol [86]. The relationship between ammonia and water concentration on the final particle size can be clearly seen. For a constant ammonia concentration, increasing water up to 8 M resulted in increased particle size, although beyond water concentrations of 8 M, particle size decreased again. On the other hand, for a constant water concentration, increasing ammonia resulted in increased particle size, up to about 6 M of ammonia at which point the particle size started to slowly decrease again. It is clear that at water concentrations of around 6 - 10 M small variations in ammonia concentration had a large effect on particle size, whereas differences in water concentration did not have a large effect.

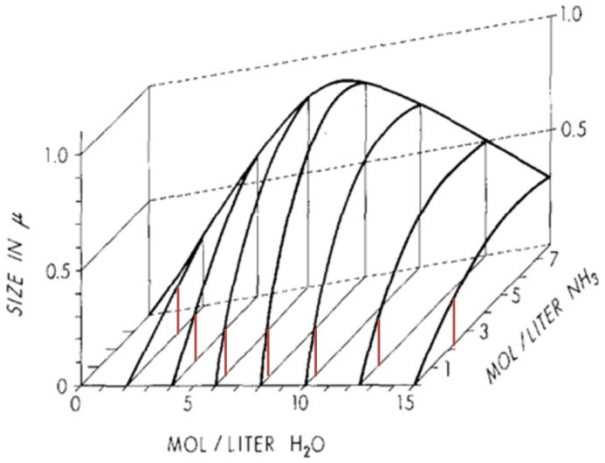


Figure 2.7 - Final particle sizes obtained by reacting 0.28M of TEOS with various concentrations of water and ammonia in ethanol, modified from [86]. The red lines shown correspond to the concentrations required to form particles of 200nm.

In contrast with Stöber's paper, Bogush *et al.* reported an increase in size with increasing TEOS concentration [93] and Van Helden noted the inverse relationship [96]. This apparent contradiction could potentially be explained by the findings of Rao *et al.*, who stated that the size of the silica nanoparticles was found to increase with TEOS at low concentrations of water, whereas at high concentrations of water the effect was reversed. I.e. the particle size is affected not by TEOS concentration, but by R value, where R = $[H_2O]/[TEOS]$ [100]. The R value was also shown to alter the effect of temperature on particle size, adding extra complications. Interestingly, Branda *et al.* showed that mixing alkoxides resulted in a faster growth rate and consequently fewer but larger particles [95]. This can be attributed to the fact that different alkoxides produce primary nuclei of different sizes which speeds up the establishment of a large size distribution where the dominant event is the aggregation between the freshly generated nuclei and large aggregates. This is recognised to be a faster aggregation event, thus speeding up particle growth [95].

It is generally accepted that pH has a large effect on particle size, thus ammonia variation is likely to be a major factor in determining the final sizes of the particles produced. Lu *et al.* observed a decrease in particles size even with a comparatively small decrease in pH from 11.52 to 10.86 [57]. This could be due to the fact that at low NH_3 concentrations, particle stability is higher and aggregation therefore stops relatively early resulting in a larger number of particles growing to a small final size [101]. In addition to this, ammonia acts as the catalyst for the reaction, with OH^- ions promoting both the hydrolysis and condensation reactions. As hydrolysis has a direct effect on nucleation, factors which promote hydrolysis also promote nucleation and therefore result in smaller particles, while factors that inhibit hydrolysis, inhibit nucleation and favour growth which should have the opposite effect, producing larger particles [94]. The effect of ammonia concentration is to promote hydrolysis so it may be predicted that increasing ammonia concentration would result in smaller particles. This

trend was seen by Rao *et al.* [100]. However, ammonia also promotes the polymerisation (condensation) rate, resulting in faster kinetics, and larger particle sizes as observed by Matsoukas *et al.*[94], Van Helden *et al.*[96], and Park *et al.*[99].

The effect of water concentration on particle size is equally controversial. While Matsoukas *et al.*[94] showed that particle size decreases with increasing water concentration, Park *et al.* claim that to minimize the particle size, the value of R (=[H_2O]/[TEOS]) must be decreased [99]. However, more consistently observed is the trend shown by Stöber *et al.* in 1968, where particle size initially increases and then decreases again with increasing water concentration [86,93,96].

By using a wide range of reactant concentrations several papers claim that it is possible to synthesise particles using this method over the range of 5 – 2000 nm [86,91,97] although others have found the maximum size to be about 800 nm [93] which is in agreement with Figure 2.7. Although it is clearly possible to synthesise a large range of particle sizes, it is unclear over what range monodisperse particles can be produced reliably and what conditions are required.

Effect of reactant concentrations on the time taken to reach the final particle size

Relatively little research has been done into the effect of reactant concentrations on the speed of particle formation. When analysing the particle growth mechanism, Van Blaaderen concluded that the production of hydrolysed monomers is the rate limiting step throughout most of the growth process [101]. Therefore, factors that speed up hydrolysis will result in faster particle formation. This is in agreement with the findings that at increased water or ammonia concentrations the nucleation rate increases, resulting in a shorter nucleation period [105]. Additionally, both increased water concentration [93], and increased ammonia concentration [94], resulted in a faster growth rate corresponding to an increased speed of particle formation. Growth rate was also faster in methanol than in ethanol [94,97].

Effect of reactant concentrations on the standard deviation of particles

Although literature has primarily focused on controlling particle size, it is also necessary to consider the effect of variations in concentration on the standard deviation of the particles produced. Where the aim is to produce monodispersed nanoparticles, the ability to synthesise a large range of average particle sizes has relatively little meaning unless the standard distributions are sufficiently low. The particle size distribution has been shown to become broader when longer-chain alcohols are used as solvents [86,100]. Park *et al.* also found that at high concentrations of water and ammonia the standard distribution of particle size increased [99]. However, this is in contrast to findings which suggest that standard deviation is independent of initial reactant concentrations and determined only by final

particle size. Several papers report that the standard deviation expressed as a percentage of average size decreases with increasing particle size [93,96,101]. If this is the case then Park's findings can only be explained if increased water and ammonia concentrations lead to a decrease in particle size, which was not observed. On the other hand TEOS concentration has not been shown to have any influence on the standard deviation, although Van Helden *et al.* did observe that particle shape became increasingly irregular beyond TEOS concentrations of 0.2 M [96].

At a variety of reactant concentrations, many papers have reported bimodal or heterogeneous distributions of particles, although no one has yet been able to give an explanation as to why or when this sometimes occurs. Bogush *et al.* found that near the maximum achievable size for any given TEOS concentration, monodispersity was often not achieved and bimodal final particle size distributions were common. Heterodisperse particle size distributions were also observed at high TEOS and ammonia concentrations (0.5 M TEOS and 2.0 - 3.0 M ammonia) [93]. Stöber stated that "the particle sizes are not precisely reproduced and, occasionally, an unusually high standard deviation of the size distribution is encountered" [86]. Reproducibility is key in all areas of research, although especially difficult to achieve in nanotechnology when there are so many different variables. Unfortunately there is still much which is not understood about this process. In current literature conclusions have often been drawn based on limited data and differences between experiments means that much data is incomparable.

2.4.4.2 Effect of Solvent

Perhaps the only effect that is universally agreed upon is the effect on particle size of the solvent used. It has been shown consistently that particle size increases with increased chain length of the alcohol, thus particles produced in methanol are significantly smaller than their counterparts produced using ethanol as a solvent [86,94,100]. Green *et al.* found that nuclei are twice as large in ethanol (Rg ≈ 8 nm) as those in methanol (Rg ≈ 4 nm) [97], attributed to differences in thermodynamic interactions of the hydrolysed monomers with the solvent resulting in different concentrations. They also showed that although reactant concentrations affect final particle size, they do not alter the size of these primary nuclei [97].

2.4.4.3 Effect of Temperature

Having determined that particle properties are heavily dependent on the rate of hydrolysis and condensation reaction, it is clear that temperature should play an important role. However, relatively little systematic research has been conducted into its affect, with experiments being carried out at a variety of temperatures. The most conclusive study was conducted by Bogush *et al.* which analysed the final particle properties over a temperature range of 9 to 55˚C for solutions of

1.0 M ammonia, 7.0 M water and TEOS concentrations ranging from 0.1 to 0.35 M. It could be expected that increasing temperature would increase the rate of particle growth, thus increasing particle size. However, in reality the reverse trend was observed showing final particle size to decrease monotonically as temperature increased [93]. This was backed up by Park *et al.* in 2002 who showed that as temperature increased both the size and standard distribution of particles decreased [99]. Bogush also observed that at the lowest temperature studied, monodispersity was not always maintained, whereas as temperature was increased from 9 - 55˚C, narrow size distributions were found for all TEOS concentrations [93]. Park *et al*. claim that temperature has the largest effect on particle properties than any of the other variables [99]. It is therefore possible, that these temperature dependent affects could have been wrongly attributed solely to reactant concentration in papers where temperature was not controlled. To complicate matters further Rao *et al.* observed an increase of particle size with increased temperature at higher R values, whereas at lower R values they observed the opposite trend with particle size decreasing with increasing temperature [100]. This reinforces the complex interdependence of all reaction parameters.

2.4.5 Incorporation of cations

The incorporation of cations into silica nanoparticles is desirable in order to create bioactive systems. Current literature predominantly focuses on the incorporation of calcium for bone regeneration applications. Soluble silica and calcium ion release stimulates cells at a genetic level causing osteogenic cells to produce bone matrix [29,107,108]. The addition of calcium increases glass dissolution by acting as a network modifier and the subsequent release of Ca^{2+} ions is critical for the formation of HCA [6]. Bioactive glass nanoparticles are also incorporated into nanocomposites [109]. Whilst the synthesis of monodispersed Stöber silica nanoparticles has been achieved previously in literature, the addition of calcium significantly complicates the procedure and can cause the particles to become irregular in morphology [82] or to agglomerate [110-112] as shown in Figure 2.8. While nominal compositions of particles are often quoted in the literature, the final compositions are rarely ratified by analytical techniques or only non-quantitative energy-dispersive X-ray spectroscopy (EDS) data is provided [16,111,113].

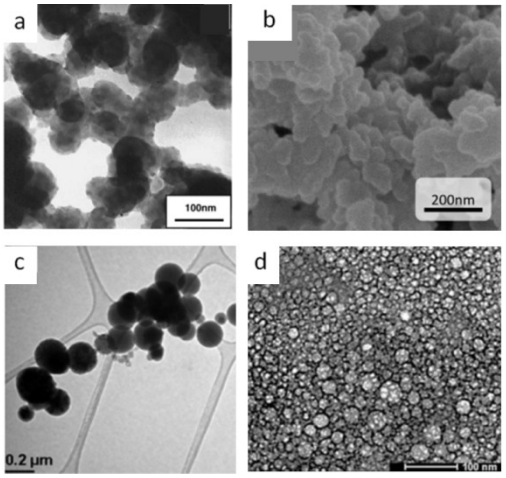


Figure 2.8 - Bioactive glass nanoparticles produced using a variety of different methods, demonstrating the difficulties in producing monodispersed particles a) Xia *et al.* [110], b) Luz *et al.* [111], c) Labbaf *et al.* [82], d) de Oliveira *et al.* [114].

Several groups have attempted to incorporate calcium into silica nanoparticles by using a two-step sol-gel process in which precursors of silica and calcium (TEOS and calcium nitrate respectively) are hydrolysed in an acidic solution before gelation under alkaline conditions [110-113,115]. While EDS data indicated that up to 30.85 at% Ca has been incorporated into these particles [111] and they induced HCA formation in simulated body fluid (SBF), little or no quantitative analysis was performed on the final elemental composition. The particles are also seen to be aggregated and irregular in both size and shape [110,111,113]. Labbaf *et al.* incorporated calcium by adapting the process used by Zhao *et al.* [116] in which Boltorn™ polymer is used as a template in the sol-gel process before being burnt out during calcination. The nanoparticles were shown to be of composition 86 mol% SiO_2 and 14 mol% CaO, verified by quantitative inductively coupled plasma optical emission spectroscopy (ICP-OES) analysis [82], although the particles were not washed prior to compositional analysis to remove any unincorporated calcium meaning that this value is likely to be artificially high. Additionally, despite being spherical and dispersed, the resulting particles did not show a homogeneous size distribution even after optimisation of the polymer:TEOS ratio. Some papers have attempted to improve the dispersion or shape of the nanoparticles by use of a surfactant [111,115]. However, this can inhibit calcium diffusion, therefore limiting the amount of calcium that enters the glass [60].

Calcium nitrate is usually used as the calcium source in the sol-gel synthesis of bioactive glass, although the calcium is not incorporated into the network until it is heated to above 400˚C [84]. The evolution of calcium distribution during sol-gel processing is shown in Figure 2.9. Before drying, the calcium nitrate is dissolved in the sol, however, as the particles are dried it precipitates onto the surface of the silica particles. Before the addition of calcium, Nuclear Magnetic Resonance (NMR) data shows that the silica network is highly connected. However, once 400˚C is reached, the calcium diffuses into the silica particles and becomes a network modifier, reducing network connectivity [84].

Further heating to above 600˚C is required to remove the nitrates from the system. Excess Ca^{2+} on the surface of the particles prior to heating may change the surface charge and cause the agglomerated particles seen in literature. Tsigkou *et al.* found the ratio of Si:Ca to be a critical factor in producing monodispersed particles [60].

Understanding the mechanism of calcium incorporation means that it is not necessary to have calcium in the sol from the start of the process. De Oliveira *et al.* [114] synthesised silica nanoparticles using a modified version of the Stöber process, including phosphate, before filtering the sol and subsequently adding calcium nitrate. However, they still did not achieve a homogeneous distribution of particles and despite nominal concentrations of 60 wt % SiO_2, 4 wt % P_2O_5, 36 wt % CaO, the actual composition, determined by lithium metaborate fusion dissolution and ICP-OES was 80.7 wt % SiO_2, 2.5 wt % P_2O_5, 16.8 wt % CaO [114]. One possible way of increasing the amount of calcium that can be incorporated would be by use of an alternative calcium source. Other potential calcium sources that have been investigated are calcium chloride and calcium methoxyethoxide (CME). Whilst it has been shown that it is possible to successfully produce hybrid materials using these precursors in the sol-gel process, hybrids containing calcium chloride were discovered to have extremely high percentages of Q^4 groups, indicating that the silica network was very well formed and that the calcium was not incorporated as a network modifier [117]. Calcium chloride was not incorporated into the network at any of the temperatures investigated and was also found to induce phase separation, making it an unsuitable calcium source for the production of bioactive glasses using the sol-gel method [118]. The CME alkoxide on the other hand, was found to incorporate into the network at low temperatures, making it an excellent alternative to calcium salts. However, it is highly reactive in comparison with the silica precursor TEOS, meaning that as it gels immediately on contact with water making the production of nanoparticles difficult [118].

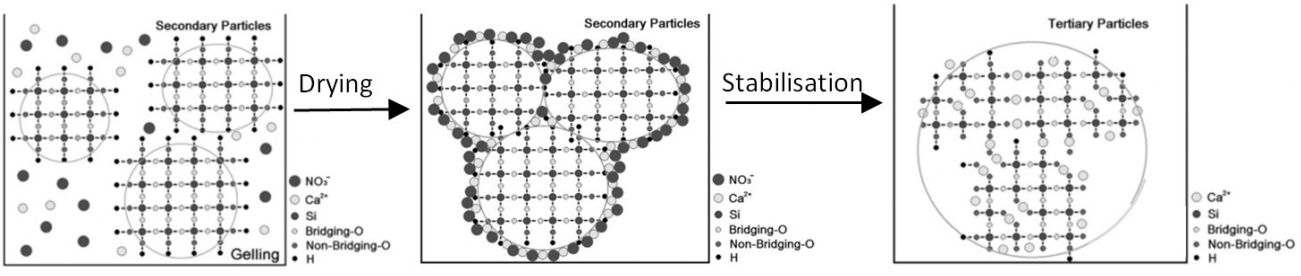


Figure 2.9 - Schematic illustrating the evolution of calcium distribution during sol-gel processing. Modified from [84].

2.4.6 Mesoporous particles

The synthesis of mesoporous materials is of great interest as they have a huge number of applications from drug delivery to catalysis or even chemical sensors. Mesoporous silica is of particular interest for biological applications such as drug delivery as it is chemically stable, easily modified and predominantly biocompatible [70]. Dense silica particles are commonly synthesised using the Stöber process as described previously. Many groups have adapted this procedure with the introduction of a surfactant in order to synthesise mesoporous silica nanoparticles [46,57,68,70,119-127]. The role of the surfactant in this process is critical in order to form pores. Above a critical micelle concentration (CMC) the surfactants will self-assemble to from micelles, shielding the hydrophobic parts from the aqueous solution. This process is known as evaporation-induced self-assembly (EISA) [124]. Further increasing the surfactant concentration results in the formation of cylindrical structures and the self-organisation of micellar phases into periodic hexagonal, cubic and lamellar mesophases [126] shown in Figure 2.10.

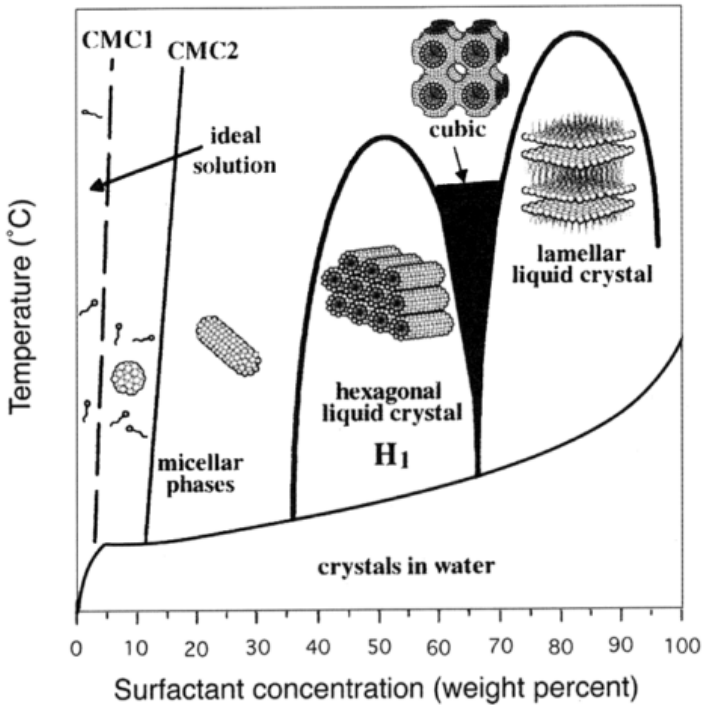


Figure 2.10 - Schematic phase diagram showing mesophases of cetyl trimethylammonium bromide (CTAB) in water with increasing concentration. Modified from [126].

Formation of mesoporous silica nanoparticles initially requires hydrolysis of a silicon precursor (TEOS) which subsequently co-assembles with surfactant micelles, resulting in silica-surfactant mesophases. Organisation of these mesostructures results in the development of liquid-crystalline mesophases which form mesoporous solids on removal of the surfactant [126]. Aggregation can be either can be either oriented or random [122]. Variation in reactants and surfactants, as well as their

concentrations, results in different final mesostructures. One of the most commonly used surfactants is cetyl trimethylammonium bromide (CTAB) which is a cationic surfactant. In comparison to non-ionic surfactants such as polyethylene glycol (PEG), it results in particles with a higher pore volume and larger surface area [63], both of which are desirable for drug delivery applications and fast degradation. Ionic surfactants also tend to form hexagonal mesophases with a higher degree of ordering [127].

Mesoporous particles have been synthesised using a huge variety of methods and the resulting particles vary greatly in size, dispersity and morphology. In 2009, Lu *et al.* designed a two-step process which they found was essential in order for them to achieve a uniform particle size distribution [57]. In the first step, silicates were pre-hydrolysed, as in the Bogush seeded batch process (for dense particles), before the addition of a large amount of TEOS in the second step. Nanoparticles with a well ordered mesoporous structure can be produced rapidly and in relatively large quantities by an aerosol assisted method using the EISA technique [124,126,127]. A solution is prepared in which the initial surfactant concentration is much less than the CMC. During aerosol dispersion, preferential alcohol evaporation results in an increase in surfactant concentration, inducing micelle self-assembly and the formation of highly ordered mesoporous particles [124]. This technique can be adapted to include ions such as Ca and P by the addition of precursors to the solution [127], however, it is not widely used as it requires specialised equipment. Additionally, whilst the particles produced are spherical due to the mechanism of assembly, they tend to have a relatively large size distribution and are therefore not ideal for biological applications where size has large effects on cell uptake and cytotoxicity.

For more traditional chemical synthesis methods, whilst mesoporous silica particles are routinely synthesised, the addition of cations significantly complicates the procedure, tending to lead to aggregated particles as produced by El-Fiqi *et al.* [63] (Figure 2.11). They used a base-catalysed sol-gel method with $Ca(NO_3)_2.4H_2O$ as the calcium source, although performed no quantitative analysis on particle composition post processing. Yun *et al.* [128] synthesised SiO_2–CaO–P_2O_5 mesoporous particles using one-step synthesis under dilute aqueous conditions, although again, they did not confirm particle composition post processing. However, they found that increasing the amount of calcium added to the solution resulted in a decrease in particle size and also had a large effect on the particle mesostructure. Both groups did confirm the apatite forming ability of the bioactive glass mesoporous particles *in vitro* as well as favourable biocompatibility.

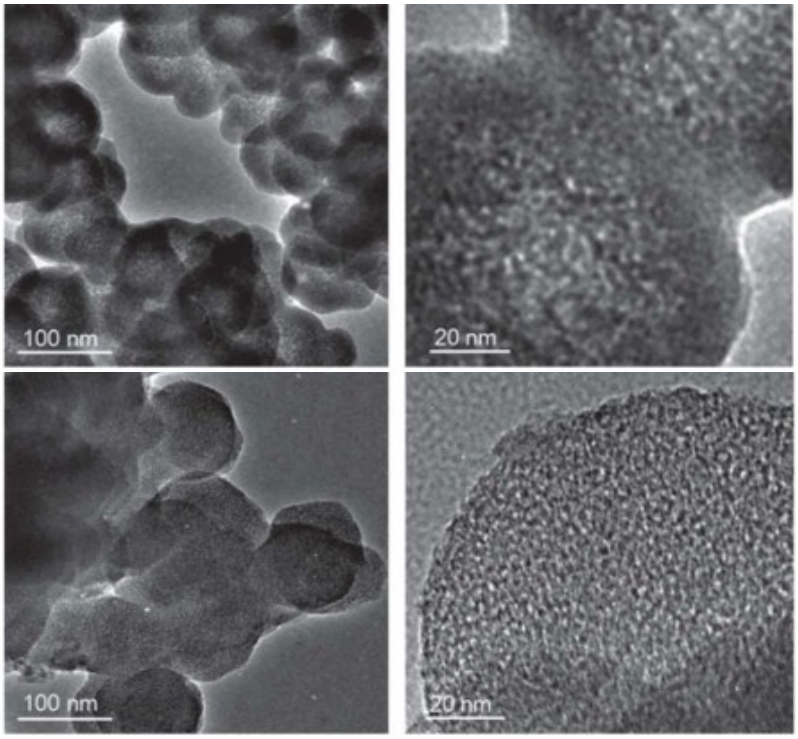


Figure 2.11 - Mesoporous bioactive glass nanoparticles produced using a sol-gel method. Modified from [63].

2.5 Bioactive glass nano-composite scaffolds for bone regeneration

Natural bone has a complex hierarchical structure, providing excellent structural and mechanical properties. It is a remarkable and dynamic material with high hardness and toughness as well as remodelling abilities. At the nanoscale bone can be modelled as a composite material with basic building blocks of collagen fibres and plate-like apatite crystals [129]. On the macro structural level, bone takes the form of either cancellous (trabecular) or cortical bone. Cortical bone contains a dense linear arrangement of fibres, whereas cancellous bone consists of a porous network as shown in Figure 2.12.

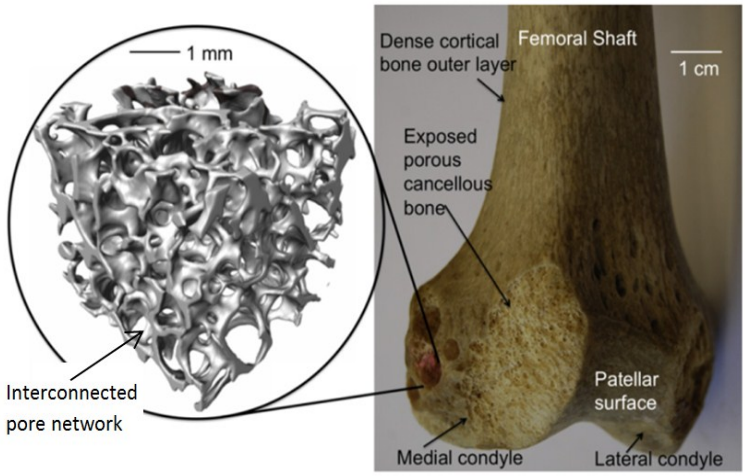


Figure 2.12 - Photograph of a human femur with an X-ray microtomography image of a region of the cancellous bone. Modified from [16].

There are four different cell types found within the bone structure; undifferentiated bone mesenchymal stem cells, osteoblasts, osteoclasts and osteocytes. Osteocytes are the most prevalent cell type in bone and are involved in controlling osteoblast and osteoclast activity. Osteoblasts are responsible for the deposition of bone matrix and mineralisation, whereas osteoclasts are responsible for bone resorption. Between them they are responsible for the regenerative capacity of bone. Nevertheless large scale defects cannot always be repaired naturally, giving rise to the need for surgical intervention. A 'critical size defect' is defined as a bone defect that cannot be repaired naturally within the lifetime of the animal, and it is in these situations that we must consider clinical treatments. Skeletal deficiencies can arise due to numerous reasons including congenital defects, trauma or disease. Common examples include tumour removal, non-union fractures, and osteoporosis [16]. Currently one in three women over the age of fifty suffers from osteoporosis and with an aging population and increasing life expectancies resulting in increased 'wear and tear' of the human body, the demand for a clinical solution to skeletal deficiencies is growing.

Current clinical treatments of skeletal deficiencies normally take the form of bone transplantation or the implantation of biomaterials. Bone transplants come in three varieties: an autograft (healthy bone harvested from elsewhere in the same individual), an allograft (bone taken from another human, often a cadaver) or a xenograft (tissue harvested from another species). Autologous bone grafts are currently the gold standard as they have optimum osteogenic properties, although the procedure is limited by a finite supply of bone and results in donor site morbidity [26]. Failure rates can also exceed 50%. However, failure rates of allografts and xenografts are even higher and introduce the added complication of possible rejection issues [130]. There has therefore been a significant shift towards the use of synthetic implants. Initial biomaterials were classified as 'bioinert' with the goal

being to “achieve a suitable combination of physical properties to match those of the replaced tissue with a minimal toxic response in the host” [107]. However, more recently the developments of resorbable and bioactive materials have been shown to be clinically successful. Bioactive materials are capable of stimulating a cellular response and forming a bond between the host bone and the implant, avoiding fibrous encapsulation [111] and allowing for improved adhesion.

An ideal scaffold material would not only act as a template for bone regeneration, but actively stimulate regrowth and then degrade away at a rate closely matched to the growth of new bone, whilst releasing non-toxic products in to the body. One potential method, currently under investigation for the active regeneration of bone, is tissue engineering using stem cells. hMSCs can be found in adult tissue, such as bone marrow, and have the capability to differentiate in to osteogenic cells including osteoblasts, making them an ideal cell source for bone regeneration applications [131]. Bioactive glass scaffolds have many of the key properties required for bone regeneration in the body, including bioactivity, porosity and controllable degradation rates. For these reasons they are amongst the most promising new materials for bone regeneration applications. Although bioceramic scaffolds are generally too brittle for load bearing applications, commercial success has been achieved by bioactive glass particulates which surgeons can mix with blood to form a putty, which can then be pressed into bone defects. PerioGlas® has been widely used to repair jaw defects and NovaBone has even been used for bone regeneration in load bearing applications with similar performance to autografts[16]. An ideal scaffold should have mechanical properties matching those of natural bone, enabling load sharing with the host bone. It should also maintain appropriate mechanical properties during the degradation and remodeling process. There has therefore recently been a shift towards hybrid materials which have a higher toughness [16].

Hybrid materials are composed of organic and inorganic interpenetrating networks components, which are indistinguishable on the nanoscale [16]. They can be split into either class I or class II hybrids depending on the type of interactions between the components. In class I hybrids the components interact via molecular entanglements, hydrogen bonding and van der Waals forces, whereas Class II hybrids also contain covalent bonds. A schematic of a class II silica/polymer hybrid material is shown in Figure 2.13. Hybrid materials have many potential benefits and it is hypothesised that these interactions at the molecular level will result in a material that behaves as one phase making it possible to achieve controlled congruent degradation and tailored mechanical properties [132]. A hybrid should also retain the biological properties of bioactive glass due to the fact that when cells approach the surface they will contact both organic and inorganic components simultaneously [132].

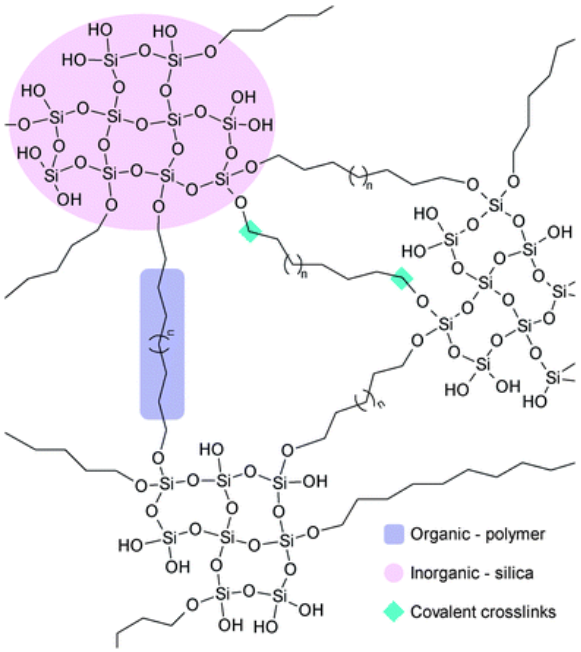


Figure 2.13 - Schematic of a class II silica/polymer II hybrid material [132].

However, one of the major challenges encountered in the synthesis of these new hybrid materials is the incorporation of calcium into the system. Calcium is desirable as it plays a direct role in encouraging the formation of hydroxyapatite by stimulating osteogenic cells to produce bone matrix [107]. As discussed previously, it can also further increase bioactivity when incorporated into the silica network by acting as a network modifier, disrupting the network and increasing degradation. However, using a calcium nitrate source, calcium can only be incorporated into the silicate network at temperatures exceeding 400˚C [84]. This is well beyond the melting point of organic polymers, making calcium incorporation in this way impossible for the synthesis of hybrid materials. Alternative approaches are:

1. To consider the use of alternative calcium sources [117];
2. To incorporate calcium in the polymer [133];
3. To synthesise bioactive glass nanoparticles and then covalently bond them to a degradable polymer network to form a nano-composite material.

The work in this thesis focuses on the third of these approaches and the synthesis of bioactive glass nanoparticles for subsequent incorporation into a nano-composite scaffold. The development of a bioactive glass/polymer composite material is recognised as a promising strategy for improving the mechanical properties of bioactive glass systems for bone regeneration applications by combining the bioactive nature of the particles with the toughness of the polymer [134]. Many studies have shown polymer/bioactive glass nanocomposites materials to have both improved compressive strength and enhanced cell attachment and proliferation [135].

2.5.1 Nanoparticle Functionalisation

Many current nano-composites do not possess covalent bonds between the particles and matrix, resulting in un-optimised mechanical propertied and unmatched degradation rates. This is particularly problematic as many conventional biocompatible polymers degrade very rapidly once hydrolysis begins [16]. It is therefore essential to first functionalise the nanoparticles in order to create covalent bonding with the polymer chains. Functionalisation has also been shown to improve dispersion of nanoparticles within the polymer matrix [92], which in turn has been shown to be key for improving mechanical strength [135,136].

Functionalisation of silica based nanoparticles is most commonly achieved by the use of silane coupling agents ($Si(OR_3)R'$) which have the ability to bond to the silica inorganic nanoparticles at one end, with an organofunctional group on the other. Commonly used silane coupling agents include vinyltriethoxysilane (VTS), methacryloxypropyltriethoxysilane (MPTS), 3-glycidyloxypropyltrimethoxysilane (GPTS), 3-aminopropyltrimethoxysilane (APTS), 3-mercaptopropyltriethoxysilane (McPTS) and chloropropyltriethoxysilane (CPTS) [92]. However, here we will focus on the use of 3-aminopropyltriethoxysilane (APTES) to create amine functionalised nanoparticles.

Amine functionalised silica nanoparticles can be created simply by the addition of APTES to the Stöber process [137,138]. The benefit of this method is that the particles are well dispersed and the unheated particles have many OH groups with which the APTES can react. However, if the APTES is added before the completion of particle formation then it can have a large effect on particle size [92] or result in aggregated particles [138]. Bioactive glass nanoparticles containing calcium cannot be functionalised in this way as calcium incorporation requires subsequent heat treatment which would also burn off the amine groups. Therefore functionalisation is required after calcination. Li *et al.* claim that there are not enough surface –OH groups present to allow for post-functionalisation of silica nanoparticles without first etching the nanoparticle surface with an HF-HNO_3 solution. They then washed the etched particles directly with 20% nitric acid or in a mixture of concentrated sulphuric acid and 30% hydrogen peroxide under reflux, prior to functionalisation with APTES [139]. However, in bioactive glass nanoparticles this would result in loss of calcium from the particles and is therefore not feasible. One possible way of breaking down Si-O bonds on the surface, without loss of calcium from the particles would be by plasma treatment [140]. Due to these difficulties there is relatively little literature on the functionalisation of bioactive glass nanoparticles.

Chen *et al.* [141] successfully post-functionalised bioactive glass nanoparticles using APTES in n-hexane, at 65˚C for 6 h under the protection of dynamic inert nitrogen. El-Fiqi *et al.* used touene as a solvent

and performed the reaction under reflux with varying %'s of APTES [142]. However, their particles were aggregated both before and after functionalisation. Other groups have also functionalised particles using APTES with toluene as a solvent [143-145]. Zelikin *et al.* used ethanol as a solvent and also added 30% ammonia solution as well as APTES [146]. Successful functionalisation is most commonly shown by Fourier transform infrared (FTIR) spectra.

2.5.2 Nano-composite synthesis

Recently, work has increased on the production of bioactive glass/polymer nano-composites for bone regeneration applications due to the benefits discussed previously. Bioactive glass nanoparticles (BGNP's) have been successfully incorporated into composite materials with a variety of biocompatible polymers. Key findings are summarised in Table 2.1.

Table 2.1 Summary of BGNP/polymer composites

Polymer Matrix	BGNP composition (mol. %)	Composite structure	Functionalised NP's?	Key findings	Ref.
Chitosan	70 SiO_2 25 CaO 5 P_2O_5	Robocast scaffold	No	- *In vitro* apatite forming ability - Favourable substrate conditions for tissue cells - Robocasting enabled production of a 3D scaffold with a macro/micro dual-pore structure	[147]
Chitosan	35.31 SiO_2 21.87 CaO 42.81 P_2O_5	Membrane film	No	- *In vitro* apatite forming ability	[111]
Collagen	85 SiO_2 15 CaO	Hydrogel	Yes	- Functionalised NP's improved mechanical properties and reduced enzyme degradation - Reduced shrinkage of hydrogel - Favourable conditions for MSCs	[142]
Polycaprolactone (PCL)	75 SiO_2 25 CaO	Monolith	No	- Uniform dispersion of NP's by melt-binding process - Improved elastic modulus - *In vitro* apatite forming ability	[148]

Poly(lactide-co-glycolide) (PGLA)	Amorphous tricalcium phosphate $Ca_3(PO_4)_2$	Film	No	- 30% increase in Young's modulus - Increased speed of polymer degradation - *In vitro* apatite forming ability	[149]
Poly(L-lactide) (PLLA)	60 SiO_2 36 CaO 4 P_2O_5 (weight ratio)	Freeze dried scaffold	No	- Increased weight loss of scaffold with increased NP/polymer ratio - Decreased porosity with increasing NP content - *In vitro* apatite forming ability	[150]
Poly(L-lactide) (PLLA)	55 SiO_2 40 CaO 5 P_2O_5	Freeze dried scaffold	No	- Decreased porosity with increasing NP content - Increased compressive modulus and compressive strength - *In vitro* apatite forming ability	[151]
Poly(L-lactide) (PLLA)	29 SiO_2 13 CaO 58 P_2O_5 (weight ratio)	Vacuum dried scaffold	Yes	- Functionalised NP's improved mechanical properties of composite (tensile strength and impact strength energy increased) - NP's increased *In vitro* apatite forming ability - NP's facilitated attachment and proliferation of MSCs	[136]

Several groups have seen an effect of nanoparticle loading on degradation, suggesting the possibility of modulating the degradation rate by varying the glass/polymer ratio. However, relatively few composites have achieved covalent coupling between the particles and the polymer matrix. In the cases where particles have been functionalised and results have been compared to scaffolds produced with non-funtionalised particles, mechanical properties and particle dispersion have both been seen to improve [136,142]. Amine functionalisation of nanoparticles has been shown to enable covalent bonding to carboxyl groups within the polymer matrix [142]. This has the potential to allow for nano-composites to be produced with a variety of biocompatible polymers possessing COOH groups on their chains (e.g. Polycaprolactone (PCL), Polyglutamic acid (ɣ-PGA), Collagen, and Alginate).

Carbodiimide compounds 1-(3-Dimethylaminopropyl)-3-ethylcarbodiimide hydrochloride (EDC) and dicyclohexyl carbodiimide (DCC) provide the most popular and versatile method of activating carboxylic acids for direct conjugation to primary amines ($–NH_2$) via amide bonds [152]. In addition to being readily available, they also offer the advantage of having low toxicity for biomedical applications [153]. EDC is water soluble and can therefore be used for aqueous crosslinking, while DCC is insoluble in water and therefore used for methods which require non-aqueous organic synthesis. Carbodiimide chemistry is widely used to immobilise proteins by creating stable amide bonds [154,155]. It has also been used to create composite hydrogels [153] and to covalently bond carboxylic acid-functionalised silica nanoparticles to an amino terminate silica substrate [137]. It has great potential to achieve covalent coupling between amine functionalised nanoparticles and carboxyl groups on polymer chains, for the synthesis of a nano-composite scaffold.

EDC crosslinking is most efficient in acidic conditions (pH 4.5) so therefore *N*-hydroxysuccinimide (NHS) (or water soluble Sulfo-NHS) is often included in EDC coupling protocols to improve efficiency at neutral pH. A schematic of the reaction chemistry is shown in Figure 2.14.

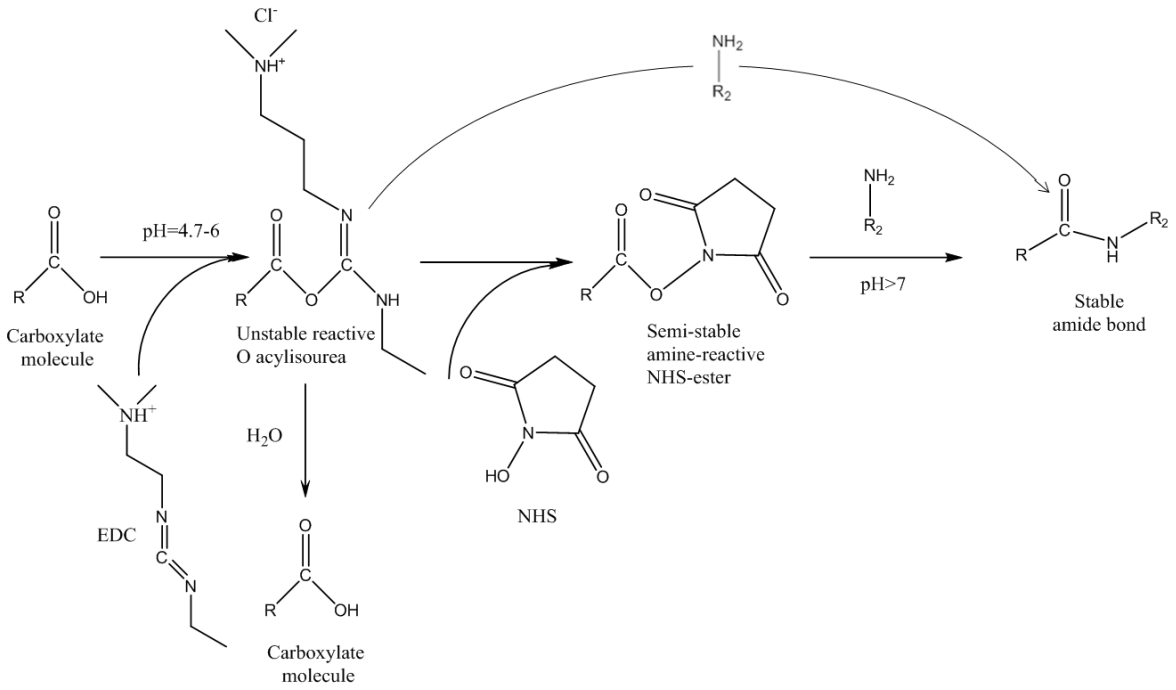


Figure 2.14 - Schematic of carbodiimide (EDC/NHS) carboxyl-to-amine crosslinking reaction. Modified from [152,156].

2.6 Research objectives

The overall objective of this thesis is to synthesise bioactive glass nanoparticles containing Zn and Ca cations for cancer treatment and bone regeneration respectively. In particular, the aim will be to create a system which will allow for the particles to be optimised for a variety of applications or as understanding advances. It is acknowledged that there is still much that is not known about nanoparticles and their fate within the body. Size, composition, morphology and charge are all important factors which will be considered throughout this thesis.

The objectives of this work are to:

1. Conduct a comprehensive study of how the processing variables in the Stöber process can be systematically altered to obtain monodispersed particles of specific sizes in the range 20 – 500 nm.
2. Investigate the incorporation of calcium and zinc cations into silica nanoparticles and perform a complete characterisation of the resulting particles (including physical, chemical, and degradation properties).
3. Synthesise mesoporous silica nanoparticles and investigate the incorporation of cations, again conducting a complete characterisation of the particles produced (including physical, chemical, and degradation properties).

4. Assess the cell uptake and cytotoxicity of SiO_2-ZnO particles to determine their potential to selectively kill cancer cells.
5. Functionalise SiO_2-CaO nanoparticles with amine groups and subsequently perform preliminary investigations into the ability to incorporate these functionalised nanoparticles into a nano-composite material for bone regeneration applications.

It is hoped that this work will form the basis of successful therapies in the future for bone regeneration and cancer treatment.

3 Instrumentation

3.1 Transmission electron microscopy (TEM)

TEM is a powerful technique that can provide high spatial resolution at nanoscale. It can also be used to obtain information about the crystallinity of a specimen by the production of diffraction patterns and chemical composition by using EDS.

In TEM, electrons accelerated towards an ultra-thin sample interact with the atoms in the specimen via columbic forces which cause the electrons to be scattered as they pass through. It is necessary for a TEM to operate in a vacuum to avoid scattering of electrons by gas molecules. A schematic of the TEM is shown in Figure 3.1. It consists of an electron source which emits electrons which are then accelerated by an electric field at a voltage of around 200kV. The TEM predominantly used in this thesis was the JEOL FX2000 which uses a tungsten filament as the electron source. At high temperature the filament emits electrons which are focused by a set of condenser lenses, the first of which controls the beam current density. The second condenser lens is used to vary the convergence of the beam and can be adjusted in practice by using the 'brightness' control. The objective lens focuses electrons emerging from the specimen into a diffraction pattern on the back focal plane and by adjusting the strength of the objective lens, the image formed on the viewing screen can be focused. An objective aperture can be inserted to increase mass-thickness contrast by selecting the angular range of the electrons contributing to the final image. The intermediate lens can be adjusted to produce an image or diffraction pattern. The projection lens, on the other hand, is fixed and is used simply to magnify the image or diffraction pattern on the viewing screen. The viewing screen of a TEM is typically a phosphor screen which converts the incident electrons into visible photons for imaging.

In bright field imaging the sample is illuminated parallel to the optic axis allowing direct transmission of the beam. An image forms from the interaction of electrons with the sample appearing bright where there is no scattering and dark where there is disturbance to the incident beam. Thus, the contrast observed in the image arises from mass-thickness variations in the specimen. The objective aperture can be inserted to improve contrast. Dark field imaging on the other hand, uses a diffracted incident beam and collects light scattered by the sample resulting in the specimen appearing bright.

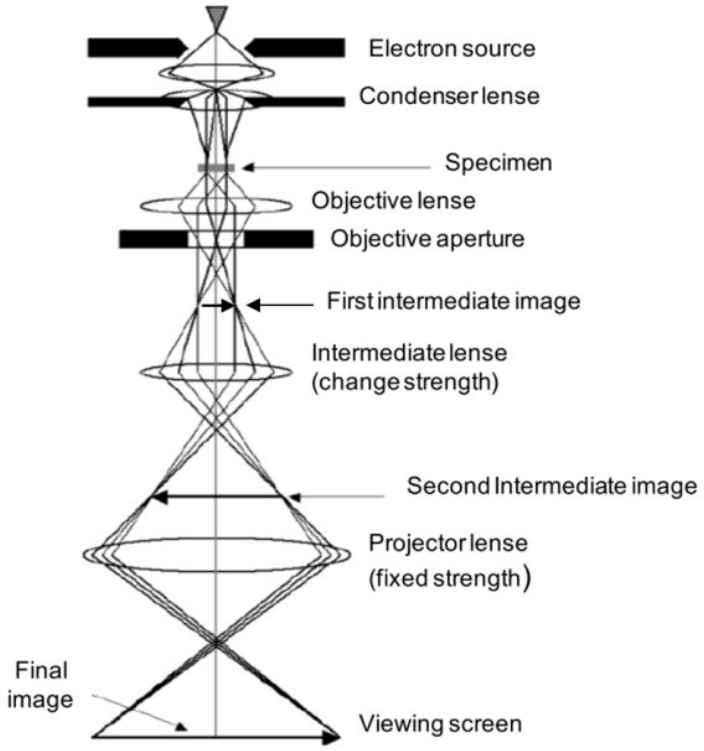


Figure 3.1 - Schematic of a TEM operating in imaging mode. Modified from [157].

3.1.1 Energy dispersive X-ray spectroscopy (EDS)

EDS provides information about the chemical composition of a material by analysing the characteristic X-ray energies emitted from each element. When the high energy electron beam interacts with an inner shell electron in an atom within the specimen, it can dislodge the electron, leaving a hole. An outer electron will drop into this lower energy state to fill the hole, resulting in the emission of an X-ray with energy equal to the difference between the electron shells involved in the transition. The number and energy of the X-rays emitted from the specimen are different for every element. They are measured by a detector recording an energy spectrum of intensity as a function of energy, allowing for information about the composition of the specimen to be found.

3.1.2 Scanning transmission electron microscopy (STEM)

STEM differs from traditional TEM in that the electron beam is focussed into a small point and scanned over the surface of the sample in a raster pattern to obtain an image. This is beneficial for determining the composition of a specific point in the sample by EDS.

3.2 X-ray fluorescence (XRF)

XRF is a similar technique to EDS, in that it provides information about the chemical composition of a material by analysing the characteristic x-ray energies emitted from each element. However, while

EDS uses an electron beam to dislodge electrons in the sample, XRF uses an X-ray beam. The outcome is still that an outer electron will drop into this lower energy state to fill the hole, resulting in the emission of an X-ray with energy equal to the difference between the electron shells involved in the transition. Energy Dispersive XRF (EDXRF) uses an energy dispersive detector, as used in EDS, to record the number and energies of the x-rays emitted. However in XRF a WD (Wavelength Dispersive) detector can also be used to give higher accuracy. Unlike with EDS, XRF is always performed with certified standards to give quantitative results.

3.3 Dynamic light scattering (DLS)

DLS can be used to measure the hydrodynamic radius of particles in a suspension by measuring the Brownian motion of particles and relating this to particle size. Brownian motion is the random movement of particles due to interactions with the solvent molecules that surround them. The larger the particle, the slower the Brownian motion will be. In DLS, a monochromatic laser beam is directed at a sample and the light scattered by particles in the illuminated volume is analysed by a detector placed at an angle θ with respect to the transmitted beam. Larger particles scatter predominantly at smaller angles whereas smaller particles scatter light at a larger angle. For accurate DLS size interpretation, a stable temperature is required since any changes in temperature will affect Brownian motion. A high dilution is also required. It is important to note that the hydrodynamic radius refers to how a particle diffuses within a medium and is often slightly larger than the actual diameter.

3.4 Fourier transform infrared (FTIR)

FTIR is a non-destructive surface analysis technique which can be used to identify specific chemical groups present in the sample. Infrared (IR) radiation is used to excite covalent bonds with a dipole moment within the sample. As the molecules on the surface of the specimen absorb energy from the IR light, the covalent bonds make the transition to the next allowed vibrational energy state. Specific functional groups (covalent bonds with dipole moments) in a material absorb IR radiation at a characteristic peak, which is related to the wave number. FTIR produces a plot of IR radiation intensity, in absorbance or transmittance, against wave number.

3.5 Inductively coupled plasma - optical emission spectroscopy (ICP-OES)

ICP-OES is a highly sensitive quantitative technique used for the detection of trace elements in solutions. Initially standards are made up containing the elements to be measured in known concentrations. The solution whose elemental concentration is to be determined is then pumped into a nebuliser where it is mixed with Argon gas to form an aerosol. Larger droplets are removed from the sample aerosol as it passes through the spray chamber before it enters the inductively

coupled plasma (ICP) torch. As the sample passes through the ICP, atoms are excited and emit electromagnetic radiation at wavelengths characteristic of particular elements. The intensity of this emission is indicative of the concentration of the element within the sample. It is converted to an electrical signal by a photomultiplier in the spectrometer and the intensity of this electric signal is compared to a previous measured intensity produced by the standards of known concentrations.

3.6 X-ray diffraction (XRD)

XRD is a method used for determining the atomic and molecular structure of a crystal. It can be used to identify crystalline phases within a structure and to determine the crystal structure by analysing the position and intensities of diffraction peaks. In XRD, an electromagnetic wave is targeted at the sample, which rotates at an angle θ at constant velocity. The diffraction pattern is produced according to Bragg's Law. Crystalline atoms cause a beam of X-rays to diffract in many specific directions, resulting in a spectrum of characteristic peaks. Amorphous fractions in the sample are only recognisable by the absence of peaks in the XRD spectrum. A typical XRD setup is shown in Figure 3.2.

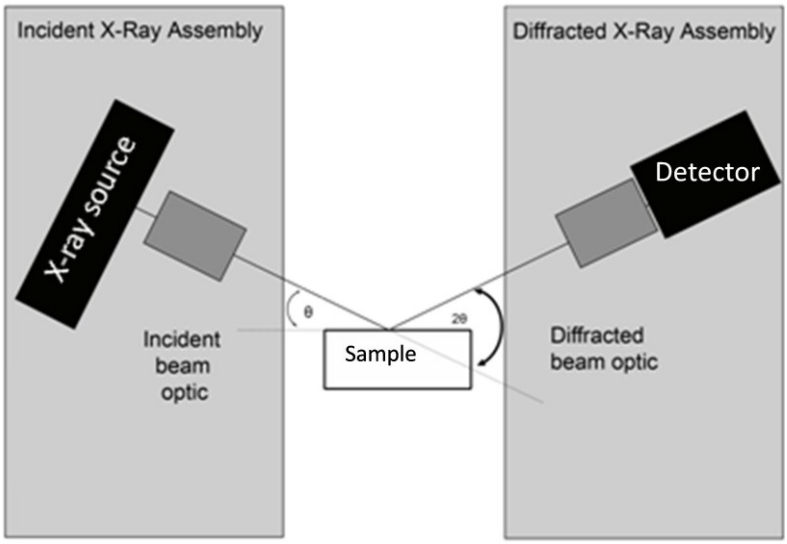


Figure 3.2- Schematic of XRD setup. Modified from [158].

3.6.1 Small-angle X-ray scattering (SAXS)

SAXS is based on the same principles as XRD and can be used to order to detect crystalline phases with characteristic peaks at smaller angles. For XRD, the detector and the X-ray source are both positioned above the sample (as seen in Figure 3.2) so at small values of θ part of the x-ray beam will incident on the detector without being diffracted by the sample. Therefore, for very small angles the detector is placed below the sample and x-rays are scattered as they pass through the sample,

producing a spectrum of characteristic peaks. At larger angles this technique is known as Wide Angle X-ray Scattering (WAXS).

3.7 Solid state Nuclear Magnetic Resonance (NMR)

NMR can be used to determine the environments of certain nuclei and can therefore help to provide an understanding of the chemical structure of certain materials. The principle behind NMR is based on the characteristic spins and charges of nuclei in different local environments. When a sample is placed in a magnetic field there is a net magnetisation along the direction of the applied magnetic field. Pulses of radio frequency are applied to the sample causing a shift away from this equilibrium to take place at the corresponding frequency and thus shifting the net magnetisation perpendicular to the applied magnetic field. As the spins return to equilibrium, current is induced in the NMR coil at the corresponding frequency. The precise resonant frequency of this signal is dependent on the effective magnetic field at the nucleus which is affected by electron shielding. As a result, the resonant frequency can be used to give information on the local chemical environment and is plotted as a chemical shift spectrum. Information can be gathered on the relative abundance of a species in a sample from the comparative intensities of the peaks at specific chemical shifts. Additional information about the local environment of the species can be gathered from observations based on peak width or peak splitting.

In contrast to classical liquid-state NMR experiment, where Brownian motion leads to an averaging of anisotropic interactions and sharper characteristic peaks, the line widths in solid state NMR become significantly broadened as the various interactions are not averaged out. To overcome this, the sample is subject to sufficiently fast spinning at the magic angle 54.74° which eliminates the direction dependence of the chemical shielding, leaving only the isotropic chemical shift. This is known as magic angle spinning (MAS) and has the effect of reducing the widths of the signals and hence increasing the resolution of the spectra.

3.8 Focused Ion Beam - Scanning Electron Microscopy (FIB-SEM)

A scanning electron microscope (SEM) produces images of a sample by accelerating electrons towards it. As with TEM, it consists of an electron source (e.g. a tungsten filament cathode) which emits electrons. These then pass through a series of lenses and deflectors, focussing them on the specimen, with the final lens deflecting the beam in the x and y axis so that it can move backwards and forwards over the sample. When the primary electron beam interacts with the specimen it results in the emission of secondary electrons by inelastic scattering. These are detected to form an image of the surface topography.

The difference between SEM and Focused Ion Beam (FIB) is that FIB uses a focused beam of ions as opposed to electrons. At low currents this can also be used for imaging, although at high currents it can be highly destructive and can therefore be used for sputtering or milling at specific sites. A FIB-SEM can combine the imaging ability of an SEM with the material processing capabilities of FIB.

3.9 Zeta Potential

Zeta potential is a physical property of particles in suspension. Charged particles in solution attract ions of the opposite charge forming a Stern layer around the surface of the particle. This layer in turn attracts counter ions and forms an outer (diffuse) region in which the ions move more freely around the particles. Together these are referred to as an electrical double layer. The zeta potential is effectively the electrokinetic potential at the boundary of this layer and not only depends upon the particle surface but also on the dispersant. To measure the zeta potential of a sample, an electric field is applied across the particles in suspension causing relative movement between the particles and the dispersant. This process is known as electrophoresis and can be measured by laser Doppler velocimetry. Provided the electric field strength or voltage gradient, the dielectric constant of medium and the viscosity of the medium are known, the zeta potential can be calculated [159].

3.10 Nitrogen Adsorption

Gas adsorption is a commonly used analysis technique for porosity and surface area measurement. In particular nitrogen sorption is often used, as nitrogen gas is readily available in high purity, it has a widely accepted cross-sectional area and a relatively strong interaction with most solids. The amount of gas adsorbed to the surface of the material is calculated at various pressures and the corresponding surface area can be calculated using the Brunauer–Emmett–Teller (BET) equation [160]. A plot of volume of gas adsorbed against the corresponding relative pressure (P/Po) is called an isotherm. Determination of specific porosity, pore size, shape and interconnectivity requires a recognition and understanding of different basic isotherm types. The original International Union of Pure and Applied Chemistry (IUAPC) recommendations have been updated in 2015, and now group physisorption isotherms into eight characteristic types relating to different pore structures (Figure 3.3).

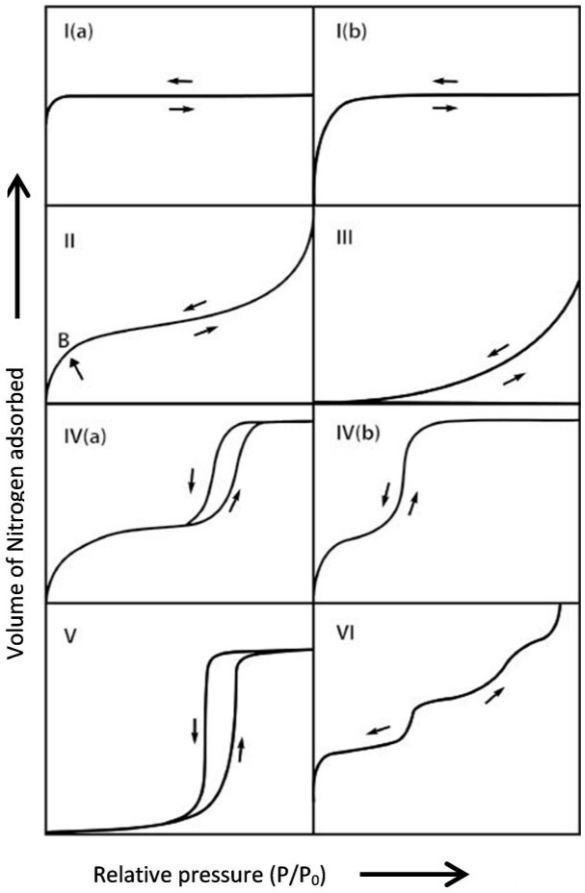


Figure 3.3 – Updated IUPAC classification of physisorption isotherms. Modified from [161].

By increasing the pressure beyond the point at which a monolayer of nitrogen forms on the surface, the pores can be filled by condensed (liquid) nitrogen and the total pore volume can be calculated at the saturation point. The Barrett–Joyner–Halenda (BJH) model [162] (based on the evaporation of a condensed meniscus from cylindrical mesopores), can be used to obtain pore size distributions of materials from the desorption curve. However, there is no differentiation between inter and intra-particle porosity and it is now evident that pore size analysis of narrow mesopores (< 40 nm) cannot be reliably achieved by the application of methods which are based on the Kelvin equation, such as the BJH model. The new IUPAC Technical Report on the physisorption of gases, instead suggests the use of density functional theory (DFT) based computational methods to obtain a reliable assessment of the size distribution of mesopores [161]. DFT is a practical method by which the pore size distribution can be determined from model isotherms calculated from mean-field density functional theory [163,164].

4 Synthesis of silica nanoparticles and control of particle size

4.1 Introduction

The size of nanoparticles has a huge effect on their cytotoxicity and effects on cells, including internalisation, distribution and fate of particles. Consequently for different applications different sizes of nanoparticles may be desirable. The ability to be able to control size reliably and to produce monodispersed particles is therefore extremely important.

Silica nanoparticles of different sizes have been produced by using variations of the Stöber process since 1968 by varying the concentration of reactants. As discussed in section 2.4.4.1, the concentration of ammonia has the greatest effect on particle size. However, reactant concentrations can also affect the standard deviation of particles and the time taken to reach maximum particle size. Therefore a compromise may be necessary and a suitable range must be found over which the concentration of ammonia can be varied to produce monodispersed particles of a variety of sizes in a realistic timescale.

The objective of this chapter is to revisit the original Stöber process to provide a comprehensive understanding of how to reliably control particle size, whilst maintaining monodispersed particles over a range of particle sizes from 50 – 500 nm. Additional elements can subsequently be added for a variety of therapeutic or diagnostic applications.

4.2 Materials and methods

Whilst silica nanoparticles have been synthesised repeatedly in literature, the methods used vary greatly in complexity and the particles produced vary in both reproducibility and monodispersity. This chapter describes an optimised method which has been simplified here to reliably produce monodispersed particles over a large size range.

It was found that it was not necessary to complicate the procedure by increasing the temperature [99], adding any reactants drop-wise [100], the use of a seeded batch process [93] or the use of a semi-batch reactor [99].

4.2.1 Particle Synthesis

All reagents were purchased from Sigma-Aldrich. Using the simplest version of the original Stöber process [86], ethanol (ethyl alcohol, 200 proof, ≥99.5%), distilled water, and ammonium hydroxide (ACS reagent, 28.0 - 30.0% NH_3 basis) were mixed in an ultrasonication bath at room temperature. After 10 minutes, TEOS (tetraethyl orthosilicate, reagent grade, 98%) was added to the solution and the solution was left overnight, or until the particles had reached maximum size (determined by

DLS). A TEOS concentration of 0.28 M was used (as per the Stöber process) with a range of water concentrations from 3 - 15 M and ammonium hydroxide concentrations varying from 0.11 – 1.13 M. TEOS concentrations of 0.045 M, 0.17 M, and 0.5 M were later analysed as these have been also used in previous papers [86,93,100]. A schematic showing the synthesis of silica particles is shown in Figure 4.1.

The solution was then centrifuged to obtain a solid pellet of particles which was dried overnight at 60˚C. Removal of solution by centrifugation was performed due to reports that drying in the presence of water can result in agglomeration phenomena caused by condensation reactions at the interparticle contacts [92].

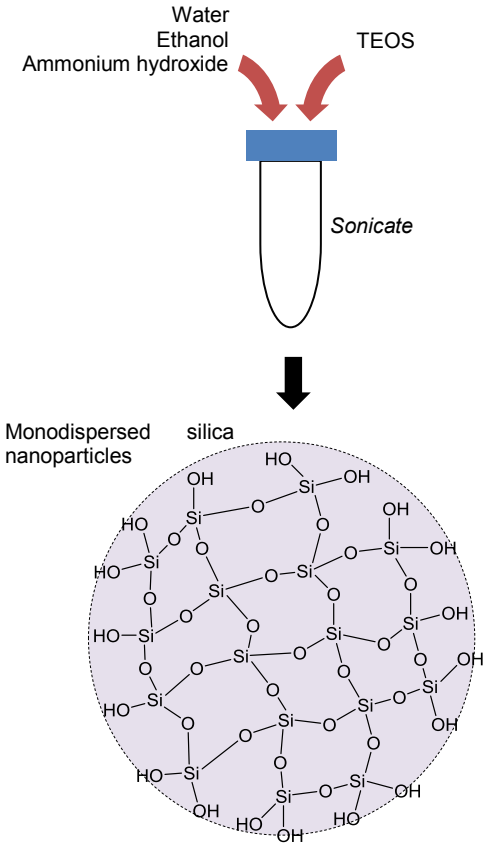


Figure 4.1 - Schematic showing the synthesis of silica nanoparticles.

4.2.2 Particle characterisation

Particle size of samples was determined by both DLS (Malvern instrument 2000) and TEM. For both techniques, samples were dispersed in ethanol and sonicated for 15 minutes in order to break up any aggregates. Stöber particles have extremely high colloidal stability and low absorption at 633 nm making DLS suitable. However, DLS inherently calculates the hydrodynamic radius of particles giving slightly larger values [165].

For bright field TEM analysis, samples were collected on 300 mesh copper TEM grids coated with holey carbon film and imaging was performed on a JEOL-2000FX TEM using with an operating voltage of 200 kV and a 10 µm objective aperture to increase mass-thickness contrast. Multiple areas of each grid were analysed and 100 particles from each sample were measured to calculate a mean particle diameter and standard deviation.

4.3 Results & Discussion

Stöber silica particles were synthesised as described and a comprehensive study of the processing variables was carried out. Figure 4.2 shows that increasing ammonium hydroxide concentration resulted in increased particle size. The trend is also confirmed by TEM images shown in Figure 4.3. TEM images showed good monodispersity which corresponds to the consistently low PDI values obtained by DLS measurements (Figure 4.2B). The role of ammonium hydroxide in the process is to raise the pH, which accelerates the polycondensation reaction but also creates an environment with a pH much higher than the isoelectric point, which for silicic acid in aqueous solution is 2.2. This creates repulsive charges between the particles, which is critical for monodispersity [85,97]. At all ammonium hydroxide concentrations, as water concentration increased from 3 – 15 M, particle size initially increased to a maximum at 9 M before decreasing again. This trend was most significant at higher ammonium hydroxide concentrations (0.85 M and 1.13 M) and is again confirmed by TEM images (Figure 4.4). Figure 4.2A indicates that particle size could be controlled from 20.5 ± 1.7 nm (3 M H_2O, 0.11 M NH_4OH) to 823.8 ± 122.4 nm (9 M H_2O, 1.13 M NH_4OH), according to DLS. All DLS values quoted are number mean.

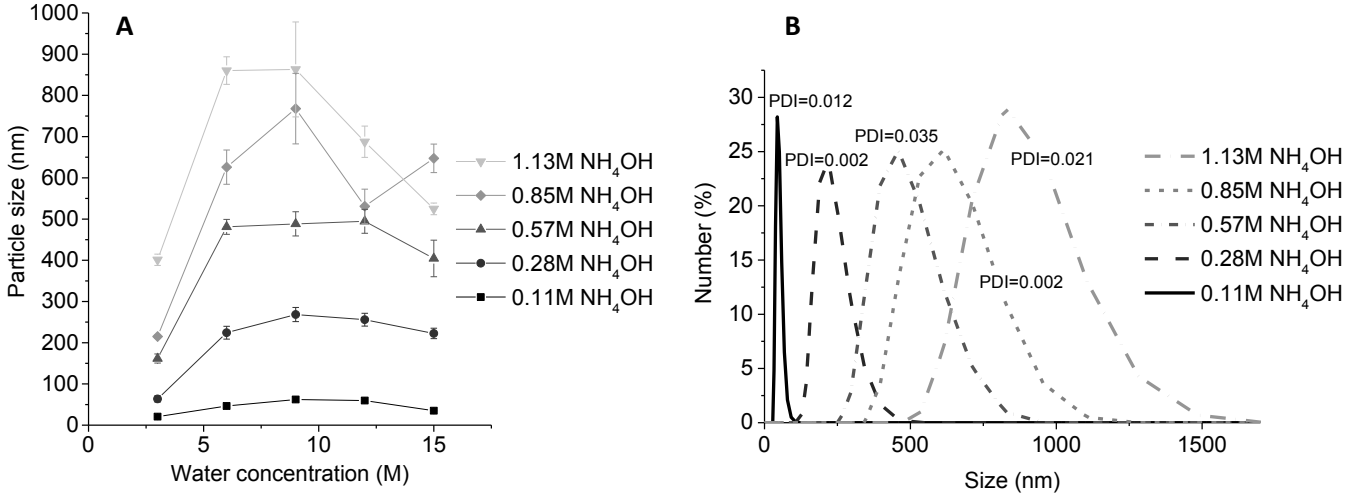


Figure 4.2- A) Mean particle size of silica particles (DLS) as a function of water and ammonium hydroxide concentration for 0.28M TEOS. Error bars show the standard deviation from the mean (n=3). B) DLS results showing particle size distribution with increasing ammonium hydroxide concentration for 0.28M TEOS and 6M H_2O.

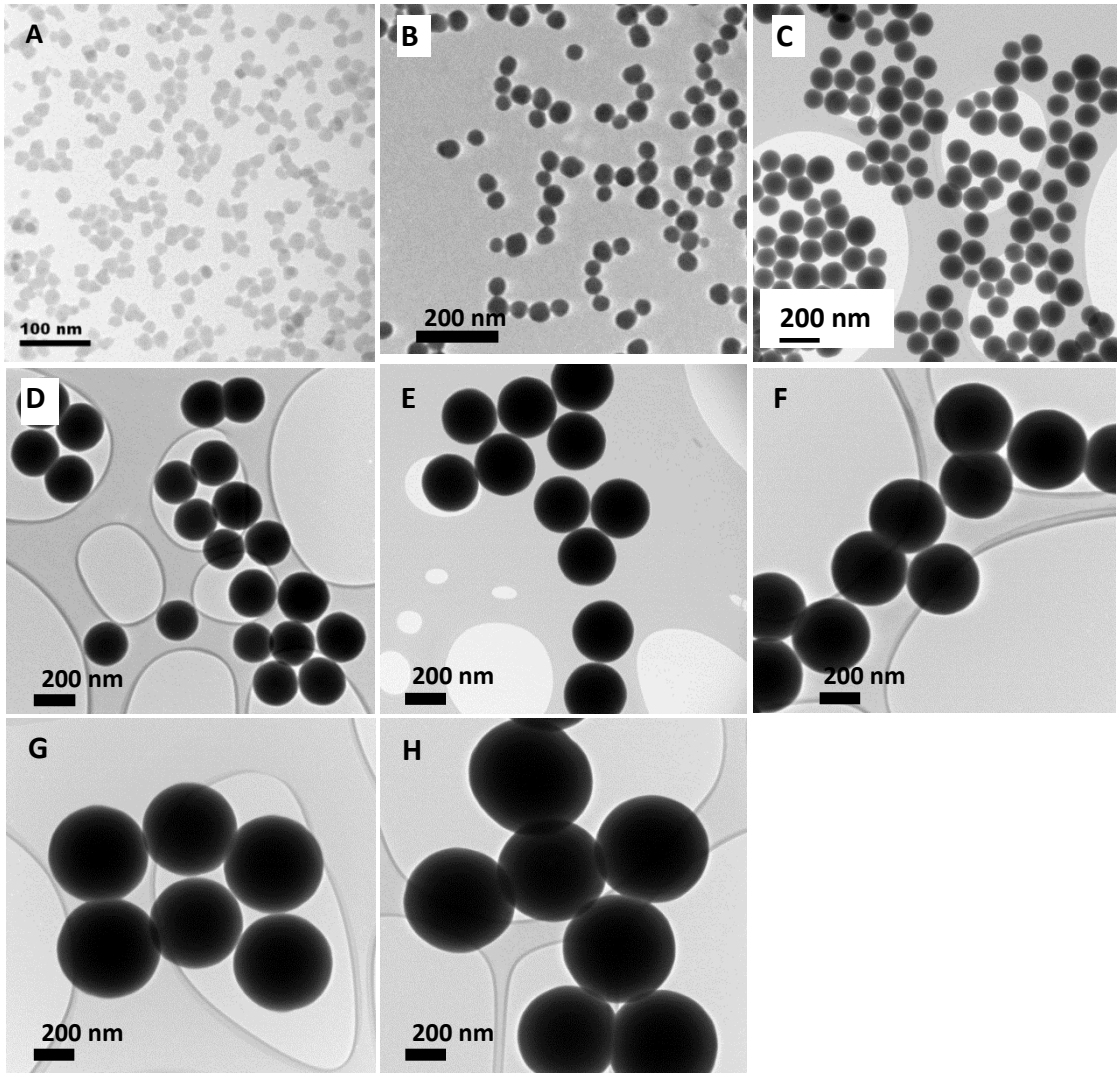


Figure 4.3 - TEM images of silica particles produced using 0.28M TEOS, 6M H_2O and varying concentrations of ammonium hydroxide: A) 0.056M NH_4OH B) 0.11M NH_4OH C) 0.17M NH_4OH D) 0.28M NH_4OH E) 0.40M NH_4OH F) 0.57M NH_4OH G) 0.85M NH_4OH H) 1.13M NH_4OH.

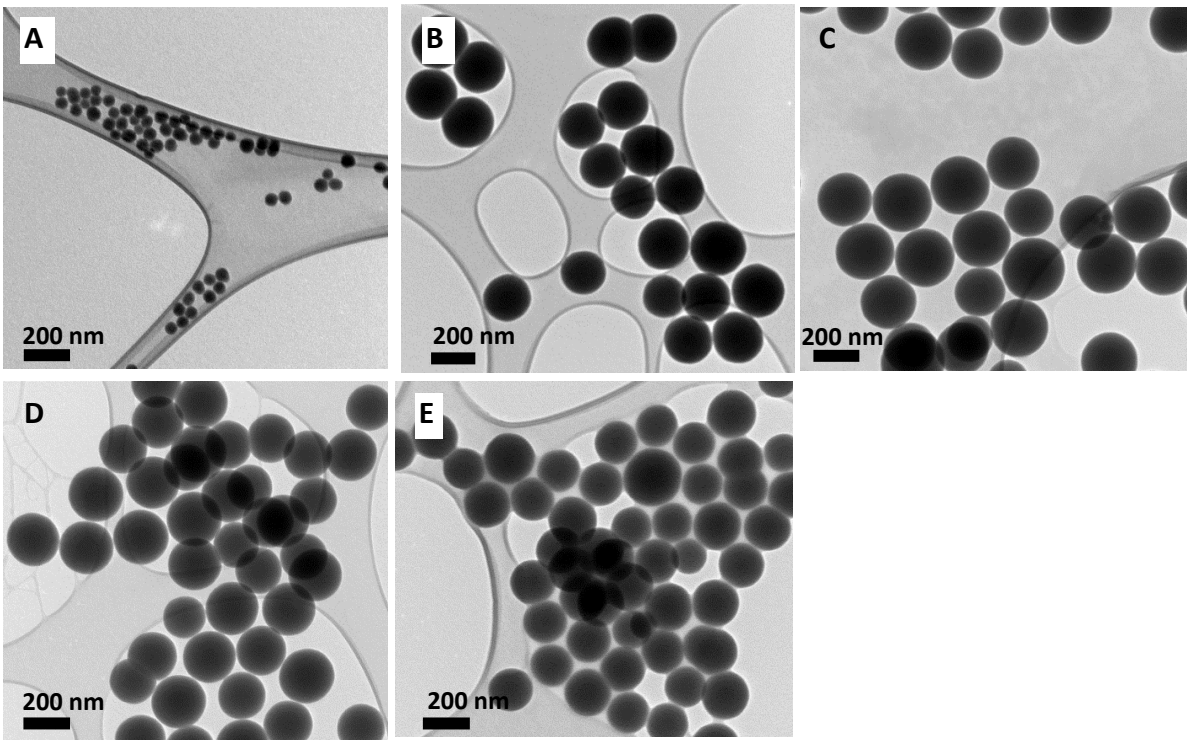


Figure 4.4 - TEM images of silica particles produced using 0.28M TEOS, 0.28M NH_4OH and varying concentrations of water: A) 3M H_2O B) 6M H_2O C) 9M H_2O D) 12M H_2O E) 15M H_2O.

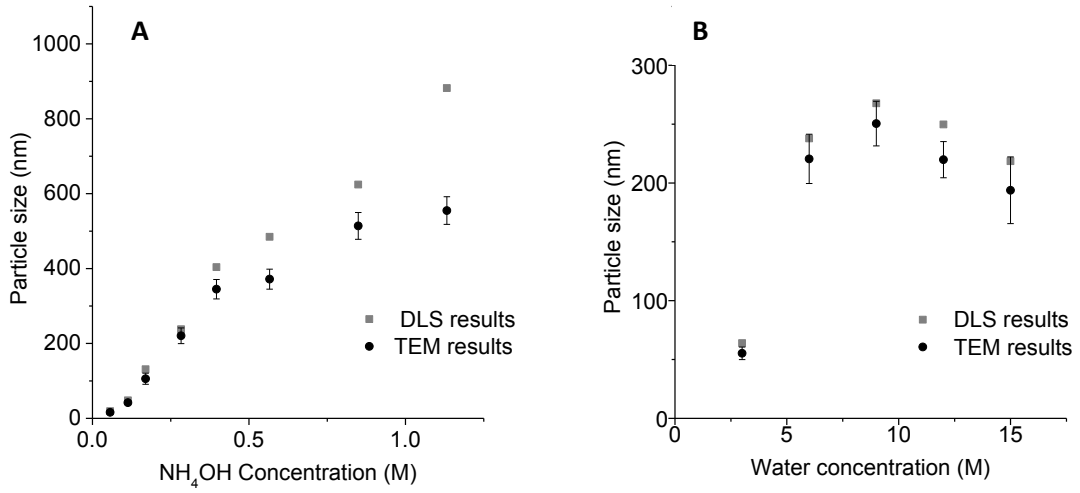


Figure 4.5- A comparison of DLS (number mean) and TEM results for silica particles showing variation of mean particle size with: A) ammonium hydroxide concentration for 0.28M TEOS and 6M H_2O and B) water concentration for 0.28M TEOS and 0.28M NH_4OH. Error bars for TEM results show the standard deviation of particle size in each sample (n=100).

Particle size measurements from TEM plotted in Figure 4.5A show that particle size increased linearly as ammonium hydroxide concentration increased from 42.0 ± 5.5 nm at 0.11 M to 344.9 ± 25.9 nm at 0.40 M (R^2 = 0.9997) before starting to level off. This trend was observed by both TEM

and DLS characterisation methods, although the plateau was less pronounced in DLS. For particle sizes in excess of 500 nm, we found that DLS no longer gave an accurate reading and instead tends to significantly overestimate particle size. Previous work analysing silica particles showed DLS to be accurate, although a maximum size of 400 nm was used [165]. This unreliability of DLS at larger particle sizes is in agreement with Figure 4.2, which showed an increase in standard deviation of particle size from the mean, as particle size increased, while the particles themselves remained monodispersed. The standard deviation for the TEM results shown in Figure 4.5 is calculated from 100 particles measured. The same sample was analysed using DLS to give a direct comparison. DLS gave a PDI of < 0.05 for the majority of samples indicating that samples were monodispersed. The distribution algorithms used by DLS are based on NNLS (non-negative least squares) and are not accurate for samples with such a low PDI. Thus standard deviation is not shown for DLS results and particles are assumed to be monodispersed.

Particle size variation was less sensitive to changes in water concentration. In the range 6 – 15 M H_2O, particle size measurements from TEM plotted in Figure 4.5B show that the mean diameter varied by less than 60 nm (for 0.28 M NH_4OH). However, there was an initial increase in mean diameter to 250.5 ± 18.9 nm at 9 M H_2O. At 0.28 M NH_4OH, for concentrations of water varying from 3 – 15 M, the particle size consistently remained below 300 nm and thus DLS gave reliable results. The particle size calculated by DLS was always slightly higher than TEM due to the fact that DLS measures the hydrodynamic radius.

Whilst the standard deviation and PDI is low for all samples, it can be seen from Figure 4.6 that standard deviation as a % of particle size actually decreases as particle size increases. This is consistent with the majority of literature [93,96,101] and suggests that within the limits of this investigation standard deviation is not affected by water or ammonium hydroxide concentration.

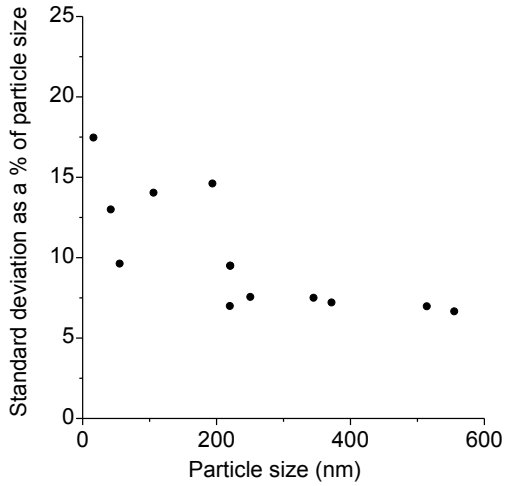


Figure 4.6 - Standard deviation as a % of particle size calculated from TEM results (n=100).

The effect of variation of TEOS concentration was also investigated. Concentrations 0.045 M, 0.17 M, 0.28 M and 0.5 M were chosen as these have been used most widely in literature [86,93,97,100]. Water concentration was kept constant at 6M and ammonium hydroxide concentration was varied between 0.11 and 0.57M. At these concentrations the particle size remains within the limits of DLS and therefore this method was used for characterisation. The results are shown in Figure 4.7.

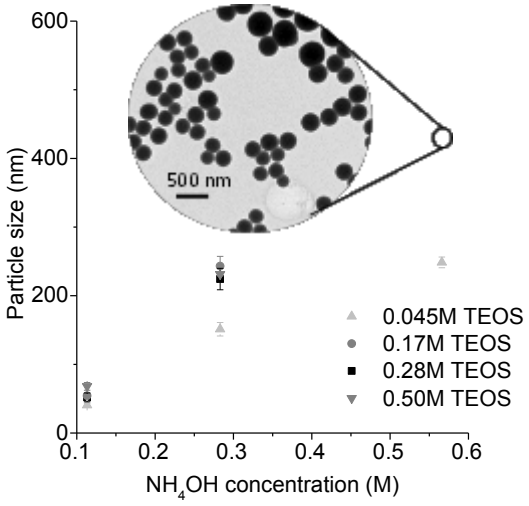


Figure 4.7 - Mean particle size of silica particles (DLS) as a function of ammonium hydroxide concentration for 6M H_2O and increasing TEOS concentrations. Error bars show the standard deviation of mean size (n=3). Inset shows heterodispersed particles at high TEOS and NH_4OH concentrations.

It can be seen that increasing TEOS concentration from 0.045 M to 0.17 M resulted in an increase in particle size (Figure 4.7), although further increasing the concentration to 0.28M resulted in no further size increase. However, increasing TEOS concentration directly resulted in an increased yield. For 20 ml volume of total solution, 0.17 M TEOS (0.17 M NH_4OH, 6 M H_2O) gave a dried nanoparticle mass of 229.7 ± 3.8 mg (n=3), whereas 0.28 M TEOS (0.17 M NH_4OH, 6 M H_2O) resulted in a corresponding 40% increase in yield, producing 384.7 ± 2.5 mg (n=3) dried mass of nanoparticles. Further increasing the TEOS to 0.5M resulted in a further increase in yield; however particle size was less consistent, giving higher standard deviations and often polydispersed particles at high ammonium hydroxide concentrations. The PDI's for these particles (0.5M TEOS, 6M H_2O, 0.57M NH_4OH) ranged from 0.024 (monodisperse) to 0.618 (polydisperse). Thus for all further investigations, 0.28M was chosen as the optimum TEOS concentration, giving a high yield and consistently monodispersed particles. Other papers have also observed heterodispersed particles at high TEOS and ammonia concentrations [93].

4.4 Conclusions

Spherical monodispersed particles with a modal size ranging from 20 – 500 nm were produced reliably by using this simple version of the original Stöber process, by varying the concentration of reactants. This negates the need for subsequent adjustments to the method which involve additional steps and introduce more sources of potential error. Of all the reactants, ammonium hydroxide concentration had the largest effect and allowed for best control of particle size, with increasing ammonium hydroxide concentration resulting in increased particle size. The theory that particle size increases with increasing water concentration (up to 9M) and then decreases was also supported, although the decrease in size was not significant except at high ammonium hydroxide concentrations (> 0.57 M). Varying the TEOS concentration from 0.28 – 0.17 M did not affect particle size or its distribution. However, reducing TEOS concentration to 0.045 M resulted in a smaller particle size, and increasing it to 0.5 M produced heterodispersed particles at high ammonium hydroxide concentrations. TEM validated the use of DLS to analyse particle sizes up to 500 nm. However, beyond this size, DLS results are less consistent and tended to significantly overestimate the size of particles.

5 Cation incorporation in to silica nanoparticles

5.1 Introduction

Having successfully synthesised monodispersed silica nanoparticles of controlled sizes, the aim of this chapter was to investigate the subsequent incorporation of Zn and Ca cations for therapeutic purposes. The motivation behind a multi-step process is to allow for maximum flexibility and the ability to tailor particles for a variety of applications.

The desire to incorporate calcium into silica nanoparticles to increase bioactivity has been the focus of much recent research for bone regeneration applications. However, as discussed in section 2.4.5, most previous attempts have resulted in incorporation of a relatively low proportion of calcium and have caused the particles to become aggregated or irregular in size and shape. The objective in this chapter was to increase the amount of calcium incorporated, whilst maintaining the ability to produce monodispersed particles of controlled sizes. A complete quantitative characterisation of the nanoparticles was then undertaken to prove the incorporation of calcium. Literature on bioactive sol-gel glasses suggests that 70S30C is a suitable composition [7-9]; therefore this was the target value. For bone regeneration applications by incorporation of nanoparticles into a hybrid, it is not necessarily required for large numbers of the particles to be internalised by cells. However, differentiation of stem cells along an osteogenic lineage is desirable. As a starting point, particle size of 100 nm was selected for the work in this thesis.

Additionally, the incorporation of zinc into silica nanoparticles for cancer treatment was investigated, with the aim of providing a safe and simple method for the delivery of toxic Zn^{2+} ions to cancer cells and subsequent release at a controlled rate. As this requires intracellular release, uptake of particles into cells is essential. A particle size of 80 nm was selected as this falls within the range of 50-100 nm which has been shown to result in maximum particle uptake by tumours [62], whilst the control silica particle at this size should not be inherently cytotoxic.

5.2 Materials and methods

While silica nanoparticles have been synthesised repeatedly in literature, the addition of calcium has typically resulted in agglomerations of particles or particles with irregular morphology. This chapter describes an optimised process which was developed here to synthesise clean, monodispersed silica nanoparticles incorporating Zn and Ca cations.

5.2.1 Particle Synthesis

For particles containing calcium, monodispersed silica particles were first synthesised using the method described previously. As 100 nm was the target particle size, reactants were added in the

concentrations 0.28 M TEOS, 6 M H_2O, 0.17 M NH_4OH. Particles were sonicated and left overnight as before, although after centrifugation particles were re-dispersed in distilled water before adding calcium nitrate tetrahydrate (ACS reagent, 99%) to the solution. After 20 minutes, the particles were centrifuged again, the supernatant was removed and the pellet was dried at 60˚C overnight. The particles were then heated to 680˚C for 3 h, at a heating rate of 3˚/min. 680˚C was chosen to allow for the removal of nitrates and incorporation of calcium into the network, without crystallisation [84]. This is due to the fact that the crystallisation of bioactive glasses is known to significantly reduce their degradation and apatite formation in comparison to amorphous glasses, resulting in a detrimental effect on bioactivity [79,114,175]. Dissolution and HCA formation has been seen to decrease in sol-gel derived bioactive glasses as temperature was increased from 700-800˚C. This was attributed to the crystallisation and densification of the silica network resulting in fewer OH groups[117]. Subsequently the particles were washed 3 times in ethanol to remove any excess calcium not incorporated into the network. A schematic depicting this process is shown in Figure 5.1.

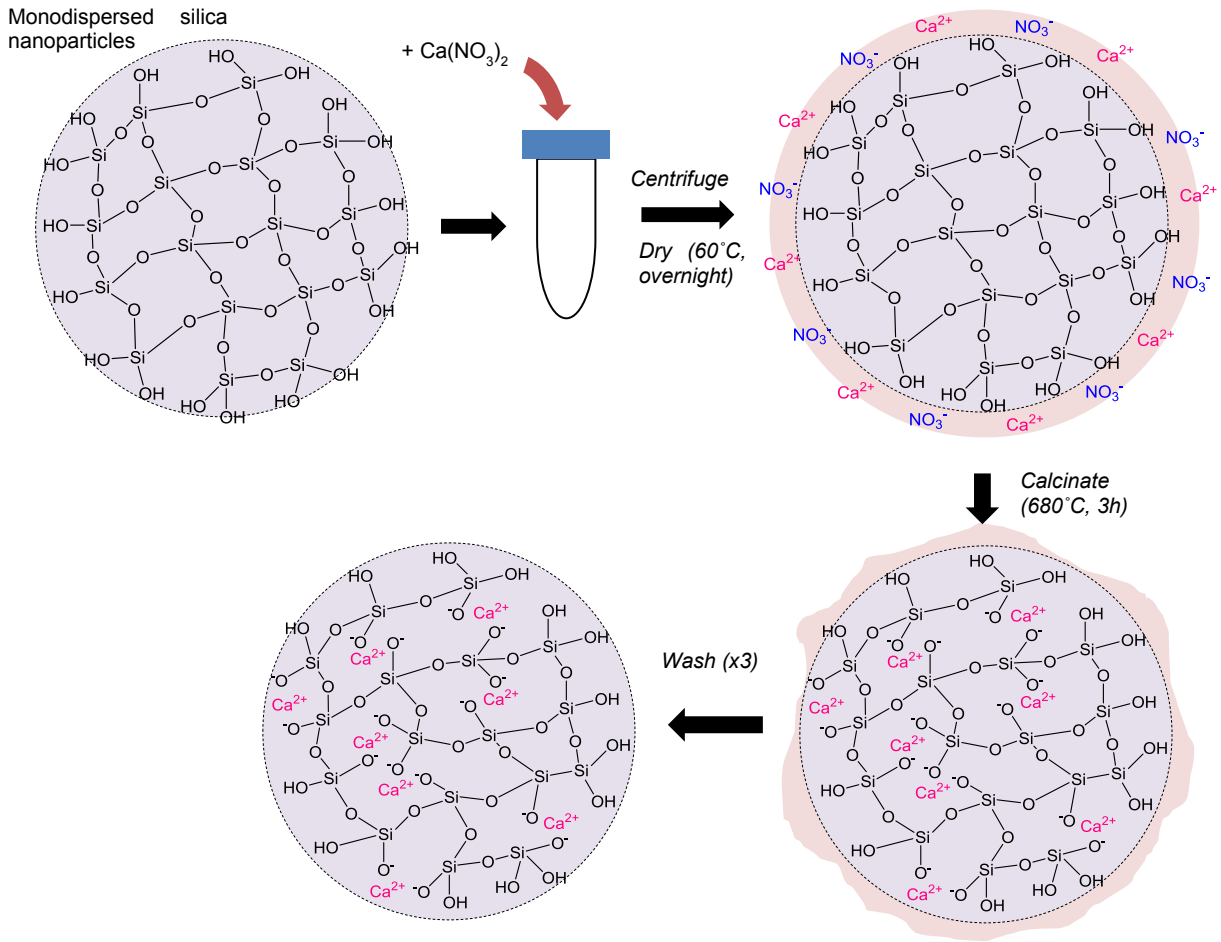


Figure 5.1 - Schematic showing the method of incorporation of calcium in to silica nanoparticles.

The same protocol was followed to produce Zn doped nanoparticles, although for these particles the target size was 80 nm so the reactants were added in the concentrations 0.28M TEOS, 6M H_2O, 0.14M NH_4OH. Zinc nitrate hexahydrate (ACS reagent, 99%) was used as the zinc source. After heating, the Zn particles were washed once in 1 M NaOH and twice in distilled water to remove any unincorporated ZnO.

Investigations were also carried out into the viability of increasing the % of calcium and zinc in the particles by increasing the amount of calcium nitrate/zinc nitrate added to the solution.

5.2.2 Acid digestion composition analysis

The composition of the particles produced was determined using the quantitative method of acid digestion and ICP-OES (Thermo Scientific ICap 6000series). 50 mg of finely ground nanoparticles was mixed with 250 mg of lithium metaborate in a clean dry platinum crucible. The mixture was fused for 40 minutes at 1050˚C and left to cool. The flux was subsequently dissolved in 2 M nitric acid and transferred to a 100 ml polypropylene volumetric flask before diluting in 2 M nitric acid a further 10 times to a concentration suitable for ICP analysis. ICP gives the concentration of each element in $mg.L^{-1}$, which was converted to a molar ratio to give the composition of the sample.

5.2.3 Particle sectioning using FIB

In order to analyse the distribution of elements through the cross-section of the particles, both zinc and calcium containing particles were sectioned using a dual beam FIB-SEM (FEI Helios 600 NanoLab). Particles of 500 nm were mixed with finely ground carbon powder and resin in order to create a conductive sample which was allowed to set before coating in platinum. A slice of the sample containing nanoparticles was milled using the focused ion beam, removed from the bulk of the sample and fixed to a TEM grid. The resulting slice was then thinned to <100 nm until it was electron transparent for TEM imaging and elemental analysis by EDS mapping.

5.2.4 Particle characterisation

After cation incorporation, the particles were again analysed using TEM and DLS (as described in Section 4.2.2) and acid digestion ICP compositional analysis was performed on samples prepared as described in Section 5.2.2. To confirm the reliability of ICP compositional analysis, calcium containing nanoparticles were additionally characterised by XRF spectroscopy using a Siemens SRS 3000 unit equipped with an Rh anode and a 60 kV X-ray generator. A Field Emission Gun Scanning Electron Microscope (FEG-SEM JEOL JSM 6700F) equipped with an EDS detector (Oxford Inca Energy 300) was also used to perform semi-quantitative analysis. Elemental standards were used as follows: C: $CaCO_3$; Si: SiO_2; Al: Al_2O_3; O: SiO_2; Ca: $CaSiO_3$, and EDS scans were obtained at 5 random points in each sample to obtain average elemental ratios.

XRD was also performed in order to detect any crystalline phases or atomic structure variations within the particles. Nanoparticles were finely ground and samples were mounted on to a zero diffraction plate made of single crystal silicon. XRD patterns were collected on a Philips PW1700 series automated powder diffractometer using Ni filtered Cu Kα radiation at 40 KV/40 mA. Data was collected between 10 - 80° 2θ with a step of 0.03° 2θ and a dwell time of 3 s to reduce noise as much as possible. Further investigation into the atomic structure of the particles was conducted using FTIR to ascertain bonding within the samples. FTIR spectra were collected on the PerkinElmer SpectrumTM 100 FTIR spectrometer, in the range of 400 - 4000 cm^{-1}.

Additional investigation into the atomic structure of the calcium containing particles was carried out using SAXS to determine whether any crystalline phases were present and to show the decomposition of calcium nitrates after heat treatment. X-ray data were collected at the BM28 at the European Synchrotron Radiation Facility (ESRF), Grenoble, France by Dr Richard A. Martin and Slobodan Sirovica (School of Engineering & Applied Science and Aston Research Centre for Healthy Ageing, University of Aston). Measurements were performed with a monochromatic (λ=0.827 Å, E=15.039 keV) incident X-ray beam of cross section 0.8 by 0.5 mm. Samples were mounted inside a brass annulus (1 cm diameter x 1 mm thickness) contained in a thin Mylar envelope. A MAR CCD (2048 by 2048 pixels) was positioned behind the sample and orthogonal to the incident beam to collect scattering data. The sample holder was positioned 30 cm from the beam source and 57 cm from the detector window to provide a Q range of 0.4 to 1.9 $Å^{-1}$, where $Q= 4\pi \sin\vartheta/\lambda$. Measurements were undertaken on the samples, empty container, direct beam, water and calibration standard to allow the diffraction patterns to be corrected for background and normalisation effects. The data was normalised and background corrected using the Fit2D software package [166]. Data was radially averaged over 360° to produce a 1D output and were subsequently fitted with Gaussian models to determine peak positions.

For the first time, both zinc and calcium containing particles were also sectioned using a dual beam FIB-SEM (FEI Helios 600 NanoLab) as described above (Section 5.2.3). EDS on a JEOL-2100F TEM with AZtec imaging software was used to map the elements present through the cross section of the particles. The EDS detector was an Oxford Instrument system, X-Max 80mm Silicon Drift Detector (SDD) and the TEM 2100F was operated at 200 kV accelerated voltage.

Finally, solid state NMR was performed on all particles to determine the effect of cation addition on the connectivity of the silica network, which can be used as an indication of potential dissolution and bioactivity. All ^{29}Si single pulse MAS NMR measurements were performed at 7.0 T using a Varian/Chemagnetics InfinityPlus spectrometer operating at a Larmor frequency of 69.62 MHz.

These experiments were performed using a Bruker 7 mm HX probe which enabled a MAS frequency of 5 kHz to be implemented. Flip angle calibration was performed on kaolinite from which a π/2 pulse time of 5.5 μs was measured. Measurements were undertaken with a π/2 tip angle along with a delay between subsequent pulses of 240 s. ^{29}Si centre of gravity (apparent) shifts were reported against the IUPAC recommended primary reference of Me_4Si (1% in $CDCl_3$, δ 0.0 ppm), via a kaolinite secondary in which the resonance is a known shift of -92.0 ppm [167]. All ^{1}H single pulse MAS NMR measurements were performed at 11.7 T using a Bruker Avance III spectrometer operating at a Larmor frequency of 500 MHz. These experiments were performed using a Bruker 2.5 mm HX probe which enabled a MAS frequency 30 kHz to be implemented. Flip angle calibration was performed on Alanine from which a π/2 pulse time of 2.2 μs was measured. Measurements were undertaken with a π/2 tip angle along with a delay between subsequent pulses of 20 s. ^{1}H centre of gravity (apparent) shifts were reported against the IUPAC recommended primary reference of Me_4Si (1% in $CDCl_3$, δ 0.0 ppm), via a Alanine secondary in which the CH_3 resonance is a known shift of 1.1 ppm [167]. All NMR experiments in this thesis were conducted by Sam Page (Department of Physics, University of Warwick) and results were interpreted through collaborative discussions. The conclusions drawn are the authors.

5.3 Results & Discussion

5.3.1 Adjustments to method

The removal of the supernatant and re-dispersion of Si particles in water before the addition of calcium was found to be necessary in order to prevent the calcium nitrate reacting with remaining ammonium hydroxide in the solution and resulting in grey particles after heating. This occurred despite the removal of the supernatant before drying and was not solved by freeze drying as opposed to oven drying, or by subsequent washing, re-heating for longer or at higher temperatures, or calcination in a high oxygen environment. The reaction was most noticeable in larger particles due to the higher quantities of ammonium hydroxide in the solution. This can be seen in Figure 5.2, showing increasing contamination as the concentration of ammonium hydroxide is increased. At a concentration of 0.17 M NH_4OH the reaction is not noticeable and the particles appear white (Figure 5.2), however as the concentration increases up to 0.51 M NH_4OH a layer of grey particles begins to appear, increasing in thickness and becoming darker in colour (Figure 5.2 B-D).

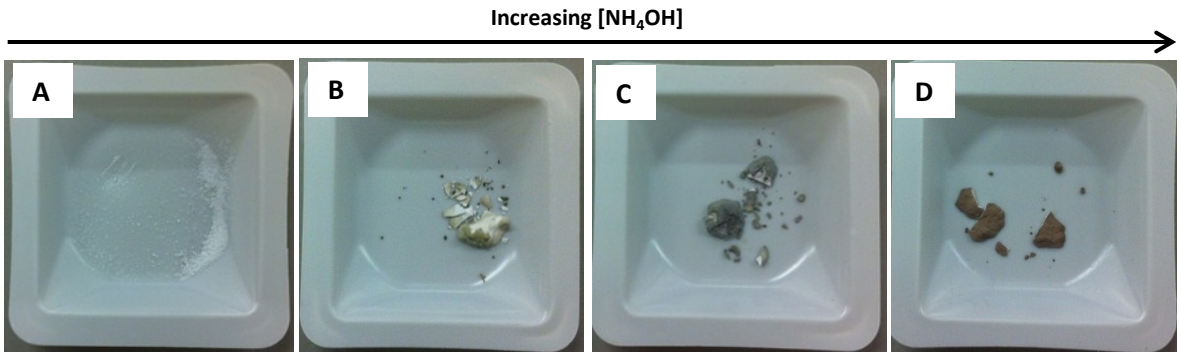


Figure 5.2 - Particles of different sizes after the addition of calcium nitrate and calcination (before the introduction of the step in which the supernatant was removed and particles were re-dispersed in distilled water). Particles are made with 0.28M TEOS, 6M H_2O and increasing ammonium hydroxide concentrations: A) 0.17M NH_4OH, B) 0.28M NH_4OH, C) 0.40M NH_4OH, D) 0.51M NH_4OH .

5.3.2 Mechanism of cation incorporation

Previous work has shown that calcium only incorporates into the silica network above 400°C, by diffusion and subsequent disruption of the silicate network as it becomes a network modifier [84]. Therefore calcium nitrate was only added after the silica particles had formed. The addition of calcium before this stage has been shown to disrupt the formation of monodispersed particles [60]. The hypothesis was that the calcium nitrate would attach onto the surface of the particles during drying and then diffuse into the particles as temperature increased above 400°C. This hypothesis for calcium incorporation in to the silicate network was also supported by X-ray diffraction data (Figure 5.3) for particles both before and after heating to 680˚C. A broad feature ~ 1.6 $Å^{-1}$ was present for all samples. Smaller Bragg peaks at 1.4 and 1.8 $Å^{-1}$ were present for the sample containing calcium before heating (Figure 5.3C). These peaks are ascribed to calcium nitrate [168] and the absence of these peaks following heating (Figure 5.3D) is indicative of calcium nitrate decomposition and calcium entering the silicate network [118]. Silica particles without calcium were completely amorphous both before and after heating, as expected.

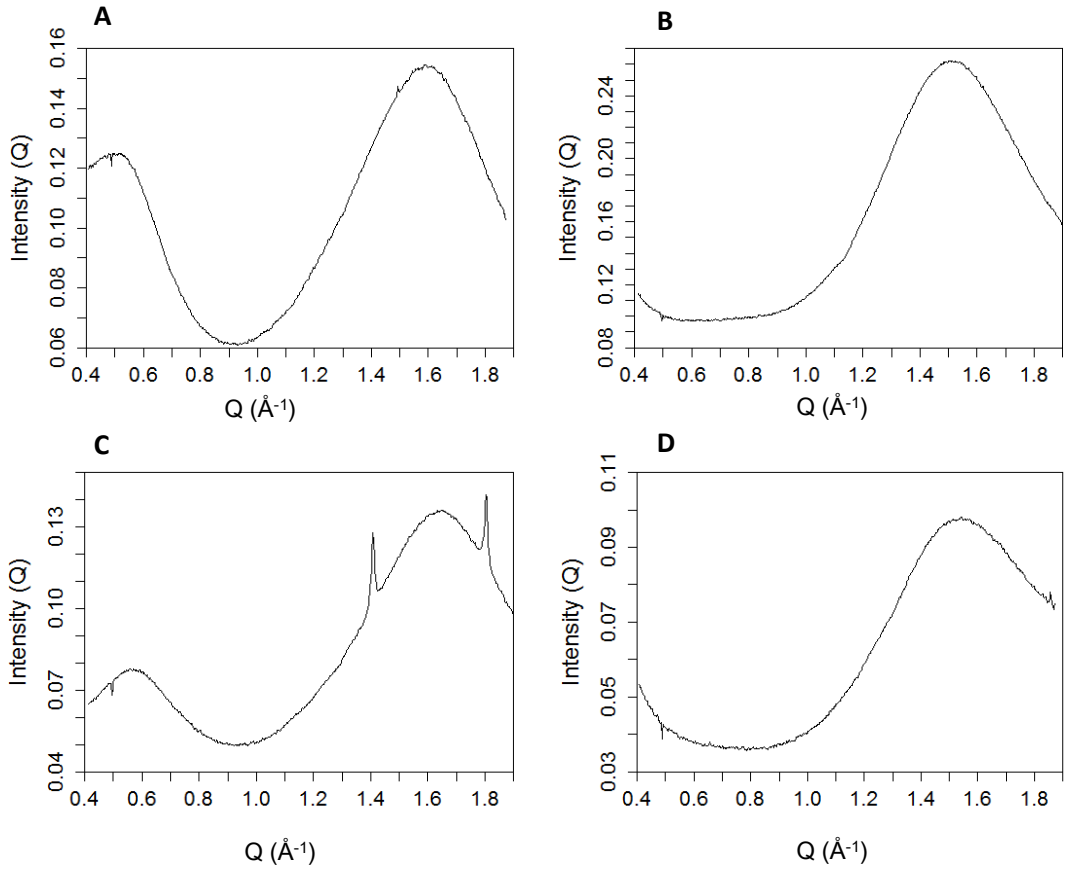


Figure 5.3 - SAXS data for: (A) silica particles, after drying at 60°C; (B) silica particles, heated to 680˚C; (C) SiO_2-CaO particles synthesised with 0.28M TEOS, 0.17M NH_4OH, 6 M H_2O and a Ca:Si ratio of 1.3:1, after drying at 60°C and (D) SiO_2-CaO particles heated to 680˚C. (courtesy of Slobodan Sirovica, University of Aston).

TEM data after heating to 680°C confirmed that the addition of calcium did not affect the size or morphology of the particles produced. This was true for all Si:Ca ratios up to 1:4, unlike recent methods [60]. However, TEM showed the washing step to be essential (Figure 5.4). EDS was used to confirm that areas of particles in Figure 5.4B were surrounded by an excess calcium-rich phase, which was removed by washing in ethanol (Figure 5.4C).

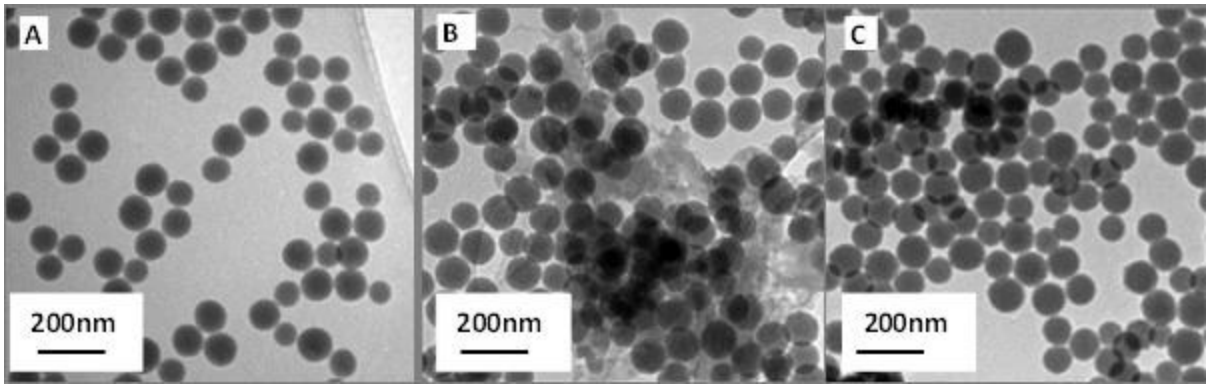


Figure 5.4 - TEM images of silica particles (0.28M TEOS, 0.17M NH_4OH, 6 M H_2O) A) before the addition of calcium B) after the addition of calcium (Ca:Si ratio of 1.3:1) and heating to 680˚C and C) after subsequent washing in ethanol.

The same findings were observed for zinc containing particles, produced following the same method. However, the unincorporated zinc-rich phase seen on TEM was not successfully removed during the washing step with ethanol. XRD analysis showed that the zinc attaches to the surface of the particles during drying as zinc nitrate hydroxide hydrate (Figure 5.5A). After heating it is clear that the unincorporated Zn is in the form of ZnO (Figure 5.5B). As ZnO is insoluble in alcohol, it was therefore not possible to remove it by washing in ethanol. However, ZnO is soluble in either acidic or basic pH. Therefore, the particles were instead washed in 0.1 M HNO_3, 0.01 M HNO_3, 2 M NaOH and 1 M NaOH and subsequently with dH_2O to remove any salt precipitate. All particles were seen to be 'clean' on TEM with no changes in morphology and the amorphous XRD patterns showed the disappearance of zinc oxide peaks (Figure 5.5C). However, as zinc has been seen to be released from silicate glasses at low pH [19], 1 M NaOH was chosen as the solvent for washing all Zn doped particles.

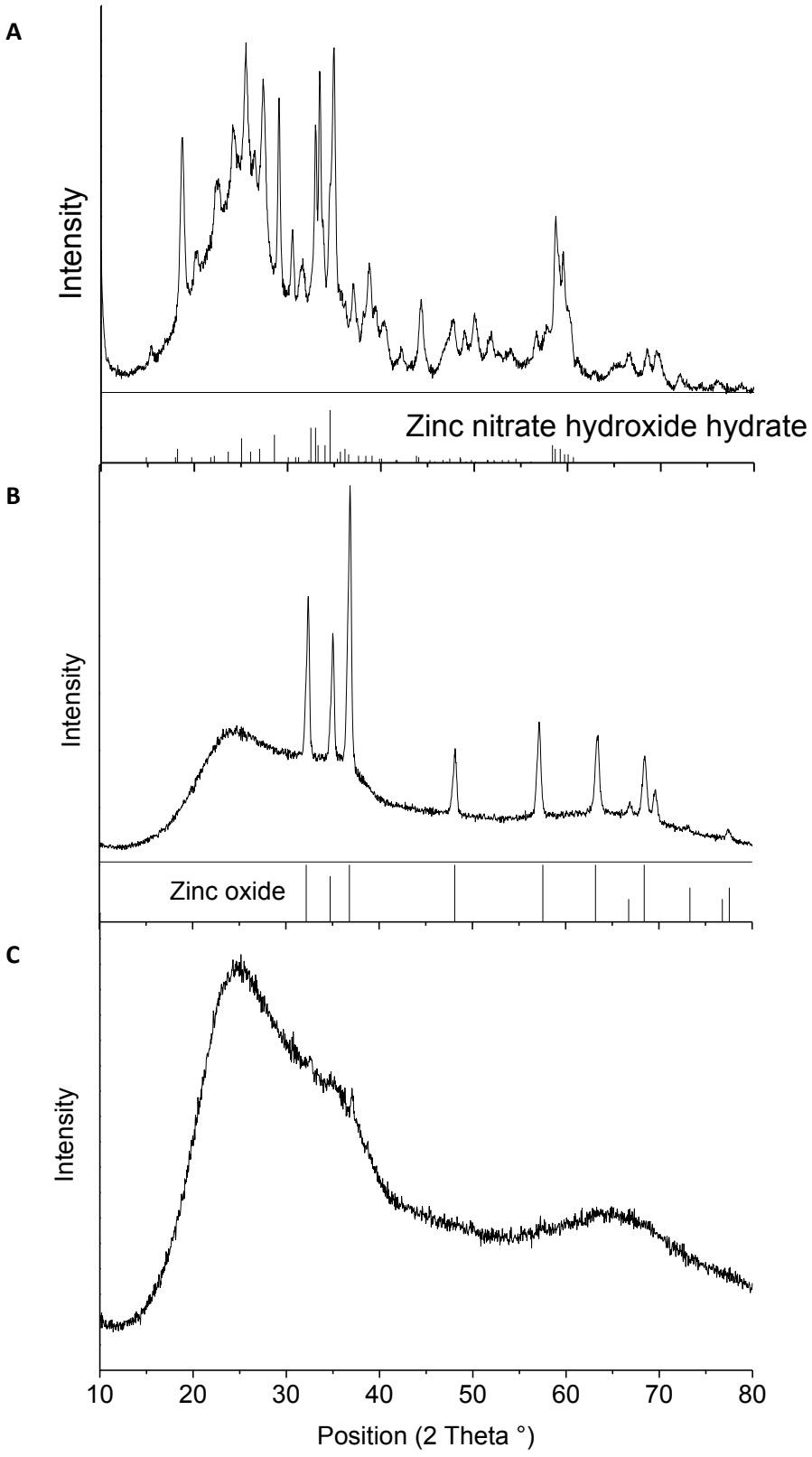


Figure 5.5 - XRD patterns of Si particles doped with Zn A) After drying, B) After heating at 680˚C and C) after washing in 1M NaOH.

The mechanism for incorporation of calcium / zinc by diffusion during heating gives the potential for an inhomogeneous distribution of elements within the particles, with the possibility for a greater concentration of modifying cations nearer to the surface. Equally, it is possible that the washing step could result in a loss of cations from the surface. However, here for the first time it is demonstrated that the calcium is present throughout the entire particles and not just on the surface. This was done by sectioning larger particles of 500 nm in diameter using FIB. After thinning, the resulting slice was electron transparent and therefore established to be <100 nm thick. The monodispersity of the sample means that it could be confirmed that for particles which still had a diameter of 500 nm, the section had been taken through the centre of the particle. Elemental mapping was then performed on the sample using AZtec imaging software as seen in Figure 5.6. In all cases, calcium, silicon and oxygen were seen to be present throughout the entire cross-section of the particle. No diffusion gradient was observed, confirming that the thermal treatment was sufficient to achieve homogeneity. It is assumed that as smaller particles will have a shorter diffusion distance, calcium will therefore penetrate throughout all the particles prepared and analysed in this thesis. For the zinc doped particles, Zn was also seen to be present throughout the entire cross section of the sectioned particles (Figure 5.7).

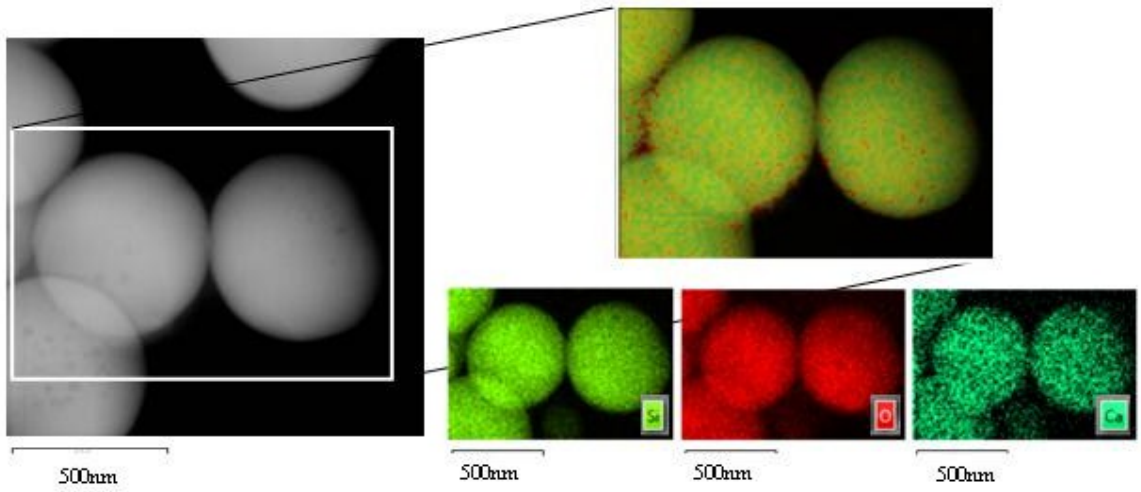


Figure 5.6 - Distribution of elements through FIB cross sections of 500 nm particles of composition 94.6 mol% SiO_2, 5.4 mol% CaO, using AZtec imaging software on TEM.

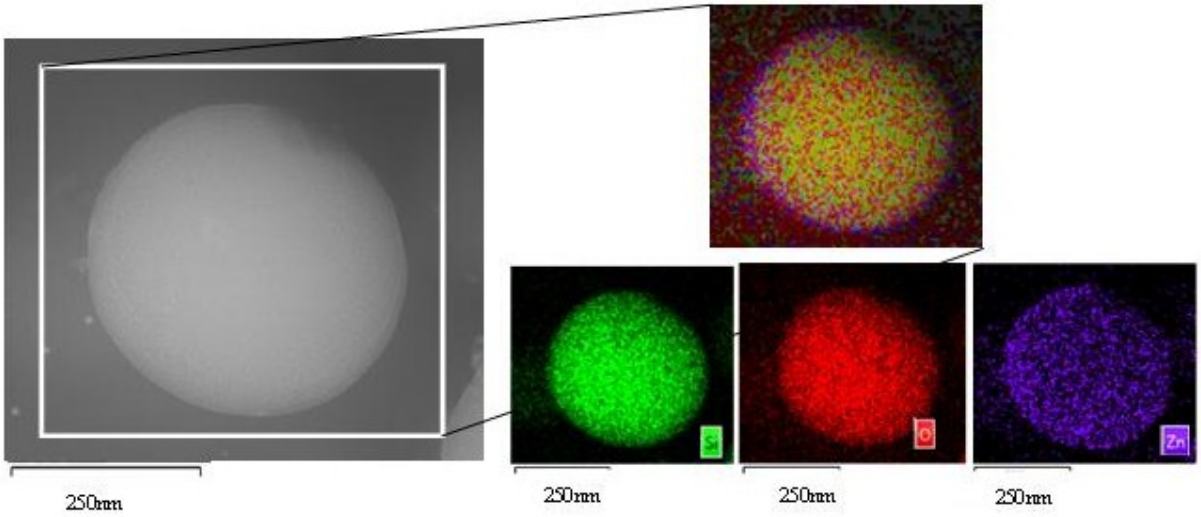


Figure 5.7 - Distribution of elements through FIB cross sections of 500 nm particles of composition 98.6 mol% SiO_2, 1.4 mol% ZnO, using AZtec imaging software on TEM.

5.3.3 Composition analysis

As not all of the calcium / zinc added is incorporated into the particles, analytical quantification post processing is required. Current literature does not report on zinc incorporation into silica nanoparticles, however, papers that state only the nominal concentrations of calcium containing particles may therefore report artificially high concentrations. It is also thought that the absence of the washing step in previous work will also have led to higher concentrations of calcium reported [60]. Additionally, selective TEM imaging of small areas could account for the apparently 'clean' particles.

Incorporation of calcium in 100 nm particles (0.28 M TEOS, 6 M H_2O, 0.17 M NH_4OH) as a function of calcium added to the solution relative to 100 mol% Si is shown in Figure 5.8. It is shown that adding the nominal amount of calcium (for composition 70S30C) actually gives only 3.7 ± 1.2 mol% of CaO incorporation due to the calcium not being incorporated into the silicate network at low temperatures and much of the calcium nitrate is removed in the supernatant. Excess unincorporated calcium-rich phase was also washed off in the washing step. ICP analysis of compositions shows that, for 100 nm particles, the addition Ca:Si in the ratio of 1.3:1, gave a composition of 8.9 ± 1.1 mol% CaO, 91.1% SiO_2, which was confirmed by XRF. This ratio was found to be optimal in that further increasing the Ca:Si ratio to 2:1 and 4:1 resulted in no further increase in calcium incorporation. EDS also showed optimal calcium incorporation at a Ca:Si ratio of 1.3:1, therefore this ratio was used to synthesise all future particles.

Increasing the particle size, by increasing ammonium hydroxide concentration, also resulted in a decrease in calcium incorporation. This supported our hypothesis for calcium incorporation as larger

particles have a smaller surface area to volume ratio and diffusion distances from the surface are greater. For 500 nm particles (0.28 M TEOS, 0.57 M NH_4OH and 6 M H_2O) the addition of calcium in the Ca:Si ratio of 1.3:1 only gave 5.4 ± 1.3 mol % CaO according to ICP analysis.

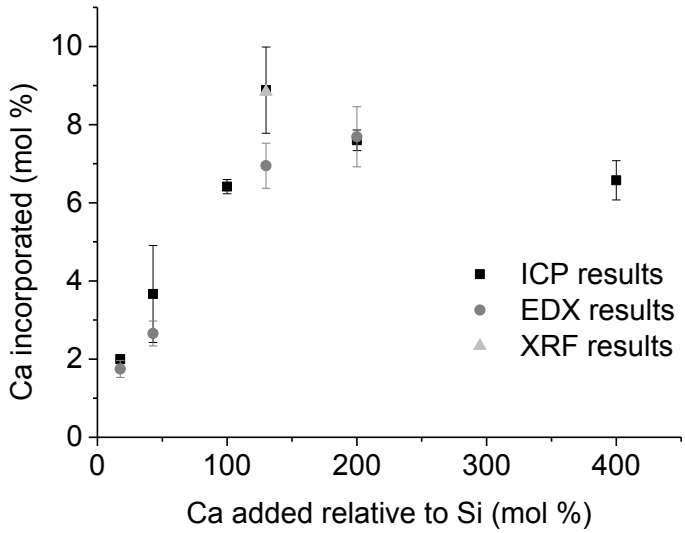


Figure 5.8 - Incorporation of calcium in 100 nm particles (0.28 M TEOS, 6 M H_2O, 0.17 M NH_4OH) as a function of Ca added relative to Si

Figure 5.8 also demonstrates that compositional analysis by ICP following acid digestion gives reliable composition data confirmed by EDS and XRF. Therefore the compositions of Zn doped silica nanoparticles were analysed using this method. The ICP results comparing the compositions of Zn and Ca containing particles for the same mol %'s added relative to Si are shown in Figure 5.9 and a summary of all compositions of particles produced is presented in Table 5.1.

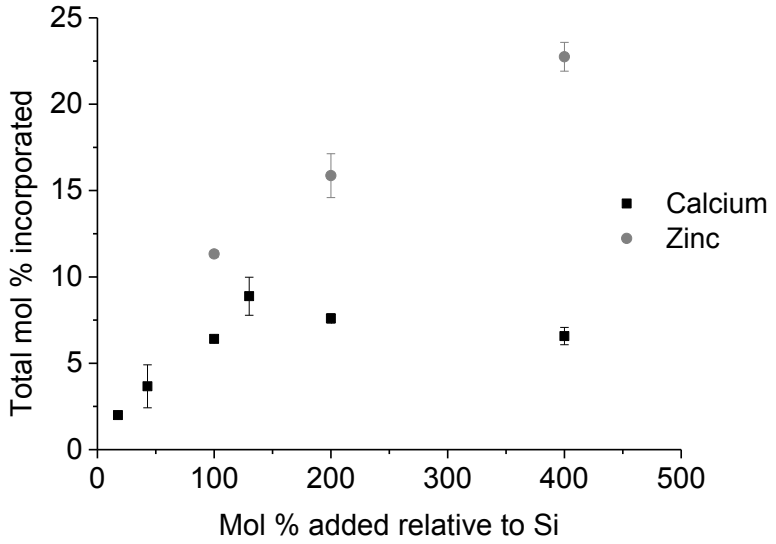


Figure 5.9 - ICP results showing incorporation of Ca into 100 nm particles (0.28 M TEOS, 6 M H_2O, 0.17 M NH_4OH) and Zn into 80 nm particles (0.28 M TEOS, 6 M H_2O, 0.14 M NH_4OH) as a function of the element added relative to 100 mol% Si.

Table 5.1- Summary of particles produced containing different quantities of cations.

Ca containing samples		
SAMPLE	**Ratio Ca:Si added**	**Ca incorporated (Mol%)**
100Si	0:1	0
2Ca	15:85	2.2 ± 0.4
4Ca	30:70	3.8 ± 1.2
6Ca	1:1	6.4 ± 0.2
9Ca	1.3:1	8.9 ± 1.1
8Ca	2:1	7.5 ± 0.3
7Ca	4:1	6.6 ± 0.5
Zn containing samples		
SAMPLE	**Ratio Zn:Si added**	**Zn incorporated (Mol%)**
11Zn	1:1	11.3 ± 0.2
16Zn	2:1	15.9 ± 1.3
23Zn	4:1	22.7 ± 0.8

Whilst a maximum for the % of Ca that can be incorporated was reached at a ratio of 1.3:1 Ca:Si, it can be seen from Figure 5.9 that using a Zn:Si ratio of 4:1 did not provide a maximum for the percentage of Zn incorporated. The ratio of both elements was therefore further increased to a ratio

of 8:1 relative to silica. However, these particles were difficult to wash, resulting in messy areas on the TEM grids. It can also be seen in Figure 5.10 that, at this concentration, the addition of both elements (in particularly Zn) began to alter the particle morphology. Therefore 22.7 ± 0.8 mol% ZnO, incorporated by the addition of Zn:Si in the ratio of 4:1 was taken to be a maximum for 80nm particles.

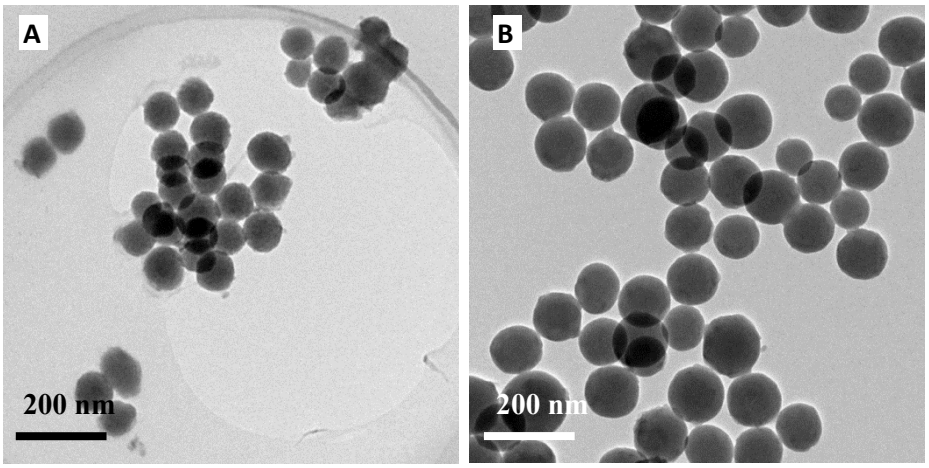


Figure 5.10 - TEM images of silica NPs containing cations Zn and Ca added in an 8:1 ratio relative to Si: A) Zn, B) Ca.

The reason for the production of different sized Ca and Zn doped nanoparticles is due to different applications described previously. Whilst we would expect a slight increase in the amount of Zn incorporated due to the slightly smaller particle size, we would not expect this to be significant and it would not account for the large differences seen in Figure 5.9. These differences are instead attributed to the fact that, whilst Ca acts solely as a network modifier, Zn can act as both a network modifier and a network former. Additionally Zn^{2+} ions are more reactive and have a smaller atomic radius which could increase their incorporation into the network.

5.3.4 Structural differences between particles

In an attempt to better understand these differences and the role that Zn plays in the silica network, NMR, XRD and FTIR experiments were performed on all particles. XRD results are shown in Figure 5.11 and Figure 5.12. It can be seen from Figure 5.11 that the incorporation of calcium does not affect the XRD pattern, with both 100Si particles and those containing 9% Ca exhibiting a typical amorphous halo. However, Figure 5.12 shows that as Zn is incorporated, a second halo begins to appear at around $2\theta^{\circ} = 35$, increasing in intensity with the increasing addition of Zn. This is indicative of a secondary phase within the material. High resolution TEM (HR-TEM) was therefore performed to look at the nano-structure of the particles (Figure 5.13).

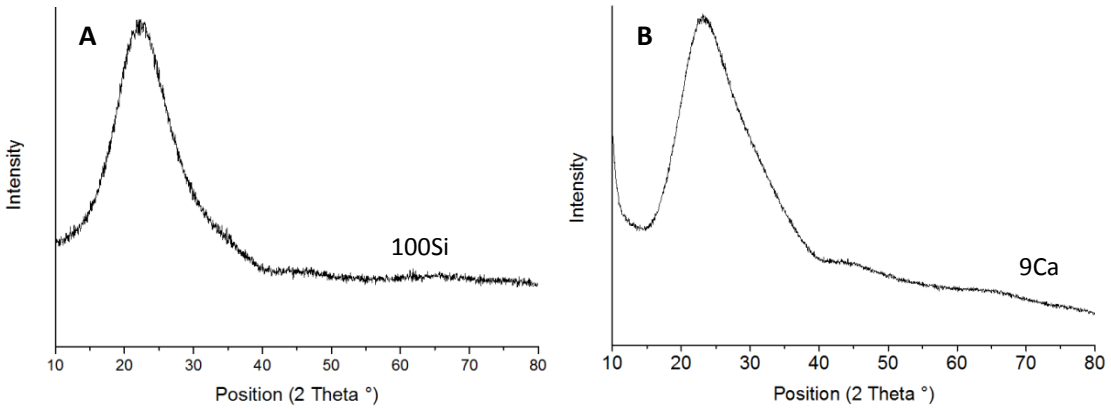


Figure 5.11- XRD patterns of A) 100 nm Stöber particles and B) 100 nm silica particles doped with 9% Ca (after calcination and washing).

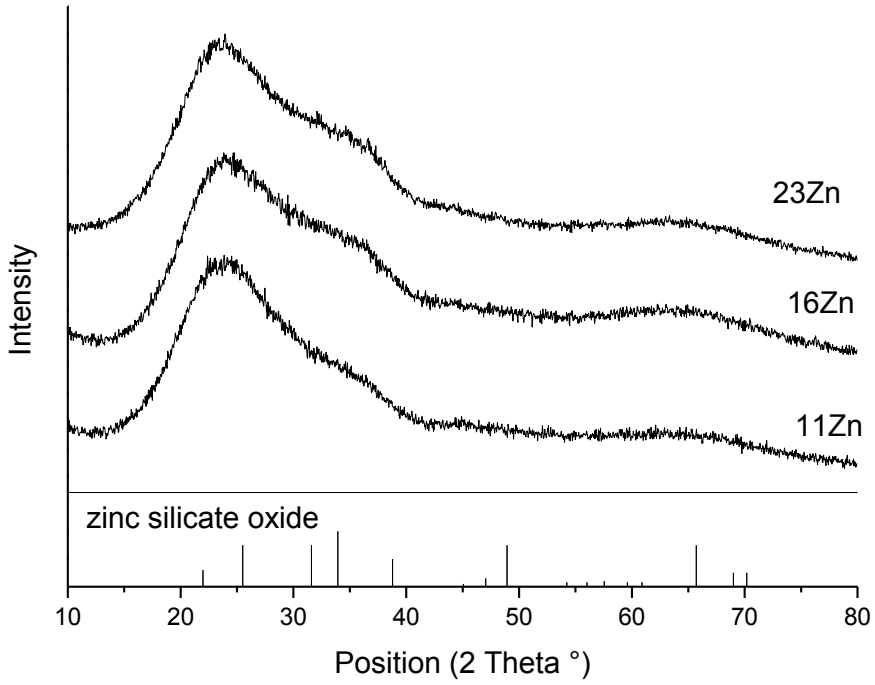


Figure 5.12- XRD patterns of silica particles doped with an increasing percentage of Zn (after calcination and washing).

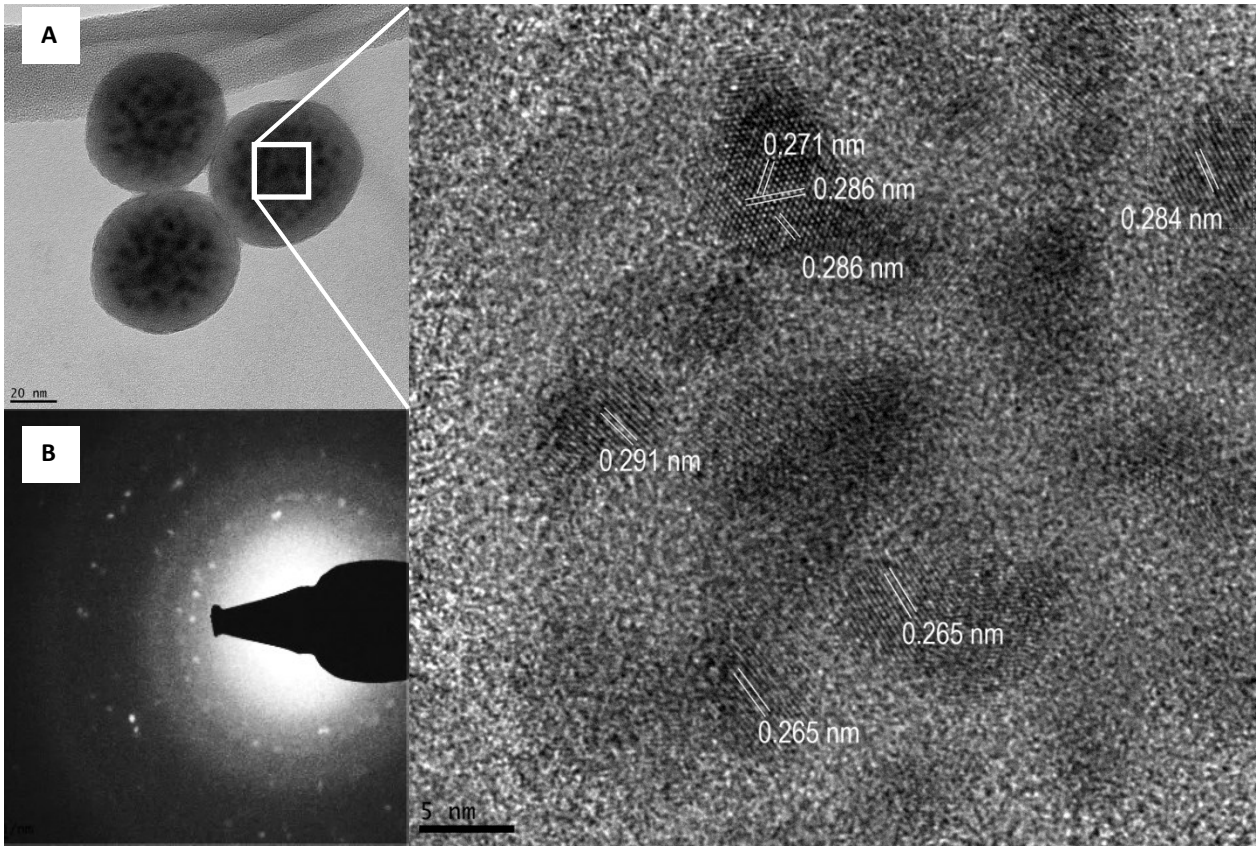


Figure 5.13 - A) HR-TEM of 23Zn particles showing small crystalline areas corresponding to zinc silicate oxide (willemite Zn_2SiO_4) within the nanoparticles B) Diffraction pattern of a crystalline area within nanoparticle (courtesy of Dr Shu Chen, Imperial College London).

It can be seen from Figure 5.13A that there are several small dense areas within the Zn doped particles. By increasing magnification it is observed that these 'dark spots' are actually small crystalline particles within the material. A diffraction pattern was taken to confirm their crystallinity (Figure 5.13B) and EDS verified that the elements present were exclusively Si, Zn and O. The lattice spacing's were therefore measured to be compared to known peak lists for compounds containing these elements. The peak list for zinc silicate oxide (willemite, Zn_2SiO_4) shown in Table 5.2, was found to be the closest match, with the atomic spacing's of high intensity peaks 3 and 4 corresponding to the lattice spacing's measured from HR-TEM. The pattern is also shown in Figure 5.12, with the position of the highest intensity peak ($2\theta = 33.9^{\circ}$) corresponding to the position of the secondary halo appearing in the XRD patterns as Zn content is increased. Whilst crystalline materials normally give sharp peaks on XRD, a nano-crystalline phase would be expected to give an extremely broad peak as seen here, comparable to an amorphous halo. This is demonstrated by XRD patterns of increasingly small ZnO nanoparticles (ranging from 2.5 - 7 nm) [169]. As the size of the nanoparticles decreased, a broadening of the XRD peaks occurred until the material appeared amorphous.

Table 5.2- Peak list for Willemite, Zn_2SiO_4

Peak No.	d (Å)	2θ(˚)	Intensity (%)
1	4.04	21.984	30
2	3.49	25.502	75
3	2.83	31.589	75
4	2.64	33.929	100
5	2.32	38.784	50
6	2.01	45.068	5
7	1.93	47.046	15
8	1.86	48.93	75
9	1.69	54.233	8
10	1.64	56.029	8
11	1.6	57.559	10
12	1.55	59.599	8
13	1.52	60.899	8
14	1.42	65.703	75
15	1.36	68.999	25
16	1.34	70.178	25
17	1.16	83.219	5
18	1.14	85.017	5
19	1.11	87.889	8
20	1.09	89.934	8
21	1.02	98.085	8

Similar findings have also been observed by Chen *et al.* for Zn containing bioactive glass [19]. While glasses with low ZnO content (<19 mol%) were amorphous, those of higher zinc loading (>21mol%) were seen to contain small amounts of crystalline sodium zinc silicate (confirmed by XRD). It is possible that this phenomenon could be prevented by reduction of calcination temperature. In a study of the sol-gel binary ZnO-SiO_2 system by Armelao *et al.*, the annealing temperature had to be carefully controlled in order to avoid the formation of Zn_2SiO_4 due to undesired reaction between the two oxides occurring between 600 and 800˚C [170].

In contrast, HR-TEM of the SiO_2-CaO particles (Figure 5.14) shows a homogeneous morphology with no crystalline areas. This is in agreement with the amorphous XRD pattern (Figure 5.11B).

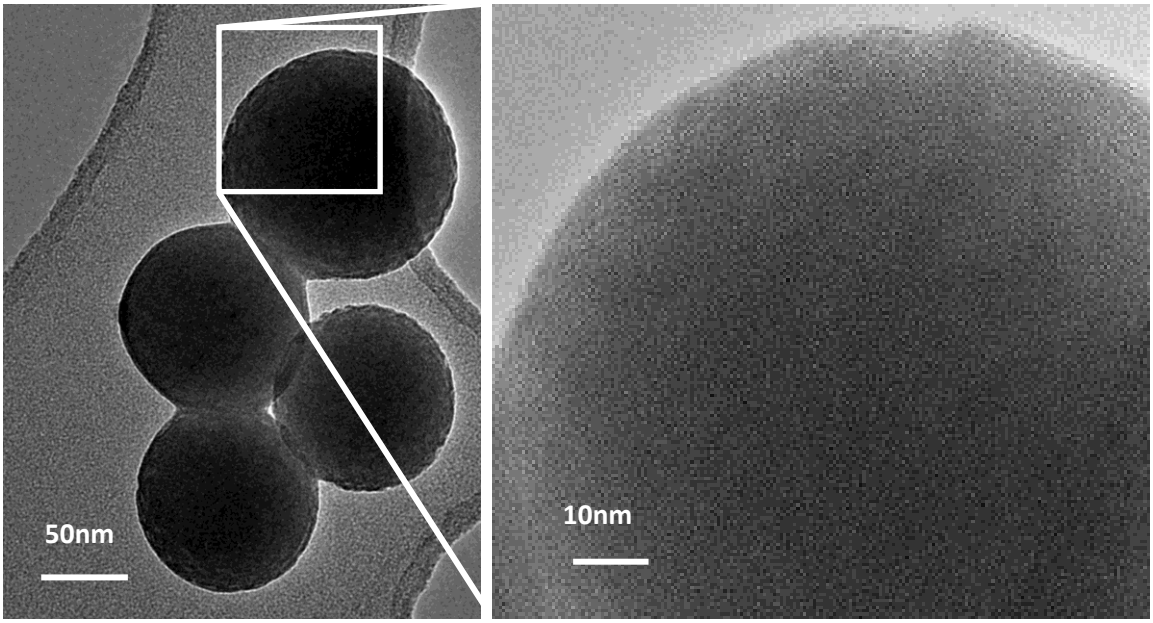


Figure 5.14– HR-TEM of 9Ca particles showing amorphous morphology (courtesy of Dr Shu Chen, Imperial College London).

Additionally, FTIR results also show a difference between Ca and Zn doped particles (Figure 5.15). All particles show distinctive peaks at 1050 cm^{-1}, 440 cm^{-1} and 800 cm^{-1}, representative of Si-O-Si asymmetric stretching [27,33,36,171-173], Si-O-Si bending [27,36,172,173] and Si-O symmetric stretching [36] respectively. In the non-heated 100Si particles there is also a distinct peak at 950 cm^{-1} (which corresponds to Si-OH stretching [174]). However, these are no longer present after calcination due to condensation of the network during heating. The addition of increasing amounts of Zn is observed to result in the increasing reappearance of the peak at 950cm^{-1}. This is indicative of Si-O-NBO [171] stretching as Zn^{2+} ions enter and break up the silica network to form non bridging oxygen's (NBO). However, the addition of calcium, at the maximum possible percentage (9Ca), had no effect on the FTIR patterns in comparison to 100Si particles, which suggests that it does not significantly affect the bonding within the particles.

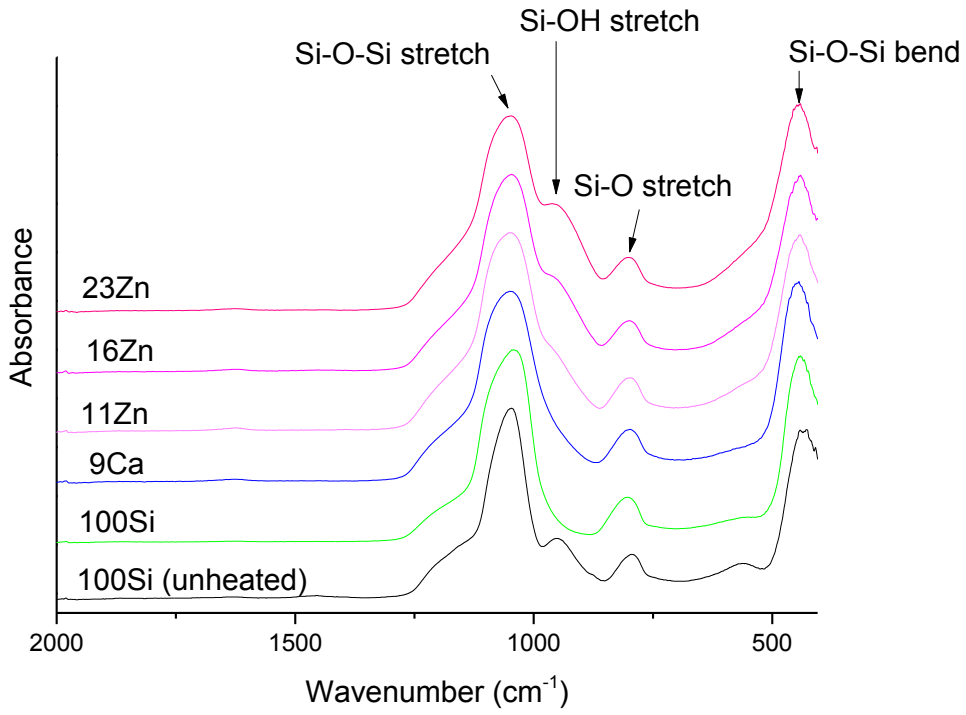


Figure 5.15 - FTIR spectra of silica NPs containing different concentrations of Zn and Ca cations after calcination and washing (unless stated).

As FTIR can only provide basic information about bonding and is not sensitive enough to detect changes in the network due to the addition of calcium at this level, solid state NMR was performed to show any changes in the network connectivity of the silicon as a result of cation addition. ^{29}Si MAS NMR was performed on calcium containing particles both before and after heating at 680˚C. Silica atoms within the network which are connected to 4 bridging oxygen's (Si-O-Si) have a different chemical shift to those bonded to 3 bridging and one non-bridging oxygen (Si-OH or Si-O-NBO). Similarly silicon atoms which have only 2 or 1 bridging oxygen will also have unique chemical shifts. These species are known as Q^4, Q^3, Q^2 and Q^1 respectively. It is hypothesised that as the calcium enters the particles it disrupts the network, acting as a network modifier, and should consequently result in reduced network connectivity (mean number of bridging oxygen bonds per silicon tetrahedron). Q distributions obtained from single pulse ^{29}Si MAS NMR spectra and corresponding network connectivity's are shown in Table 5.3. The shifts reported are representative of conventional Q speciation, as evidenced by the 29Si MAS NMR spectra (Figure 5.16) and the measured parameters (Table 5.3).

Network connectivity (NC) was calculated according to the equation:

$$Network\ connectivity\ (NC) = \frac{4.Q^4\% + 3.Q^3\% + 2.Q^2\% + 1.Q^1\%}{100} \quad [5]$$

As expected, NMR results (Figure 5.16C and D) show a reduction in Q^4 species in particles containing calcium, and a corresponding increase in Q^1, Q^2 and Q^3 species, reducing the NC from 3.85 in pure silica particles to 3.68 in those containing 9% Ca as a network modifier. However, both particles have a much higher network connectivity than their unheated counterparts (Figure 5.16 A and B). This suggests that during calcination there are two conflicting processes occurring. In unheated particles there are large numbers of Si-OH bonds within the network (as seen on FTIR) which reduce the network connectivity. However, as the particles are heated the network condenses, resulting in fewer Si-OH bonds within the network, while at the same time, for calcium containing particles, Ca^{2+} ions diffuse into the particles breaking up the network.

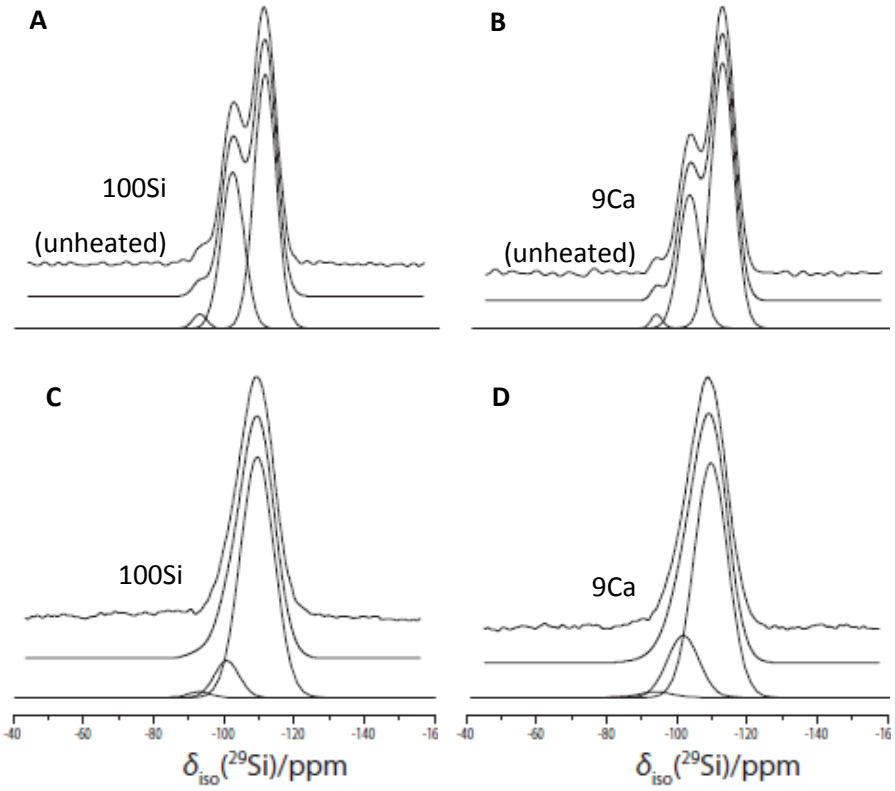


Figure 5.16- 29Si MAS NMR spectra for (A) 100Si particles (unheated) (B) 9Ca particles (unheated) (C) 100Si particles (heated) and (D) 9Ca particles (heated) (courtesy of Sam Page, University of Warwick).

Theoretical NC of melt derived glasses can be calculated from their composition using the following equation [175]:

$$NC_{Si\ particles\ doped\ with\ Ca} = \frac{NC_{Si\ particles}\,[SiO_2]-2[CaO]}{[SiO_2]} \qquad [6]$$

Assuming a theoretical NC of 4 for pure SiO_2 would give a theoretical NC of 3.8 for a nominal composition of 91% SiO_2, 9% CaO. However, as is common in sol-gel glasses, the NC measured by NMR was lower in both of these cases due to the fact that particles also contain some remaining OH groups where H^+ ions act as an additional network modifier. Using the above equation, the observed decrease in network connectivity (from 3.85 to 3.68) corresponds to a theoretical incorporation of only 7.8 % Ca. Therefore in order to better understand how calcium is incorporated into this system, ^{1}H MAS NMR was performed on the particles after heat treatment to look at the role of modifying H^+ ions and the effect of calcium addition. The results are shown in Figure 5.17. In ^{1}H MAS NMR the sharp peak on the right represents sterically hindered OH groups within the network whereas the broad peak on the left represents non sterically hindered OH groups (ie in physically adsorbed water molecules). Some of the broadening is due to dipolar interactions between different protons, whereas in the sterically hindered case there aren't so many protons in such close proximity and therefore the local field around the nuclei is not changing as much, creating a sharper peak. Mobility also sharpens the peak by averaging the position that we see more effectively so the sharper peak could also indicate that the hydroxyl is more mobile and can rotate, bend and stretch around the oxygen whereas in water the protons are packed tighter into the structure. We can assume that the physically adsorbed water (represented by the broad peak on the left) is about the same for all samples (after heating) so the relative intensity of the two peaks can therefore give an indication of the number of sterically hindered OH groups within the network.

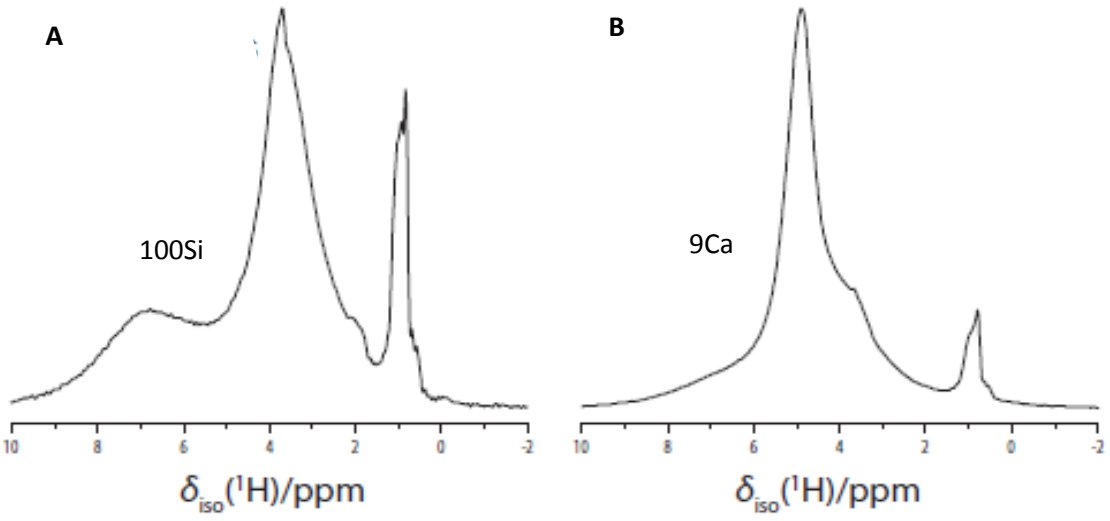


Figure 5.17 - 1H MAS NMR spectra for (A) 100Si particles (heated) and (B) 9Ca particles (heated) (Courtesy of Sam Page, University of Warwick).

The relative intensity of sterically hindered OH groups was significantly lower in the particles containing calcium, suggesting that many of the calcium ions may have replaced existing modifying H^+ ions instead of acting as additional network modifiers. When this is the case, then in order to maintain charge balance, each Ca^{2+} ion that enters the network will only break one bond instead of two and the network connectivity equation is likely to predict a lower network connectivity than is actually observed.

The mechanism for Zn incorporation is far more complex as it can enter the network as both a modifier and a former, so cannot be theoretically calculated from a single equation [19]. The ^{29}Si MAS NMR and ^{1}H MAS NMR spectra for the Zn containing particles are shown in Figure 5.18 and the corresponding Q distributions and network connectivity values are tabulated in Table 5.3. It can be clearly seen that as the amount of Zn is increased, the network connectivity decreases accordingly, suggesting that at least some of the zinc is acting as network modifier. When acting as a network former, zinc is primarily found in tetrahedral coordination[19,30,32,37,176,177] however zinc has also been shown to act as 5 or 6 coordinate [20,30]. Alternatively it can have octahedral coordination as a network modifier [177,178] which would result in significantly reduced network connectivity. This would also be expected to correspond to increased degradation of the particles [19].

Table 5.3 - Q distributions obtained from single pulse 29Si MAS NMR spectra for dense particles (courtesy of Sam Page, University of Warwick).

Sample	Q^1		Q^2		Q^3		Q^4		Network Connectivity (NC)
	δ_{Iso} [ppm]	I [%]	δ_{Iso} [ppm]	I [%]	δ_{Iso} [ppm]	I [%]	δ_{Iso} [ppm]	I [%]	
100Si (unheated)	-	-	-92.1±0.1	2.2±0.2	-102.1±0.1	37.7±0.1	-112.0±0.1	60.1±0.1	3.58±0.01
9Ca (unheated)	-	-	-91.9±0.1	1.7±0.2	-102.0±1	31.9±0.3	-112.0±0.0	66.4±0.1	3.65±0.01
100Si	-	-	-91.7±0.1	2.9±0.4	-101.3±0.1	9.0±0.6	-110.5±0.1	88.1±0.1	3.85±0.02
9Ca	-80.5±0.9	1.8±0.2	-93.1±1.3	7.2±1.3	-100.5±0.2	12.0±1.4	-110.5±0.1	79.0±0.2	3.68±0.05
11Zn	-78.2±1.7	1.5±0.4	-91.8±0.7	12.8±0.2	-100.5±0.2	15.2±0.4	-110.1±0.1	70.6±0.1	3.55±0.02
16Zn	-77.1±4.9	4.1±1.2	-89.8±0.6	12.4±1.2	-99.1±0.1	18.6±0.4	-109.8±0.2	65.0±0.3	3.45±0.03
23Zn	-76.9±0.4	1.2±0.5	-89.7±0.4	22.4±0.6	-99.6±0.2	17.8±0.5	-110.1±0.4	58.6±0.3	3.34±0.02

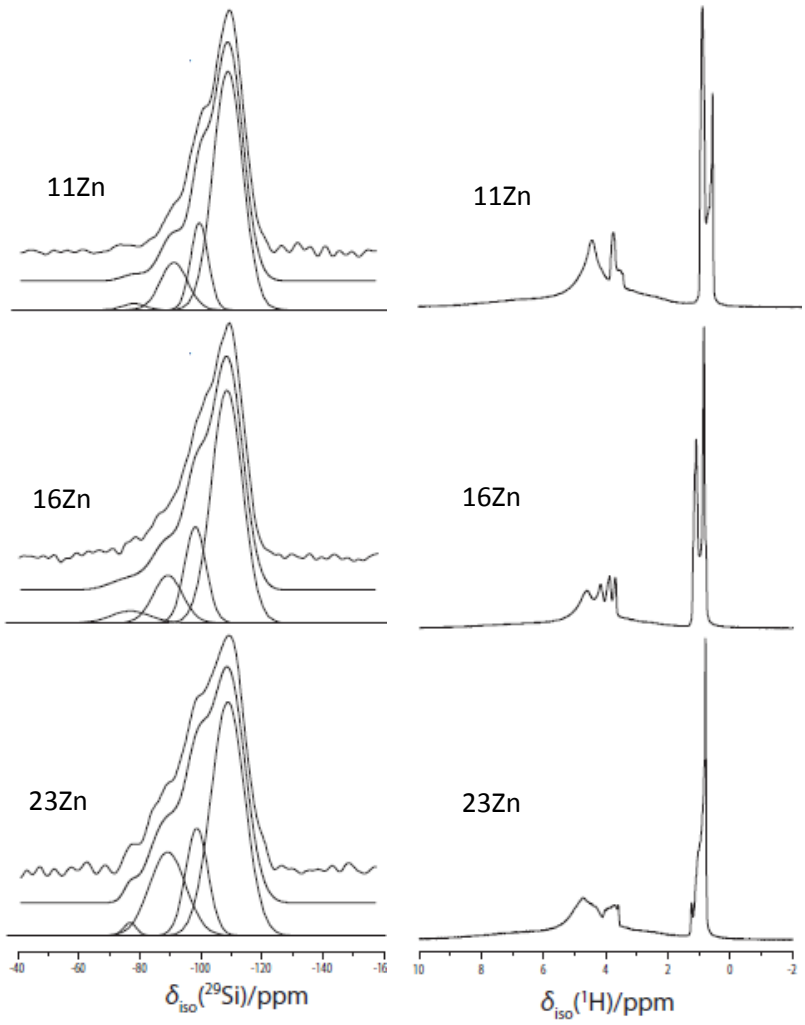


Figure 5.18 - 29Si MAS NMR spectra (left) and 1H MAS NMR spectra (right) for Zn containing particles (11Zn, 16Zn and 23Zn) (courtesy of Sam Page, University of Warwick).

In contrast to the addition of calcium, it can be interpreted from the relative intensities of peaks in the ^{1}H MAS NMR spectra (Figure 5.18), that instead of replacing modifying H^{+} ions, the addition of zinc actually results in the creation of additional sterically hindered OH groups within the network. This supports FTIR results, where we see the reappearance of the peak at 950 cm^{-1} with increasing Zn content. Although the mechanism by which this occurs is unclear, it is likely that the negatively charged $[ZnO_4]^{2-}$ tetrahedral units [19] (created when zinc takes on a network forming role) attract H^{+} ions as charge compensators. In multi-component glasses it has been observed that as the concentration of other cations increases, zinc is more likely to act as a network former due to the availability of other cations to act as charge compensators [23,176,177]. However, in this binary system it is suggested that H^{+} ions could take on this charge compensating role, thus resulting in an increase in the sharp proton signal seen in Figure 5.18. The effect of the nano-crystalline phase (zinc silicate oxide) on the network is also unknown, although these nano-crystals could also disrupt the silica network further, forming additional OH groups around them.

5.4 Conclusions

Having successfully synthesised monodispersed silica nanoparticles of controlled size, this chapter demonstrates that it is possible to subsequently incorporate both Ca and Zn cations from nitrate precursors without affecting the size, morphology or homogeneity of the particles. It is observed that after heat treatment at 680˚C both ions successfully diffuse homogeneously throughout the network resulting in reduced network connectivity. However, not all of the calcium or zinc enters the particles so a washing step is required before composition analysis. Previous papers which incorporate calcium into silica nanoparticles are therefore likely to have significantly overestimated the amount of calcium incorporation. A ratio of 1.3:1 Ca:Si is found to be optimum, resulting in a maximum of 8.9 ± 1.1 mol% CaO in the particles. Zn incorporation on the other hand continues to increase up to 22.7 ± 0.8 mol% ZnO by the addition of Zn:Si in the ratio of 4:1. This difference in behaviour is attributed to the fact that whilst calcium acts purely as a network modifier, zinc can also act as a network former. The presence of nano-crystals of zinc silicate oxide is also observed in the particles containing high quantities of zinc.

6 Synthesis of mesoporous silica nanoparticles and incorporation of cations

6.1 Introduction

Having understood the method behind cation incorporation into dense silica particles, it is believed that as mesoporous particles have a larger surface area it may be possible to incorporate higher percentages of cations. A larger surface area should also allow for faster degradation within cells resulting in a faster release of ions. In the case of calcium containing particles the assumption is that this should lead to increased bioactivity, and in the case of zinc containing particles it may result in greater cytotoxicity in cancer cells.

This chapter first looks at various different synthesis methods for mesoporous silica nanoparticles discussed previously in literature, before proceeding with the most promising method and looking at Zn and Ca cation incorporation. (This work was assisted by Mr Konstantinos Pietris as part of his MSc research project).

6.2 Materials and methods

6.2.1 Particle Synthesis

Particles were synthesised using various methods from literature. Due to the aim of creating monodispersed particles for biological applications, in which size is likely to be a critical parameter, purely chemical synthesis processes were investigated as opposed to aerosol assisted methods.

The methods used to synthesise mesoporous silica nanoparticles are summarised in Table 6.1. All methods used TEOS as a silica precursor and CTAB as a surfactant to produce pores, which was subsequently either burnt out or removed chemically. Methods using CTAB as a surfactant were chosen due to research which suggests that these particles exhibit a greater degree of deterioration than those produced using nonionic surfactants such at F127 [127]. As with the Stöber process, all methods are performed under basic conditions. The, solvents, reactants and concentrations vary slightly between all methods, as do the synthesis conditions such as temperature and time.

Table 6.1 - Methods used for the synthesis of mesoporous silica nanoparticles.

Method	Reactants	Temperature (˚C)	Time (h)	Surfactant Removal
Lin *et al.* 2005 [68]	H_2O Ethanol NH_4OH CTAB TEOS	40	24	HCl / ethanol solution
Shimura & Ogawa, 2007 [120]	H_2O Methanol NH_4OH CTAB TEOS	Room Temp	20	Calcination (550˚C, 10h)
Shi *et al.* 2010 [121]	H_2O 2M NaOH CTAB TEOS	70	2	Calcination (500˚C, 4h)
Nooney *et al.* 2002 [122]	H_2O Ethanol NH_4OH CTAB TEOS	Room Temp / 50	2 / 2.5	Calcination (540˚C, 6h)
Chang *et al.* 2013 [70]	H_2O 2M NaOH CTAB TEOS Ethyl acetate	70	2	Calcination (550˚C, 16h) - **Lang & Tuel, 2004** [179]
Cui *et al.* 2013 [180]	H_2O, 2M polyacrylic acid NH_4OH CTAB TEOS Ethyl acetate	Room Temp (25)	48	Calcination (550˚C, 6h)

After TEM analysis of all particles produced (shown in section 6.3) the method used by Chang et al., 2013 [70] was chosen to move forward with for cation incorporation. In more detail, this method used 500 ml H_2O, 1 g CTAB and 3 ml NaOH (2 M). The reactants were then stirred on a hot plate and left to reach 70˚C before adding 5 ml TEOS and, after 1 min, 5 ml Ethyl Acetate. After 30 s the stirring was turned off and the solution was left on the hotplate for a further 2 h before centrifugation. The particles were then washed three times in ethanol by cycles of sonication followed by centrifugation. For particles containing cations, either zinc nitrate or calcium nitrate was added to the particle suspension on the third washing cycle. All particles were then dried overnight in a 60˚C oven before calcination at 550˚C for 16 h to remove the surfactant. For the particles containing cations, this heat treatment was also sufficient to burn off any nitrates. The cation containing particles were also washed three times in ethanol after heating, as with the dense particles, to remove any unincorporated Ca or Zn before characterisation.

6.2.2 Particle characterisation

Mesoporous particles were characterised using the same methods as for dense nanoparticles (described in section 4.2.2). TEM was used to analyse particle morphology, while acid digestion and ICP analysis and EDS were used to determine particle composition for those containing cations. All particles were also analysed by XRD, FTIR and NMR to determine the effects of cation addition on the silicate network.

Additionally, the surface area and pore size of particles produced was analysed using nitrogen adsorption. Measurements were performed on a Quantachrome Autosorb-1 using an outgas time of 40 h, an outgas temperature of 100˚C and a bath temperature of 77.3K. Samples (approx. 65 mg) were weighed on a small piece of aluminium foil and wrapped up to prevent them sticking from the sides of the glass tube. (This is permissible as the aluminium foil has a negligible surface area in comparison to the mesoporous nanoparticles). Each sample was then degassed for 24 h to remove any moisture in the pores before being reweighed. A 5 point BET analysis (from 0.1 to 0.3 $cm^3.g^{-1}$) and 20 point adsorption/ 40 point desorption analysis were performed. DFT was used to determine pore size distribution using a nonlocal density functional theory (NLDFT) equilibrium model for N_2 at 77K on silica, with Oxygen (zeolite) selected as the absorbent.

6.3 Results & Discussion

6.3.1 Synthesis of mesoporous silica nanoparticles

Whilst many of the methods used to synthesise mesoporous nanoparticles showed good results in literature, there is a possibility that TEM images presented are not representative of the sample. Variations in lab conditions such as humidity may also have an effect on synthesis.

TEM images showing the samples produced using the synthesis methods described in literature are shown in Figure 6.1. All methods tried here resulted in particles which were noticeably mesoporous, with the exception of Sample G produced using one method described by Nooney *et al*.[122]. The second method used by Nooney *et al*., which did not use any ethanol and required the addition of CTAB once at 50°C, did produce mesoporous particles (Sample H), although these were not monodispersed. Particles produced using the method used by Lin *et al.*[68] (Sample A), the method described by Shi *et al.*[121] using two different H_2O concentrations (Samples E and F), and the method used by Cui *et al.* [180] (Sample J), were also all irregular in size and/or shape. Samples B-D on the other hand, synthesised using the Shimura & Ogawa method [120] with varying concentrations of CH_3OH and NH_4OH, showed that it was possible to produce monodispersed particles of varying modal size, by varying the concentration of reactants. However, this method used large quantities of methanol and produced a very low yield. Therefore the method used by Chang *et al.*[70] (Sample I) was chosen to proceed with as it produced monodispersed mesoporous spherical nanoparticles within the desired range of 50-100 nm.

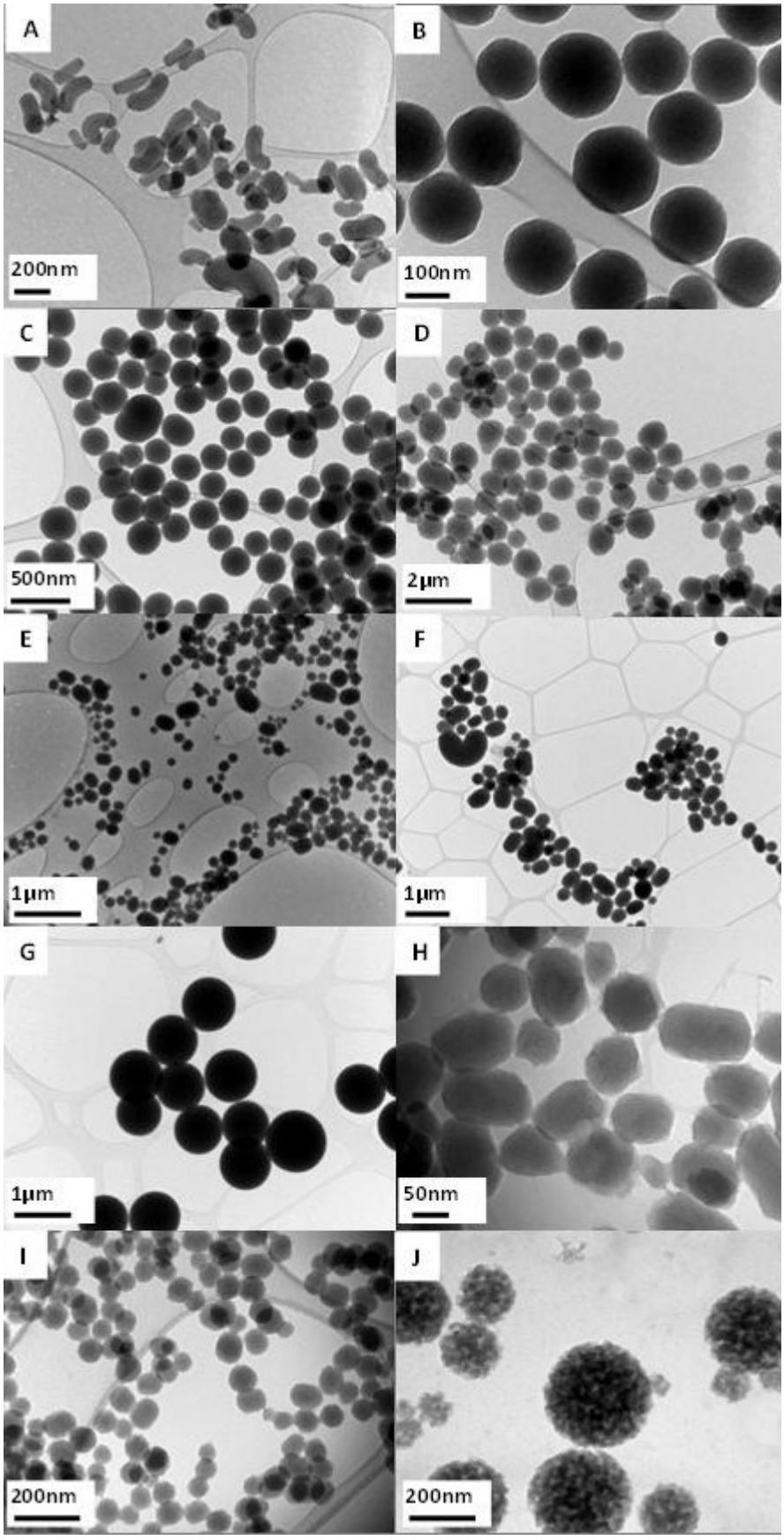


Figure 6.1 - TEM images of mesoporous particles synthesised using methods from literature. A) Lin *et al.* 2005 [68], B-D) Shimura & Ogawa, 2007 [120], E,F) Shi *et al.* 2010 [121], G,H) Nooney *et al.* 2002 [122], I) Chang *et al.* 2013 [70], J) Cui *et al*. 2013 [180]

Particles produced by using the Chang method [70] are shown in Figure 6.2. It can be seen from the low magnification TEM image in Figure 6.2A that the particles are largely monodispersed with an average diameter of 63 ± 10 nm (n=150). At higher magnification (Figure 6.2B) the pores are clearly visible and the particles have a highly ordered mesoporous structure.

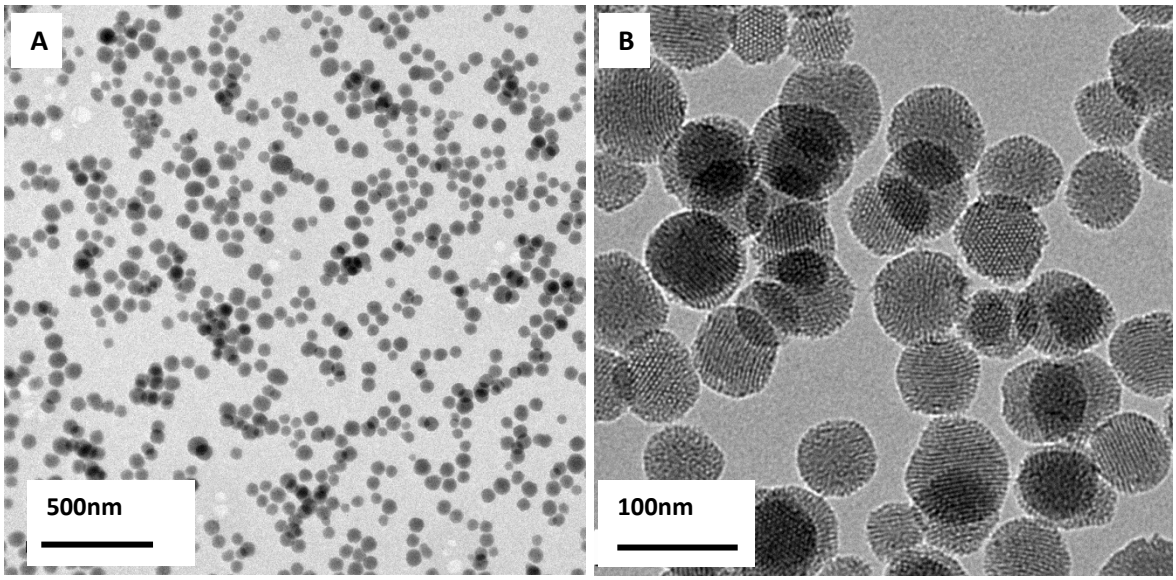


Figure 6.2 - TEM images of mesoporous silica nanoparticles synthesised using method by Chang et al. [70] at A) Low magnification and B) High magnification.

6.3.2 Cation incorporation into mesoporous particles

The addition of cations to the particles, using the method described above, had no significant effects on the size, morphology or dispersity of particles, although the point of the synthesis process at which the cations were added was found to be crucial. Particles with the addition of Zn and Ca in a ratio of 2:1 Zn:Si and Ca:Si are shown in Figure 6.3 A and B respectively. The only noticeable difference observed between the particles containing Zn and Ca was an apparent lack in porosity for those containing Ca (Figure 6.3B). Nitrogen sorption measurements were therefore performed on all particles in order to understand the differences in pore size and surface area. The results are summarised in Table 6.2.

EDS spectra were also taken at 3 different locations on each TEM grid. Sample A was shown to contain 17.5 ± 0.85 atomic % Zn, and sample B was seen to contain 16.9 ± 0.79 atomic % Ca. Whilst EDS is non quantitative, the low standard deviations of these results confirm the homogeneity of the samples produced. In order to quantitatively analyse the compositions of the particles, acid digestions and ICP analysis was performed. As with the dense particles, various different ratios of cations were added to the solution with respect to silica. The results are shown in Figure 6.4.

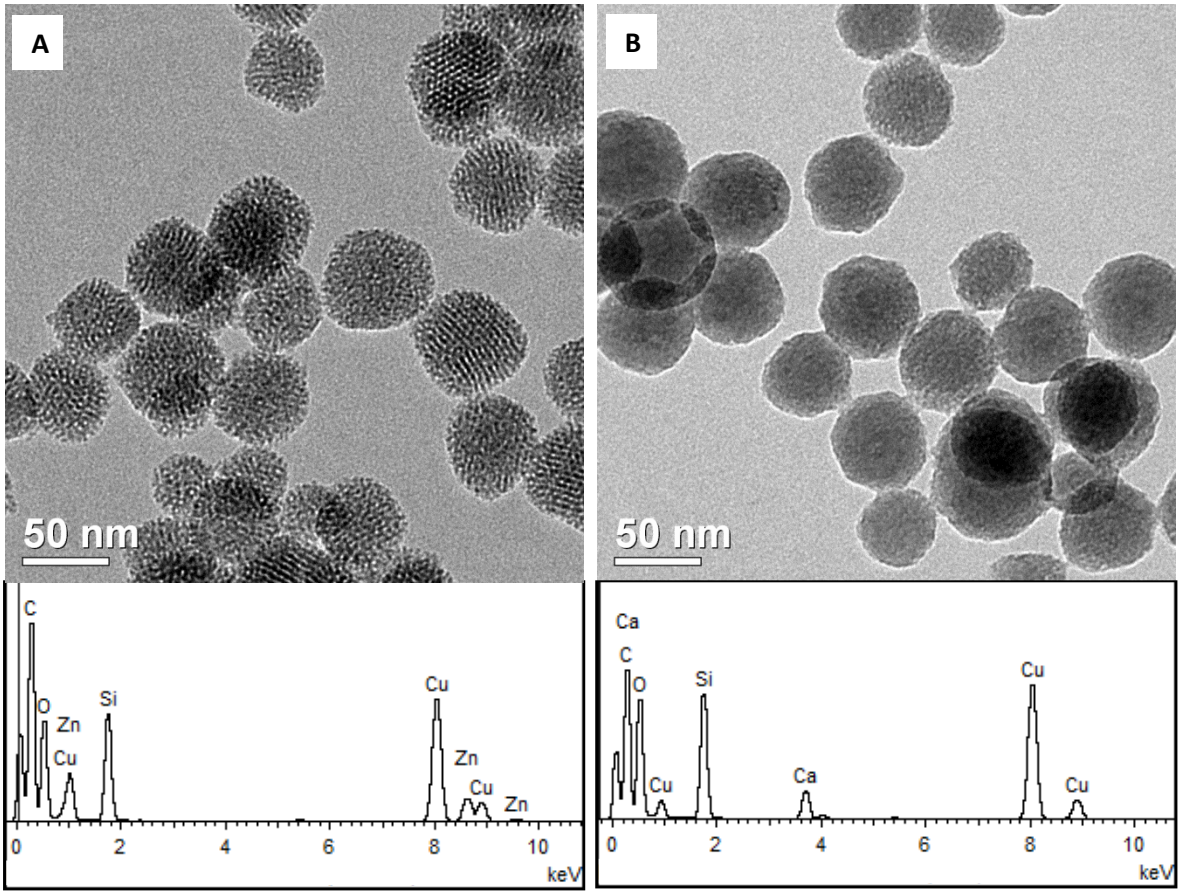


Figure 6.3 - TEM images with EDS spectra (below) for mesoporous silica nanoparticles with incorporated cations A) 22Zn and B) 19Ca.

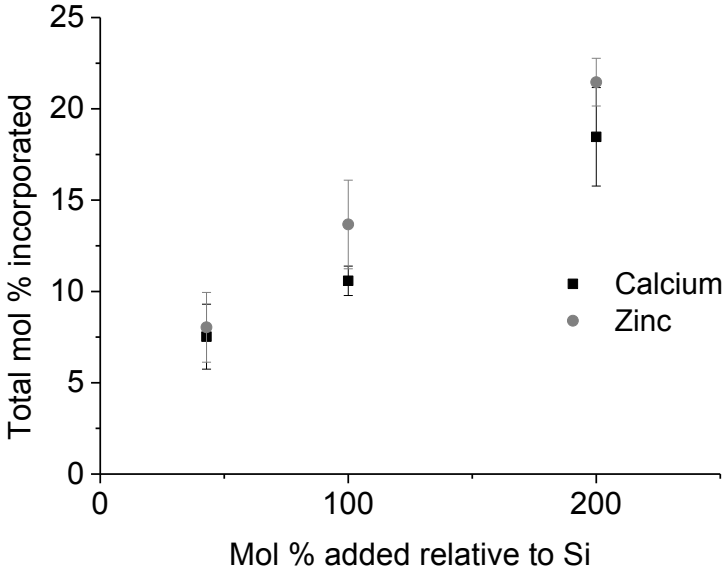


Figure 6.4- ICP results showing incorporation of Ca and Zn into mesoporous silica nanoparticles (as a function of the element added relative to 100 mol% Si).

It can be seen that whilst Ca incorporation was constantly below that of Zn, this difference lies mainly within the standard deviation of the results. Unlike for dense particles the incorporation of calcium does not level off at <10 mol% and instead follows the same trend as Zn, increasing up to 18.5 ± 2.7 mol % Ca when Ca:Si is added in the ratio 2:1. Zn was seen to increase up to 21.5 ± 1.3 mol % for the same ratio added. A summary of particles produced is shown in Table 6.2.

Table 6.2 - Summary of mesoporous nanoparticles produced containing different quantities of cations.

Ca containing samples					
SAMPLE	**Ratio Ca:Si added**	**Ca incorporated (Mol%)**	**Surface area (m^2g^{-1})**	**Modal pore width (nm)**	**Pore volume ($cm^3.g^{-1}$)**
100Si	0:1	0	623	4.252	0.5181
8Ca	30:70	7.5 ± 1.8	354	4.57	0.3256
11Ca	1:1	10.6 ± 0.8	257	5.086	0.2456
19Ca	2:1	18.5 ± 2.7	68	(2.425)	0.0748
Zn containing samples					
SAMPLE	**Ratio Zn:Si added**	**Zn incorporated (Mol%)**	**Surface area (m^2g^{-1})**	**Modal pore width (nm)**	**Pore volume ($cm^3.g^{-1}$)**
8Zn	30:70	8.0 ± 1.9	525	4.57	0.4578
14Zn	1:1	13.7 ± 2.4	426	4.57	0.3611
22Zn	2:1	21.5 ± 1.3	362	4.093	0.2739

As expected, higher percentages of cations can be incorporated into mesoporous nanoparticles than dense particles of equal size (section 5.3.3), due to the larger surface area. However, this difference is most significant for Ca containing particles. Unlike the results for dense particles, ICP compositional results show similar incorporation for both Ca and Zn. Whereas the large differences between incorporation of the two cations into dense particles were attributed to the different roles played by each cation in the silica network, in mesoporous particles these differences appear to be less significant. This is likely to be due to the fact that the larger surface area and disrupted network with more OH groups allows for easier diffusion of the larger calcium ions. However, it can be seen that there are significant differences between the effect of Zn and Ca cation incorporation on the surface area and pore volumes of samples.

The surface area information was calculated from BET analysis in which the value of the correlation coefficient shows the approximation of the multi-point BET plot to a linear function. The closer this value is to 1, the better the data corresponds to the point at which a single layer of gas molecules exist on the surface and the greater the accuracy of the model. All correlation coefficients were >0.9999 suggesting that the surface area values presented in Table 6.2 are reliable.

In literature, silica particles synthesised using this method were reported to have a surface area of 950 m^2g^{-1} and a pore volume of 1.7 cm^3g^{-1} [70]. The pore diameter calculated in literature was also smaller (2.9 nm), although this value was calculated using the BJH analysis method and is therefore inaccurate. For small mesopores the BJH method significantly underestimates pore size (for pore diameters of less than 10 nm this underestimation is as large as ~ 20–30 %) [161]. Therefore, in this thesis, pore size was calculated using DFT analysis as the pores were below the range of the BJH model. The surface area of the 100Si mesoporous nanoparticles produced here was found to be 622.5 m^2g^{-1}, with a pore volume of 0.518 $cm^3.g^{-1}$, which was significantly higher than the surface area of dense silica nanoparticles synthesised using the Stöber process as described in Chapter 4. 100 nm dense particles were found to have a surface area of 27.98 m^2g^{-1} and a pore volume of 0.0256 $cm^3.g^{-1}$.

Figure 6.5 shows the isotherms plotted from the raw nitrogen sorption data collected from each sample (using 20 adsorption and 40 desorption points). An isotherm shows the relationship, at a constant temperature (in this case 77K), between the volume of gas adsorbed and the pressure relative to P_0 (where P_0 is the saturation pressure of pure nitrogen). With the exception of the dense silica particles, all isotherms obtained here were Type IV, which is representative of mesoporous absorbents [161]. The actual pore size distributions for each sample are shown in Figure 6.6 where the vertical axis is a derivative of the volume of nitrogen adsorbed into the surface of the particles at each pore diameter.

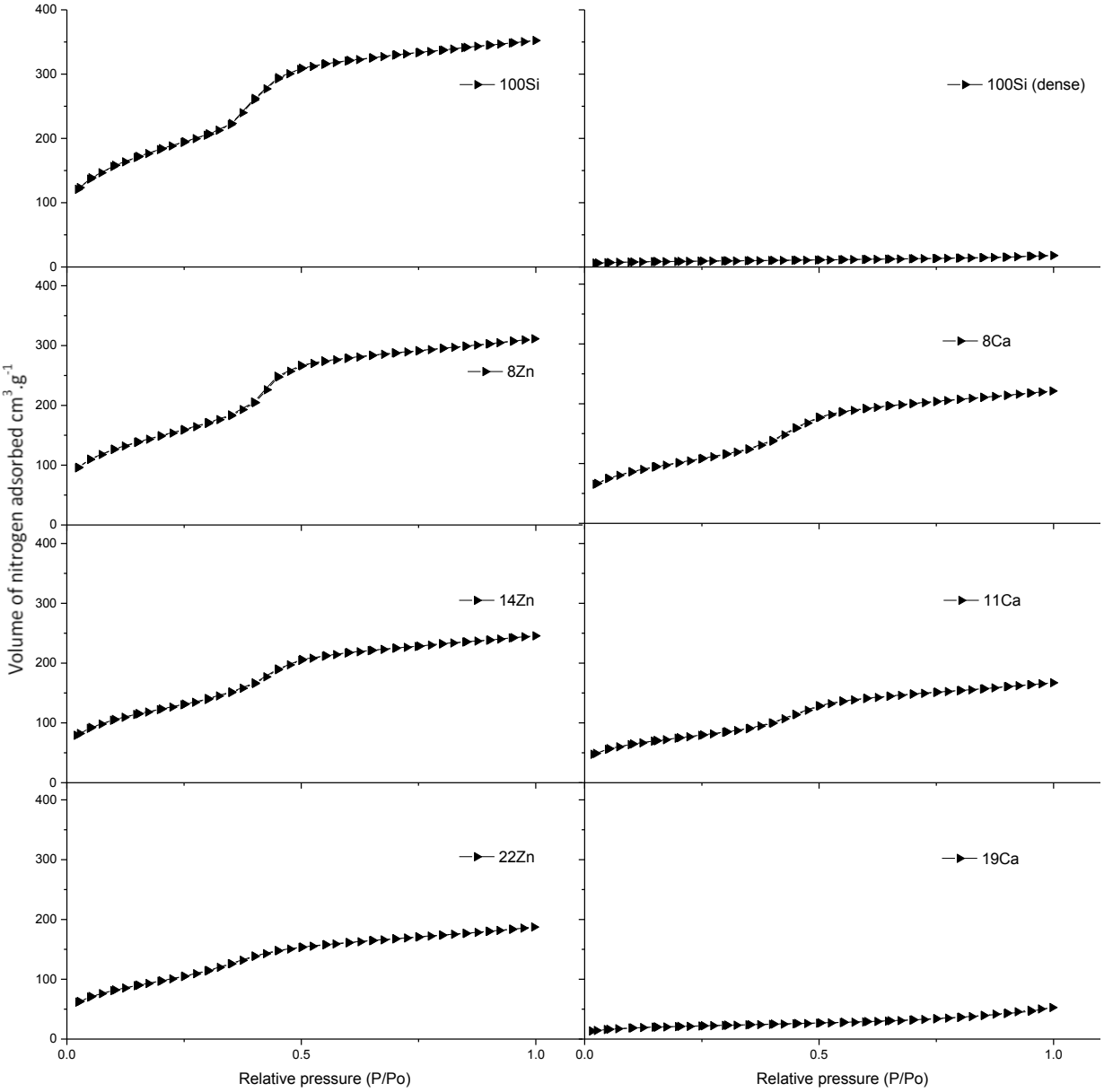


Figure 6.5 - Nitrogen sorption isotherms for mesoporous silica nanoparticles containing different concentrations of Ca and Zn cations

It is clear that the addition of zinc results in a steady reduction in the surface area of the particles from 622.5 m^2g^{-1} to 361.2 m^2g^{-1} for 21.5 mol% Zn incorporation. This is consistent with surface area analysis of mesoporous zinc doped bioactive glass systems in literature [23,31] which also show a reduction in surface area with the addition of Zn, related to the network modifying behavior of zinc. However, these papers also report a reduction in pore size with the increasing addition of Zn which is not seen here. In contrast to this, Bejarano *et al.*[32] show that the incorporation of Cu and Zn into sol-gel synthesised bioactive glasses resulted in an increase in the surface area and the pore volume of 58S. However, in their study the zinc was substituted for calcium instead of silica. Therefore these

results also back up the findings here which show a far greater reduction in surface area due to the addition calcium (to 67.98 m^2g^{-1} for 18.5 mol% Ca incorporation). If both ions played a purely network modifying role it would be expected that Ca^{2+} ions would result in a greater reduction in surface area as a result of greater expansion of the silica network due to their larger ionic radius. A similar network expansion has been observed when strontium, which has a larger ionic radius, is substituted for calcium in bioactive glasses [181]. Alternatively, the difference could be attributed to the fact that Zn can act as both a network modifier and a network former. When zinc is acting as a network former it forms Si-O-Zn bonds as part of the silica network which does not have a significant impact on the surface area. This could therefore result in a less significant surface area reduction in the zinc doped glasses in comparison with their calcium counterparts. However, these reports are based on acid catalysed sol-gel systems without the use of a surfactant, so the mechanisms of mesostructure formation are likely to differ significantly from in the formation of particles. The use of a surfactant could account for the fact that in this work the addition of cations does not appear to have a large effect on the pore size distribution within the nanoparticles, with the pores in all samples ranging between 2.5 and 7 nm and a modal pore size of around 4.5 nm (Figure 6.6). The results however do confirm a significant reduction in total pore volume with increasing cation incorporation, especially for calcium.

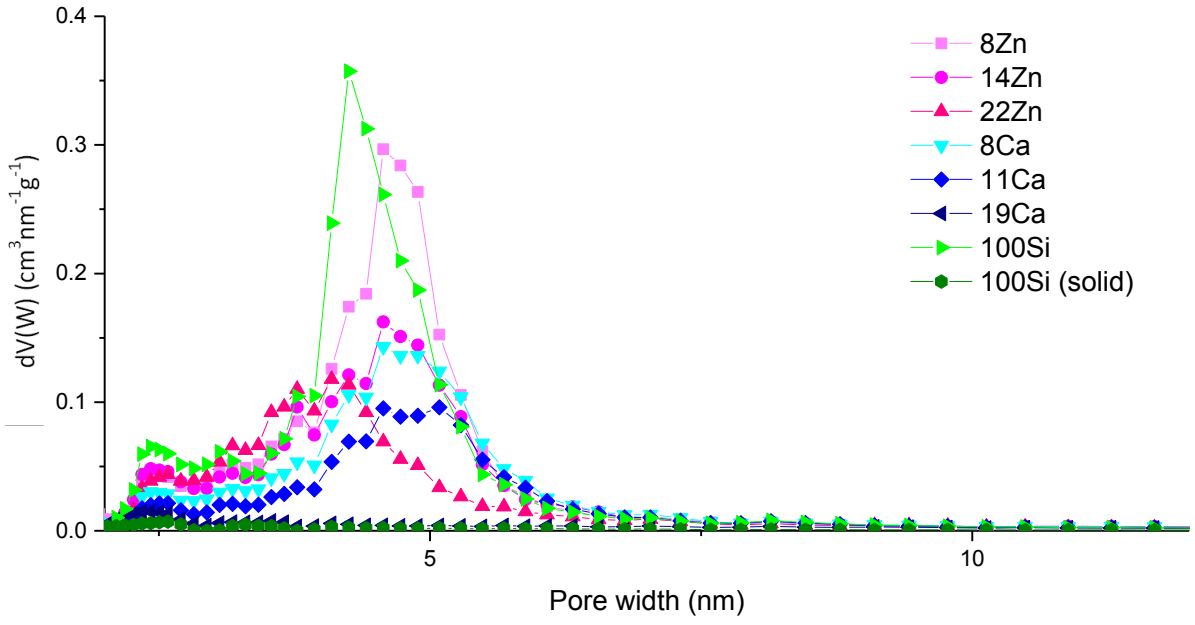


Figure 6.6 - Pore size distribution of mesoporous silica nanoparticles containing different concentrations of Ca and Zn cations , obtained by DFT analysis of nitrogen sorption data.

Arcos *et al.* investigated the effect of Ca addition on the mesoporous structure of mesoporous bioactive glass microspheres, produced using the EISA method, for a variety of surfactants (under acidic conditions). For CTAB they found that whilst pure silica particles exhibited highly ordered mesopores, the addition of 10% Ca resulted in an amorphous mesostructure and a significant reduction in surface area. This was in contrast to particles produced using non-ionic surfactants P123 and F127 where the addition of calcium had far less significant effects on the resultant mesoporous structure. The formation of mesopores by ionic surfactant such as CTAB is highly dependent on ionic interactions which could be modified by charged Ca^{2+} cations [127]. This could explain the disrupted pore formation due to the addition of increasing calcium. However, further work would be required to understand the differences between the effects of Ca^{2+} and Zn^{2+} ions observed here.

Yun *et al.* [128] analysed the effect of calcium addition on the surface area of mesoporous bioactive glass nanospheres synthesised using CTAB as a surfactant, under basic conditions and with calcium nitrate as a Ca precursor. They found that whilst the addition of calcium has a large impact on the final size and mesostructure of the particles, the surface area and pore volume remained high. It is likely that these differences in findings from what we have seen here are due to the point at which calcium is added in the synthesis process. Whereas in this thesis, the calcium is added after the formation of silica particles, Yun *et al.* added calcium nitrate at the start of the process which therefore affected the formation of particles and also resulted in differences in particle size. However this is not necessarily desirable for applications in which it may be beneficial to control both particle size and calcium content independently.

As for the dense particles, NMR, XRD and FTIR experiments were also performed on all mesoporous particles in an attempt to understand the incorporation of both Ca and Zn. It can be seen from XRD results in Figure 6.7 that all particles exhibit a typical amorphous halo. However, unlike for dense particles, there is no evidence of a broad peak/secondary amorphous halo due to the presence of nano-crystals, even at equally high percentages of Zn incorporation. This is likely to be due to the fact that the larger surface area and more open network of the mesoporous particles allows for easier diffusion of zinc, whereas in the dense particles areas saturated with zinc ions could have resulted in the formation of a Zn_2SiO_4 phase. Alternatively it could simply be due to the lower heating temperature of the mesoporous particles (<600˚C) [170]. The only noticeable difference between samples is a slight broadening of the amorphous halo in sample 19Ca. This is could be indicative of changes within the network which is also suggested by the lack of porosity of this sample.

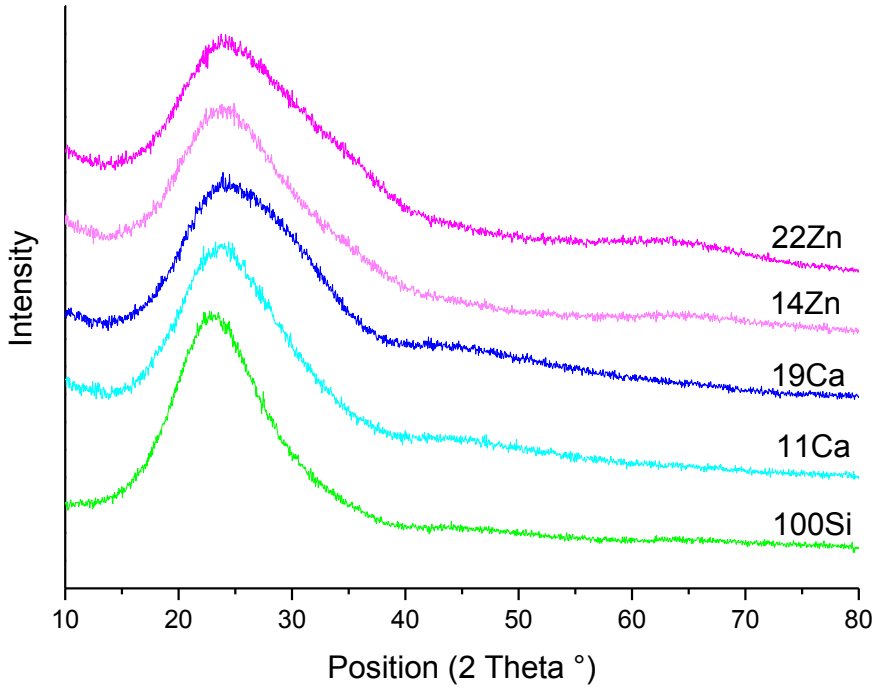


Figure 6.7- XRD patterns of mesoporous silica nanoparticles containing different concentrations of Ca and Zn cations after calcination and washing.

FTIR results are shown in Figure 6.8. All particles exhibit the same distinctive peaks as the dense particles at 1050 cm^{-1}, 440 cm^{-1} and 800 cm^{-1}, representative of Si-O-Si asymmetric stretching [27,33,36,171-173], Si-O-Si bending [27,36,172,173] and Si-O symmetric stretching [36] respectively. Samples 11Ca, 14Zn and 22Zn also show a peak appearing (in increasing intensity) at 500 cm^{-1}, corresponding to Si-OH stretching [174] or Si-O-NBO [171], as the cations enter and break up the silica network. However, this is not present in sample 19Ca, indicating a more compact network. Instead, sample 19Ca shows a slight shift in the Si-O-Si band at 1050 cm^{-1} towards lower values which has previously been suggested to be indicative of a decrease in silica concentration [33].

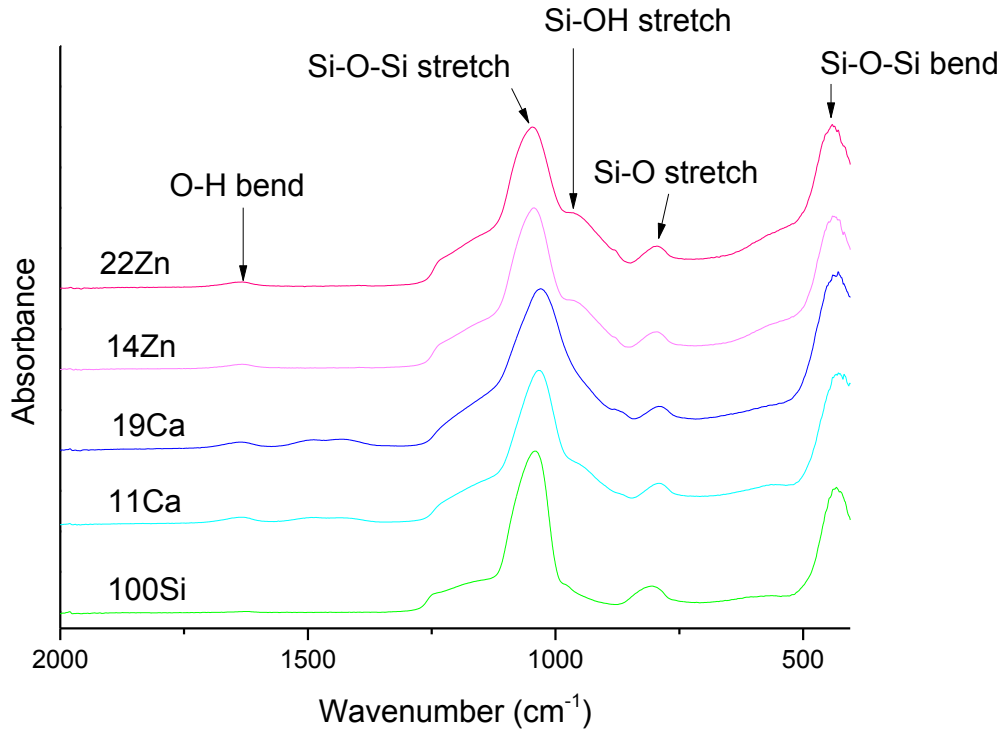


Figure 6.8 - FTIR spectra of mesoporous silica nanoparticles containing different concentrations of Ca and Zn cations, after calcination and washing.

In order to better understand the effect of cation addition on the mesoporous network structure and the differences in surface area and pore volume, ^{29}Si MAS NMR and ^{1}H MAS NMR were again performed on all particles (after heat treatment and surfactant removal). The spectra are shown in Figure 6.9, and the Q distributions and network connectivity values for all samples are tabulated in Table 6.3. The shifts are representative of conventional Q speciation. The network connectivity of each sample is also plotted in Figure 6.10 to illustrate the effects of cation addition.

Table 6.3 - Q distributions obtained from single pulse 29Si MAS NMR spectra for mesoporous silica nanoparticles containing different concentrations of Ca and Zn cations (courtesy of Sam Page, University of Warwick).

Sample	Q^1		Q^2		Q^3		Q^4		Network Connectivity (NC)
	δ_{Iso} [ppm]	I [%]	δ_{Iso} [ppm]	I [%]	δ_{Iso} [ppm]	I [%]	δ_{Iso} [ppm]	I [%]	
100Si	-	-	-93.3±0.2	5.7±0.3	-101.2±0.1	21.0±0.3	-110.0±0.1	73.3±0.1	3.68±0.01
8Ca	-80.4±0.4	1.8±0.3	-93.0±0.1	14.9±0.4	-101.1±0.1	26.3±0.3	-110.0±0.1	57.0±0.2	3.39±0.01
11Ca	-81.9±0.3	4.4±1.2	-92.8±0.1	17.2±1.2	-101.0±0.9	29.3±0.4	-110.0±0.9	49.1±0.3	3.23±0.03
19Ca	-82.0±0.7	8.3±0.4	-93.0±0.4	28.4±0.4	-101.3±0.3	24.2±0.3	-110.1±0.1	39.2±0.2	2.95±0.02
8Zn	-84.3±0.9	2.0±0.3	-92.3±0.5	9.7±0.3	-101.0±0.1	25.9±0.2	-110.0±0.1	62.4±0.1	3.49±0.01
14Zn	-82.0±1.0	2.5±0.3	-92.8±0.2	11.0±0.3	-100.8±0.1	26.5±0.2	-109.5±0.2	60.0±0.1	3.44±0.01
22Zn	-76.3±1.2	6.5±0.4	-92.9±0.5	29.0±0.5	-101.0±0.1	21.3±0.4	-110.0±0.1	43.3±0.3	3.02±0.02

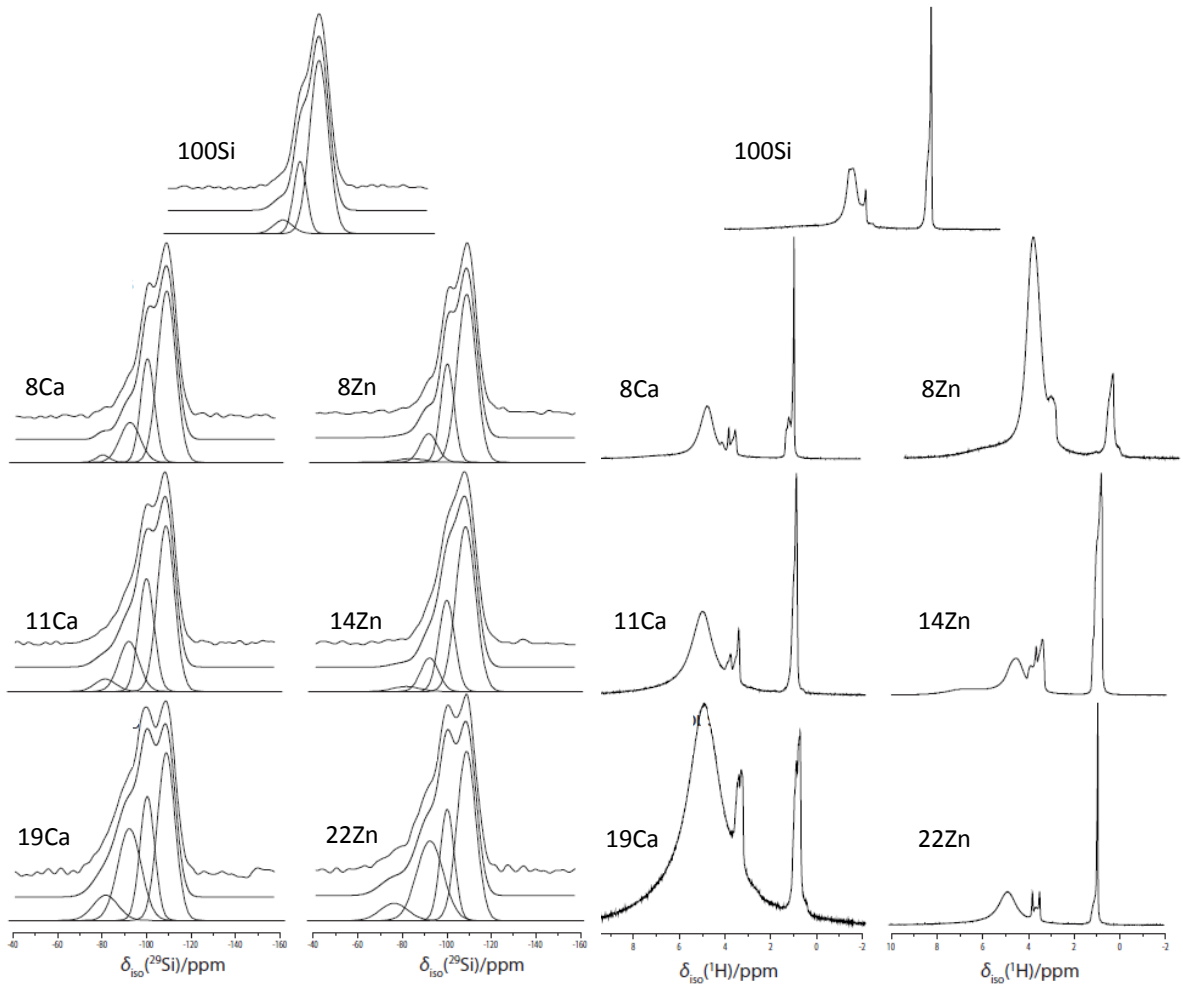


Figure 6.9 - ^{29}Si MAS NMR spectra (left) and ^{1}H MAS NMR spectra (right) for mesoporous silica nanoparticles containing different concentrations of Ca and Zn cations (courtesy of Sam Page, University of Warwick).

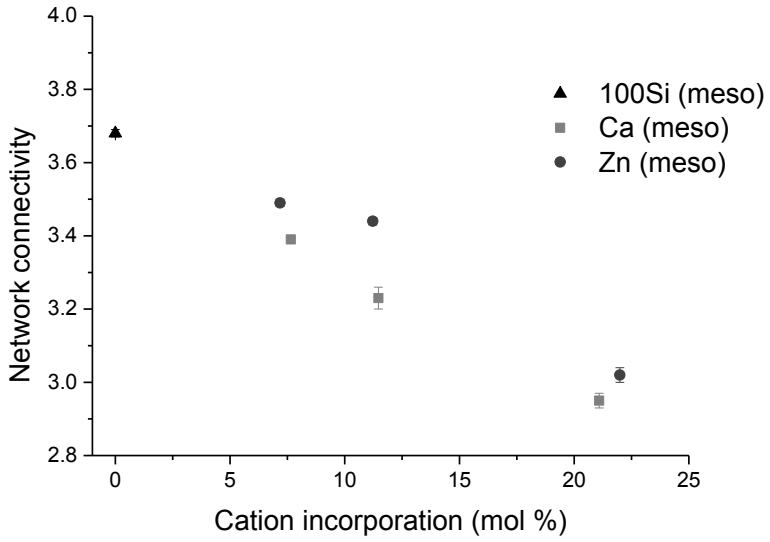


Figure 6.10 - Effect of Zn and Ca cation incorporation on network connectivity of mesoporous silica nanoparticles.

As expected, increasing the amount of both zinc and calcium resulted in a corresponding decrease in network connectivity. However, in all cases the network connectivity decreased more than would be predicted by the NC equation (in section 5.3.4), demonstrating the complexity of the system.

This decrease in network connectivity was slightly more significant in the calcium containing particles, suggesting that, while the calcium acts purely as a network modifier, some of the zinc also acted as a network former which has a less considerable effect on network connectivity. As with the dense particles, the addition of calcium reduced the number of sterically hindered OH groups within the network, seen by the decrease in intensity of the sharp peak in the ^{1}H MAS NMR spectra in Figure 6.9 (relative to the broad peak) as calcium concentration is increased. This is in agreement with FTIR results which show no Si-OH bonds for sample 19Ca. However, the significant drop in network connectivity suggests that while some of the calcium may be replacing modifying H^{+} ions, the majority is breaking up the network further. In contrast to dense particles the ability of calcium to enter the network is increased, due to the larger surface area and lower NC of the 100Si MSNs, making it easier for the larger Ca^{2+} ions to enter the network. In sol-gel calcium-silica bioactive glasses, calcium has been reported to have a Ca-O coordination as large as 5 or 6 [21,22], which would explain the large decrease in network connectivity seen here. As the calcium enters and modifies the silica network it is likely to cause expansion of the network [181], however the overall size of the particles remained unchanged. This could therefore account for the significant decrease in pore volume seen in the calcium containing samples. It could also explain the maximum calcium incorporation seen in dense particles due to low porosity meaning that the network is unable to expand. It would therefore be expected that further addition of calcium to the mesoporous particles would reach a maximum as the particles became fully dense and the network was no longer able to expand in order to accommodate additional calcium ions.

Although the mesoporous zinc containing particles show similar ^{29}Si MAS NMR spectra to their calcium counterparts (with just a slightly reduced decrease in network connectivity) significant differences can be observed in the ^{1}H MAS NMR spectra, suggesting very different mechanisms of ion incorporation. It appears that the initial addition of zinc cations results in a sharp drop in the numbers of sterically hindered OH groups within the network, although as zinc % incorporation is increased the relative quantity significantly increases again to beyond that seen in 100Si mesoporous particles. The hypothesis is that as zinc first enters the network, it initially replaces modifying H^{+} ions before breaking up the network further. However, it is likely that this behaviour was not noticeable in dense particles due to fewer original sterically hindered OH groups within the network of the dense 100Si particles. Nevertheless, as zinc concentration is increased, the same trend is observed as

seen in the dense particles (Chapter 5). Increasing zinc results in decreased network connectivity due to the zinc acting partly as a network modifier (with octahedral coordination). However, it can also act as a network former (creating Si-O-Zn bonds and $[ZnO_4]^{2-}$ tetrahedral units, charge balanced with H^+ ions). The network connectivity is reduced more than in the dense particles, suggesting that a higher percentage of the zinc is acting as a network modifier.

6.4 Conclusions

This chapter demonstrates the difficulties in reproducing sensitive methods for the synthesis of mesoporous silica particles found in literature. However, it establishes a simple and reliable method for producing monodispersed mesoporous silica nanoparticles within the desired size range of 50 - 100 nm and subsequently shows that it is possible to successfully incorporate both Zn and Ca cations without affecting the size or homogeneity of the particles. Unlike in dense particles, the incorporation of calcium did not level off at <10 mol% and instead followed the same trend as Zn, increasing up to 18.5 ± 2.7 mol % Ca when Ca:Si was added in the molar ratio of 2:1. This is attributed to the decreased network connectivity and larger surface area of the 100Si mesoporous particles, allowing for easier diffusion of the larger Ca cations. Zn was seen to increase up to 21.5 ± 1.3 mol % for the same ratio added. Both cations were shown to significantly decrease the network connectivity of the particles, suggesting that they are likely to be biodegradable; however the addition of calcium in particular resulted in a significant drop in surface area and pore volume of the particles. Future work could look at increasing the ratios of Zn:Si and Ca:Si added to these particles. It is predicted that as with the dense particles, the maximum amount of calcium that it is possible to incorporate may level off below that for Zn.

7 Particle degradation and fate within cells

7.1 Introduction

Considering that the ultimate aim of this work is to synthesise nanoparticles for therapeutic applications, it is necessary to first establish how they will interact with cells *in vitro*. This knowledge will serve to optimise the synthesis parameters for better results *in vivo*.

For the zinc containing particles, the objective is to selectively kill cancer cells by taking advantage of the intrinsic toxicity of Zn^{2+} ions. It is hypothesised that zinc incorporation into silica nanoparticles will provide controlled release of zinc at acidic pH resulting in preferential cytotoxicity to cancer cells due to their acidic microenvironment, faster metabolism and reduced ability to withstand high zinc concentrations. However, it is first necessary to investigate the internalisation of nanoparticles by cancer cells *in vitro* and their fate within cells, including any cytotoxic effects.

The cancer cell lines investigated in this chapter, MDA-MB-231 and MCF-7, are both triple-negative breast cancers (TNBCs) [182] (i.e. their tumours do not express predictive markers like estrogen receptor (ER), progesterone receptor (PR) or human epidermal growth factor receptor 2 (HER2)). This makes treatment options very limited as they do not respond to hormonal therapy [183,184]. Approximately 15–20% breast cancer cases involve TNBCs [182]. Therefore exploring other treatment options for TNBCs such as ionic therapy is extremely important.

Subsequently ion dissolution studies will also be performed to provide a valuable insight into the mechanism of particle degradation within the cells and cation incorporation into the particles. This will allow for future optimisation of particles.

As discussed previously, one of the main aims of increasing the amount of calcium incorporated in to the nanoparticles is to increase their bioactivity. Bioactivity is closely linked with degradation and the formation of HCA, both of which can be established by performing ion dissolution studies on particles in simulated body fluids. As these particles are intended to be incorporated into a nano-composite material, it is necessary to consider how they will behave both as part of the scaffold and also following cell uptake of individual nanoparticles after biodegradation of the composite.

7.2 Materials and methods

All cell work in this chapter, HR-TEM and STEM-EDS were performed by Dr Shu Chen.

7.2.1 Cell studies

Cell studies were performed on Zn containing bioactive glass nanoparticles in order to determine their ability to be internalised by cancer cells and result in cytotoxicity due to the release of Zn^{2+} ions. The following cells were used in this work:

MCF7 (ATCC® HTB22™) - Tissue: mammary gland, breast; derived from metastatic site: pleural effusion. Disease: adenocarcinoma. Cell Type: epithelial

MCF 10A (ATCC® CRL-10317™) - Tissue: mammary gland/breast, Disease: fibrocystic disease. Cell Type: epithelial

MDA-MB-231(ATCC® HTB-26™) - Tissue: mammary gland/breast; derived from metastatic site: pleural effusion. Disease: adenocarcinoma. Cell Type: epithelial

MDA-MB-231 and MCF-7 are both breast cancer cell lines but of different metastatic and invasive capacities. MDA-231 is highly metastatic and invasive [185], whereas MCF 7 is non-metastatic and much less invasive. MCF-10a is a healthy epithelial cell line used as a control.

7.2.1.1 Cell culture

MDA-MB-231, MCF-7 and MCF-10-A cell lines were purchased from ATCC (Manassas, VA, USA). MDA-MB-231 and MCF-7 were maintained in Dulbecco's Modified Eagle's Medium (DMEM) and Minimum Essential Medium (MEM) respectively, supplemented with 10% fetal bovine serum (FBS) and Penicillin/Streptomycin solution (10,000 units.ml^{-1} penicillin, 10,000 µg.ml^{-1} streptomycin). MCF-10a cells were grown in DMEM: F-12 media supplemented with 20 ng.ml^{-1} epidermal growth factor (Invitrogen, Life Technologies Ltd, UK), 100 ng.ml^{-1} cholera toxin (Sigma-Aldrich Ltd, UK), 0.01 mg.ml^{-1} insulin, 100 ng.ml^{-1} hydrocortisone, and 5% horse serum. Cells were cultured in a humidified incubator at 37°C and 5% CO_2.

7.2.1.2 Cell uptake and TEM sample preparation

Cells were seeded in a 6-well plate with a density of 150 x 10^3 cells per well and incubated with NPs at a concentration of 50 µg.ml^{-1} for 24 h. 50 µg.ml^{-1} was chosen as this concentration was found to be non-toxic whilst being a high enough dose to find sufficient particles within the cells for imaging. Cells were rinsed briefly in saline (0.9% NaCl) to remove any non-ingested particles and were then fixed in 2% glutaraldehyde (Sigma) and 2% formaldehyde (Sigma) in 0.1 M sodium cacodylate (Sigma) buffer at pH 7.4 for 1 h at room temperature. The fixatives were then removed by washing

cells with 0.1 M sodium cacodylate buffer for 3 times. Cells were scraped and transferred into 1.5 ml Eppendorf tubes and cell pellets were obtained by centrifugation at 10,000 g for 20 min. All samples were stained with 1% Osmium tetroxide in 0.1 M sodium cacodylate solution (pH 7.4) and samples containing dense particles were also stained with 1 % uranyl acetate water solution for 30 min. They were dehydrated in a graded ethanol series of 50%, 70%, 95%, and 100% (volume ratio of ethanol to dH_2O) for 5 min each then rinsed three times in acetronitrile (Sigma) for an additional 10 min each, all at room temperature. After dehydration, samples were progressively infiltrated with an Epon based resin, created by combining 23.5 g Epoxy embedding medium (Sigma), 12.5 g dodecenylsuccinic anhydride (Agar scientific), 14 g methyl acid anhydride (Agar scientific) and 0.75 ml benzyl dimethylamine (Agar scientific). Samples were first re-suspended in 25% resin/acetonitrile solution (volume ratio of resin to acetonitrile) and centrifuged for 30 s at 2,000 g. This step was repeated with 50, 75, 100, 100 and 100% resin. Samples were cured at 100˚C for 2 h. Thin sections (70 nm) were cut directly into a water bath using an ultramicrotome with a diamond knife with a wedge an angle of 35˚. Sections were immediately collected on bare, 250 mesh TEM grids (Agar Scientific), dried and kept under vacuum for TEM analysis. Low resolution TEM images were taken on a JEM-2100F Transmission Electron Microscope. HRTEM and STEM-HAADF/EDS analysis were performed on an FEI Titan 80–300 scanning/transmission electron microscope (S/TEM) operated at 80 kV, fitted with Cs (image) corrector and SiLi EDS spectrometer (EDAX, Leicester UK). STEM experiments were performed with a convergence semiangle of 14 mrad and inner and outer high angle annular dark field (HAADF) collection angles of 49 and 239 mrad, respectively. The probe diameter was <0.5 nm. This method of TEM sample preparation and staining was not found to induce zinc release or result in any changes in the morphology of the particles.

7.2.1.3 Cell viability assay (WST-1)

Cell vitality after nanoparticle treatment was determined using Cell Proliferation Reagent WST-1 assay (Roche Applied Biosystems) according to the manufacturer's instructions with modifications. WST-1 assay is a colorimetric assay and analyses the number of viable cells by the cleavage of tetrazolium salts to formazan by cellular enzymes, i.e. mitochondrial dehydrogenases. An increase in the number of viable cells results in an increase in the overall enzyme activity in the sample. This leads to an increase in the amount of formazan dye formed, which directly correlates to the number of metabolically active cells in the sample. Briefly, cells were seeded in a 96-well plate with a density of 15 x 10^3 cells per well, differentiated and incubated with $Zn(NO_3)_2$ (3 replicates per concentration) at Zn concentrations of 5, 10, 15, 20, 30 and 40 $\mu g.ml^{-1}$ and silica NPs containing Zn (3 replicates per concentration) at NP concentrations of 25, 50, 100, 150, 200 and 250 $\mu g.ml^{-1}$. After 24 h, the medium was removed and the cells were washed once with Hanks' Balanced Salt solution (Sigma).

WST-1 reagent was diluted with the medium to 5% (v/v) in the dark, and the plates were then treated with 100 µl of WST-1 5% solution and incubated in a humidified atmosphere at 37°C and 5% CO_2 for 2 h. Finally spectrophotometric evaluation was performed by measuring the absorbance of the formazan product at 430 nm wavelength. The relative viability (% viability compared to untreated cells) was calculated as mean value ± standard error of the mean (SEM) as a result of at least 3 independent experiments.

7.2.2 Ion dissolution studies

A method for testing a material's bioactivity by submersion in SBF, was first proposed by Kokubo *et al.* in the 1980's [186]. SBF has been developed so that it contains similar ion concentrations and pH to blood plasma. When placed in SBF bioactive materials have been seen to form an HCA layer on their surface. Although the validity of SBF testing has been the subject of much debate it is still a popular way of testing the bioactivity of materials. Recently, a proposed test method using a fixed mass per solution volume ratio and agitated solution has been proposed to allow for direct comparison between bioactive glasses [187]. However, these concentrations are higher than would be used for nanoparticles in therapeutic applications. Additionally, as nanoparticles < 250 nm are likely to be internalised by cells after which the vesicle they are contained within fuses with a lysosome [60], it is more meaningful to perform a dissolution study in Artificial Lysosomal Fluid (ALF) to determine how particles might degrade after internalisation. ALF was prepared by the addition of reagents to dH_2O, at 37˚C according to Table 7.1. All reagents were purchased from Sigma-Aldrich UK and used as received without further purification. ALF was stored at 37˚C and the pH was adjusted to 4.5 using NaOH before use. Dissolution studies were also performed in Minimum Essential Medium (Gibco® MEM, ThermoFisher Scientific) both with and without 10% FBS so that results could be compared to cell uptake studies and the effects of proteins could be analysed. MEM is one of the most commonly used of all cell culture media and can be used with a variety of suspension and adherent mammalian cells. However, as MEM contains no proteins, lipids or growth factors it is often supplemented with FBS.

Table 7.1 - Reagents used for making artificial lysosomal fluid (ALF) [188-191].

Chemicals (g.L^{-1})	**ALF (pH = 4.5)**
Magnesium chloride, $MgCl_2$	0.050
Sodium chloride, NaCl	3.21
Disodium hydrogen phosphate, Na_2HPO_4	0.071
Sodium sulphate, Na_2SO_4	0.039
Calcium chloride dihydrate, $CaCl_2.2H_2O$	0.128
Sodium citrate dihydrate, $C_6H_5Na_3O_7.2H_2O$	0.077
Sodium hydroxide, NaOH	6.00
Citric acid, $C_6H_8O_7$	20.8
Glycine, H_2NCH_2COOH	0.059
Sodium tartrate dihydrate, $C_4H_4O_6Na_2.2H_2O$	0.090
Sodium lactate, $C_3H_5NaO_3$	0.085
Sodium pyruvate, $C_3H_3O_3Na$	0.086

In the past, dissolution experiments have tended to involve making up different samples of nanoparticles in solution for each time point. At each time-point nanoparticles are removed from solution by centrifugal ultrafiltration [192-194]. However, this requires extremely accurate measurements of both mass of nanoparticles and volume of solution in order to achieve comparable results. It also requires large quantities of particles, which limits the number of possible time-points and introduces more sources of possible error when comparing results in different media if multiple batches of particles are required. A protocol was therefore developed here for performing a dissolution study based on experiments previously conducted by Misra *et al.* [195] and Bailey *et al.* [196] (all experiments were repeated in triplicate):

- 2.5 mg of bioactive glass nanoparticles were dispersed in 2.5 ml of solution by sonication and pipetted into SnakeSkin Dialysis Tubing (3.5K MWCO, 16 mm dry I.D), which was sealed and placed in a pot made up with solution to a final volume of 50 ml. This is equal to a final nanoparticle concentration of 50µg.ml^{-1}, which is the same concentration as used for cell studies.
- All samples were incubated at 37 °C in an orbital shaker at 120 rpm. A schematic showing the experimental set-up is shown in Figure 7.1.
- Aliquots of 2 ml were taken at time points 1 h, 2 h, 4 h, 6 h, 8 h and 24 h from the bulk solution and replaced with 2 mL of fresh solution. Aliquots collected at each time point were then diluted with 3ml 1w/w% HNO_3 for analysis by ICP-OES (Thermo Scientific ICap 6000series). Dilution with HNO_3 plays the dual role of terminating any reactions and stabilising the solution as well as diluting to a suitable volume/concentration for ICP. Standards of 0, 0.01, 0.05, 0.1, 0.5, 2, 5, 10, 20 and 40 ppm were used for the calibration

curve. It was necessary to use a lower concentration of nitric acid than typically used, in order to prevent precipitation of cell culture media. For samples in cell culture media, aliquots were also filtered through a 0.2 µm cellulose filter (VWR International) to remove any proteins before dilution with nitric acid.

- After 24 h, the particles inside the dialysis tubing were collected by centrifugation and washed using distilled water and ethanol before TEM analysis.

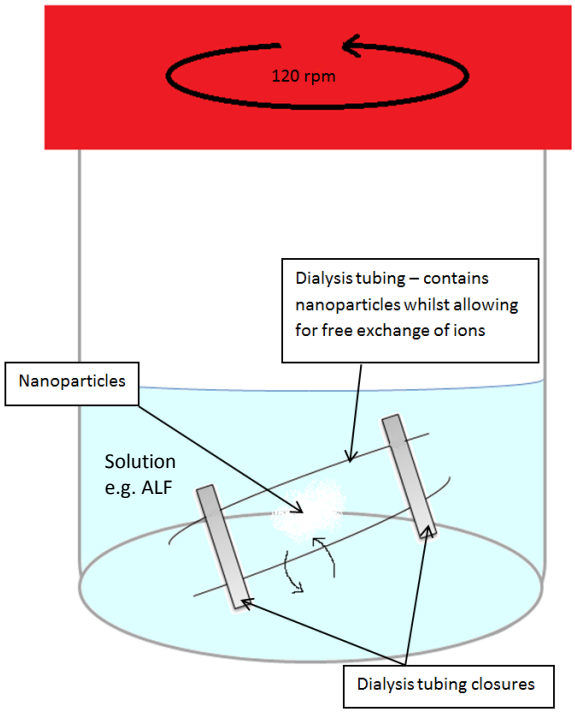


Figure 7.1 - Experimental setup for ionic dissolution study of bioactive glass nanoparticles in solution.

7.3 Results and discussion

7.3.1 Cell uptake of SiO_2-ZnO particles

7.3.1.1 Mechanisms of particle internalisation

Particle uptake experiments were first conducted on MCF-7 cells (as described in section 7.2.1.2) with dense 11Zn NPs of 80 nm diameter. TEM images taken after 24 h are shown in Figure 7.2 and Figure 7.3.

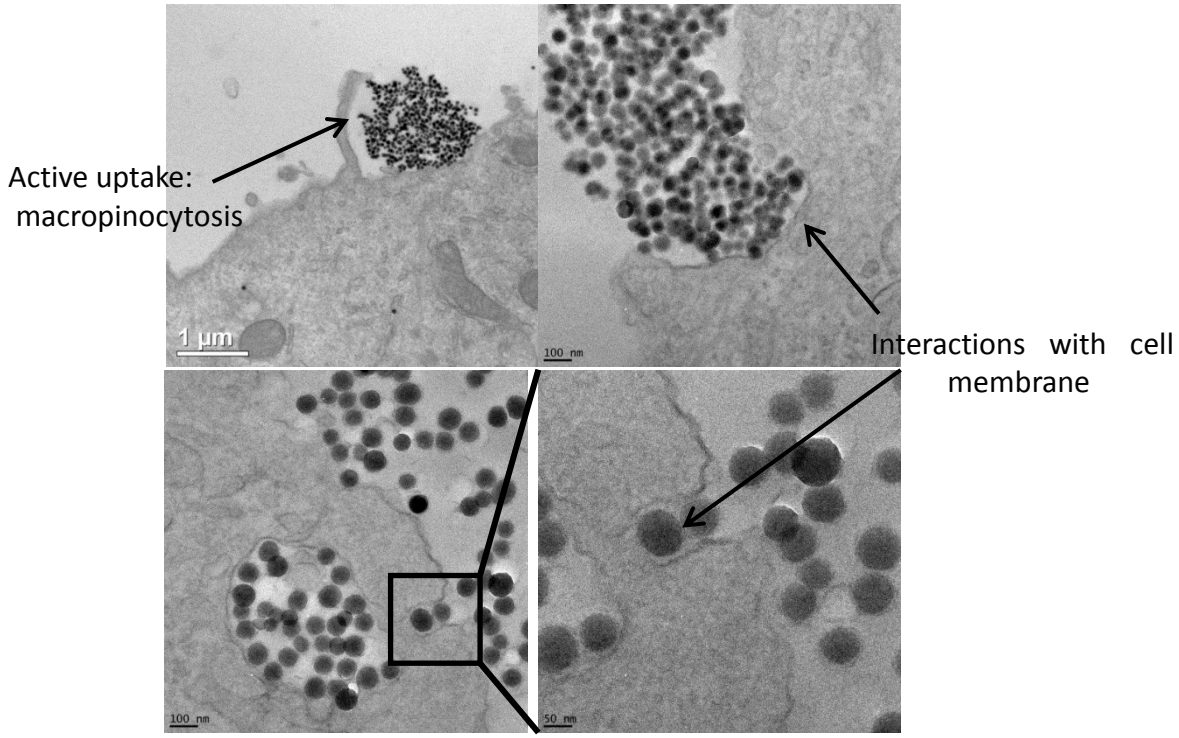


Figure 7.2 - TEM images showing particle uptake of dense 11Zn NPs into MCF-7 cells after 24h incubation at a concentration of 50 µg.ml^{-1} (courtesy of Dr Shu Chen, Imperial College London) showing active uptake of clusters of particles by macropinocytosis and interactions of both individual and clusters of particles with the cell membrane.

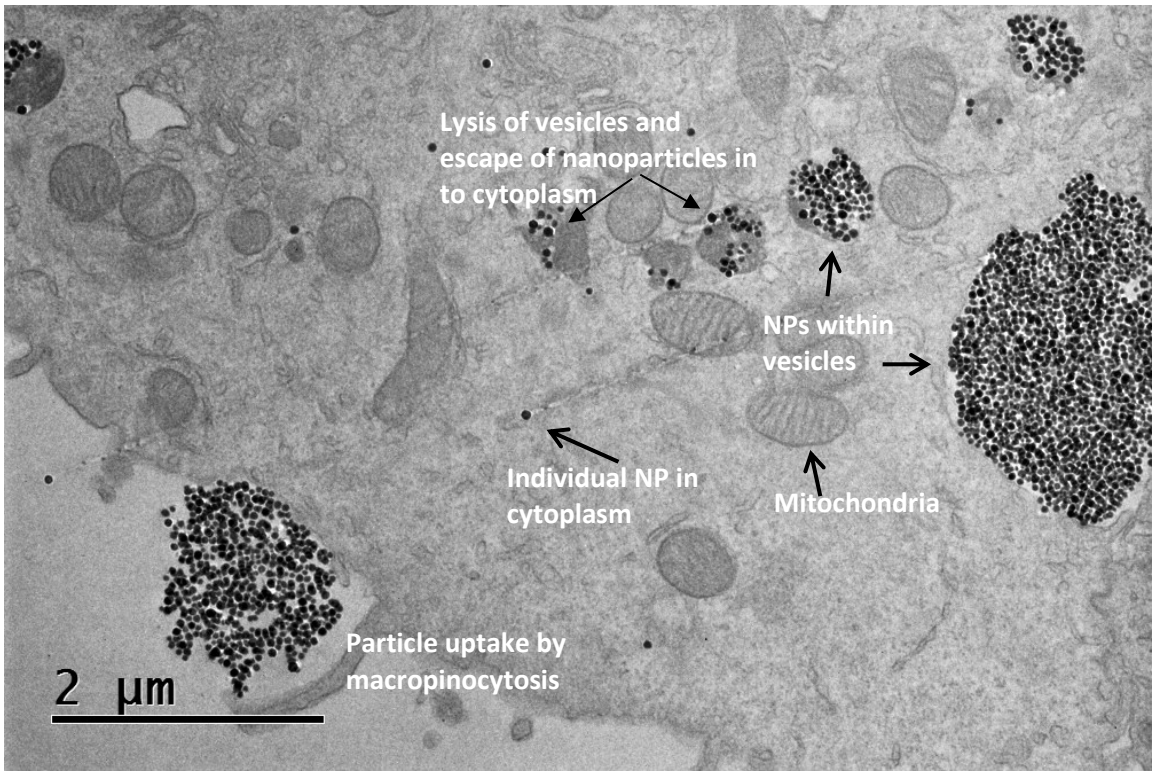


Figure 7.3 - TEM image of MCF-7 cell showing internalised particles after 24 h exposure to dense 80 nm 11Zn NPs at a concentration of 50 µg.ml^{-1} (courtesy of Dr Shu Chen). Particles can be seen both within vesicles and in the cytoplasm.

Figure 7.2 shows that active uptake of large clusters of particles occurred by macropinocytosis, indicated here by the formation of a cell membrane protrusion, surrounding a large number of nanoparticles. The particles are subsequently encapsulated by the cell membrane in large irregular vesicles (> 1μm) called macropinosomes. Interactions between the cell membrane and individual nanoparticles are also observed. These particles appear to uptaken by protein mediated endocytosis (e.g. clathrin-mediated and caveolin-mediated). As size, shape and surface charge have a large effect on nanoparticle uptake, it is likely that agglomerations of particles will result in different mechanisms of particle uptake. Small oxide nanoparticles (of 50 nm or less) have been reported to undergo fast agglomeration upon contact with cell culture media unless they are surface modified [53]. Zeta potential experiments were therefore performed on these particles in cell culture media to give an indication of their stability in suspension and likelihood of agglomeration. The results for different media are shown in Table 7.2. A zeta potential value typically greater than +30 mV or less than -30 mV indicates that the particles will tend to repel each other and the system is considered to be stable [159]. Therefore zeta potential, not only has the ability to determine the surface charge of particles, but can also give an indication of whether the particles are likely to aggregate in different media and under different conditions. Zeta potential measurements were taken on a Malvern Instrument 2000 and particles were dispersed in solution by sonication prior to being injected into a disposable capillary cell. For cell culture media the following parameters were used [197]: temperature = 25˚C, dielectric constant = 80, viscosity = 1.054 cP (confirmed by rheometry measurements), and refractive index (RI) = 1.335 (measured).

Table 7.2 - Zeta potential measurements for particles in distilled water and cell culture media.

Sample	Zeta potential in solution (mV)		
	dH_2O	**MEM**	**MEM + FBS**
100Si	-35.7±0.4	-26.9±0.1	-12.3±1.4
11Zn	-32.5± 5.3	-29.9±1.9	-13.0±0.6

It can be seen from the change in zeta potential that in MEM + FBS the particles are most likely to agglomerate. This is likely to be due to the presence of proteins in the FBS resulting in the formation of a protein corona around the particles and altering the surface charge. The formation of a protein corona could also make particles more recognisable to macrophages. Therefore these findings suggest that particles may need to be functionalised in order to avoid clearance by the MPS. As discussed previously in section 2.2, studies have suggested that uptake by macrophages occurs

fastest for either highly positively or negatively charged particles [11]. Additionally, it has been reported that nanoparticles in the 10–100 nm size range and with a surface charge either slightly positive or slightly negative should have the greatest accessibility to tumour tissue when dosed into the circulatory system [62]. Similar charge alterations could therefore be particularly beneficial for cancer applications, provided the particles do not agglomerate.

The process of osmium tetroxide staining crosslinks phospholipids found in the cell membrane to provide increased electron contrast. It therefore allows for the membranes of both the cell and it's organelles to be easily seen on TEM images. In Figure 7.2 this allows for interactions of nanoparticles with the cell membrane to be seen more clearly. In Figure 7.3 it also shows various cell organelles including mitochondria and vesicles containing nanoparticles. Uranyl acetate staining, on the other hand, stains proteins by hydrostatic interactions. This allows for lysosomes to be identified due to their higher protein concentration resulting in a darker colouring on TEM. In Figure 7.3 it can be seen that after internalisation, groups of particles are present inside the cell enclosed within endosomes, while some are also seen within lysosome-like vesicles. However, individual particles are also present in the cytoplasm suggesting that they have somehow escaped the endosomal pathway. One hypothesis for this observation is uptake of particles by endocytosis and subsequent release of particles from endosomes into the cytoplasm. This has previously been observed for bioactive glass nanoparticles (~250 nm) [60,82] in which cases the escape from the phagocytic pathway is attributed to release of Ca^{2+} ions from the particles resulting in elevated levels of intracellular calcium [198]. It is hypothesised that in the presence of Ca^{2+} ions, $Ca(PO_4)$ precipitates are responsible for endosomal release by the lysis of endosome/lysosome membranes [199]. A similar mechanism could occur due to the release of Zn^{2+} ions as seen here. However, this would not account of the presence of pure silica mesoporous nanoparticles which have also been found in the cytoplasm of cells [49,200] and as such the mechanism by which particles escape from vesicles is still unclear. Another hypothesis is that the strong interactions between negative silanol groups on the particle surface with positive amine groups on the cell membrane could lead to disturbance of the cell membrane and direct entry into the cytoplasm. A TEM image showing the interaction of individual particles with the cell membrane is shown in Figure 7.4, suggesting that these particles may be internalised in this way.

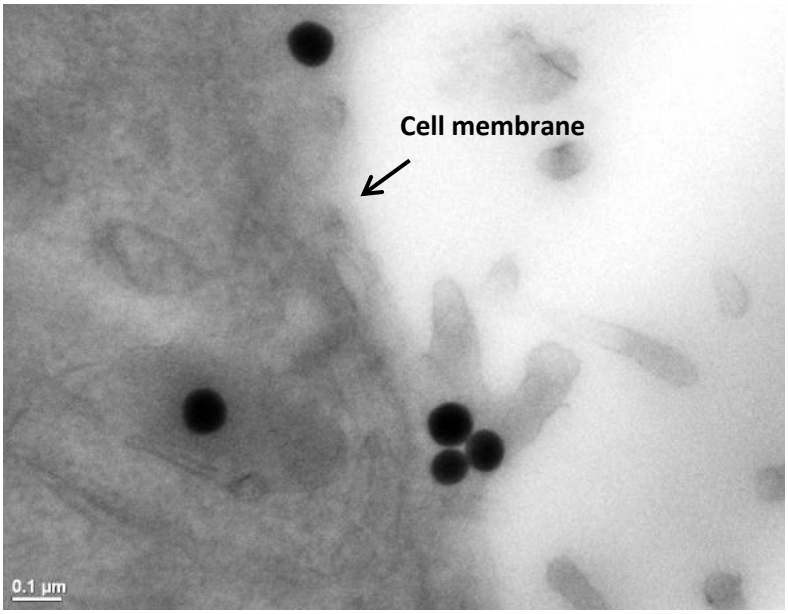


Figure 7.4 - TEM image of MCF-7 cell after 24 h exposure to dense 80 nm 11Zn NPs at a concentration of 50 µg.ml^{-1} showing particles appearing to diffuse directly through the cell membrane (courtesy of Dr Shu Chen).

This effect is undesirable in therapeutic applications as if the particles interact with red blood cells in this way when injected into the blood stream it can result in haemolysis (rupturing of red blood cells). However, haemolysis has not been observed to be significant in previous experiments conducted on mesoporous silica nanoparticles of around 100 nm. It can also be suppressed by altering the size or surface chemistry of the particles [201,202].

For drug delivery applications, it is desirable for nanoparticles to release their cargo in the cytoplasm. Therefore further work is required in order to understand the mechanism of escape of these particles from the endocytic pathway.

7.3.1.2 Fate of internalised nanoparticles

Having seen that bioactive glass nanoparticles containing zinc can be internalised by cells and located within endosome/lysosome-like vesicles, it is hypothesised that subsequent degradation and release of zinc ions could lead to cell death. It can be seen from Figure 7.5 that both dense 100Si and 11Zn particles were present in lysosomes inside the cells. Lysosomes are identified by Uranyl acetate staining due to their high protein content. The lysosome containing 100 Si NPs shows intact, spherical morphology, similar to that observed in the control cell, whilst the lysosome containing Zn loaded NPs is no longer spherical and the membrane appears to be starting to break down. It is clear that the 11Zn particles have altered the lysosome morphology, indicating potential cytotoxicity. STEM-EDS was therefore performed on these particles after 24 h incubation to determine if the zinc had been released from inside the particles. However, it is clear from Figure 7.6 that at least some of the zinc is still present inside the particles (STEM-EDS Area 1). The dark spots located outside the

particles represent the presence of a heavy element, although STEM-EDS (Area 2) confirmed that this was likely to be iron (as opposed to zinc released from the particles). Iron is a naturally occurring element in cells, present in iron-containing proteins. STEM-EDS was also performed on an area within the cytoplasm as a control. The spectrum is shown in Appendix 1 and does not show traces of any Si or Zn.

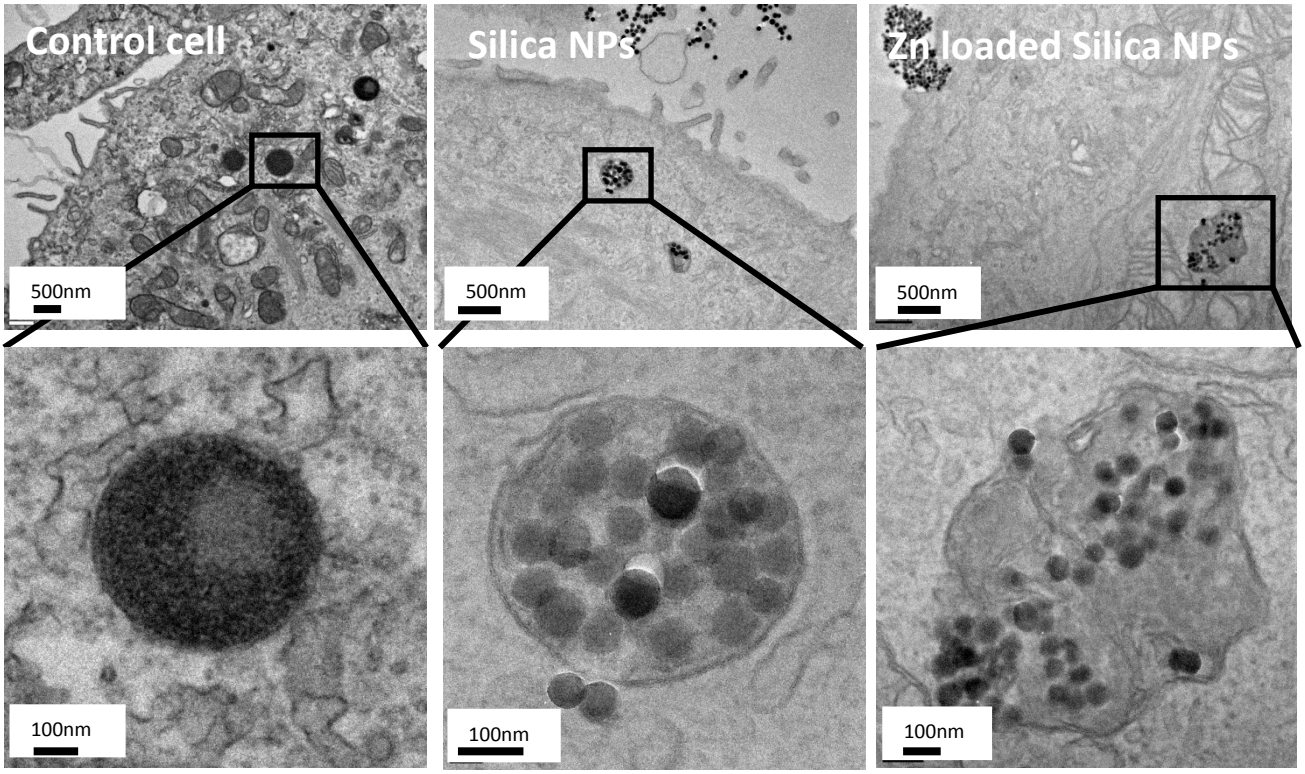


Figure 7.5- TEM images of 100Si and 11Zn nanoparticles found in a lysosome of a MCF-7 cell after 24 h exposure. The lysosome in a control cell is also shown. (Courtesy of Dr Shu Chen). Unlike the pure silica particles, the zinc containing particles appear to affect the morphology of the lysosome.

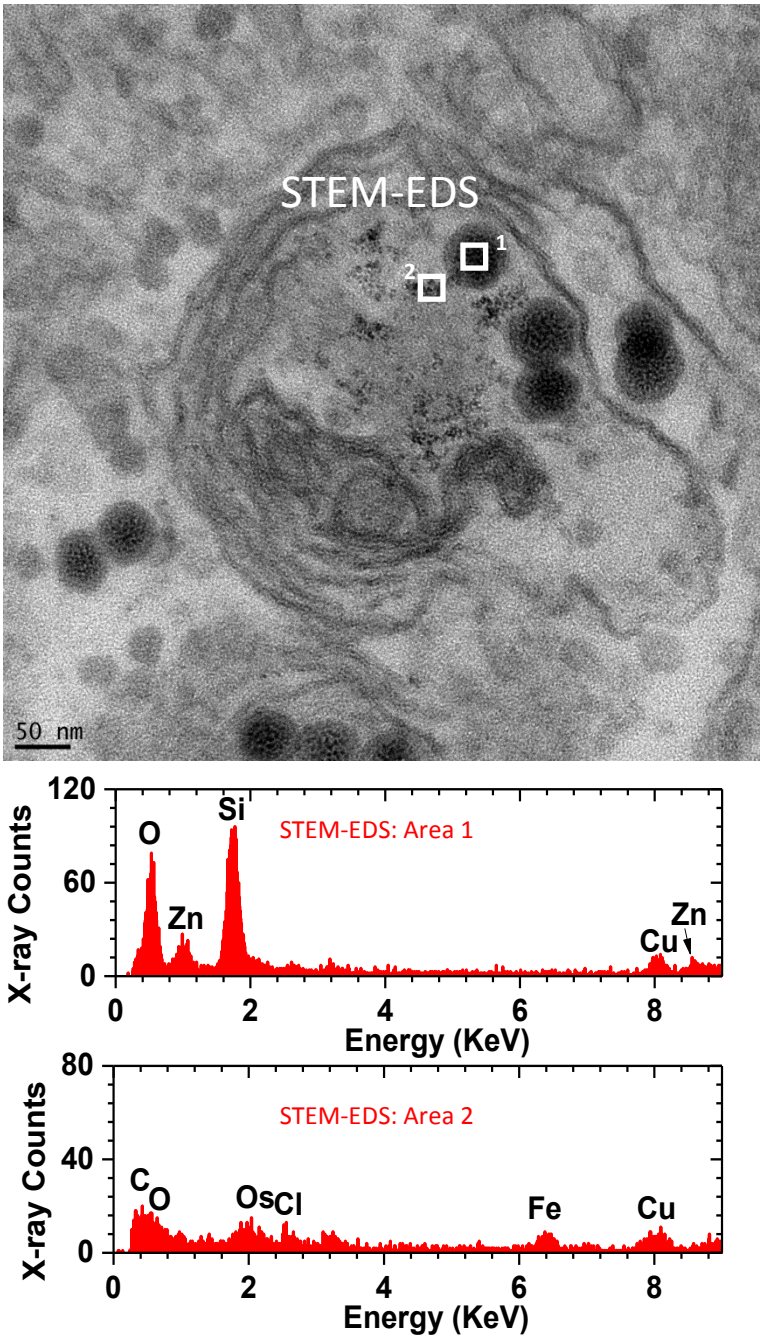


Figure 7.6 - TEM images of dense 80 nm 11Zn particles internalised by an MCF-7 cell after 24 h exposure at a concentration of 50 µg.ml^{-1}. STEM-EDS results show that zinc is still present inside the particles (area 1), although is not present outside the particles (area 2). (Courtesy of Dr Shu Chen).

Cell uptake studies were also performed on mesoporous silica and mesoporous 14Zn nanoparticles. The particles were imaged after 24 h to observe any changes in morphology. The results are shown in Figure 7.7. Whilst the 100Si MSNs remained intact, the 14Zn MSNs were seen to hollow out. Additionally, STEM-EDS confirms the lack of any Zn remaining inside the particles. This increased degradation of the Zn containing particles, in comparison to 100Si particles, is evidence that zinc is entering and breaking up the silica network. Hollowing out has previously been seen for calcium containing bioactive glass particles inside hMSCs [82], implying that a similar degradation mechanism

could be occurring here. The remaining silica rich shell is also consistent with the kinetic mechanism of bioactivity in bioactive glasses [27], previously described in Section 2.1.2. These findings support the theory that these particles could be used to deliver Zn^{2+} ions intracellularly for therapeutic applications.

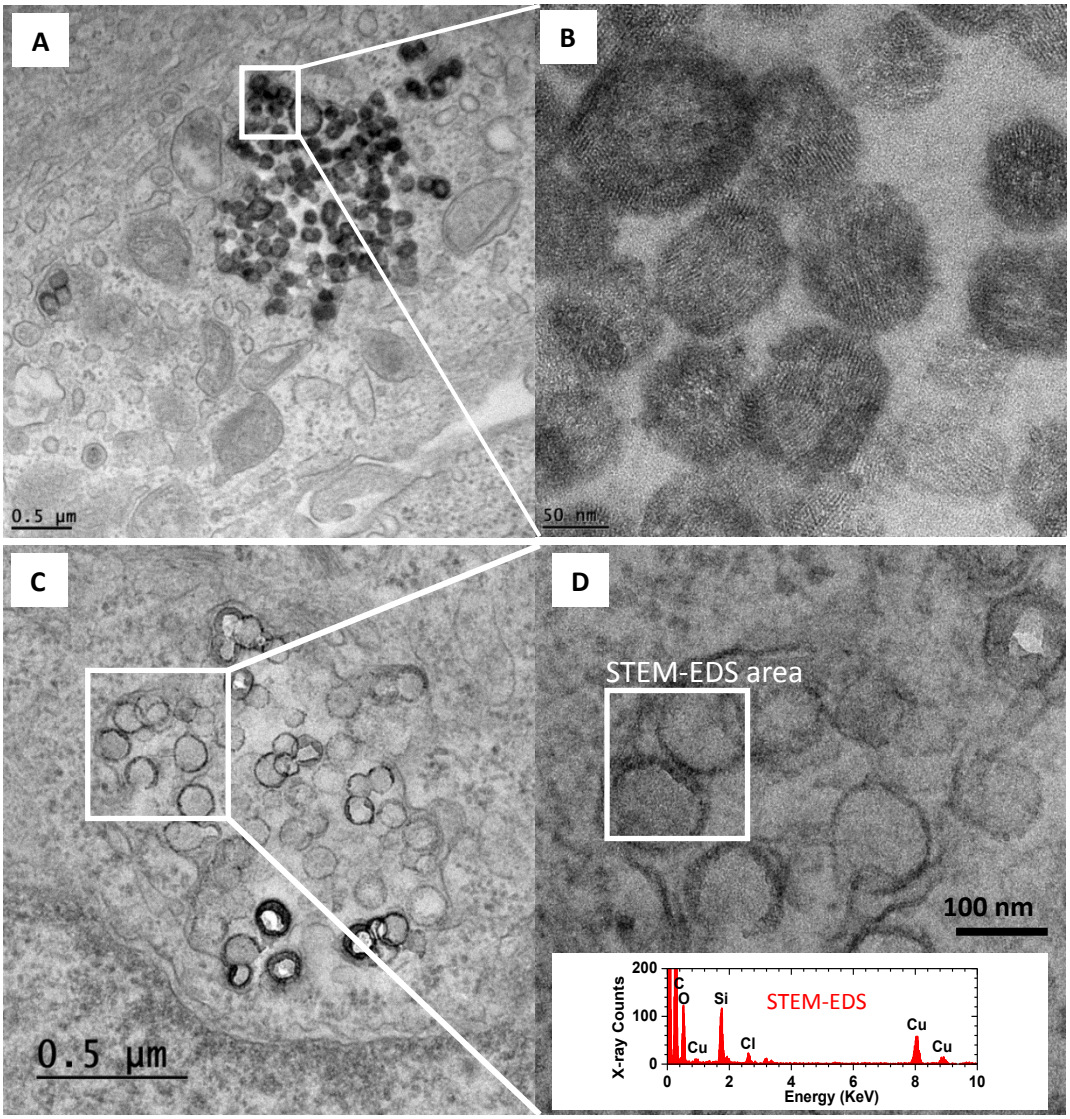


Figure 7.7- TEM images after 24 h exposure of A,B) Mesoporous 100Si particles inside an MCF-10a cell (low and high mag) and C,D) Mesoporous 14Zn particles inside an MCF-7 cell (low and high mag). An area of STEM-EDS showing the absence of zinc is also shown (courtesy of Dr Shu Chen).

7.3.2 Particle toxicity

Cell uptake experiments of SiO_2-ZnO nanoparticles have demonstrated that both dense and mesoporous particles are internalised by cells and found within lysosomes. It has subsequently been observed that the dense 11Zn particles have resulted in altered lysosome morphology, suggesting potential toxicity. Additionally mesoporous 14Zn particles have been shown to hollow out releasing

toxic Zn^{2+} ions. Cell viability experiments were therefore performed as described in section 7.2.1.3 using a WST-1 colorimetric assay to determine the cytotoxicity of the particles.

There have been many investigations into the toxicity of ZnO nanostructures (including nanoparticles) on mammalian cells [76], with toxicity most often being linked to oxidative stress. However, the mechanism by which this occurs is still improperly understood. It is recently recognised that the toxicity of ZnO nanoparticles is due to dissolution and release of Zn^{2+} ions which disrupts cellular zinc homeostasis leading to mitochondrial and lysosomal damage and subsequently cell death [12]. To verify this hypothesis two lines of TNBC cells (MCF-7 and MDA-MB-231) were exposed to varying concentrations of Zn^{2+} ions (from $Zn(NO_3)_2$). Experiments were also carried out using 100Si nanoparticles as a control (as these have been shown to be non-cytotoxic).

Results from a WST-1 assay showing cell viability of the two types of breast cancer cell exposed to Zn^{2+} ions, dense 80 nm 100Si nanoparticles and dense 80 nm 11Zn particles, are plotted in Figure 7.8. A cell viability of greater than 80% is taken to represent no significant toxicity.

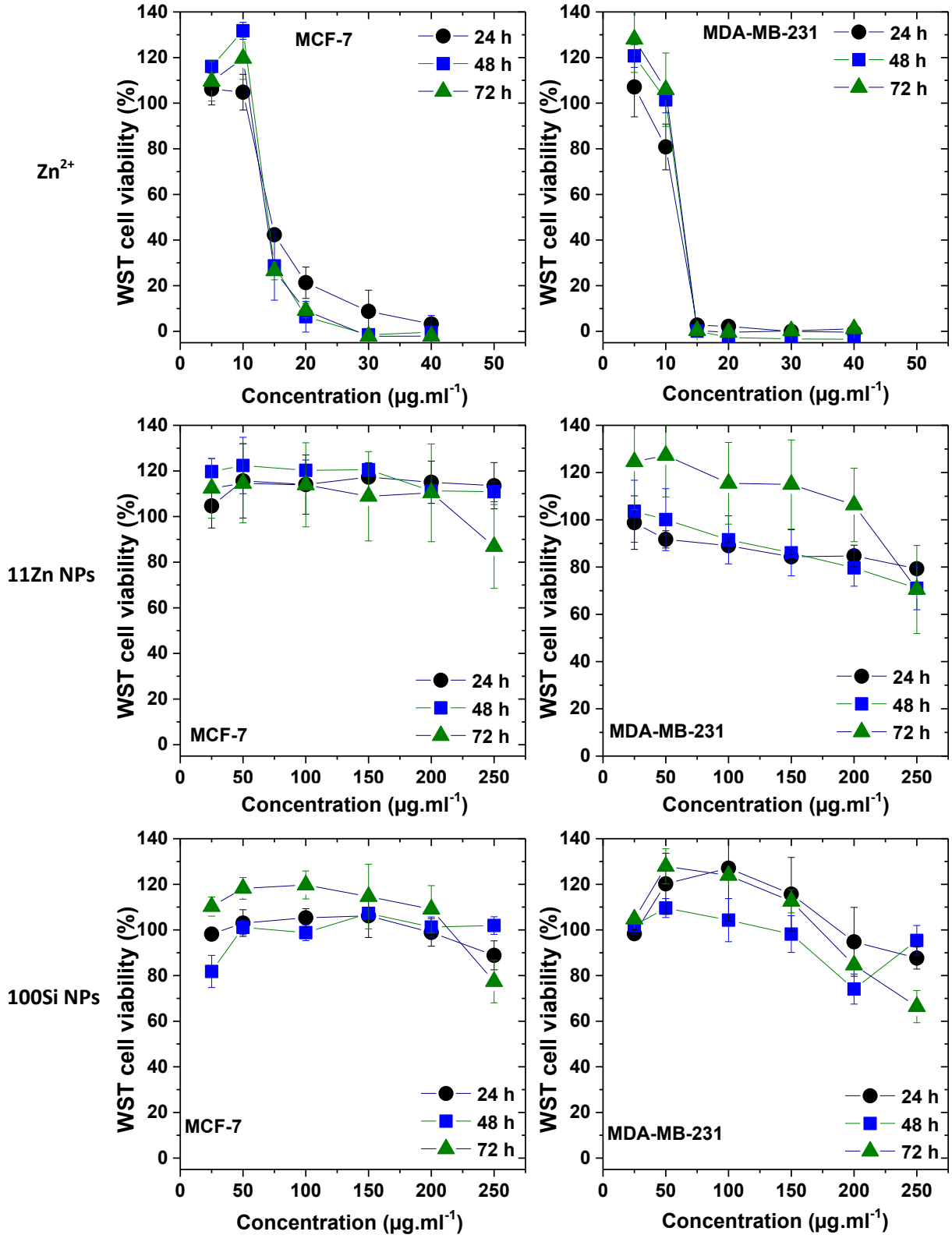


Figure 7.8 - Cell viability assay (WST-1) results for MCF-7 and MDA-MB-231 cell lines exposed for 24, 48 and 72 h with Zn^{2+} ions (from $Zn(NO_3)_2$), 11Zn NPs and 100Si NPs of 80 nm at concentrations 25 - 250 µg.ml^{-1} (n=3) (courtesy of Dr Shu Chen).

Figure 7.8 shows that a concentration of only 15 µg.ml^{-1} of Zn^{2+} ions is highly toxic to the both strains of cancer cells after 24 h. The 100Si NP control, on the other hand, shows no significant toxicity to either cell line, as expected, apart from at extremely high concentrations > 200 µg.ml^{-1} which are not suitable for *in vivo* use. It is therefore predicted that the 11Zn particles will not cause toxicity unless they are releasing sufficient quantities of Zn^{2+} ions into the cells. However, the same trend is observed as for the 100Si particles, with the particles only causing significant toxicity at concentrations greater than 200 µg.ml^{-1}. Thus, it is concluded that insufficient zinc is being released from the particles to result in cytotoxicity. This could be due to either premature release of zinc from the particles before uptake or the more likely scenario that the zinc is remaining inside the particles (as shown previously by STEM-EDS in Figure 7.6).

However, STEM-EDS of internalised mesoporous particles showed far more promising results. All of the zinc appeared to be released from the particles after 24 h. A WST-1 assay was therefore performed on TNBC cells exposed to the mesoporous sample 14Zn as well as a mesoporous 100Si sample as a control. A healthy cell line (MCF-10A) was also used to see if the particles could be used to kill cancer cells preferentially. The results after 24 h exposure are shown in Figure 7.9.

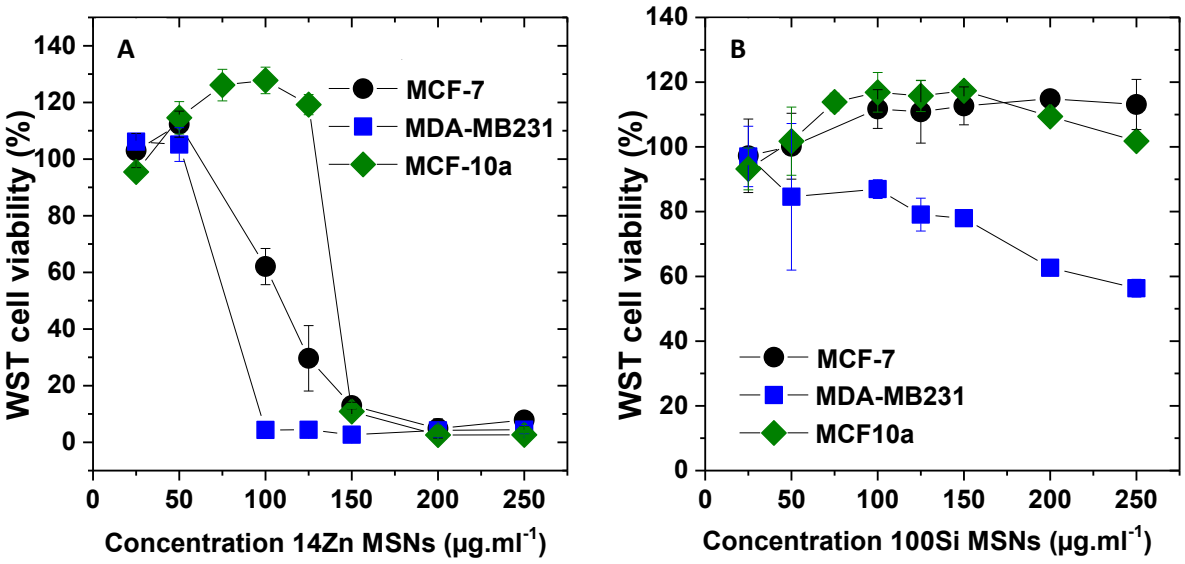


Figure 7.9 - Cell viability assay (WST-1) results for MCF-7, MDA-MB-231 and MCF-10A cell lines exposed for 24 h to A) 14Zn MSNs and B) 100Si MSNs of 80nm at concentrations 25 - 250 µg.ml^{-1} (courtesy of Dr Shu Chen).

It can be seen from Figure 7.9B that after 24 h, the mesoporous silica particles, as previously seen, caused no toxicity in healthy cells [46,68] or MCF-7 cells, and only caused significant toxicity in MDA-MB231 cells at high concentrations. The zinc loaded mesoporous nanoparticles however, caused

significant toxicity in all cell types as particle concentration was increased to 150 μg.ml^{-1}. 14Zn MSNs were most toxic to MDA-MB231 cells, which is expected due to the fact that these are the most aggressive type of metastatic breast cancer cells and therefore metabolise fastest resulting in increased metabolism of toxic Zn^{2+} ions. At 100 and 125 μg.ml^{-1} however, the particles were also toxic to MCF-7 cells, whilst having no negative effect on healthy MCF-10A cells. This could be due to faster metabolism in cancer cells resulting in increased uptake of particles and increased metabolism of toxic Zn^{2+} ions, or due the acidic cancer microenvironment resulting in higher zinc release [50]. It is not possible to tell from this study whether Zn^{2+} ions are released in the acidic microenvironment of the cancer cells before uptake, or within the cells after particles internalisation. However, both are effective mechanisms for localised ion release and the end result achieved here is the death of cancer cells. Another theory for preferential toxicity of zinc in cancer cells is the fact that cancer cells have been shown to exhibit zinc depletion, suggesting that they may be able to withstand a lower zinc concentration than healthy cells [78]. Our finding suggest that by careful concentration selection, zinc loaded MSNs could potentially be used to selectively treat breast cancer by relying on increased uptake into cancer tissue due to the EPR effect and preferential toxicity to cancer cells without the need for active targeting.

7.3.3 Particle degradation

Ion dissolution studies were performed on dense and mesoporous 100Si particles, as well as those doped with Zn and Ca to try and understand the mechanisms of particle degradation. Degradation studies were performed as decribed in section 7.2.2, in ALF (pH 4.5), MEM (pH 7.6) and MEM + FBS (pH 7.7) in order to mimic the both the lysosomal environment after particle uptake and the extracelluar environment in cell studies. The ICP results are shown in Figure 7.10, Figure 7.11 and Figure 7.12 respectively. In order to gain a better understanding of particle degradation, the particles were removed from solution after 24 h, washed, and imaged on TEM to observe any changes in morphology. The results are shown in Table 7.3. (STEM-EDS performed on particles after dissolution is shown in Appendix 2)

This discussion will first examine the results for SiO_2-ZnO particles with reference to the cell studies. The results for SiO_2-CaO particles will then be considered in relation to their bioactivity and potential application for incorporation into a nano-composites for bone regeneration. Finally comparisons will be made between all particles and conclusions on the mechanisms of particle incorporation will be drawn.

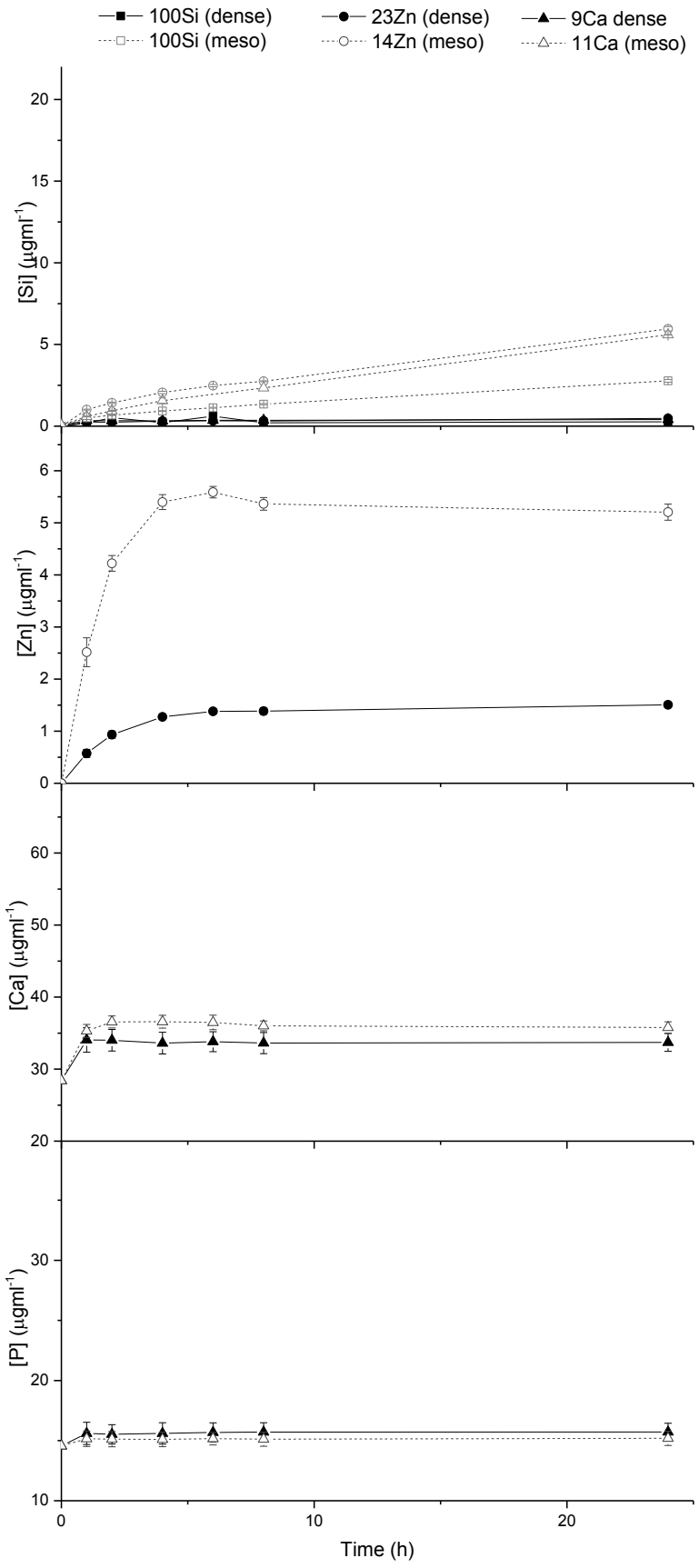


Figure 7.10 - Ion release profiles for particles over 24 h in ALF.

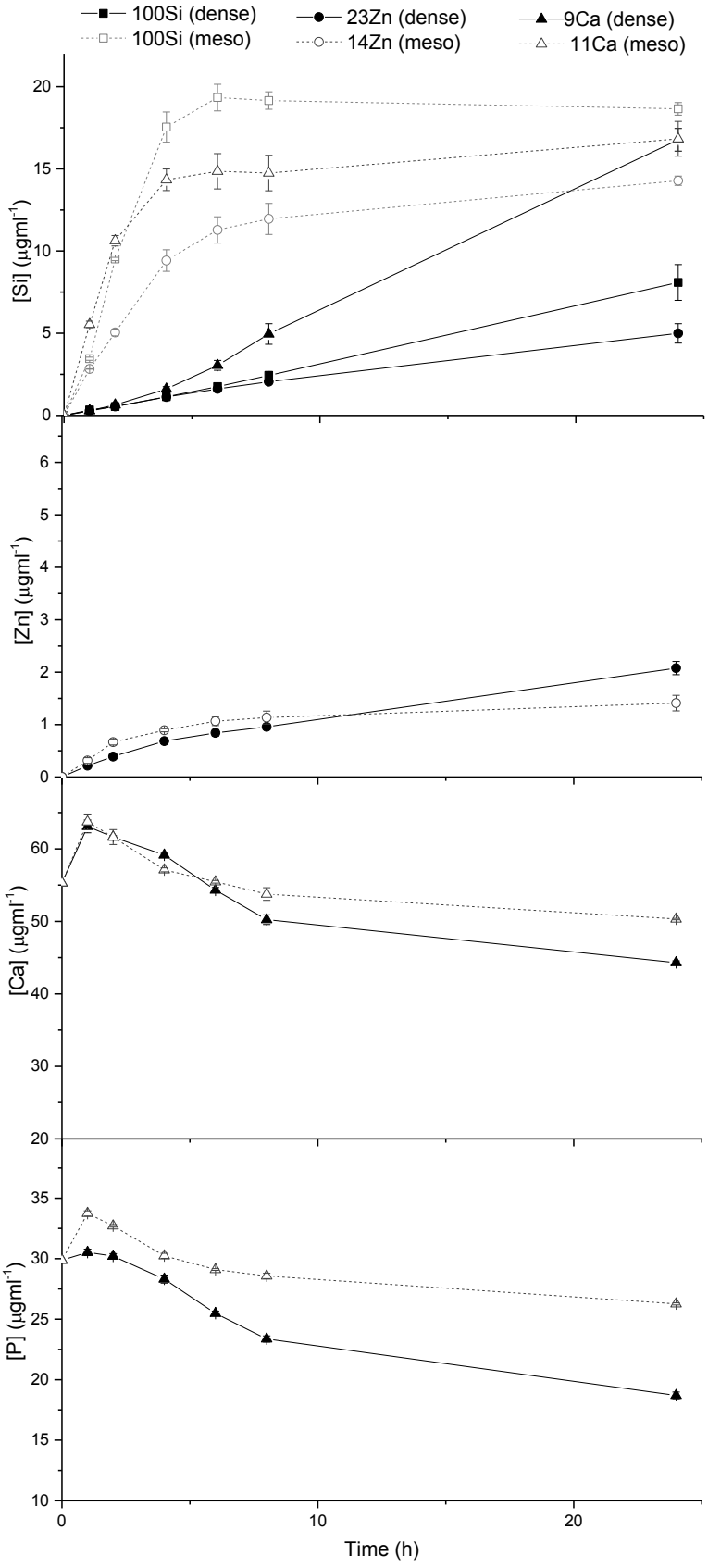


Figure 7.11 - Ion release profiles for particles over 24 h in MEM.

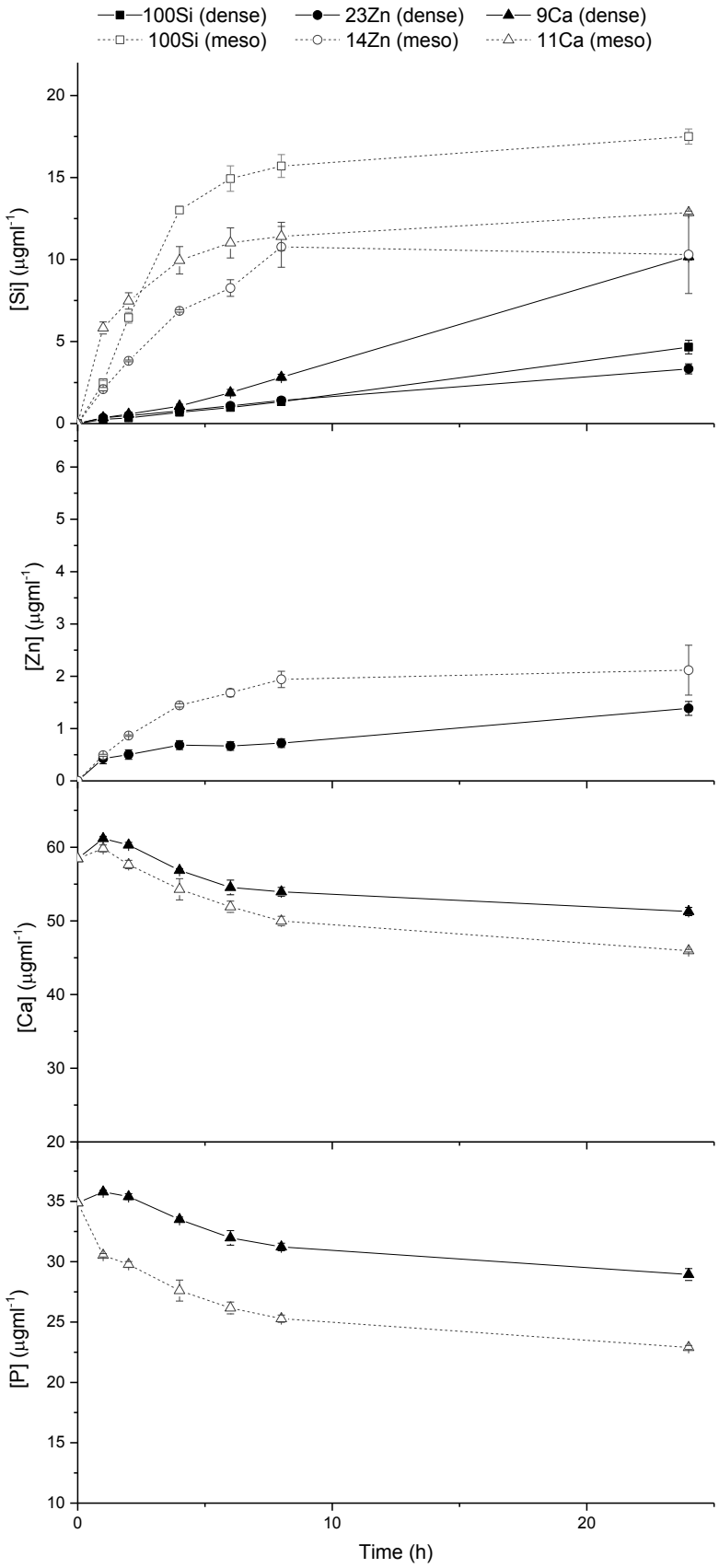
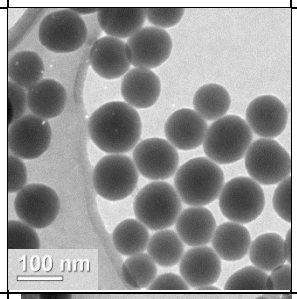
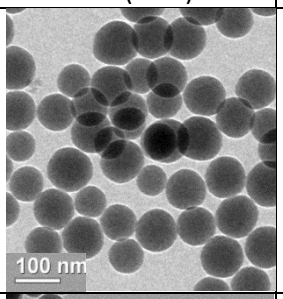
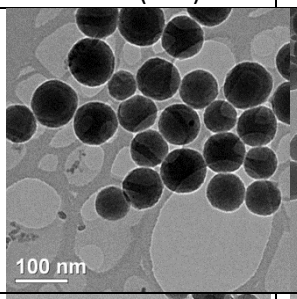
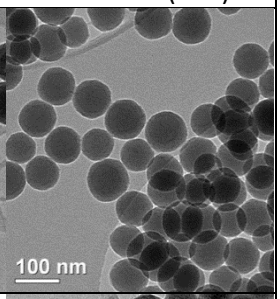
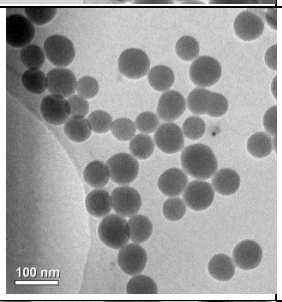
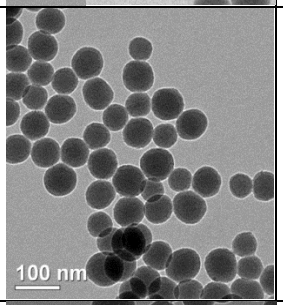
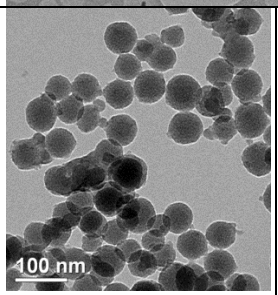
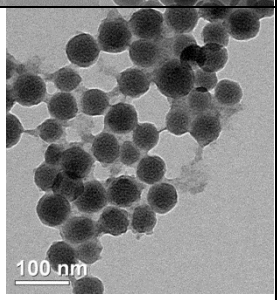
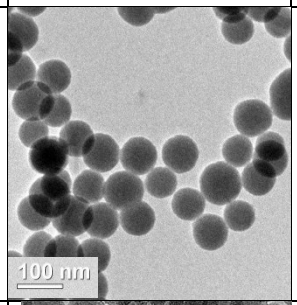
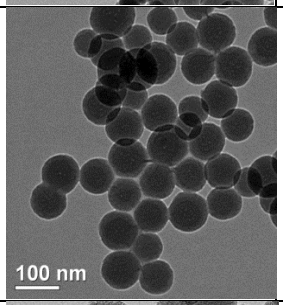
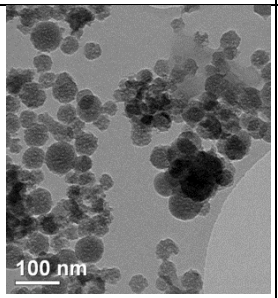
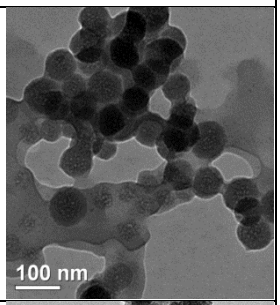
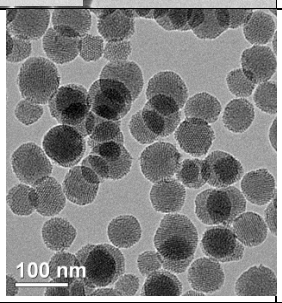
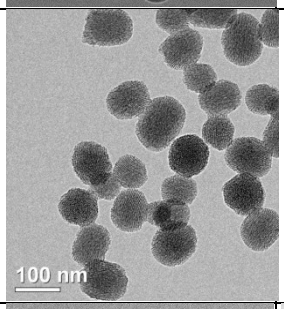
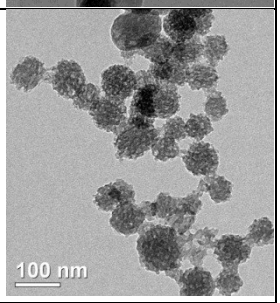
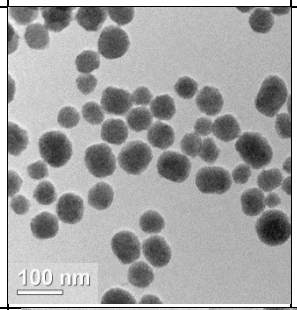
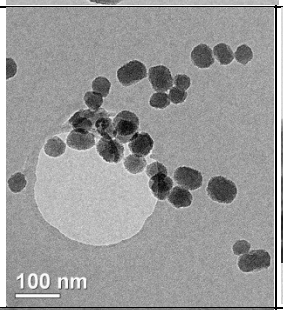
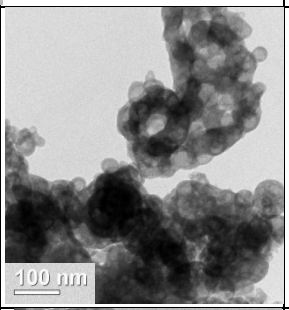
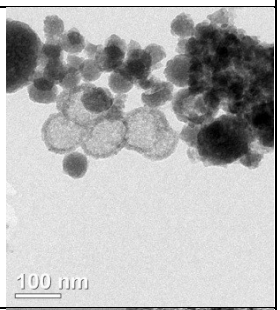
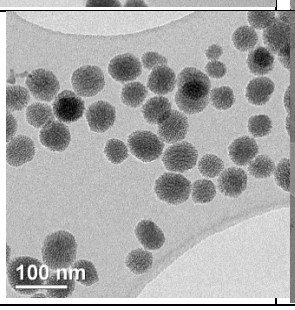
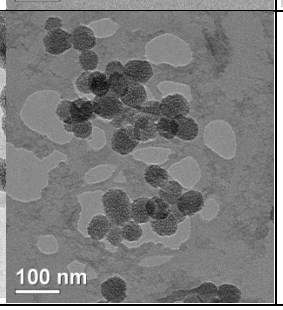
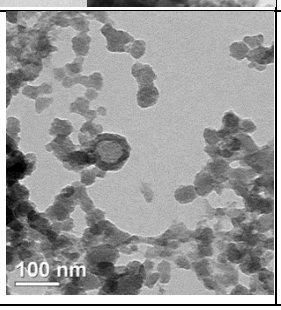
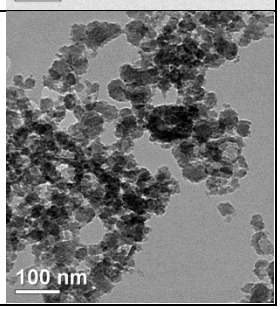


Figure 7.12- Ion release profiles for particles over 24 h in MEM + FBS.

Table 7.3 - TEM images of particles before and after 24 h dissolution in ALF, MEM and MEM + FBS.

		Before dissolution	ALF (24 h)	MEM (24h)	MEM+FBS (24h)
Solid particles	100Si				
	23Zn				
	9Ca				
Mesoporous particles	100Si			*Could not be retrieved by centrifugation, suggesting significant degradation*	
	14Zn				
	11Ca				

Looking at the ICP results for SiO_2-ZnO particles, it suggests that significant zinc release only occurs from the mesoporous particles in ALF (Figure 7.10). STEM-EDS of these particles after 24 h dissolution also confirms that no zinc can be detected inside the particles. This corresponds to the results of the cell viability studies which show toxicity was only caused by the mesoporous particles. Additionally it suggests that this toxicity is a result of zinc release from the particles at acidic pH. TEM images of the zinc-containing particles after dissolution show minimal alteration to the morphology of the dense particles after 24 h in all solutions, which supports the TEM images of these particles seen in cells. However, whilst the mesoporous particles appear to remain intact in ALF, there are many precipitates observed in cell culture media. One of the disadvantages of ICP is that it can only measure the concentrations of elements present in the solution. It can therefore not account for any ions that have been released and subsequently re-precipitated before escaping from the dialysis tubing. Examination of these precipitates by STEM-EDS shows them to contain Zn, Ca, P and even some Mg (Appendix 2). This suggests that the levels of zinc release suggested by ICP are artificially low and that that the majority of particles have in fact degraded significantly. However, at neutral pH the Zn^{2+} ions have subsequently re-precipitated with elements found in cell culture media.

One major concern for many current drug delivery systems for cancer treatment, including MSNs, is premature release of anticancer drugs upon administration [70]. The same could occur here if zinc is released from the particles prior to uptake by cancerous cells. However, it has previously been observed that the toxic effects of Zn^{2+} ions are prevented by the presence of culture medium [42]. These results suggest that this decrease in toxicity is likely to be due to the re-precipitation of toxic zinc ions to form precipitates at neutral pH. Therefore, it is hypothesised that these particles will only cause toxicity if the zinc is released either in the acidic environment of a tumour or within the lysosome of a cell after internalisation. The lack of precipitates observed in the cells by TEM suggests that these particles have been internalised before they start to degrade in cell culture media (while any particles not internalised would have been washed away in sample preparation before imaging). However, *in vivo* it would therefore be required for the particles to reach the tumour site quickly before this degradation occurs, suggesting that active targeting mechanisms may be desirable.

Looking at the ICP results for SiO_2-CaO particles, it can be seen that in ALF both the dense and mesoporous calcium containing particles release 5.7 and 6.9 $\mu g.ml^{-1}$ of Ca ions within the first hour, corresponding to 95 and 97% of the total Ca in the particles respectively. In MEM, the calcium containing particles also release 100% of their calcium within the first hour. This is due to the cation exchange between Ca^{2+} from the particles and H^+ ions from the solution. However, over the period of the study the calcium levels then reduce in line with phosphorous levels, suggesting the

precipitation of calcium ions and formation of calcium phosphate precipitates (backed up by TEM and STEM-EDS analysis, Appendix 2). For Ca containing particles in MEM + FBS, there was no significant release of calcium detected, although the dramatic decrease in phosphorous levels for mesoporous particles could be indicative of burst release of Ca and precipitation before the 1 hour time-point. Formation of HCA (indicated by the precipitation of Ca and P ions from the media) is desirable for bone regeneration applications and is a good indicator of bioactivity. A burst release, as seen here however, is not usually beneficial and sustained release is preferred. A sudden increase in Ca^{2+} ions can cause an increase in local pH and result in cytotoxicity, however, no such increase in pH was detected here. Additionally, when incorporated into a nano-composite, only the particles on the surface in contact with body fluids will release calcium, therefore as the polymer network degrades and more particles are exposed, sustained release of calcium could be achieved.

Aside from increased bioactivity, another advantage of incorporating bioactive glass nanoparticles into nano-composites would be to improve the mechanical properties. TEM images of the particles after 24 h show huge amounts of degradation of the calcium containing mesoporous particles at neutral pH in comparison to their dense counterparts. Whilst ion release is desirable for bioactivity, such rapid degradation is likely to result in a breakdown of the composite at the nanoparticle-polymer interface causing a subsequent loss in mechanical strength of the scaffolds. Dense particles are therefore likely to be preferable for incorporation into nano-composites as they are more likely to retain their structure as they degrade, resulting in sustained mechanical strength of the scaffold. However, in order to confirm these hypotheses, dissolution studies would have to be performed on nano-composite scaffolds in solution.

By comparing the results of these degradation studies, it is also possible to infer information about the mechanisms of cation incorporation for both dense and mesoporous particles and the affects that both zinc and calcium have on the silica network. It is clear from the ion release profiles for silica that in all cases, as expected, the mesoporous particles degraded significantly faster than their dense counterparts. In ALF, the release of silica is considerably lower than in cell culture media and for dense particles there is apparently negligible degradation. This is due to the fact that a higher pH promotes the breaking of Si-O-Si bonds. The mesoporous particles also followed a more linear release profile in ALF. Conversely in MEM and MEM + FBS, the dense particles appeared to release silica at a steady rate, while the mesoporous particles gave a burst release of silica in the first 4 h, before levelling off between 10 and 20 $\mu g.ml^{-1}$. For mesoporous particles in cell culture media, the addition of cations (especially zinc) appears to reduce the degradation of silica, while in ALF the reverse is observed and degradation is accelerated. For dense particles in cell culture media the

addition of zinc results in a slight decrease in silica release, whereas calcium significantly accelerates silica release to levels equivalent to the mesoporous particles after 24 h.

The different degradation patterns seen here in the zinc and calcium containing particles are likely to be indicative of the different roles played by each ion in the glass network as described previously. Significant zinc release is only observed from mesoporous particles in ALF. A burst release is seen over the first 4 h to a maximum of 5.6 $\mu g.ml^{-1}$, corresponding to 36.9% of the total Zn present within the nanoparticles. In contrast to this, in ALF and MEM, both the dense and mesoporous calcium containing particles release between 95 and 100% of their calcium within the first hour. The burst release of calcium from the particles suggests that it is incorporated purely as a network modifier, as predicted. However, the lower levels of Zn released at neutral pH and its apparent stabilising effect on the silica network, back up the theory that Zn is incorporated as both a network modifier and a network former. Chen *et al.*[19] studied the dissolution of Zn containing bioactive glasses in Tris buffer (pH 7.35) and acetic acid/sodium acetate buffer (pH 4.5). At neutral pH, they observed very low levels of Zn released (<10%) as seen here, suggesting that Zn is entering the network as a network former resulting in the formation of Si-O-Zn bonds. Conversely, at pH 4.5 they observed both Zn and Si release to increase linearly with Zn content (as seen for mesoporous particles here), implying that Si-O-Zn bonds are acid hydrolysable in a similar fashion to Si-O-Al bonds.

Whilst a significant release of Zn was observed from the mesoporous particles at an acidic pH which would back up this theory, we do not see the same trend for the dense particles, suggesting an alternative mechanism of incorporation/degradation. It is hypothesised that the nano-crystals of $ZnSiO_4$ previously observed in the 23Zn dense particles (Chapter 4) do not degrade and therefore result in low release of Zn from the dense particles. This theory was supported by HRTEM and STEM-HAADF/EDS. Dark field TEM images (Figure 7.13) of dense 11Zn particles inside cells, show the presence of small dense nano-crystals still within the particles.

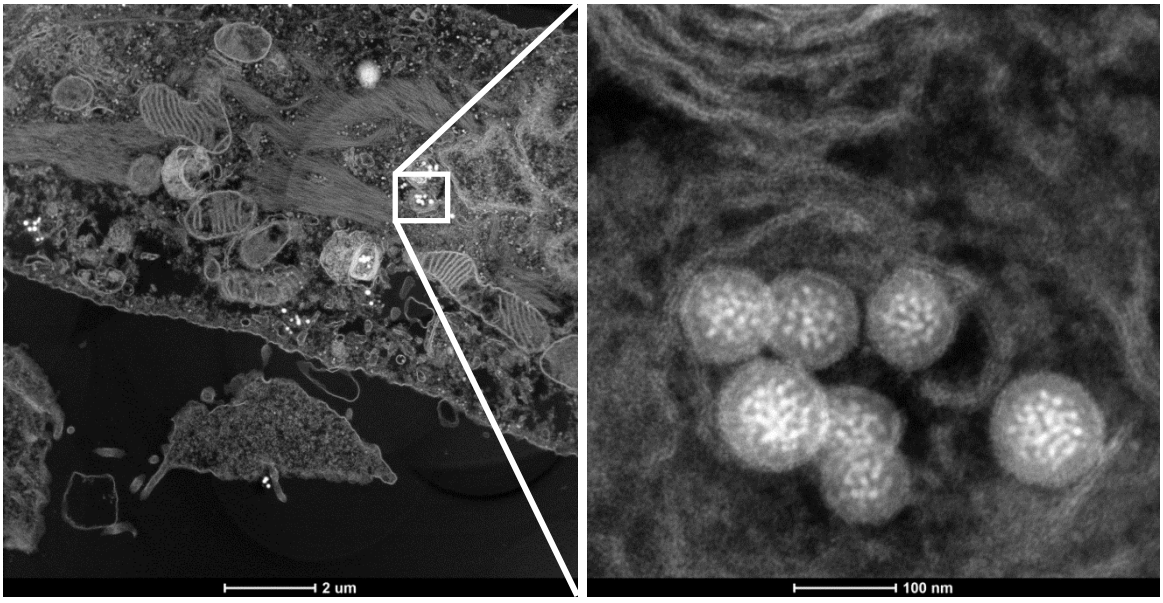


Figure 7.13 - Dark field TEM images of MCF-7 cell showing internalised dense 80 nm 11Zn NPs particles after 24 h exposure at a concentration of 50 µg.ml^{-1} (courtesy of Dr Shu Chen).

Looking at the morphology of the particles after the degradation study (Table 7.3) it can be seen for the dense 100Si particles that the morphology was unchanged after 24 h in all media. This is in agreement with ICP data. For the mesoporous silica particles, on the other hand, although very little change is observed in ALF, there was significant degradation and opening up of the mesoporous structure in MEM + FBS. Degradation occurred from both the outer as well as the inner surfaces, as seen by Yolanda *et al.* who investigated the degradation of mesoporous silica nanoparticles in phosphate buffer saline (PBS) [203]. The particles in MEM alone could not be retrieved by centrifugation, suggesting more significant degradation (supported by ICP). These observations are likely to be due to the increasing solubility of silica with increasing pH. The proteins in FBS could also be forming a protein corona around the particles (as suggested by zeta potential results), which may slow degradation.

For all particles in ALF there was little noticeable degradation suggesting that the silica network still remained largely intact under acidic conditions. However, in MEM there was far more noticeable degradation of the dense calcium containing particles compared to dense zinc containing particles, suggesting that Zn may be acting as a network former and strengthening the silica network by the formation of stable Si-O-Zn bonds, while once the modifying Ca^{2+} ions were released, the silica network begins to degrade more rapidly at the higher pH (as seen by ICP). All mesoporous particles degraded more rapidly in cell culture media and underwent significant changes in morphology. For the zinc containing mesoporous particles, a few areas of intact particles were found (more in MEM + FBS, due to the formation of a protective protein corona) and these were also examined by STEM-EDS. Unlike in ALF, they still contained zinc, suggesting that at neutral pH the zinc was only released

as the silica network degraded. These findings agree with the earlier hypothesis zinc is at least partially incorporated as a network former and that Si-O-Zn bonds are hydrolysable only in an acidic environment.

7.4 Conclusions

In this chapter, the particles produced (of 80-100 nm) were readily internalised by cells, where they were located both within endosomes/lysosomes and also as individual particles within the cytoplasm (having escaped from the endosomal pathway). Both zeta potential and degradation experiments, showing an alteration in surface charge and reduced degradation of particles in MEM with added FBS, are indicative of the formation of a protein corona around the particles.

For the zinc containing particles, high quantities of Zn^{2+} ions were not seen to be released by dense particles, resulting in no cytotoxicity. It was therefore decided that dense zinc-containing bioactive glass nanoparticles made in this way were not likely to be suitable for therapeutic applications. However, SiO_2-ZnO mesoporous particles were seen to release high quantities of zinc both in ALF and within cells. The results of cell viability studies indicated preferential cytotoxicity in cancer cells, suggesting that that these particles could therefore provide a promising method for cancer treatment by localised ion release.

Dissolution studies showed calcium and silica release from both dense and mesoporous SiO_2-CaO nanoparticles, and precipitation of calcium phosphates, suggesting good bioactivity of these particles. However, fast degradation of the mesoporous particles indicates that dense particles may be preferable for incorporation into nano-composites due to their sustained ion release and steady degradation at neutral pH which is likely to result in maintained mechanical strength of the scaffolds.

Degradation experiments also confirm the different incorporation mechanisms for zinc and calcium as discussed previously. While calcium is incorporated as a network modifier, zinc can also be incorporated as a network former, forming acid hydrolysable Si-O-Zn bonds.

8 Functionalisation of particles and incorporation into nano-composites

8.1 Introduction

In previous chapters it has been shown that it is possible to produce monodispersed silica nanoparticles of controlled size (ranging from 50-500 nm) and subsequently to incorporate Zn and Ca cations. There are two main motivations behind the desire to functionalise these particles in this chapter:

1. For incorporation into nano-composite scaffolds for bone regeneration, enabling bonding of the particles to the polymer matrix;
2. For modification of the surface charge to allow for control over particle uptake into cells.

Stöber particles are naturally covered with OH groups and therefore possess a negative charge. This chapter will focus on functionalisation using APTES to produce a positively charged amine covering on the nanoparticle surface. NH_2 groups can subsequently react with -COOH groups on polymer chains to form a nano-composite material with covalent coupling between the nanoparticles and the polymer. This is critical to enable control of degradation rate and to maximise mechanical properties. Work will be presented on the synthesis of a nanoparticle-alginate composite to demonstrate the potential for these functionalised nanoparticles to be incorporated in to scaffolds for bone regeneration.

As discussed previously, the size of particles is critical in determining particle uptake and fate within the cells. However, surface charge has also been shown to be equally important [46-48]. Recently, amine functionalised MSNs have been shown to have higher cell uptake by the human squamous cell carcinoma cell line (SCC25) compared to negatively charged particles, due to the electrostatic interaction between the positively charged particles and the negatively charged cancer cells [204]. Similar anticancer activity was also exhibited. Functionalisation with different chemical groups could also allow for subsequent attachment of peptides for potential cell targeting if necessary.

8.2 Materials and methods

Bioactive glass nanoparticles were synthesised as previously described (in Chapter 5) prior to functionalisation.

8.2.1 Functionalisation

A functionalisation procedure for the attachment of amine groups to the surface of the nanoparticles was adapted from a method used by Zelikin *et al.* [146]. Functionalisation was performed in a non-aqueous, basic environment in order to prevent release of cations from the nanoparticles. After calcination and washing, 50 mg of particles were dispersed in 10 ml of ethanol (ethyl alcohol, ≥99.5%) in an ultrasonication bath. 500 µl of ammonium hydroxide (ACS reagent, 28.0-30.0% NH_3 basis) and 2 ml APTES were subsequently added to the suspension and it was left to mix overnight at 37˚C before retrieval of the particles by centrifugation. The particles were then washed three times in ethanol to remove any unreacted APTES before characterisation.

8.2.2 Fluorescein Coupling

Fluorescein isothiocyanate (FITC) molecules were coupled to the amine functionalised nanoparticles through a reaction between the surface $–NH_2$ groups on the nanoparticles and the –N=C=S groups on the FITC molecules. A method was adapted from Xu *et al*.[143]. 20 mg FITC was dissolved in 20 ml absolute ethanol and 20 mg of amine functionalised nanoparticles were added to the solution. The solution was sonicated to ensure that the nanoparticles were fully dispersed before mixing at room temperature for 16 h in a dark environment. The fluorescent labelled particles were recovered by centrifugation and washed twice in ethanol and once in distilled water to remove any unreacted FITC.

8.2.3 Particle characterisation

After functionalisation, the particles were imaged using TEM (as described in section 4.2.2) to determine any effect on particle morphology. The success of functionalisation was also investigated by both FTIR (collected on the PerkinElmer Spectrum™ 100 FTIR spectrometer, in the range of 400 - 4000 cm^{-1}) and zeta potential (Malvern instrument 2000). For zeta potential measurements, samples were first dispersed in distilled water and sonicated for 15 minutes in order to break up any aggregates.

The success of functionalisation was further investigated by the optical and fluorescent imaging of particles coupled with the fluorescent dye FITC. An Olympus IX71 digital wide-field fluorescence microscope was used and images were taken on a 60x oil immersion objective with help from Dr Rona Chandrawati.

8.2.4 NP-Alginate nano-composite synthesis

The aim of nanoparticle functionalisation with APTES was to allow for incorporation of the bioactive glass nanoparticles into a nano-composite material for bone regeneration applications by subsequent reaction with –COOH groups on polymer chains using carbodiimide chemistry. As proof

of this hypothesis, functionalised particles were incorporated into a NP-Alginate nano-composite. This work was done by Dr Yuliya Vueva.

Alginate bio-nanoglass composite hybrids were fabricated by dispersing 20 wt% APTES-functionalised nanoparticles in 15 ml dH_2O. Next, 0.45g sodium alginate (Mw = 12 - 40 kDa) was added at a concentration 30 $mg.ml^{-1}$ and mixed until completely dissolved (15-20 minutes). The carboxylic groups on the alginate were functionalised by the addition of EDC and NHS (in a molar ratio of alginate:EDC =1:2 and EDC:NHS = 2:1). The solution was left to mix for 15 min to activate the alginate carboxylic groups before adding APTES drop-wise (in a molar ratio of alginate:APTES 2:1). The solution was stirred until slight gelation, when it was 3D printed to form a scaffold.

Scaffolds were fabricated using an Ultimaker 3D printer with a 3 axis stage controlled by software Cura 13.06.4. The NP-alginate nano-composite ink with appropriate viscosity was extruded using a Harvard syringe pump at flow rate 0.12 $ml.min^{-1}$ and constant speed 550 $mm.s^{-1}$, through a 250 µm flexible polypropylene nozzle (EFD Nordson). 38-layer scaffolds were printed with distance between the struts ~ 1.5 mm, and overall dimension of approximately 1.2 cm × 1.2 cm × 0.6 cm. After printing, the scaffolds were frozen at –20 ^{o}C and freeze-dried for three days.

8.2.5 Nano-composite characterisation

3D printed scaffolds were imaged using SEM and TEM. For SEM analysis, a section of the scaffold was cut and attached to a metal SEM stub using carbon tape. The sample was then gold-coated using a sputter coater (Emitech K550) for 2 minutes at 25 µA. Imaging was performed on a JSM5610LV SEM in normal scanning mode, with an accelerating voltage of 5 kV. TEM analysis was performed by Dr Shu Chen. The scaffolds were progressively infiltrated with a Quetol-based resin, created by combining 8.75 g quetol, 13.75 g nonenyl succinic anhydride, 2.5 g methyl acid anhydride, and 0.62 g benzyl dimethylamine (all from Agar Scientifc). Samples were infiltrated in 50% resin/acetonitrile solution (volume ratio of resin to acetonitrile) for 2 h, followed by infiltration in a 75% resin/acetonitrile solution for 2 h, 100% resin for 2 h, and finally 100 % resin for another 2 h. Embedded samples were cured at 60˚C for 24 h. Thin sections (80 nm) were cut directly into a water bath using an ultramicrotome with a diamond knife with a wedge angle of 35˚. Sections were immediately collected on bare, 300 mesh copper TEM grids (Agar Scientifc), dried and kept under vacuum for TEM analysis. TEM analysis was carried out on the JEOL 2000 operated at 80 kV.

Uni-axial compression tests were performed using Zwick/Roell Z2.5 machine, with a load cell of 2 kN and compression extension speed 0.5 $mm.min^{-1}$. Square samples were prepared by 3D printing with dimension 5 mm × 5 mm × 5 mm (n=5).

8.3 Results & Discussion

8.3.1 Functionalisation

It was found that the age of the APTES reagent was critical in successfully functionalising nanoparticles. APTES < 2 months old was therefore used for all functionalisation experiments shown in this thesis. Figure 8.1 shows that the functionalisation of nanoparticles had no effect on the morphology, size or dispersity of nanoparticles. This was true for silica particles, those containing Ca and those containing Zn.

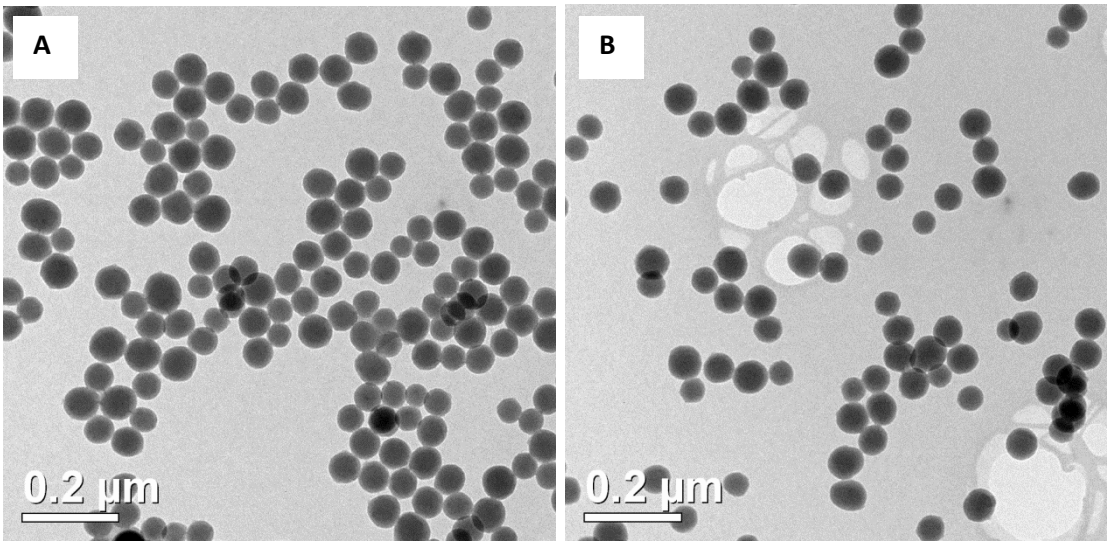


Figure 8.1 - TEM images showing morphology of SiO_2-ZnO bioactive glass nanoparticles (0.28M TEOS, 6MH_2O, 0.14M NH_4OH) A) Before functionalisation, B) After functionalisation with APTES.

Zeta potential measurements (Figure 8.2) were used to confirm that the functionalisation of particles had been successful. Unlike previously suggested [139], prior etching of the particle surface was not found to be necessary. It is predicted that the presence of ammonium hydroxide in the solution resulted in sufficient creation of -OH groups on the particle surface for successful functionalisation.

Before functionalisation, it would be expected that the nanoparticles should possess a negative zeta potential due to the presence of negatively charged –OH groups on the surface of the particles. If amine functionalisation is successful, the zeta potential after functionalisation should be positive due to the positively charged $–NH_2$ groups. Results are shown in Figure 8.2. The addition of Zn or Ca does not have a significant effect on the zeta potential of the particles, nor does the addition of cations affect the ability to functionalise the nanoparticles using this method. Before functionalisation the particles had a zeta potential of -32.9±5.3 mV, which shifts to +27.4±3.0 mV after functionalisation. As zeta potential values typically greater than +30mV or less than -30mV

suggest that the particles will repel each other [159], the nanoparticles are considered to be stable both before and after functionalisation.

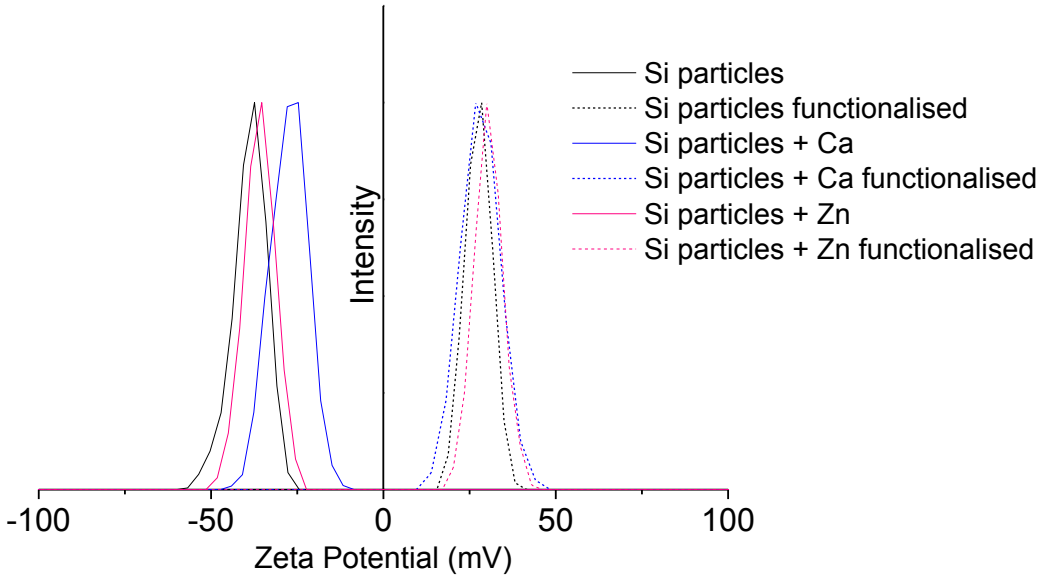


Figure 8.2 - Zeta potential measurements of bioactive glass nanoparticles before and after functionalisation with APTES.

FTIR was also performed on all samples both before and after functionalisation. The results for a sample of calcium containing nanoparticles (Figure 8.3) shows the appearance of peaks corresponding to bonds in APTES in the functionalised particles. The peak at 1390 cm^{-1} is assigned to N-H bonding in the amine groups and the peaks at 2900 cm^{-1} and 2975 cm^{-1} are assigned to C-H vibrations due to the presence of CH_2 groups in the APTES chain [138,141,142]. However, these peaks were not observed for all successfully functionalised particles (confirmed by positive zeta potential measurements). It was therefore concluded that FTIR was not sensitive enough to reliably detect the small numbers of $–NH_2$ groups on the surface of the nanoparticles and should not be used alone to test for functionalisation.

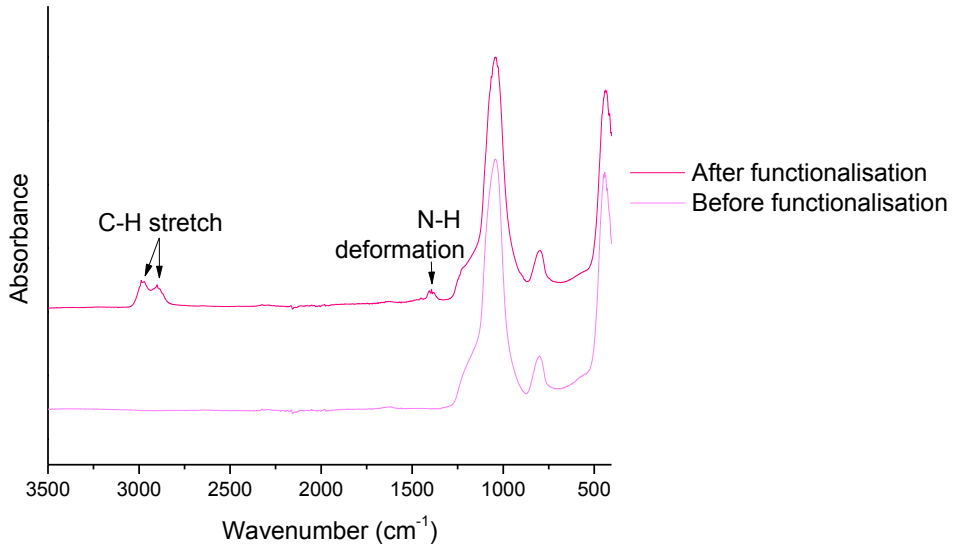


Figure 8.3 - FTIR results for 100nm SiO_2-CaO nanoparticles before and after functionalisation with APTES.

Additionally, nanoparticles were coupled with the fluorescent dye FITC to confirm amine functionalisation. Fluorescein experiments were performed as described in Section 8.2.2, using both functionalised and non-functionalised particles. As a secondary control, functionalised particles, without fluorescein coupling were also dispersed in ethanol for imaging. For this experiment particles of 500 nm were synthesised (0.28 M TEOS, 6 M H_2O, 0.57 M NH_4OH) so that small aggregations would be visible on an optical microscope. The presence of the FITC molecule should result in green fluorescence. The results are shown in Figure 8.4.

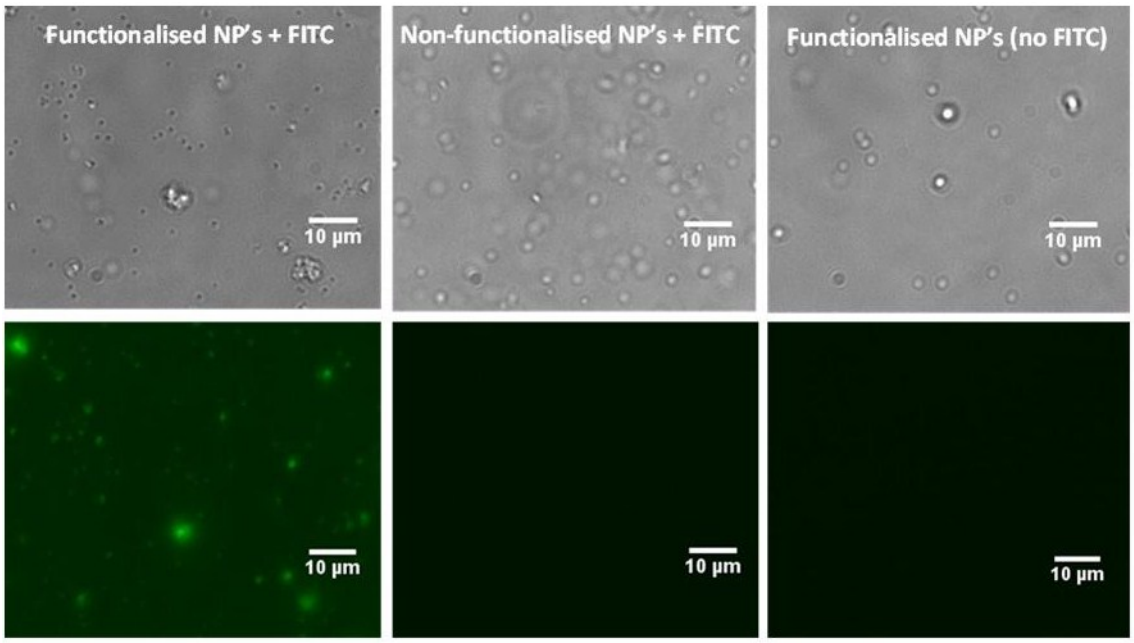


Figure 8.4 - Optical microscope images of functionalised NPs + FITC, Non-functionalised NPs + FITC and functionalised NPs (no FITC). Corresponding fluorescent microscope images are shown below.

Only the functionalised particles were successfully coupled with the FITC and areas of bright green fluorescence can be seen on the microscope where there are clusters of particles present. This confirms the presence of amine groups on their surface, which are required in order to form a successful bond with the FITC molecule. The successful attachment of the FITC molecule to the amine functionalised particles demonstrates that the attachment of other molecules or peptides for a variety of applications could also be possible.

8.3.2 Nano-composite Synthesis

NP-Alginate nano-composite scaffolds were printed as described (Section 8.2.4). Images of a 3D printed scaffold, before and after freeze drying are shown in Figure 8.5. The material appears uniform in colour and texture, suggesting that the nanoparticles were distributed homogeneously throughout the scaffold. Uniform shrinkage occurred on drying and the scaffolds maintain their porosity, which is essential for bone regeneration applications to allow for bone ingrowth and eventually revascularization. Typically an interconnected network is required with pore sizes ranging from 100 – 200 µm [205].

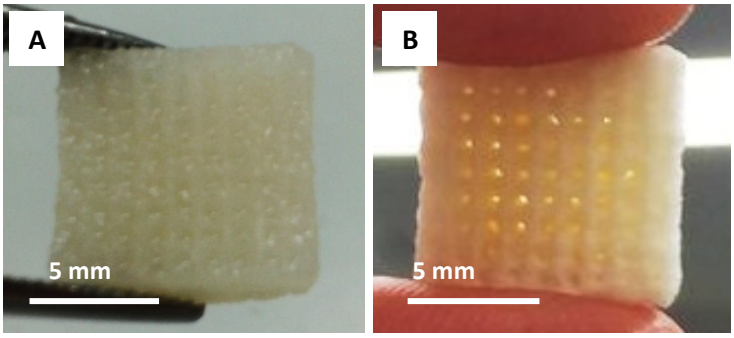


Figure 8.5- Photos of 3D printed NP-Alginate scaffold A) Before freeze drying and B) After freeze drying (courtesy of Dr Yuliya Vueva).

TEM and SEM images of freeze dried scaffolds are shown in Figure 8.6 and demonstrate the presence of nanoparticles throughout the material. Nanoparticles are also visible on the surface of the material (Figure 8.6A), which is beneficial for bioactivity and cell attachment. However, it is clear from Figure 8.6B that better dispersion of nanoparticles is required in order to achieve a more homogeneous distribution.

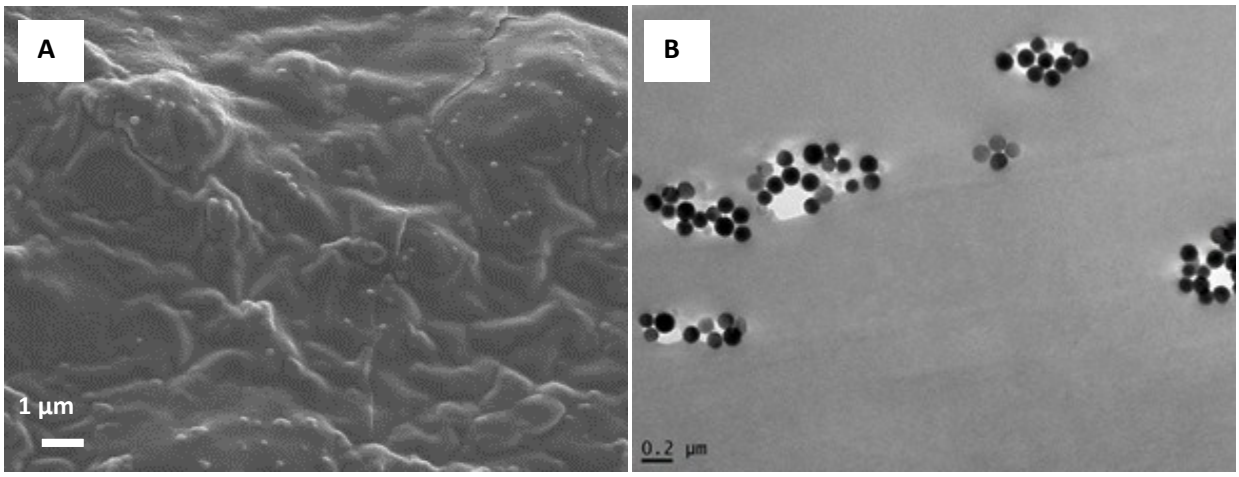


Figure 8.6 - A) SEM image (courtesy of Dr Yuliya Vueva) and B) TEM image (courtesy of Dr Shu Chen), of a freeze dried NP-Alginate nano-composite scaffold.

For bone regeneration applications the scaffold will also have to maintain its structure and in a wet environment. Therefore 3D printed scaffolds were immersed in distilled water for 24 h and observed. As a control, a silica-alginate hybrid scaffold, synthesised using the same method but without the addition of nanoparticles, was also studied. It can be seen from Figure 8.7 that the scaffold containing 20 wt% nanoparticles maintained its structure far better than the scaffold without nanoparticles. This demonstrates a clear benefit for the inclusion of nanoparticles and also suggests that the amine functionalised nanoparticles have successfully formed covalent bonds with the –COOH groups on the alginate.

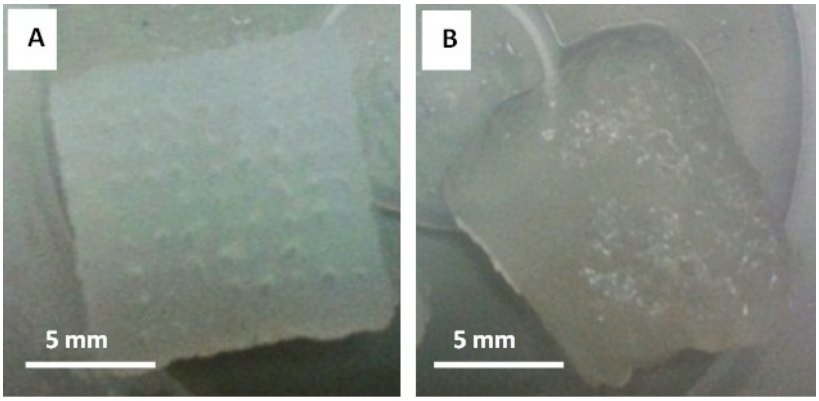


Figure 8.7 - 3D printed scaffolds after 24 hour immersion in dH_2O for A) NP-Alginate nano-composite scaffold and B) silica-alginate hybrid scaffold (without NPs) (courtesy of Dr Yuliya Vueva).

Mechanical testing was also performed on scaffolds, both with and without nanoparticles, and it was observed that the NP-alginate nanoparticle scaffold with 20 wt% NPs had a far higher compressive strength than the silica-alginate hybrid scaffold (without nanoparticles) in both wet and dry environments. In dry conditions a fourfold increase in compressive strength from 1.7 ± 0.4 MPa to 6.6 ± 1.4 MPa was seen. In wet conditions, although the mechanical properties of both samples drastically decreased, a threefold increase in compressive strength from 0.04 ± 0.005 MPa to 0.13 ± 0.03 MPa was still observed after the addition of 20 wt% NPs. The results are shown in Figure 8.8.

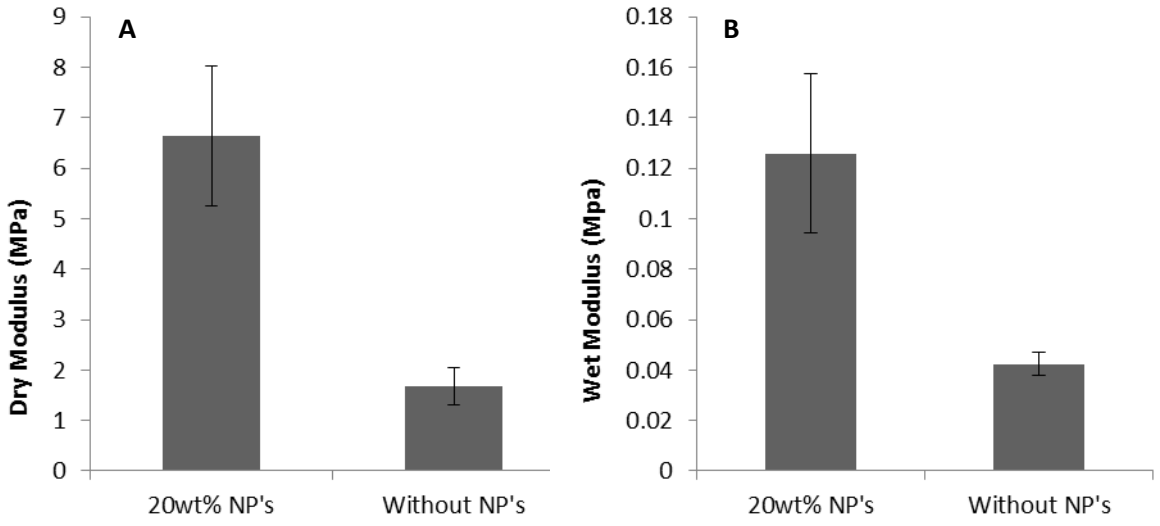


Figure 8.8 - Mechanical testing results for silica-alginate scaffolds showing the compressive strength under A) Dry conditions, and B) Wet conditions (courtesy of Dr Yuliya Vueva).

Whilst the addition of nanoparticles clearly increased the structural and mechanical properties of the scaffold, the compressive strength was still well below that of natural bone. However, by optimisation of the particle size, particle loading and 3D printing parameters, the mechanical properties could be improved. The alginate could also be substituted for another biocompatible polymer with carboxylic functional groups (e.g. PCL). This is discussed in more detail under Future

Work (Section 9.1). However, it would require alteration of the solvent used due to the fact that PCL is not soluble in water and DCC would also have to be used in place of EDC in a non-aqueous solution.

8.4 Conclusions

It has been demonstrated that the bioactive glass nanoparticles produced in this work can be successfully functionalised with APTES to give positively charged amine groups on their surface. This charge alteration could potentially have a significant impact on cell uptake. Additionally it was demonstrated that these amine groups could subsequently be successfully bonded to –N=C=S groups on FITC molecules. Functionalised nanoparticles were also incorporated into NP-Alginate composite scaffolds and were shown to be homogeneously dispersed throughout the matrix as well as resulting in improved mechanical strength of the scaffolds. Whilst more work is required to prove that the amine groups on the nanoparticles have been covalently bonded to the carboxylic acid groups on the alginate, this work done demonstrates a huge potential for these nanoparticles to be used for the synthesis of nano-composite scaffolds for bone regeneration applications.

9 Overall conclusions and future work

This thesis investigated the synthesis of inorganic nanoparticles for therapeutic applications, specifically bioactive glass nanoparticles for cancer treatment and bone regeneration. Although the field of nanomedicine is constantly expanding there is still much that is unknown and there are both conflicting opinions and gaps in current literature. Specifically there is much that we still don't know about nanoparticle uptake and their effect on cells. It is known that size, composition, release of ions and charge all play important roles but in complex *in vivo* systems their combined effects are still unclear.

It is therefore preferable that nanoparticles for therapeutic applications are designed with maximum flexibility and the ability to tailor factors such as size, degradation and charge without affecting the system as a whole. Thus, as understanding increases, the particles can be easily adapted and optimised for different applications. Here this is achieved by use of a multi-step process.

Initially this work revisited the original Stöber process to provide a comprehensive understanding of how to reliably control silica nanoparticle size. It was found that spherical monodispersed particles with a modal size ranging from 20 – 500 nm could be produced reliably and simply by varying the concentration of reactants. Of all the reactants, ammonium hydroxide concentration had the largest effect, with increased ammonia concentration resulting in increased particle size. As seen in literature, particle size was also shown to increase with increasing water concentration (up to 9 M) and then subsequently start to decrease again. Increasing the TEOS concentration from 0.28 – 0.17 M did not affect particle size or its distribution. However, reducing TEOS concentration to 0.045 M resulted in a smaller particle size, and increasing it to 0.5 M produced heterodispersed particles at high ammonia concentrations. The use of DLS to analyse particle size was also validated by TEM for particle sizes of up to 500 nm. However, beyond this size, DLS results tended to significantly overestimate the size of particles and should not be used.

Having successfully synthesised monodispersed silica nanoparticles of controlled sizes, it was then demonstrated that it is possible to subsequently incorporate both Ca and Zn cations from nitrate precursors without affecting the size, morphology or homogeneity of the particles. After heat treatment at 680˚C both ions successfully diffused homogeneously throughout the network (verified by sectioning using FIB and subsequent cross-sectional elemental mapping of particles). However, not all of the cations entered the particles, so a washing step was required before composition analysis. A maximum of 8.9 ± 1.1 mol% CaO or 22.7 ± 0.8 mol% ZnO could be incorporated into the particles. This difference is attributed to the fact that whilst calcium acts purely as a network modifier, zinc can also act as a network former. Zn^{2+} ions are also more reactive and have a smaller

ionic radius, allowing them to penetrate and break up the silica network more easily. The presence of nano-crystals of zinc silicate oxide was also observed in the particles containing high quantities of zinc, which is likely due to occur at high concentrations of zinc during the heating process.

A method for synthesising spherical, monodispersed, mesoporous silica nanoparticles was also found and both Zn and Ca cations were successfully incorporated without affecting the size or dispersity of the particles. Up to 18.5 ± 2.7 mol% CaO and 21.5 ± 1.3 mol% ZnO were incorporated; although, within the range of concentrations investigated, a limit was not reached for either cation. The increase in calcium incorporation in the mesoporous particles (in comparison to the dense particles) was attributed to the decreased network connectivity and larger surface area of the 100Si mesoporous particles, allowing for easier diffusion of the larger Ca^{2+} cations. It is also believed that the porous structure allows for expansion of the glass network as it is modified by cations. This would explain the decrease in surface area observed as cation incorporation in increased and also explain the maximum incorporation into dense particles before changes to morphology are observed.

In all particles synthesised, the network connectivity was seen to decrease with increasing cation incorporation. Decreased network connectivity is linked to the modifying effect of cations on the silica network and it would be expected that this would result in faster degradation of the particles. Ion dissolution studies were therefore performed on the particles *in vitro* and confirmed the different incorporation mechanisms for zinc and calcium cations. Calcium was released rapidly from all particles as it is only incorporated as a network modifier. However, the zinc partially acts as a network former, which acts to maintain the structure of the silica network at neutral pH and is only released in an acidic environment (when the Si-O-Zn bonds are hydrolysed). As expected, all mesoporous particles degraded faster than their dense counterparts due to increased surface area and reduced connectivity.

For incorporation into hybrids for bone regeneration it is concluded that dense particles are preferable as these were seen to release Ca, resulting in the precipitation of calcium phosphates, whilst maintaining their structural integrity on degradation. This should prevent a breakdown of the composite at the nanoparticle-polymer interface and allow for sustained mechanical strength of the scaffold. These particles were subsequently functionalised with amine groups and successfully incorporated into a NP-Alginate composite scaffold, demonstrating their potential for incorporation into a variety of nano-composite materials for bone regeneration.

For therapeutic applications, dense zinc-containing particles were not found to be suitable, as high quantities of Zn^{2+} ions were not released, resulting in no cytotoxicity when cell viability experiments were performed. However, mesoporous particles were seen to release high quantities of zinc both in ALF and within cells. The results of cell viability studies also indicated preferential cytotoxicity in cancer cells, suggesting that that these particles could therefore provide a promising method for cancer treatment by localised ion release.

In conclusion, a flexible method of creating bioactive glass nanoparticles has been developed. Size, composition and surface functionalisation can all be varied independently without affecting the size, morphology or dispersity of the resultant particles. For the mesoporous system developed here, composition can also be controlled without affecting particle size or dispersity and it is predicted that post-functionalisation would also be possible. However, in the current system, surface area, pore volume and connectivity cannot be varied independently of composition. Nevertheless, the levels of flexibility incorporated into each system are likely to allow for optimisation of these particles for a variety of applications as understanding progresses. The incorporation of additional cations and functionalisation with different chemical groups to allow for subsequent attachment of a variety of polymers or peptides could also expand the potential uses of these particles beyond the scope of this thesis.

9.1 Future Work

Future work could look at the incorporation of different ions into this system for various applications. In addition to Ca and Zn, it is possible to incorporate P, K and Sr. It is also possible to incorporate multiple elements to provide additional benefits (for example Sr could also be incorporated [17] with the aim of inhibiting osteoclast activity in osteoporosis sufferers). Small quantities of zinc could also be added to the SiO_2-CaO nanoparticles to delay Ca diffusion and enhance the growth of a surface calcium phosphate layer to improve bioactivity [41].

Since the precise mechanism by which the zinc is being incorporated into the network is yet to be determined, further NMR experiments could also be performed using O^{17} doped H_2O. This should enable the precise role that zinc is playing within the network to be better understood by looking at the local environment of oxygen atoms within the sample. However, the large quantities of water involved in the mesoporous system and the high cost of O^{17} doped H_2O potentially limits this investigation to the dense particles only.

As suggested previously, work could be done to incorporate the amine functionalised SiO_2-CaO nanoparticles into an alternative nano-composite. PCL would be the recommended choice of

polymer as it is biocompatible, approved by the Food and Drug Administration (FDA) for applications in the human body, and is degradable by hydrolysis of the ester linkage in physiological conditions, releasing non-toxic by-products. PCL is also associated with long term degradation (up to 3-4 years) [206] which is more suitable for bone regeneration applications than rapidly degrading polymers such as PGA and PLLA. In particular, PCL diol can be oxidised to produce a carboxyl group on either end, which could subsequently be used to create a 3D network by forming covalent bonds with the amine groups on the nanoparticles. However, PCL is not soluble in water, so a solvent such as chloroform or tetrahydrofuran (THF) would be required [207]. DCC would also have to be used in place of EDC in a non-aqueous solution in order for form bonds between the NH_2 and COOH groups [137,155,208]. As conducted on the NP-Alginate composites, if successful, this system could be optimised for 3D printing and both mechanical testing and cell studies could be performed on the resultant scaffolds. PCL has better mechanical properties than alginate and it is expected that these could be further improved by optimisation of both the molecular weight and % NP loading.

Further work is also required on the SiO_2-ZnO nanoparticles in order to ascertain their true potential for cancer treatment. As discussed, one of the major problems of using nanoparticles in therapeutic applications is clearance by the MPS. Uptake studies should therefore be conducted on macrophages and if necessary the size or charge of the particles could be altered to try and avoid internalisation by macrophages. Alternatively the particle surface could be PEGylated [209] to avoid protein corona formation and increase circulation time, which would be particularly beneficial for passive targeting by EPR. PEGylation could also have the added benefit of preventing potential aggregation of particles in blood due to the steric effects of polymer chains [210]. Additionally ligands could also be attached to the nanoparticles to investigate active targeting of overexpressed receptors on the tumour surface.

References

1 Wagner, V., Dullaart, A., Bock, A.-K. & Zweck, A. The emerging nanomedicine landscape. *Nat Biotech* **24**, 1211-1217, doi:http://www.nature.com/nbt/journal/v24/n10/suppinfo/nbt1006-1211_S1.html (2006).

2 BECK, J. *et al.* A NEW FAMILY OF MESOPOROUS MOLECULAR SIEVES PREPARED WITH LIQUID CRYSTAL TEMPLATES. (1992).

3 Kempen, P. J. *et al.* Theranostic Mesoporous Silica Nanoparticles Biodegrade after Pro-Survival Drug Delivery and Ultrasound/Magnetic Resonance Imaging of Stem Cells. *Theranostics* **5**, 631-642, doi:10.7150/thno.11389 (2015).

4 Jokerst, J. V., Khademi, C. & Gambhir, S. S. Intracellular aggregation of multimodal silica nanoparticles for ultrasound-guided stem cell implantation. *Science translational medicine* **5**, 177ra135, doi:10.1126/scitranslmed.3005228 (2013).

5 Werier, J. M. Bone graft substitutes in oncology, paediatrics, and hip arthroplasty. *COA Bulletin* **95** (2011).

6 Hench, L. L., Splinter, R. J., Allen, W. C. & Greenlee, T. K. Bonding mechanisms at the interface of ceramic prosthetic materials. *Journal of biomedical materials research* **5**, 117-141, doi:10.1002/jbm.820050611 (1971).

7 Jones, J. R. *et al.* Extracellular matrix formation and mineralization on a phosphate-free porous bioactive glass scaffold using primary human osteoblast (HOB) cells. *Biomaterials* **28**, 1653-1663, doi:10.1016/j.biomaterials.2006.11.022 (2007).

8 Midha, S. *et al.* Preconditioned 70S30C bioactive glass foams promote osteogenesis in vivo. *Acta biomaterialia* **9**, 9169-9182, doi:10.1016/j.actbio.2013.07.014 (2013).

9 Midha, S. *et al.* Bioactive glass foam scaffolds are remodelled by osteoclasts and support the formation of mineralized matrix and vascular networks in vitro. *Advanced healthcare materials* **2**, 490-499, doi:10.1002/adhm.201200140 (2013).

10 UK, C. R. *Cancer mortality statistics*, <http://www.cancerresearchuk.org/health-professional/cancer-statistics/mortality> (

11 Sun, T. *et al.* Engineered nanoparticles for drug delivery in cancer therapy. *Angew Chem Int Ed Engl* **53**, 12320-12364, doi:10.1002/anie.201403036 (2014).

12 Xia, T. *et al.* Comparison of the Mechanism of Toxicity of Zinc Oxide and Cerium Oxide Nanoparticles Based on Dissolution and Oxidative Stress Properties. *ACS nano* **2**, 2121-2134, doi:10.1021/nn800511k (2008).

13 Sasidharan, A. *et al.* Rapid dissolution of ZnO nanocrystals in acidic cancer microenvironment leading to preferential apoptosis. *Nanoscale* **3**, 3657-3669, doi:10.1039/c1nr10272a (2011).

14 Bini, M. *et al.* SiO2−P2O5−CaO Glasses and Glass-Ceramics with and without ZnO: Relationships among Composition, Microstructure, and Bioactivity. *The Journal of Physical Chemistry C* **113**, 8821-8828, doi:10.1021/jp810977w (2009).

15 Balamurugan, A. *et al.* Development and in vitro characterization of sol-gel derived CaO-P2O5-SiO2-ZnO bioglass. *Acta biomaterialia* **3**, 255-262, doi:10.1016/j.actbio.2006.09.005 (2007).

16 Jones, J. R. Review of bioactive glass: from Hench to hybrids. *Acta biomaterialia* **9**, 4457-4486, doi:10.1016/j.actbio.2012.08.023 (2013).

17 Lao, J., Jallot, E. & Nedelec, J.-M. Strontium-Delivering Glasses with Enhanced Bioactivity: A New Biomaterial for Antiosteoporotic Applications? *Chemistry of Materials* **20**, 4969-4973, doi:10.1021/cm800993s (2008).

18 Azevedo, M. M. *et al.* Synthesis and characterization of hypoxia-mimicking bioactive glasses for skeletal regeneration. *Journal of Materials Chemistry* **20**, 8854, doi:10.1039/c0jm01111h (2010).

19 Chen, X. *et al.* 'Smart' acid-degradable zinc-releasing silicate glasses. *Materials Letters* **126**, 278-280, doi:10.1016/j.matlet.2014.04.009 (2014).

20 Xiang, Y. *et al.* Structure and diffusion of ZnO–SrO–CaO–Na2O–SiO2 bioactive glasses: a combined high energy X-ray diffraction and molecular dynamics simulations study. *RSC Advances* **3**, 5966, doi:10.1039/c3ra23231j (2013).
21 Mead, R. N. & Mountjoy, G. Modeling the Local Atomic Structure of Bioactive Sol−Gel-Derived Calcium Silicates. *Chemistry of Materials* **18**, 3956-3964, doi:10.1021/cm0527975 (2006).
22 Skipper, L. J. *et al.* The structure of a bioactive calcia–silica sol–gel glass. *Journal of Materials Chemistry* **15**, 2369, doi:10.1039/b501496d (2005).
23 Sánchez-Salcedo, S. *et al.* In vitro antibacterial capacity and cytocompatibility of SiO2–CaO–P2O5meso-macroporous glass scaffolds enriched with ZnO. *Journal of Materials Chemistry B* **2**, 4836, doi:10.1039/c4tb00403e (2014).
24 Wers, E. & Oudadesse, H. Thermal behaviour and excess entropy of bioactive glasses and Zn-doped glasses. *Journal of Thermal Analysis and Calorimetry* **115**, 2137-2144, doi:10.1007/s10973-013-3280-3 (2013).
25 Pedone, A., Charpentier, T., Malavasi, G. & Menziani, M. C. New Insights into the Atomic Structure of 45S5 Bioglass by Means of Solid-State NMR Spectroscopy and Accurate First-Principles Simulations. *Chemistry of Materials* **22**, 5644-5652, doi:10.1021/cm102089c (2010).
26 Giannoudis, P. V., Dinopoulos, H. & Tsiridis, E. Bone substitutes: An update. *Injury* **36**, S20-S27, doi:http://dx.doi.org/10.1016/j.injury.2005.07.029 (2005).
27 Jones, J. R., Sepulveda, P. & Hench, L. L. Dose-dependent behavior of bioactive glass dissolution. *Journal of biomedical materials research* **58**, 720-726, doi:10.1002/jbm.10053 (2001).
28 Martínez, A., Izquierdo-Barba, I. & Vallet-Regí, M. Bioactivity of a CaO−SiO2 Binary Glasses System. *Chemistry of Materials* **12**, 3080-3088, doi:10.1021/cm001107o (2000).
29 Xynos, I. D., Edgar, A. J., Buttery, L. D. K., Hench, L. L. & Polak, J. M. Gene-expression profiling of human osteoblasts following treatment with the ionic products of Bioglass® 45S5 dissolution. *Journal of biomedical materials research* **55**, 151-157, doi:10.1002/1097-4636(200105)55:2<151::AID-JBM1001>3.0.CO;2-D (2001).
30 Goel, A., Kapoor, S., Tilocca, A., Rajagopal, R. R. & Ferreira, J. M. F. Structural role of zinc in biodegradation of alkali-free bioactive glasses. *Journal of Materials Chemistry B*, doi:10.1039/c3tb20163e (2013).
31 Anand, V., Singh, K. J. & Kaur, K. Evaluation of zinc and magnesium doped 45S5 mesoporous bioactive glass system for the growth of hydroxyl apatite layer. *Journal of Non-Crystalline Solids* **406**, 88-94, doi:10.1016/j.jnoncrysol.2014.09.050 (2014).
32 Bejarano, J., Caviedes, P. & Palza, H. Sol-gel synthesis and in vitro bioactivity of copper and zinc-doped silicate bioactive glasses and glass-ceramics. *Biomedical materials (Bristol, England)* **10**, 025001, doi:10.1088/1748-6041/10/2/025001 (2015).
33 Goh, Y.-F., Alshemary, A. Z., Akram, M., Abdul Kadir, M. R. & Hussain, R. In vitro study of nano-sized zinc doped bioactive glass. *Materials Chemistry and Physics* **137**, 1031-1038, doi:10.1016/j.matchemphys.2012.11.022 (2013).
34 Kaur, G. *et al.* Synthesis, cytotoxicity, and hydroxyapatite formation in 27-Tris-SBF for sol-gel based CaO-P2O5-SiO2-B2O3-ZnO bioactive glasses. *Sci Rep* **4**, 4392, doi:10.1038/srep04392 (2014).
35 Rabiee, S. M., Nazparvar, N., Azizian, M., Vashaee, D. & Tayebi, L. Effect of ion substitution on properties of bioactive glasses: A review. *Ceramics International* **41**, 7241-7251, doi:10.1016/j.ceramint.2015.02.140 (2015).
36 Shruti, S. *et al.* Mesoporous bioactive scaffolds prepared with cerium-, gallium- and zinc-containing glasses. *Acta biomaterialia* **9**, 4836-4844, doi:10.1016/j.actbio.2012.09.024 (2013).

37 Wang, H. *et al.* Three-dimensional zinc incorporated borosilicate bioactive glass scaffolds for rodent critical-sized calvarial defects repair and regeneration. *Colloids Surf B Biointerfaces* **130**, 149-156, doi:10.1016/j.colsurfb.2015.03.053 (2015).
38 Abrisham, S. M., Yaghmaei, M., Abbas, F. M., Sharifi, D. & Abrisham, S. M. Effect of oral zinc therapy on osteogenesis in rabbits. *J Oral Maxillofac Surg* **68**, 1676-1680, doi:10.1016/j.joms.2009.07.048 (2010).
39 Hoppe, A., Mourino, V. & Boccaccini, A. R. Therapeutic inorganic ions in bioactive glasses to enhance bone formation and beyond. *Biomaterials Science* **1**, 254-256, doi:10.1039/C2BM00116K (2013).
40 Kraus, V. B. Osteoarthritis: The zinc link. *Nature* **507**, 441-442, doi:10.1038/507441a (2014).
41 Courthéoux, L., Lao, J., Nedelec, J. M. & Jallot, E. Controlled Bioactivity in Zinc-Doped Sol−Gel-Derived Binary Bioactive Glasses. *The Journal of Physical Chemistry C* **112**, 13663-13667, doi:10.1021/jp8044498 (2008).
42 Aina, V. *et al.* Cytotoxicity of zinc-containing bioactive glasses in contact with human osteoblasts. *Chem Biol Interact* **167**, 207-218, doi:10.1016/j.cbi.2007.03.002 (2007).
43 Nel, A., Xia, T., Mädler, L. & Li, N. Toxic Potential of Materials at the Nanolevel. *Science* **311**, 622-627, doi:10.1126/science.1114397 (2006).
44 Society, R. & Engineering, R. A. o. *Nanoscience and Nanotechnologies: Opportunities and Uncertainties*. (Royal Society, 2004).
45 Dhawan, A. & Sharma, V. Toxicity assessment of nanomaterials: methods and challenges. *Anal Bioanal Chem* **398**, 589-605, doi:10.1007/s00216-010-3996-x (2010).
46 Chung, T.-H. *et al.* The effect of surface charge on the uptake and biological function of mesoporous silica nanoparticles in 3T3-L1 cells and human mesenchymal stem cells. *Biomaterials* **28**, 2959-2966, doi:http://dx.doi.org/10.1016/j.biomaterials.2007.03.006 (2007).
47 Chou, S. W. *et al.* In vitro and in vivo studies of FePt nanoparticles for dual modal CT/MRI molecular imaging. *Journal of the American Chemical Society* **132**, 13270-13278, doi:10.1021/ja1035013 (2010).
48 Mortensen, N. P. *et al.* Dynamic development of the protein corona on silica nanoparticles: composition and role in toxicity. *Nanoscale*, doi:10.1039/c3nr33280b (2013).
49 Huang, X., Teng, X., Chen, D., Tang, F. & He, J. The effect of the shape of mesoporous silica nanoparticles on cellular uptake and cell function. *Biomaterials* **31**, 438-448, doi:10.1016/j.biomaterials.2009.09.060 (2010).
50 Rasmussen, J. W., Martinez, E., Louka, P. & Wingett, D. G. Zinc oxide nanoparticles for selective destruction of tumor cells and potential for drug delivery applications. *Expert opinion on drug delivery* **7**, 1063-1077, doi:10.1517/17425247.2010.502560 (2010).
51 Soo Choi, H. *et al.* Renal clearance of quantum dots. *Nat Biotech* **25**, 1165-1170, doi:http://www.nature.com/nbt/journal/v25/n10/suppinfo/nbt1340_S1.html (2007).
52 Garnett, M. C. & Kallinteri, P. Nanomedicines and nanotoxicology: some physiological principles. *Occupational medicine* **56**, 307-311, doi:10.1093/occmed/kql052 (2006).
53 Limbach, L. K. *et al.* Oxide Nanoparticle Uptake in Human Lung Fibroblasts: Effects of Particle Size, Agglomeration, and Diffusion at Low Concentrations. *Environmental science & technology* **39**, 9370-9376, doi:10.1021/es051043o (2005).
54 Cho, M. *et al.* The impact of size on tissue distribution and elimination by single intravenous injection of silica nanoparticles. *Toxicology letters* **189**, 177-183, doi:10.1016/j.toxlet.2009.04.017 (2009).
55 Hirota, K. & Ter, H. Endocytosis of Particle Formulations by Macrophages and Its Application to Clinical Treatment. doi:10.5772/45820 (2012).
56 Rejman, J., Oberle, V., Zuhorn, I. S. & Hoekstra, D. Size-dependent internalization of particles via the pathways of clathrin- and caveolae-mediated endocytosis. *The Biochemical journal* **377**, 159-169, doi:10.1042/bj20031253 (2004).

57 Lu, F., Wu, S. H., Hung, Y. & Mou, C. Y. Size effect on cell uptake in well-suspended, uniform mesoporous silica nanoparticles. *Small* **5**, 1408-1413, doi:10.1002/smll.200900005 (2009).
58 Soenen, S. J., Manshian, B., Doak, S. H., De Smedt, S. C. & Braeckmans, K. Fluorescent non-porous silica nanoparticles for long-term cell monitoring: Cytotoxicity and particle functionality. *Acta biomaterialia*, doi:http://dx.doi.org/10.1016/j.actbio.2013.04.026.
59 Park, M. V. D. Z. *et al.* In vitro developmental toxicity test detects inhibition of stem cell differentiation by silica nanoparticles. *Toxicology and Applied Pharmacology* **240**, 108-116, doi:http://dx.doi.org/10.1016/j.taap.2009.07.019 (2009).
60 Tsigkou, O., Labbaf, S., Stevens, M. M., Porter, A. E. & Jones, J. R. Monodispersed bioactive glass submicron particles and their effect on bone marrow and adipose tissue-derived stem cells. *Advanced healthcare materials* **3**, 115-125, doi:10.1002/adhm.201300126 (2014).
61 Li, S.-D. & Huang, L. Pharmacokinetics and Biodistribution of Nanoparticles. *Molecular Pharmaceutics* **5**, 496-504, doi:10.1021/mp800049w (2008).
62 Davis, M. E., Chen, Z. G. & Shin, D. M. Nanoparticle therapeutics: an emerging treatment modality for cancer. *Nature reviews. Drug discovery* **7**, 771-782, doi:10.1038/nrd2614 (2008).
63 El-Fiqi, A. *et al.* Capacity of mesoporous bioactive glass nanoparticles to deliver therapeutic molecules. *Nanoscale* **4**, 7475-7488, doi:10.1039/c2nr31775c (2012).
64 Brigger, I., Dubernet, C. & Couvreur, P. Nanoparticles in cancer therapy and diagnosis. *Advanced drug delivery reviews* **54**, 631-651, doi:http://dx.doi.org/10.1016/S0169-409X(02)00044-3 (2002).
65 O'Brien, M. E. R. Reduced cardiotoxicity and comparable efficacy in a phase III trial of pegylated liposomal doxorubicin HCl (CAELYXTM/Doxil") versus conventional doxorubicin for first-line treatment of metastatic breast cancer. *Annals of Oncology* **15**, 440-449, doi:10.1093/annonc/mdh097 (2004).
66 Peer, D. *et al.* Nanocarriers as an emerging platform for cancer therapy. *Nat Nano* **2**, 751-760 (2007).
67 Huang, X., P, N. & E, H. Characterization and Comparison of Mesoporous Silica Particles for Optimized Drug Delivery. *Nanomaterials and Nanotechnology*, 1, doi:10.5772/58290 (2014).
68 Lin, Y.-S. *et al.* Well-Ordered Mesoporous Silica Nanoparticles as Cell Markers. *Chemistry of Materials* **17**, 4570-4573, doi:10.1021/cm051014c (2005).
69 Bernardos, A. *et al.* Enzyme-Responsive Intracellular Controlled Release Using Nanometric Silica Mesoporous Supports Capped with “Saccharides”. *ACS nano* **4**, 6353-6368, doi:10.1021/nn101499d (2010).
70 Chang, B. *et al.* Bioresponsive Controlled Drug Release Based on Mesoporous Silica Nanoparticles Coated with Reductively Sheddable Polymer Shell. *Chemistry of Materials* **25**, 574-585, doi:10.1021/cm3037197 (2013).
71 Muhammad, F. *et al.* pH-Triggered controlled drug release from mesoporous silica nanoparticles via intracelluar dissolution of ZnO nanolids. *Journal of the American Chemical Society* **133**, 8778-8781, doi:10.1021/ja200328s (2011).
72 Knezevic, N. Z. & Lin, V. S. Y. A magnetic mesoporous silica nanoparticle-based drug delivery system for photosensitive cooperative treatment of cancer with a mesopore-capping agent and mesopore-loaded drug. *Nanoscale* **5**, 1544-1551, doi:10.1039/C2NR33417H (2013).
73 Chen, J. *et al.* Gold Nanocages: A Novel Class of Multifunctional Nanomaterials for Theranostic Applications. *Advanced functional materials* **20**, 3684-3694, doi:10.1002/adfm.201001329 (2010).
74 Kam, N. W. S., O'Connell, M., Wisdom, J. A. & Dai, H. Carbon nanotubes as multifunctional biological transporters and near-infrared agents for selective cancer cell destruction. *Proceedings of the National Academy of Sciences of the United States of America* **102**, 11600-11605, doi:10.1073/pnas.0502680102 (2005).

75 Vandebriel, R. J. & De Jong, W. H. A review of mammalian toxicity of ZnO nanoparticles. *Nanotechnology, Science and Applications* **5**, 61-71, doi:10.2147/NSA.S23932 (2012).
76 Othman, B. *Breast Cancer Targeted Therapy Using ZnO Nanostructures* PhD thesis, Imperial College London, (2014).
77 Muller, K. H. *et al.* pH-dependent toxicity of high aspect ratio ZnO nanowires in macrophages due to intracellular dissolution. *ACS nano* **4**, 6767-6779, doi:10.1021/nn101192z (2010).
78 Costello, L. C. & Franklin, R. B. Cytotoxic/tumor suppressor role of zinc for the treatment of cancer: an enigma and an opportunity. *Expert Rev Anticancer Ther* **12**, 121-128, doi:10.1586/era.11.190 (2012).
79 Hench, L. L. The story of Bioglass. *Journal of materials science. Materials in medicine* **17**, 967-978, doi:10.1007/s10856-006-0432-z (2006).
80 Sepulveda, P., Jones, J. R. & Hench, L. L. Characterization of melt-derived 45S5 and sol-gel–derived 58S bioactive glasses. *Journal of biomedical materials research* **58**, 734-740, doi:10.1002/jbm.10026 (2001).
81 Hench, L. L. Sol-gel materials for bioceramic applications. *Current Opinion in Solid State and Materials Science* **2**, 604-610, doi:http://dx.doi.org/10.1016/S1359-0286(97)80053-8 (1997).
82 Labbaf, S. *et al.* Spherical bioactive glass particles and their interaction with human mesenchymal stem cells in vitro. *Biomaterials* **32**, 1010-1018, doi:10.1016/j.biomaterials.2010.08.082 (2011).
83 Hench, L. L. & West, J. K. The sol-gel process. *Chemical Reviews* **90**, 33-72, doi:10.1021/cr00099a003 (1990).
84 Lin, S., Ionescu, C., Pike, K. J., Smith, M. E. & Jones, J. R. Nanostructure evolution and calcium distribution in sol–gel derived bioactive glass. *Journal of Materials Chemistry* **19**, 1276, doi:10.1039/b814292k (2009).
85 Brinker, C. J. & Scherer, G. W. *Sol-Gel Science: The Physics and Chemistry of Sol-Gel Processing*. (Academic Press, 1990).
86 Stöber, W., Fink, A. & Bohn, E. Controlled growth of monodisperse silica spheres in the micron size range. *Journal of colloid and interface science* **26**, 62-69, doi:http://dx.doi.org/10.1016/0021-9797(68)90272-5 (1968).
87 Jones, J. R., Ehrenfried, L. M. & Hench, L. L. Optimising bioactive glass scaffolds for bone tissue engineering. *Biomaterials* **27**, 964-973, doi:10.1016/j.biomaterials.2005.07.017 (2006).
88 Fu, Q., Saiz, E. & Tomsia, A. P. Bioinspired Strong and Highly Porous Glass Scaffolds. *Advanced functional materials* **21**, 1058-1063, doi:10.1002/adfm.201002030 (2011).
89 Brunner, T. J., Grass, R. N. & Stark, W. J. Glass and bioglass nanopowders by flame synthesis. *Chemical Communications* **0**, 1384-1386, doi:10.1039/B517501A (2006).
90 López-Quintela, M. A. Synthesis of nanomaterials in microemulsions: formation mechanisms and growth control. *Current Opinion in Colloid & Interface Science* **8**, 137-144, doi:http://dx.doi.org/10.1016/S1359-0294(03)00019-0 (2003).
91 Matsoukas, T. & Gulari, E. Monomer-addition growth with a slow initiation step: A growth model for silica particles from alkoxides. *Journal of colloid and interface science* **132**, 13-21, doi:http://dx.doi.org/10.1016/0021-9797(89)90210-5 (1989).
92 Rahman, I. A. & Padavettan, V. Synthesis of Silica Nanoparticles by Sol-Gel: Size-Dependent Properties, Surface Modification, and Applications in Silica-Polymer Nanocomposites—A Review. *Journal of Nanomaterials* **2012**, 15, doi:10.1155/2012/132424 (2012).
93 Bogush, G. H., Tracy, M. A. & Zukoski Iv, C. F. Preparation of monodisperse silica particles: Control of size and mass fraction. *Journal of Non-Crystalline Solids* **104**, 95-106, doi:http://dx.doi.org/10.1016/0022-3093(88)90187-1 (1988).

94 Matsoukas, T. & Gulari, E. Dynamics of growth of silica particles from ammonia-catalyzed hydrolysis of tetra-ethyl-orthosilicate. *Journal of colloid and interface science* **124**, 252-261, doi:http://dx.doi.org/10.1016/0021-9797(88)90346-3 (1988).
95 Branda, F., Silvestri, B., Luciani, G. & Costantini, A. The effect of mixing alkoxides on the Stöber particles size. *Colloids and Surfaces A: Physicochemical and Engineering Aspects* **299**, 252-255, doi:10.1016/j.colsurfa.2006.11.048 (2007).
96 Van Helden, A. K., Jansen, J. W. & Vrij, A. Preparation and characterization of spherical monodisperse silica dispersions in nonaqueous solvents. *Journal of colloid and interface science* **81**, 354-368, doi:http://dx.doi.org/10.1016/0021-9797(81)90417-3 (1981).
97 Green, D. L. *et al.* Size, volume fraction, and nucleation of Stober silica nanoparticles. *Journal of colloid and interface science* **266**, 346-358, doi:10.1016/s0021-9797(03)00610-6 (2003).
98 Harris, M. T., Brunson, R. R. & Byers, C. H. The base-catalyzed hydrolysis and condensation reactions of dilute and concentrated TEOS solutions. *Journal of Non-Crystalline Solids* **121**, 397-403, doi:http://dx.doi.org/10.1016/0022-3093(90)90165-I (1990).
99 Park, S. K., Kim, K. D. & Kim, H. T. Preparation of silica nanoparticles: determination of the optimal synthesis conditions for small and uniform particles. *Colloids and Surfaces A: Physicochemical and Engineering Aspects* **197**, 7-17, doi:http://dx.doi.org/10.1016/S0927-7757(01)00683-5 (2002).
100 Rao, K. S., El-Hami, K., Kodaki, T., Matsushige, K. & Makino, K. A novel method for synthesis of silica nanoparticles. *Journal of colloid and interface science* **289**, 125-131, doi:10.1016/j.jcis.2005.02.019 (2005).
101 Van Blaaderen, A., Van Geest, J. & Vrij, A. Monodisperse colloidal silica spheres from tetraalkoxysilanes: Particle formation and growth mechanism. *Journal of colloid and interface science* **154**, 481-501, doi:http://dx.doi.org/10.1016/0021-9797(92)90163-G (1992).
102 Bogush, G. H. & Zukoski Iv, C. F. Studies of the kinetics of the precipitation of uniform silica particles through the hydrolysis and condensation of silicon alkoxides. *Journal of colloid and interface science* **142**, 1-18, doi:http://dx.doi.org/10.1016/0021-9797(91)90029-8 (1991).
103 LaMer, V. K. & Dinegar, R. H. Theory, Production and Mechanism of Formation of Monodispersed Hydrosols. *Journal of the American Chemical Society* **72**, 4847-4854, doi:10.1021/ja01167a001 (1950).
104 Bogush, G. H. & Zukoski Iv, C. F. Uniform silica particle precipitation: An aggregative growth model. *Journal of colloid and interface science* **142**, 19-34, doi:http://dx.doi.org/10.1016/0021-9797(91)90030-C (1991).
105 Lee, K., Sathyagal, A. N. & McCormick, A. V. A closer look at an aggregation model of the Stober process. *Colloids and Surfaces A: Physicochemical and Engineering Aspects* **144**, 115-125, doi:10.1016/S0927-7757(98)00566-4 (1998).
106 Feeney, P. J., Napper, D. H. & Gilbert, R. G. Coagulative nucleation and particle size distributions in emulsion polymerization. *Macromolecules* **17**, 2520-2529, doi:10.1021/ma00142a010 (1984).
107 Hench, L. L. & Polak, J. M. Third-generation biomedical materials. *Science* **295**, 1014-1017, doi:10.1126/science.1067404 (2002).
108 Hoppe, A., Guldal, N. S. & Boccaccini, A. R. A review of the biological response to ionic dissolution products from bioactive glasses and glass-ceramics. *Biomaterials* **32**, 2757-2774, doi:10.1016/j.biomaterials.2011.01.004 (2011).
109 Marelli, B. *et al.* Accelerated mineralization of dense collagen-nano bioactive glass hybrid gels increases scaffold stiffness and regulates osteoblastic function. *Biomaterials* **32**, 8915-8926, doi:10.1016/j.biomaterials.2011.08.016 (2011).
110 Xia, W. & Chang, J. Preparation and characterization of nano-bioactive-glasses (NBG) by a quick alkali-mediated sol–gel method. *Materials Letters* **61**, 3251-3253, doi:10.1016/j.matlet.2006.11.048 (2007).

111 Luz, G. M. & Mano, J. F. Preparation and characterization of bioactive glass nanoparticles prepared by sol-gel for biomedical applications. *Nanotechnology* **22**, 494014, doi:10.1088/0957-4484/22/49/494014 (2011).
112 Nedelec, J.-M., lao, j., Lacroix, J. & Lukowiak, A. Bioactive Glass Nanoparticles through Sol-Gel Chemistry. *Chemical Communications*, doi:10.1039/C3CC00003F (2013).
113 Hong, Z. *et al.* Mono-dispersed bioactive glass nanospheres: preparation and effects on biomechanics of mammalian cells. *Journal of biomedical materials research. Part A* **95**, 747-754, doi:10.1002/jbm.a.32898 (2010).
114 de Oliveira, A. A. *et al.* Synthesis, characterization and cytocompatibility of spherical bioactive glass nanoparticles for potential hard tissue engineering applications. *Biomedical materials (Bristol, England)* **8**, 025011, doi:10.1088/1748-6041/8/2/025011 (2013).
115 Hong, Z., Liu, A., Chen, L., Chen, X. & Jing, X. Preparation of bioactive glass ceramic nanoparticles by combination of sol–gel and coprecipitation method. *Journal of Non-Crystalline Solids* **355**, 368-372, doi:http://dx.doi.org/10.1016/j.jnoncrysol.2008.12.003 (2009).
116 Zhao, Y., Zou, J., Shi, W. & Tang, L. Preparation and characterization of mesoporous silica spheres with bimodal pore structure from silica/hyperbranched polyester nanocomposites. *Microporous and Mesoporous Materials* **92**, 251-258, doi:http://dx.doi.org/10.1016/j.micromeso.2006.01.007 (2006).
117 Yu, B., Poologasundarampillai, G., Turdean-Ionescu, C., Smith, M. E. & Jones, J. R. A New Calcium Source for Bioactive Sol-Gel Hybrids. *Bioceramics Development and Applications* **1**, 1-3, doi:10.4303/bda/D110178 (2011).
118 Yu, B. *et al.* Effect of calcium source on structure and properties of sol-gel derived bioactive glasses. *Langmuir : the ACS journal of surfaces and colloids* **28**, 17465-17476, doi:10.1021/la303768b (2012).
119 Slowing, II, Vivero-Escoto, J. L., Wu, C. W. & Lin, V. S. Mesoporous silica nanoparticles as controlled release drug delivery and gene transfection carriers. *Advanced drug delivery reviews* **60**, 1278-1288, doi:10.1016/j.addr.2008.03.012 (2008).
120 Shimura, N. & Ogawa, M. Preparation of surfactant templated nanoporous silica spherical particles by the Stöber method. Effect of solvent composition on the particle size. *Journal of Materials Science* **42**, 5299-5306, doi:10.1007/s10853-007-1771-y (2007).
121 Shi, Y.-T. *et al.* The size-controllable synthesis of nanometer-sized mesoporous silica in extremely dilute surfactant solution. *Materials Chemistry and Physics* **120**, 193-198, doi:10.1016/j.matchemphys.2009.10.045 (2010).
122 Nooney, R. I., Thirunavukkarasu, D., Chen, Y., Josephs, R. & Ostafin, A. E. Synthesis of Nanoscale Mesoporous Silica Spheres with Controlled Particle Size. *Chemistry of Materials* **14**, 4721-4728, doi:10.1021/cm0204371 (2002).
123 Nandiyanto, A. B. D., Kim, S.-G., Iskandar, F. & Okuyama, K. Synthesis of spherical mesoporous silica nanoparticles with nanometer-size controllable pores and outer diameters. *Microporous and Mesoporous Materials* **120**, 447-453, doi:10.1016/j.micromeso.2008.12.019 (2009).
124 Lu, Y. *et al.* Aerosol-assisted self-assembly of mesostructured spherical nanoparticles. *Nature* **398**, 223-226 (1999).
125 Huh, S., Wiench, J. W., Yoo, J.-C., Pruski, M. & Lin, V. S. Y. Organic Functionalization and Morphology Control of Mesoporous Silicas via a Co-Condensation Synthesis Method. *Chemistry of Materials* **15**, 4247-4256, doi:10.1021/cm0210041 (2003).
126 Brinker, C. J. Evaporation-Induced Self-Assembly: Functional Nanostructures Made Easy. *MRS Bulletin* **29**, 631-640, doi:doi:10.1557/mrs2004.183 (2004).
127 Arcos, D., López-Noriega, A., Ruiz-Hernández, E., Terasaki, O. & Vallet-Regí, M. Ordered Mesoporous Microspheres for Bone Grafting and Drug Delivery. *Chemistry of Materials* **21**, 1000-1009, doi:10.1021/cm801649z (2009).

128 Yun, H.-s., Kim, S.-h., Lee, S. & Song, I.-h. Synthesis of high surface area mesoporous bioactive glass nanospheres. *Materials Letters* **64**, 1850-1853, doi:10.1016/j.matlet.2010.04.053 (2010).
129 Rho, J. Y., Kuhn-Spearing, L. & Zioupos, P. Mechanical properties and the hierarchical structure of bone. *Medical engineering & physics* **20**, 92-102 (1998).
130 Saiz, E., Zimmermann, E. A., Lee, J. S., Wegst, U. G. & Tomsia, A. P. Perspectives on the role of nanotechnology in bone tissue engineering. *Dental materials : official publication of the Academy of Dental Materials* **29**, 103-115, doi:10.1016/j.dental.2012.08.001 (2013).
131 Li, W.-J., Tuli, R., Huang, X., Laquerriere, P. & Tuan, R. S. Multilineage differentiation of human mesenchymal stem cells in a three-dimensional nanofibrous scaffold. *Biomaterials* **26**, 5158-5166, doi:http://dx.doi.org/10.1016/j.biomaterials.2005.01.002 (2005).
132 Valliant, E. M. & Jones, J. R. Softening bioactive glass for bone regeneration: sol-gel hybrid materials. *Soft Matter* **7**, 5083-5095, doi:10.1039/C0SM01348J (2011).
133 Valliant, E. M. *et al.* Bioactivity in silica/poly(γ-glutamic acid) sol-gel hybrids through calcium chelation. *Acta biomaterialia*, doi:http://dx.doi.org/10.1016/j.actbio.2013.04.037.
134 Hong, Z., Reis, R. L. & Mano, J. F. Preparation and in vitro characterization of novel bioactive glass ceramic nanoparticles. *Journal of biomedical materials research. Part A* **88**, 304-313, doi:10.1002/jbm.a.31848 (2009).
135 Boccaccini, A. R. *et al.* Polymer/bioactive glass nanocomposites for biomedical applications: A review. *Composites Science and Technology* **70**, 1764-1776, doi:10.1016/j.compscitech.2010.06.002 (2010).
136 Liu, A. *et al.* Surface modification of bioactive glass nanoparticles and the mechanical and biological properties of poly(L-lactide) composites. *Acta biomaterialia* **4**, 1005-1015, doi:10.1016/j.actbio.2008.02.013 (2008).
137 An, Y., Chen, M., Xue, Q. & Liu, W. Preparation and self-assembly of carboxylic acid-functionalized silica. *Journal of colloid and interface science* **311**, 507-513, doi:10.1016/j.jcis.2007.02.084 (2007).
138 Chen, S. *et al.* Sol-Gel Synthesis and Microstructure Analysis of Amino-Modified Hybrid Silica Nanoparticles from Aminopropyltriethoxysilane and Tetraethoxysilane. *Journal of the American Ceramic Society* **92**, 2074-2082, doi:10.1111/j.1551-2916.2009.03135.x (2009).
139 Li, X., He, Y. & Swihart, M. T. Surface Functionalization of Silicon Nanoparticles Produced by Laser-Driven Pyrolysis of Silane followed by HF−HNO3 Etching. *Langmuir : the ACS journal of surfaces and colloids* **20**, 4720-4727, doi:10.1021/la036219j (2004).
140 Yan, W., Han, Z. J., Phung, B. T. & Ostrikov, K. Silica Nanoparticles Treated by Cold Atmospheric-Pressure Plasmas Improve the Dielectric Performance of Organic–Inorganic Nanocomposites. *ACS Applied Materials & Interfaces* **4**, 2637-2642, doi:10.1021/am300300f (2012).
141 Chen, X., Guo, C. & Zhao, N. Preparation and characterization of the sol–gel nano-bioactive glasses modified by the coupling agent gamma-aminopropyltriethoxysilane. *Applied Surface Science* **255**, 466-468, doi:10.1016/j.apsusc.2008.06.061 (2008).
142 El-Fiqi, A., Lee, J. H., Lee, E.-J. & Kim, H.-W. Collagen hydrogels incorporated with surface-aminated mesoporous nanobioactive glass: Improvement of physicochemical stability and mechanical properties is effective for hard tissue engineering. *Acta biomaterialia* **9**, 9508-9521, doi:http://dx.doi.org/10.1016/j.actbio.2013.07.036 (2013).
143 Xu, W. *et al.* Amine Surface Modifications and Fluorescent Labeling of Thermally Stabilized Mesoporous Silicon Nanoparticles. *The Journal of Physical Chemistry C* **116**, 22307-22314, doi:10.1021/jp303199s (2012).
144 Lenza, R. F., Vasconcelos, W. L., Jones, J. R. & Hench, L. L. Surface-modified 3D scaffolds for tissue engineering. *Journal of materials science. Materials in medicine* **13**, 837-842 (2002).

145 Kang, S. *et al.* Preparation and characterization of epoxy composites filled with functionalized nanosilica particles obtained via sol–gel process. *Polymer* **42**, 879-887, doi:http://dx.doi.org/10.1016/S0032-3861(00)00392-X (2001).
146 Zelikin, A. N., Li, Q. & Caruso, F. Degradable Polyelectrolyte Capsules Filled with Oligonucleotide Sequences. *Angewandte Chemie* **118**, 7907-7909, doi:10.1002/ange.200602779 (2006).
147 Dorj, B., Park, J.-H. & Kim, H.-W. Robocasting chitosan/nanobioactive glass dual-pore structured scaffolds for bone engineering. *Materials Letters* **73**, 119-122, doi:10.1016/j.matlet.2011.12.107 (2012).
148 Ji, L., Wang, W., Jin, D., Zhou, S. & Song, X. In vitro bioactivity and mechanical properties of bioactive glass nanoparticles/polycaprolactone composites. *Materials Science and Engineering: C* **46**, 1-9, doi:10.1016/j.msec.2014.09.041 (2015).
149 Loher, S. *et al.* Improved degradation and bioactivity of amorphous aerosol derived tricalcium phosphate nanoparticles in poly(lactide-co-glycolide). *Nanotechnology* **17**, 2054-2061, doi:10.1088/0957-4484/17/8/044 (2006).
150 El-Kady, A. M., Ali, A. F. & Farag, M. M. Development, characterization, and in vitro bioactivity studies of sol–gel bioactive glass/poly(l-lactide) nanocomposite scaffolds. *Materials Science and Engineering: C* **30**, 120-131, doi:10.1016/j.msec.2009.09.008 (2010).
151 Hong, Z., Reis, R. L. & Mano, J. F. Preparation and in vitro characterization of scaffolds of poly(L-lactic acid) containing bioactive glass ceramic nanoparticles. *Acta biomaterialia* **4**, 1297-1306, doi:10.1016/j.actbio.2008.03.007 (2008).
152 Scientific, T. *Carbodiimide Crosslinker Chemistry*, <https://www.thermofisher.com/uk/en/home/life-science/protein-biology/protein-biology-learning-center/protein-biology-resource-library/pierce-protein-methods/carbodiimide-crosslinker-chemistry.html#/legacy=www.piercenet.com> (
153 Rafat, M. *et al.* PEG-stabilized carbodiimide crosslinked collagen-chitosan hydrogels for corneal tissue engineering. *Biomaterials* **29**, 3960-3972, doi:10.1016/j.biomaterials.2008.06.017 (2008).
154 Dong, R., Krishnan, S., Baird, B. A., Lindau, M. & Ober, C. K. Patterned Biofunctional Poly(acrylic acid) Brushes on Silicon Surfaces. *Biomacromolecules* **8**, 3082-3092, doi:10.1021/bm700493v (2007).
155 Salimi, A., Rahmatpanah, R., Hallaj, R. & Roushani, M. Covalent attachment of thionine onto gold electrode modified with cadmium sulfide nanoparticles: Improvement of electrocatalytic and photelectrocatalytic reduction of hydrogen peroxide. *Electrochimica Acta* **95**, 60-70, doi:10.1016/j.electacta.2013.01.154 (2013).
156 Hermanson, G. T. *Bioconjugate techniques*. (Academic press, 2013).
157 Williams, D. B. *Transmission electron microscopy : a textbook for materials science*. (Plenum, 1996).
158 *Analytical Methods, Procedures and Theory for the Physical Characterization of Fats. Section 1: XRD*, <http://lipidlibrary.aocs.org/physics/xray/index.htm> (
159 *Technical note: Zeta Potential*, <www.malvern.com> (
160 Brunauer, S., Emmett, P. H. & Teller, E. Adsorption of Gases in Multimolecular Layers. *Journal of the American Chemical Society* **60**, 309-319, doi:10.1021/ja01269a023 (1938).
161 Thommes, M. *et al.* Physisorption of gases, with special reference to the evaluation of surface area and pore size distribution (IUPAC Technical Report). *Pure and Applied Chemistry* **0**, doi:10.1515/pac-2014-1117 (2015).
162 Barrett, E. P., Joyner, L. G. & Halenda, P. P. The Determination of Pore Volume and Area Distributions in Porous Substances. I. Computations from Nitrogen Isotherms. *Journal of the American Chemical Society* **73**, 373-380, doi:10.1021/ja01145a126 (1951).
163 Tarazona, M., and Evans. Phase equilibria of fluid interfaces and confined fluids--Non-local versus local density functionals. *Molecular Physics* **60**, 573 - 595 (1987).

164 Seaton, N. A., Walton, J. P. R. B. & quirke, N. A new analysis method for the determination of the pore size distribution of porous carbons from nitrogen adsorption measurements. *Carbon* **27**, 853-861, doi:http://dx.doi.org/10.1016/0008-6223(89)90035-3 (1989).

165 Bell, N. C., Minelli, C., Tompkins, J., Stevens, M. M. & Shard, A. G. Emerging techniques for submicrometer particle sizing applied to Stober silica. *Langmuir : the ACS journal of surfaces and colloids* **28**, 10860-10872, doi:10.1021/la301351k (2012).

166 Hammersley, A. P., Svensson, S. O. & Thompson, A. Calibration and correction of spatial distortions in 2D detector systems. *Nuclear Instruments and Methods in Physics Research Section A: Accelerators, Spectrometers, Detectors and Associated Equipment* **346**, 312-321, doi:http://dx.doi.org/10.1016/0168-9002(94)90720-X (1994).

167 Harris, R. K., Becker, E. D., Cabral de Menezes, S. M., Goodfellow, R. & Granger, P. NMR nomenclature. Nuclear spin properties and conventions for chemical shifts (IUPAC Recommendations 2001). *Pure and Applied Chemistry* **73**, 1795-1818 (2001).

168 FitzGerald, V. *et al.* Bioactive glass sol-gel foam scaffolds: Evolution of nanoporosity during processing and in situ monitoring of apatite layer formation using small- and wide-angle X-ray scattering. *Journal of biomedical materials research. Part A* **91**, 76-83, doi:10.1002/jbm.a.32206 (2009).

169 Jacobsson, T. J. *Synthesis and characterisation of ZnO nanoparticles. An experimental investigation of some of their size dependent quantum effects*, Uppsala University, (2010).

170 Armelao, L., Fabrizio, M., Gialanella, S. & Zordan, F. Sol–gel synthesis and characterisation of ZnO-based nanosystems. *Thin Solid Films* **394**, 89-95, doi:http://dx.doi.org/10.1016/S0040-6090(01)01158-0 (2001).

171 Aguiar, H., Serra, J., González, P. & León, B. Influence of the Stabilization Temperature on the Structure of Bioactive Sol–Gel Silicate Glasses. *Journal of the American Ceramic Society* **93**, 2286-2291, doi:10.1111/j.1551-2916.2010.03733.x (2010).

172 Sepulveda, P., Jones, J. R. & Hench, L. L. In vitro dissolution of melt-derived 45S5 and sol-gel derived 58S bioactive glasses. *Journal of biomedical materials research* **61**, 301-311, doi:10.1002/jbm.10207 (2002).

173 R. Li, A. E. C. a. L. L. H. An investigation of Bioactive Glass Powders by sol-Gel Processing. *Journal of Applied Biomaterials* **2**, 231-239 (1991).

174 De, G., Kundu, D., Karmakar, B. & Ganguli, D. FTIR studies of gel to glass conversion in TEOS-fumed silica-derived gels. *Journal of Non-Crystalline Solids* **155**, 253-258, doi:http://dx.doi.org/10.1016/0022-3093(93)91259-6 (1993).

175 Hill, R. G. & Brauer, D. S. Predicting the bioactivity of glasses using the network connectivity or split network models. *Journal of Non-Crystalline Solids* **357**, 3884-3887, doi:10.1016/j.jnoncrysol.2011.07.025 (2011).

176 Boyd, D. & Towler, M. The processing, mechanical properties and bioactivity of zinc based glass ionomer cements. *Journal of Materials Science: Materials in Medicine* **16**, 843-850 (2005).

177 Rosenthal, A. B. & Garofalini, S. H. Structural Role of Zinc Oxide in Silica and Soda-Silica Glasses. *Journal of the American Ceramic Society* **70**, 821-826, doi:10.1111/j.1151-2916.1987.tb05634.x (1987).

178 Hudon, P. & Baker, D. R. The nature of phase separation in binary oxide melts and glasses. I. Silicate systems. *Journal of Non-Crystalline Solids* **303**, 299-345, doi:http://dx.doi.org/10.1016/S0022-3093(02)01043-8 (2002).

179 Lang, N. & Tuel, A. A Fast and Efficient Ion-Exchange Procedure To Remove Surfactant Molecules from MCM-41 Materials. *Chemistry of Materials* **16**, 1961-1966, doi:10.1021/cm030633n (2004).

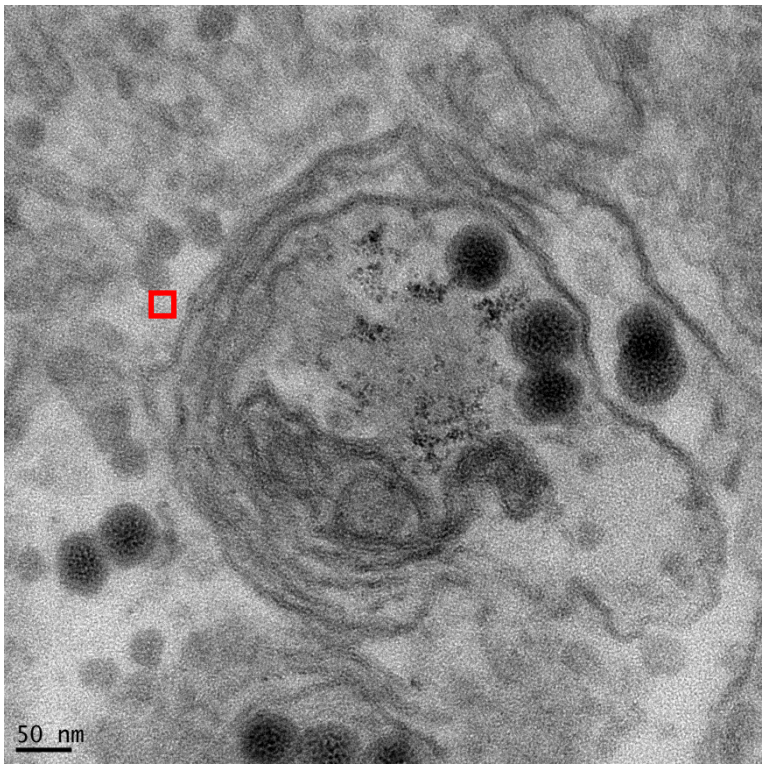
180 Cui, J. *et al.* Mechanically Tunable, Self-Adjuvanting Nanoengineered Polypeptide Particles. *Advanced materials* **25**, 3468-3472 (2013).

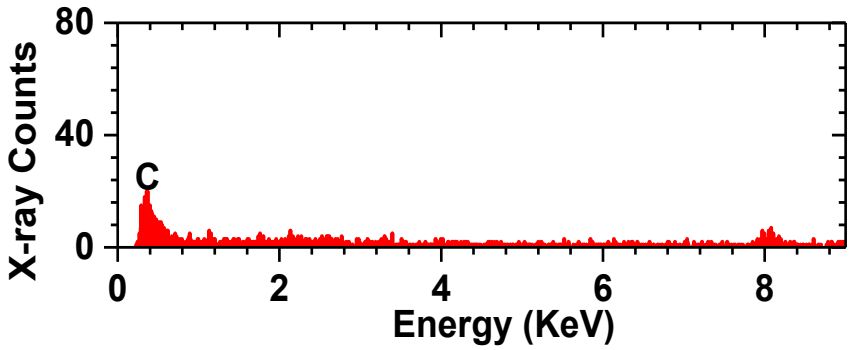
181 O'Donnell, M. D. & Hill, R. G. Influence of strontium and the importance of glass chemistry and structure when designing bioactive glasses for bone regeneration. *Acta biomaterialia* **6**, 2382-2385, doi:10.1016/j.actbio.2010.01.006 (2010).
182 von Minckwitz, G. & Martin, M. Neoadjuvant treatments for triple-negative breast cancer (TNBC). *Annals of oncology : official journal of the European Society for Medical Oncology / ESMO* **23 Suppl 6**, vi35-39, doi:10.1093/annonc/mds193 (2012).
183 Brenton, J. D., Carey, L. A., Ahmed, A. A. & Caldas, C. Molecular classification and molecular forecasting of breast cancer: ready for clinical application? *Journal of clinical oncology : official journal of the American Society of Clinical Oncology* **23**, 7350-7360, doi:10.1200/jco.2005.03.3845 (2005).
184 Sirohi, B. *et al.* Platinum-based chemotherapy in triple-negative breast cancer. *Annals of oncology : official journal of the European Society for Medical Oncology / ESMO* **19**, 1847-1852, doi:10.1093/annonc/mdn395 (2008).
185 Tu, Y.-F., Kaipparettu, B. A., Ma, Y. & Wong, L.-J. C. Mitochondria of highly metastatic breast cancer cell line MDA-MB-231 exhibits increased autophagic properties. *Biochimica et Biophysica Acta (BBA) - Bioenergetics* **1807**, 1125-1132, doi:http://dx.doi.org/10.1016/j.bbabio.2011.04.015 (2011).
186 Kokubo, T., Kushitani, H., Sakka, S., Kitsugi, T. & Yamamuro, T. Solutions able to reproduce in vivo surface-structure changes in bioactive glass-ceramic A-W. *Journal of biomedical materials research* **24**, 721-734, doi:10.1002/jbm.820240607 (1990).
187 Maçon, A. B. *et al.* A unified in vitro evaluation for apatite-forming ability of bioactive glasses and their variants. *Journal of Materials Science: Materials in Medicine* **26**, 1-10, doi:10.1007/s10856-015-5403-9 (2015).
188 Colombo, C., Monhemius, A. J. & Plant, J. A. Platinum, palladium and rhodium release from vehicle exhaust catalysts and road dust exposed to simulated lung fluids. *Ecotoxicology and environmental safety* **71**, 722-730, doi:10.1016/j.ecoenv.2007.11.011 (2008).
189 Hedberg, Y., Gustafsson, J., Karlsson, H. L., Moller, L. & Odnevall Wallinder, I. Bioaccessibility, bioavailability and toxicity of commercially relevant iron- and chromium-based particles: in vitro studies with an inhalation perspective. *Particle and fibre toxicology* **7**, 23, doi:10.1186/1743-8977-7-23 (2010).
190 Midander, K., de Frutos, A., Hedberg, Y., Darrie, G. & Wallinder, I. O. Bioaccessibility studies of ferro-chromium alloy particles for a simulated inhalation scenario: a comparative study with the pure metals and stainless steel. *Integrated environmental assessment and management* **6**, 441-455, doi:10.1002/ieam.32 (2010).
191 Marques, M. R. C. Simulated biological fluids with possible application in dissolution testing. *Dissolution technologies* **18**, 15 (2011).
192 Misra, S. K., Dybowska, A., Berhanu, D., Luoma, S. N. & Valsami-Jones, E. The complexity of nanoparticle dissolution and its importance in nanotoxicological studies. *The Science of the total environment* **438**, 225-232, doi:10.1016/j.scitotenv.2012.08.066 (2012).
193 Stebounova, L. V., Guio, E. & Grassian, V. H. Silver nanoparticles in simulated biological media: a study of aggregation, sedimentation, and dissolution. *Journal of Nanoparticle Research* **13**, 233-244, doi:10.1007/s11051-010-0022-3 (2010).
194 Pettibone, J. M. *et al.* Inflammatory response of mice following inhalation exposure to iron and copper nanoparticles. *Nanotoxicology* **2**, 189-204, doi:10.1080/17435390802398291 (2008).
195 Misra, S. K. *et al.* Isotopically modified nanoparticles for enhanced detection in bioaccumulation studies. *Environmental science & technology* **46**, 1216-1222, doi:10.1021/es2039757 (2012).
196 Bailey, M. M., Gorman, E. M., Munson, E. J. & Berkland, C. Pure insulin nanoparticle agglomerates for pulmonary delivery. *Langmuir : the ACS journal of surfaces and colloids* **24**, 13614-13620, doi:10.1021/la802405p (2008).

197 Dauty, E., Behr, J. P. & Remy, J. S. Development of plasmid and oligonucleotide nanometric particles. *Gene therapy* **9**, 743-748, doi:10.1038/sj.gt.3301759 (2002).
198 Motskin, M. *et al.* Hydroxyapatite nano and microparticles: correlation of particle properties with cytotoxicity and biostability. *Biomaterials* **30**, 3307-3317, doi:10.1016/j.biomaterials.2009.02.044 (2009).
199 Zaitsev, S. *et al.* Histone H1-mediated transfection: role of calcium in the cellular uptake and intracellular fate of H1-DNA complexes. *Acta Histochem* **104**, 85-92, doi:10.1078/0065-1281-00633 (2002).
200 Meng, H. *et al.* Engineered Design of Mesoporous Silica Nanoparticles to Deliver Doxorubicin and P-Glycoprotein siRNA to Overcome Drug Resistance in a Cancer Cell Line. *ACS nano* **4**, 4539-4550, doi:10.1021/nn100690m (2010).
201 Slowing, II, Wu, C. W., Vivero-Escoto, J. L. & Lin, V. S. Mesoporous silica nanoparticles for reducing hemolytic activity towards mammalian red blood cells. *Small* **5**, 57-62, doi:10.1002/smll.200800926 (2009).
202 Zhao, Y. *et al.* Interaction of Mesoporous Silica Nanoparticles with Human Red Blood Cell Membranes: Size and Surface Effects. *ACS nano* **5**, 1366-1375, doi:10.1021/nn103077k (2011).
203 Yamada, H. *et al.* Preparation of Colloidal Mesoporous Silica Nanoparticles with Different Diameters and Their Unique Degradation Behavior in Static Aqueous Systems. *Chemistry of Materials* **24**, 1462-1471, doi:10.1021/cm3001688 (2012).
204 Jambhrunkar, S. *et al.* Effect of surface functionality of silica nanoparticles on cellular uptake and cytotoxicity. *Mol Pharm* **11**, 3642-3655, doi:10.1021/mp500385n (2014).
205 Freyman, T. M., Yannas, I. V. & Gibson, L. J. Cellular materials as porous scaffolds for tissue engineering. *Progress in Materials Science* **46**, 273-282, doi:http://dx.doi.org/10.1016/S0079-6425(00)00018-9 (2001).
206 Woodruff, M. A. & Hutmacher, D. W. The return of a forgotten polymer—Polycaprolactone in the 21st century. *Progress in Polymer Science* **35**, 1217-1256, doi:10.1016/j.progpolymsci.2010.04.002 (2010).
207 Tang, Z. G. *et al.* Surface properties and biocompatibility of solvent-cast poly[-caprolactone] films. *Biomaterials* **25**, 4741-4748, doi:10.1016/j.biomaterials.2003.12.003 (2004).
208 Wei, J. & Huang, J. Synthesis of an Amphiphilic Star Triblock Copolymer of Polystyrene, Poly(ethylene oxide), and Polyisoprene Using Lysine as Core Molecule. *Macromolecules* **38**, 1107-1113, doi:10.1021/ma048383z (2005).
209 Yu, S. S. *et al.* Size- and charge-dependent non-specific uptake of PEGylated nanoparticles by macrophages. *International journal of nanomedicine* **7**, 799-813, doi:10.2147/ijn.s28531 (2012).
210 Otsuka, H., Nagasaki, Y. & Kataoka, K. PEGylated nanoparticles for biological and pharmaceutical applications. *Advanced drug delivery reviews* **64**, 246-255, doi:10.1016/j.addr.2012.09.022 (2012).

Appendix 1 – STEM-EDS of cell cytoplasm

11Zn particles internalised by an MCF-7 cell, 24 h

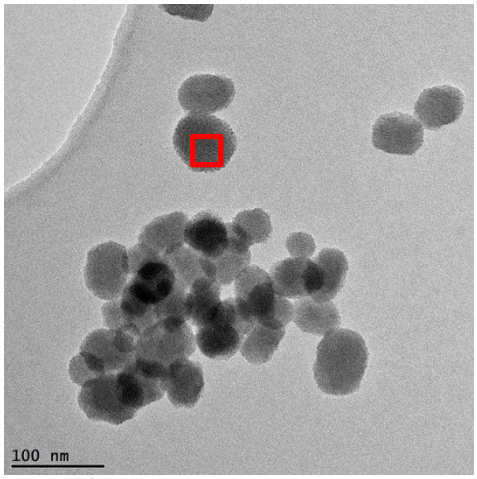




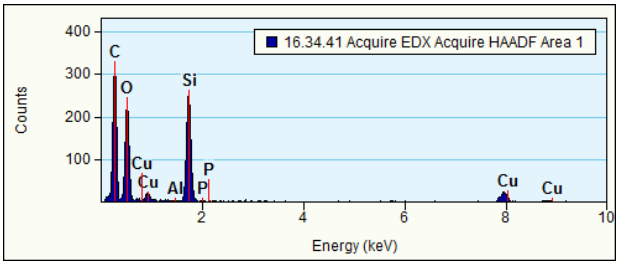
Appendix 2 – STEM-EDS on dissolution products

14Zn MSNs:

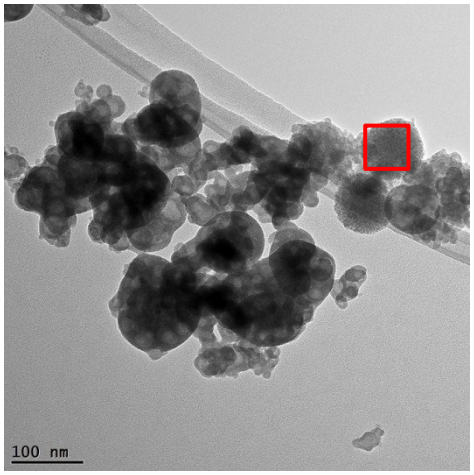
24 h, ALF



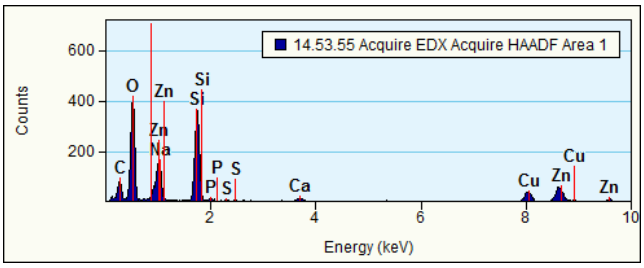
Si	O	Mg	P	Ca	Zn	Na
1	2.19	–	–	-	-	–

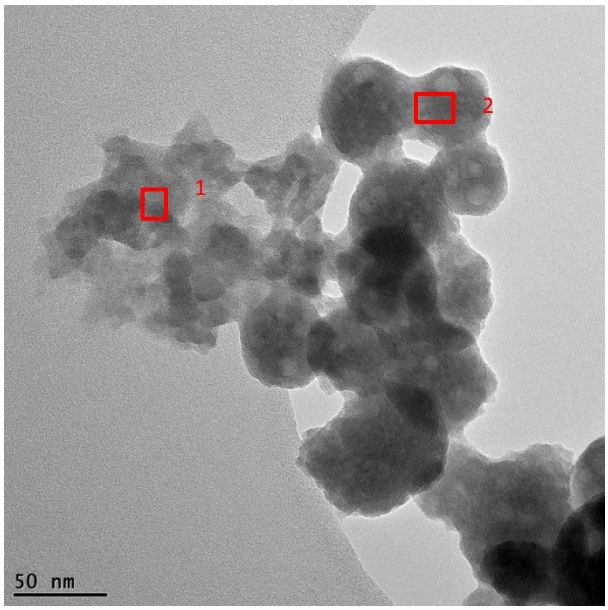


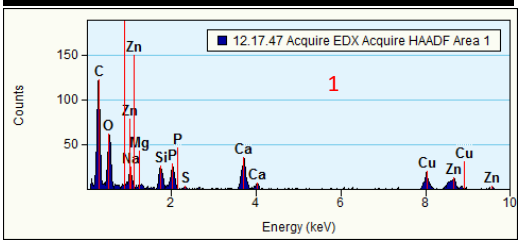
24 h, MEM + FBS

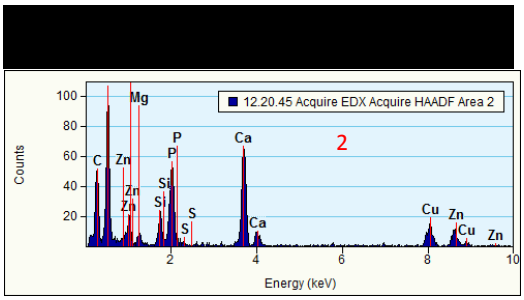


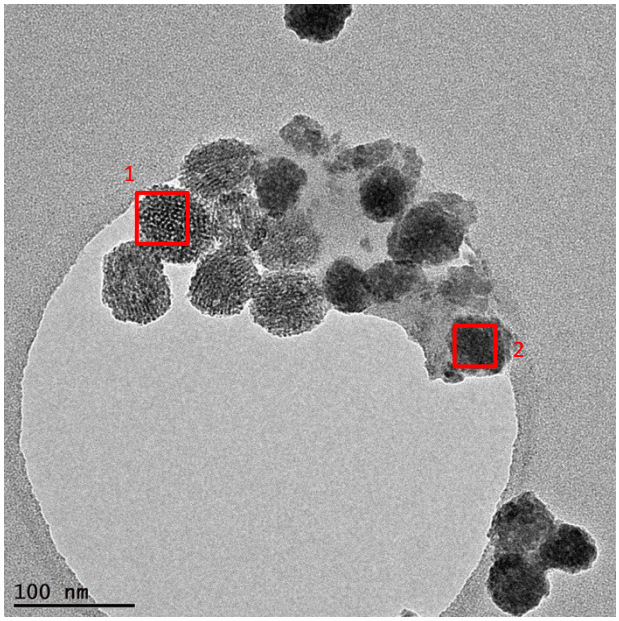
Si	O	Mg	P	Ca	Zn	Na
1	2.52	–	–	0.04	0.24	0.51



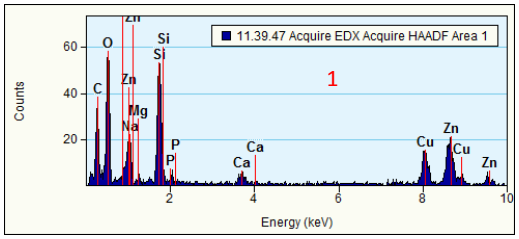




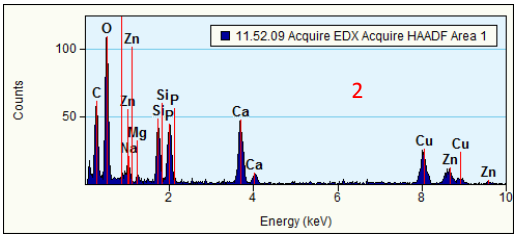




Si	O	Mg	P	Ca	Zn	Na
1	2.85	–	0.02	0.06	0.42	–

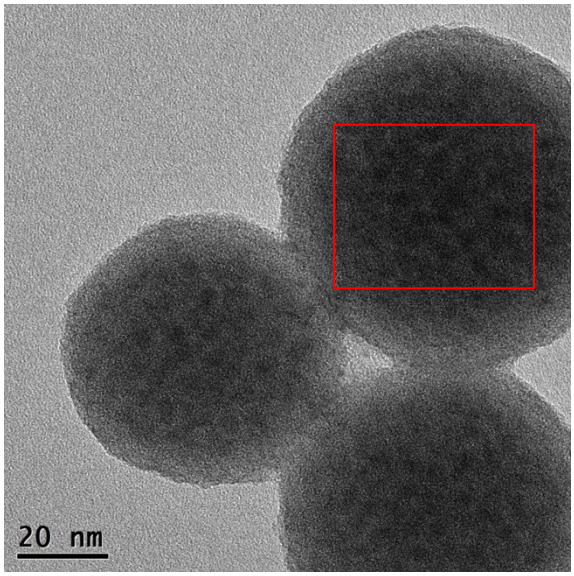


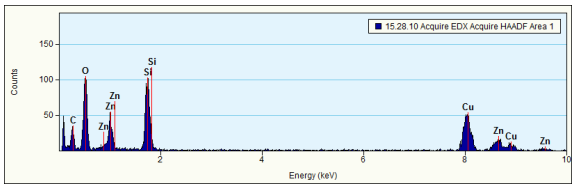
Si	O	Mg	P	Ca	Zn	Na
1	3.84	0.05	0.78	0.83	0.38	0.26



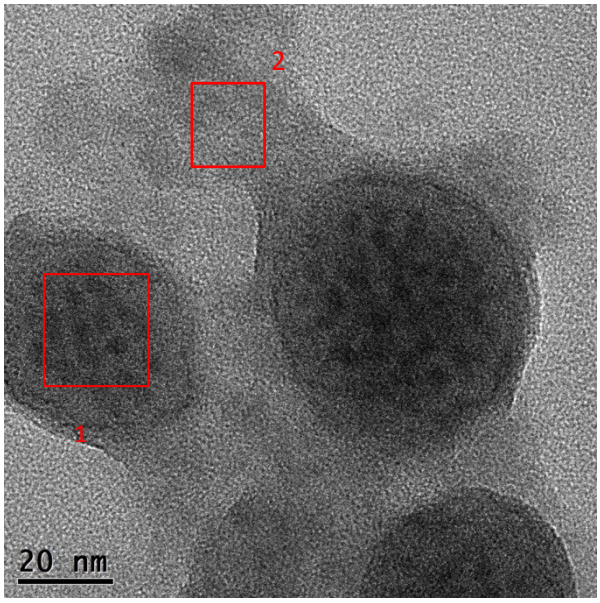
23Zn Dense NPs:

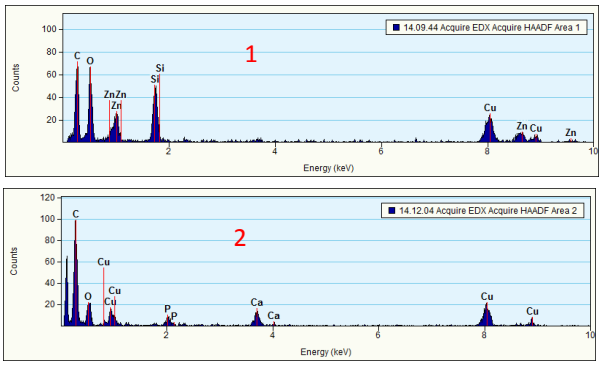
24 h, ALF





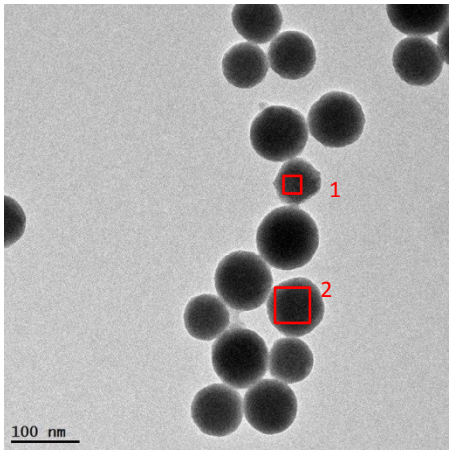
24 h, MEM-FBS

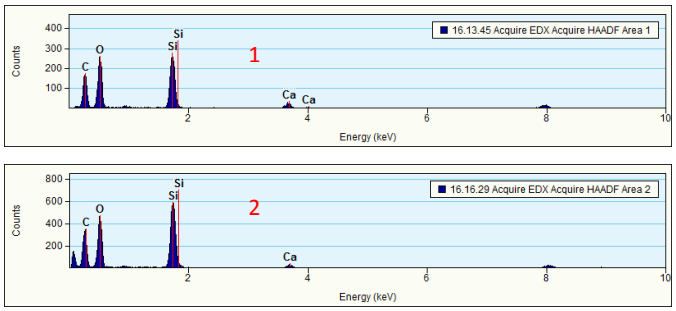




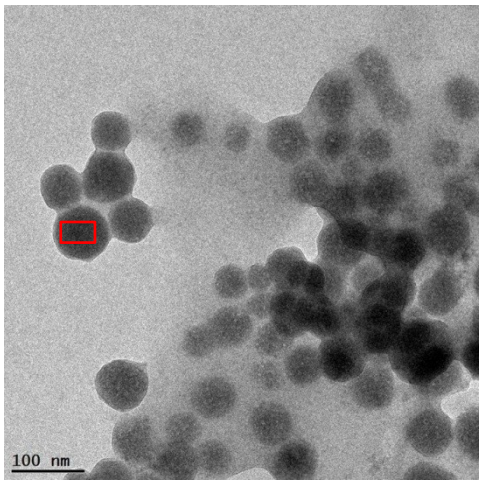
9Ca Dense NPs:

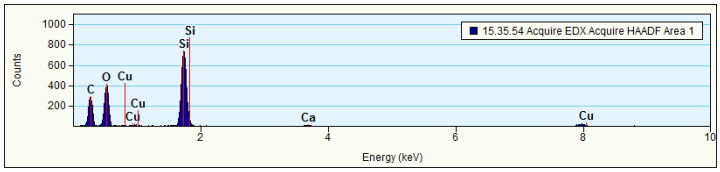
24 h, ALF





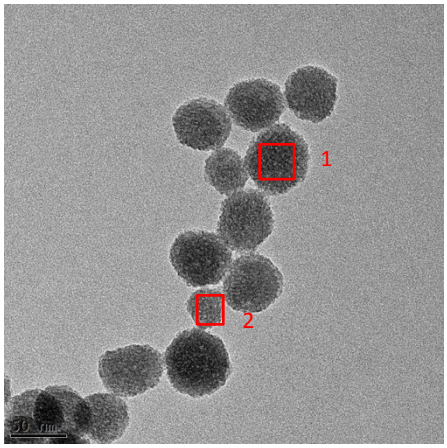
24 h, MEM-FBS

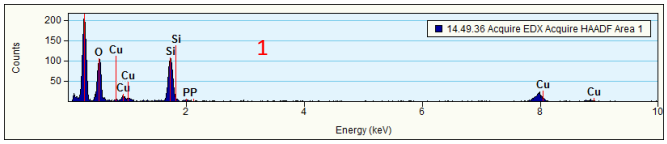


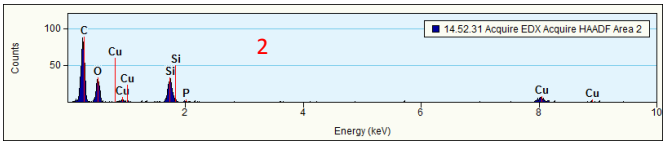


11Ca MSNs:

24 h, ALF







24 h, MEM + FBS

